Vibration Assisted Drilling of Multidirectional Fiber Reinforced Polymer Laminates

Ahmad Sadek

Department of Mechanical Engineering

McGill University

Montreal, Quebec

April 2014

A thesis submitted to McGill University in partial fulfillment of the requirements of the degree of Doctor of Philosophy

Abstract

Defects associated with drilling of Carbon Fiber Reinforced Polymers (CFRPs) are of major economic and safety concerns for aerospace manufacturers. Delamination of layers and thermal damage of the matrix are the most critical defects associated with drilling of FRP laminates, which can be avoided by keeping the drilling forces and temperatures below some threshold levels. Vibration-Assisted Drilling (VAD) is an emerging drilling process that uses intermittent cutting to reduce the drilling forces and temperatures, and achieve easier chip removal and longer tool life.

This research provides insights into the mechanical and thermal aspects of VAD of FRPs, which have not been studied before. In order to achieve this, a comprehensive experimental investigation was performed on the effects of the key independent and combined VAD parameters on the drilling forces and temperatures as well as on the produced hole quality. The experimental results of VAD were compared to corresponding results of conventional drilling to assess the amount of improvement or deterioration achieved by the VAD process. This comparison showed that VAD could reduce the axial drilling forces by up to 40%, and the drilling temperature by up to 30%. The VAD also could eliminate exit delamination and thermal damage that took place in conventional drilling through a range of drilling conditions.

A generalized novel force model for conventional and vibration assisted drilling of multidirectional FRP laminates was developed to provide a reliable and feasible predictive capability for process design and optimization. The developed model was based on a semi-analytical approach that employs the feasibility of the mechanistic modeling techniques and respects the fundamental mechanics of the different chip formation mechanisms at different FRP fiber orientations. The developed model has the capability of capturing the force and torque features in the steady state and transient stages within an error range of -10% to +20% for conventional drilling and ±20% for VAD, with a confidence interval of 95%. This prediction capability and accuracy have not been achieved before for conventional and vibration assisted drilling of multidirectional FRP.

Résumé

Les défauts liés au perçage de polymères renforcés de fibres de carbone (PFRC) sont de grandes préoccupations économiques et de sécurité pour les fabricants de l'aérospatiale. Le délaminage des couches et les dommages thermiques de la matrice sont les défauts les plus critiques associés au perçage de panneaux de (PFR); ils peuvent être évités en maintenant les forces de forage et des températures inférieures à certains niveaux de seuil. Le perçage assisté par vibration (PAV) est un procédé de perçage émergent qui utilise la coupe intermittente afin de réduire les forces de forage et les températures, de rendre plus facile l'évacuation des copeaux, et de prolonger la durée de vie de l'outil par rapport au perçage conventionnel.

Cette recherche permet de mieux comprendre les aspects physiques et thermiques du PAV de PFR, un procédé qui n'a pas été étudié auparavant. Pour ce faire, une étude expérimentale extensive a été réalisée sur les effets des paramètres principaux du PAV, indépendants et combinés, sur les forces de perçage, les températures ainsi que sur la qualité du trou produit. Les résultats expérimentaux de mesure du PAV ont été comparés aux résultats correspondants au perçage conventionnel pour évaluer l'amélioration ou de la détérioration atteinte par le PAV. Cette comparaison a montré que le PAV peut réduire les forces axiales de perçage jusqu'à 40 %, et la température de perçage jusqu'à 30%. Le PAV pourrait également éliminer le délaminage à la sortie du trou et les dommages thermiques inhérents au perçage conventionnel à travers une gamme de conditions de perçage.

Un nouveau modèle généralisé des efforts de perçage conventionnel et du PAV associés au PRF stratifiés multidirectionnels a été développé pour fournir une prédiction fiable en vue de conception et optimisation du procédé. Le modèle développé est basé sur une approche semi-analytique qui emploie les techniques de modélisation mécaniste et respecte principes gouvernant les différents mécanismes de formation de coupeaux à différentes orientations de fibres de PRF. Le modèle permit de capturer les efforts de coupe et le couple dans les régimes permanents et transitoires dans une gamme d'erreur entre -10% et +20% pour le perçage conventionnel et ± 20% pour le PAV, avec un intervalle de confiance de 95 %. Une telle précision n'a jamais été atteinte pour prédire ces caractéristiques tant pour le perçage conventionnel que le PAV utilisés pour des PRF stratifiés multidirectionnels.

Claims of Originality

1. A new generalized predictive force model for conventional and vibration assisted drilling of multidirectional FRPs has been developed. The developed model deals with a wide range of process parameters, material configurations and drilling tool geometries. It accounts also for the workpiece deformation and the dynamic tool-workpiece interaction during drilling. The model accurately predicts the details of the force and torque features due to variable uncut chip thickness and fiber orientation through the steady state and transient stages under different drilling conditions, which has not been achieved by the models in the open literature.
2. The mechanism of heat dissipation in VAD was investigated and explained through modeling the cooling effect of the air flow in the gap created during the separation between the tool and the workpiece. This aspect has not been addressed before in the open literature.
3. A unique experimental setup was developed to control the LFHA VAD parameters independently, monitor the cutting temperatures, system dynamics and perform in-process rectification of the measured forces. This allowed performing a systematic study of VAD parameters, covering a wider range of parameters that were not investigated before. This study led to defining global optimum VAD conditions for maximum productivity.
4. The force reduction in VAD is explained, for the first time, through the analysis of the process kinematics and the resultant effect of the modulation amplitude and the phase difference between the trajectories of the cutting edges on the maximum uncut chip thickness. In contrast, the research reported in the open literature has considered only the effect of the phase difference on chip breakage in VAD of metals, which does not apply to FRPs.
5. New multi-dimensional machinability maps of LFHA VAD of CFRP were generated to establish the effect of the independent VAD parameters on various hole quality attributes. This provides the VAD process designer with a powerful tool for the design and optimization of the VAD of CFRP laminates.

Acknowledgment

I would like to thank my supervisor Dr. Helmi Attia and Dr. Pascal Hubert for their continuous and invaluable support throughout my PhD research work. Additionally, I would like to express my sincere gratitude to Dr. Helmi Attia for his great support and guidance on the scientific, professional and personal levels. I really am honored to be his student and to learn from him in various aspects of life, which made working with him a process of comprehensive development.

I would like to thank the National Research Council (NRC) of Canada, for hosting my entire PhD work in the lab of the Aerospace Advanced Material Removal Processes, and for the full financial support throughout my PhD research.

I would like to express my deep gratitude to Dr. Mouhab Meshreki at the NRC for all what I learned from him, and I can confidently say that this research wouldn't have been in such a form without his great and sincere support. I would like also to thank the research and technical officers at the material removal group of the NRC for being so helpful and cooperative.

Special thanks go to my coach Mohamad Lotfi, and my friend Ahmed Korashy for always being there for me with true guidance, sincere advice and endless support.

Words cannot express my gratitude to my father Amr for being such a great inspiration, my mother Khaleda for all her invaluable support, and my wife Eness for her great patience and sincere support and love. Finally, I would like to thank my children Amena, Abdullah, and Mariam for their understanding and for having to reschedule many of their planned weekend entertainment activities for the sake of this research.

Table of Contents

List of Figures

List of Tables

Nomenclature

Symbols

A_{chip}	Projected uncut chip area (mm^2)
A_m	Modulation amplitude (mm).
b	Width of cut (mm)
$\boldsymbol{C}$	The matrix of the damping coefficients
C_d	Damping coefficient of the dynamometer (N.s/m)
$C_{h,i}$	Rake angle correction factors in the horizontal direction
C_s	Damping coefficient of the shaker (N.s/m)
$C_{v,i}$	Rake angle correction factors in the vertical directions
d	Total uncut chip thickness (mm)
d_c	Modified uncut chip thickness of the chisel edge after deflection (mm)
d_d	Dynamic uncut chip thickness (mm)
D_h	Nominal drilled hole diameter (mm)
D_m	Maximum diameter of the circle encompassing the observed delamination (mm)
d_o	Conventional uncut chip thickness (mm)
d_p	Modified uncut chip thickness of the primary cutting edge after deflection (mm)
E_T	Total modulus of elasticity of the deflecting laminate in the fiber direction (GPa)
E_x	Modulus of elasticity of a single ply in the fiber direction (GPa)

$\boldsymbol{F}$	Vector of external forces acting on dynamometer face (N)
f_a	Axial feed (mm/min)
F_c	Orthogonal cutting force (N)
$F_{c,m}$	Measured chisel edge axial force (N)
F_d	Drilling force measured by the dynamometer (N)
F_E	External force acting on the dynamometer face (N)
$F_{p,m}$	Measured primary edge axial force (N)
f_r	Feed (mm/rev)
F_x *and* F_y	Predicted in plane oblique drilling forces (N)
F_z	Predicted oblique thrust forces (N)
g	Gap width between the tool and the workpiece (mm)
G	Normalized gap width
h_g	Coefficient of heat transfer in the air gap (W/m^{2}k)
H_l	Total laminate thickness (mm)
h_s	CHT at the lateral surface of the rotating tool (W/m^{2}k)
H_V	Vertical height of the cutting lip (mm)
$\boldsymbol{K}$	Dynamic stiffness matrix of the VAD system (N/m)
K_a	Thermal conductivity of air (W/(m.K))
K_c	Experimentally defined cutting pressure for orthogonal cutting (N/mm^2)
K_d	Dynamic stiffness of the dynamometer (N/m)
$K_{F,c}$	Axial force cutting pressure of the chisel edge (N/mm^2)
$\boldsymbol{K_{F,c}}$	Vector of axial force cutting pressures on the chisel edge (N/mm^2)

$K_{F,p}$	Axial force cutting pressure of the primary cutting edge (N/mm^2)
$\boldsymbol{K_{F,P,r}}$	Vector of axial force cutting pressures on the primary cutting edge (N/mm^2)
$K_{h,I}$, $K'_{h,I}$ *and* $K_{v,i}$	Corrected on-axis (orthogonal) cutting pressures of the primary cutting edge (N/mm^2)
$K_{h,r,I}$, $K'_{h,r,I}$ *and* $K_{v,r,i}$	Uncorrected on-axis (orthogonal) cutting pressures of the primary cutting edge (N/mm^2)
K_s	Dynamic stiffness of the shaker (N/m)
$K_{T,c}$	Torque cutting pressure of the chisel edge (N.m/mm^2)
$\boldsymbol{K_{T,c}}$	Vector of torque cutting pressures on the chisel edge (N.m/mm^2)
$K_{T,p}$	Torque cutting pressure of the primary cutting edge (N.m/mm^2)
$\boldsymbol{K_{T,P,r}}$	Vector of torque cutting pressures on the primary cutting edge (N.m/mm^2)
$K_{X,I}$, $K'_{Y,I}$ *and* $K_{Z,i}$	Corrected off-axis (oblique) cutting pressures of the primary cutting edge (N.m/mm^2)
$K_{X,r,I}$, $K'_{Y,r,I}$ *and* $K_{Z,r,i}$	Uncorrected off-axis (oblique) cutting pressures of the primary cutting edge (N.m/mm^2)
L_c	Chisel edge length (mm)
L_p	Primary cutting edge length
$\boldsymbol{M}$	Matrix of dynamic masses (kg)
M_1	Dynamic lumped mass of the dynamometer face plate and workpiece (kg)
M_2	Dynamic lumped mass of the dynamometer base and shaker head (kg)

n	Rotational speed of the tool (rpm)
N	Total number of the laminate plies
N_c	Numbers of layers engaged with the chisel edge
N_p	Number of layers engaged with the primary edge
Nu	Nusselt Number
R	Outer drilling tool radius (mm)
Ra	Mean surface roughness parameter (μm)
R_c	Thermal contact resistance (m^2K/W)
Re	Reynolds number
Re_{cr}	Critical Reynolds number
R_{fin}	The thermal resistance of the annular fin element (m^2K/W)
r_i	Radius of the point i from the tool central axis (mm)
t	time (sec)
T_b	Temperature of the tool base (K°)
$T_{c,m}$	Measured chisel edge torque (N.m)
t_p	Thickness of a single cured ply (mm)
$T_{p,m}$	Measured primary edge torque (N.m)
t_w	Drilling tool web thickness (mm)
v	Kinematic viscosity of air
$v_{c,i}$	Linear cutting speed of a point "*i*" on the cutting tool lip (m/min)
v_r	Reference cutting velocity of the middle section of the primary cutting edge (m/min)

w	Uniform thickness of an annular fin element (mm)
$\boldsymbol{x}$	Vector of displacements of the VAD system (m)
x_m	The displacement of the dynamometer face mass (m)
x_s	Displacement of the dynamometer base and shaker head mass (m)
Z_c	Axial position of the tool tip (mm)
Z_{fi}	Vertical position of the interface between ply "i" and "$i+1$" (mm)
α	the rake angle of the cutting edge (deg)
α_m	Mean rake angle of the primary cutting edge (deg)
δ_l	Laminate deflection (mm)
Δt	Force model time increment (sec)
ΔZ_c	Axial position increment of the tool tip (mm)
ε	Drilling tool point angle (deg)
θ_e	Effective fiber orientation angle (deg)
$\boldsymbol{\theta_{e,c}}$	Vector of effective orientation angles on the chisel edge (deg)
$\boldsymbol{\theta_{e,p}}$	Vector of effective orientation angles on the primary cutting edge (deg)
θ_i	Fiber orientation of a ply 'i' (deg)
λ	Inclination angle between the cutting edge and the normal to the cutting direction (deg)
τ	Period of one tool vibration cycle (sec)
Φ	Cone vertex angle (deg)
φ	Phase difference between the peaks of two successive machined surfaces (deg)

ψ	Angular position of the primary cutting (deg)
ψ_c	Angular positions of the chisel edge (deg)
ψ_c'	Chisel edge angle (deg)
ψ_p	Angular position of the primary cutting edge (deg)
Ω_s	Sampling rate of the experimental force measurement (Hz)
ϕ_d	Delamination factor
ω_m	Modulation frequency (Hz)

Abbreviations

ASR	Axial Speed Ratio
CFRP	Carbon Fiber Reinforced Polymer
CHT	Coefficient of Heat Transfer
DOC	Depth of Cut
FD	Finite Difference
FEM	Finite Element Modeling
FRP	Fiber Reinforced Polymer
GFRP	Glass Fiber Reinforced Polymer
HFLA	High Frequency Low Amplitude
HSD	High Speed Drilling
HSS	High Speed Steel
LFHA	Low Frequency High Amplitude
MQL	Minimum Quantity Lubrication
OD	Orbital Drilling

PCD	Polycrystalline Diamond
p-p	Peak -to-Peak
rpm	Revolution Per Minute
UHS	Ultra-High Speed
VAD	Vibration Assisted Drilling
VAM	Vibration Assisted Machining

CHAPTER 1

Introduction

The industrial use of fiber-reinforced plastics (FRP) has been growing since they were first introduced in the thirties of the last century. Their enhanced thermal resistance, damping capacity, and strength to weight ratio are the main reasons they were promoted from being used to build secondary parts to being used now in aircraft structures and load carrying elements. Assembly of composite parts for aerospace application represents a huge challenge. This stems from either the limited reliability of the joints made by different methods of assembly (e.g. adhesive bonding), or from the material damage that can be associated with the drilling processes required for mechanical fastening of composite structures and parts. However, mechanical fastening is still the most widely used method of assembly in the aerospace industry. Therefore, there are tremendous efforts exerted towards improving the performance of the existing conventional processes and introducing new nonconventional drilling processes that can provide root solutions to the challenges facing the industry.

1.1. Research Motivation

As will be shown later in the literature review in chapter 2, research efforts have been done to consume all the possible chances of success of the conventional drilling of FRPs before thinking of other nonconventional processes. This included testing conventional drilling with different modes of lubrication (MQL and air), as well as drilling tool geometry and coating optimization as a means of reducing drilling associated defects via reducing the drilling forces and temperatures, while maintaining the process productivity. However, such techniques did not significantly reduce or eliminate the undesirable drilling defects. The other alternative was testing the performance of high speed conventional drilling, which was expected to reduce

the drilling forces and to enhance productivity, but it exhibited significant limitations on the tool life and the effect of tool dynamics.

The intermittent cutting processes (vibration assisted drilling (VAD) and orbital drilling) were considered as an alternative that can overcome the limitations of conventional drilling. The preliminary results of both processes have shown a significant capability of reducing the drilling forces and temperatures and eliminating delamination. However, the orbital drilling process has significant limitations on the productivity and the hole geometric accuracy. On the other hand, the VAD process, has exhibited a huge potential in force and temperature reduction in drilling of metallic materials. Additionally, one important advantage of the VAD process is that the process productivity is not affected by the means of introducing the intermittent tool motion to the process via superimposing a harmonic motion over the conventional axial feed motion.

The extensive investigation of the available literature and the discussions with other recognized research teams in the same field shows that the mechanics of VAD of multidirectional FRP laminates is not yet fully understood. Additionally, the fact that there are no well-established predictive force models that can predict the principal force and torque features during conventional drilling of FRP laminates in the first place represent a remarkable gap which needs to be addressed.

1.2. Research Objectives

Based on the aforementioned discussion, the present research is aiming at addressing the following two priorities:

The first research priority is to provide insight into the mechanics of the VAD process from mechanical and thermal aspects, as well as into the effect of the independent and combined process parameters on the drilling forces and temperature behavior, which controls the final produced hole quality. This priority necessitates building a reliable experimental setup that facilitates independent control of the main VAD parameters. The experimental investigation of the VAD process is performed to study the effects of

the main independent process parameters (speed, feed, frequency and amplitude) on the drilling force, temperature, and hole quality attributes. In addition, the hypothesis that the VAD combined parameters have unique intrinsic effects on the process outputs will be tested. The ratio of the maximum speed of tool vibration to the axial speed of the tool feed is a key parameter, known as axial speed ratio (ASR). The effect of different ASR values that fulfill the intermittent cutting condition of ASR >1 will be investigated to test the aforementioned hypothesis.

The second research priority is to develop a generalized force model for drilling of FRP laminates that can predict the principal force and torque features in the steady state and transient stages of conventional and vibration assisted drilling. This model completes the comprehensive understanding of the drilling processes of FRP laminates, through revealing details that cannot be measured experimentally (e.g. force distribution along the cutting edges). It also provides interactive prediction capabilities that can be used for tool design and process parameters optimization.

The predictive model for drilling of multidirectional FRP laminates has to incorporate the following features:

- Utilizes a feasible modeling approach and at the same time, respects the fundamental mechanics of the different chip formation mechanisms at different FRP fiber orientations
- Requires minimal efforts in terms of experimental calibration.
- Represents a reliable, flexible and generic tool that can deal with a wide range of variability in FRP material layup configurations, process parameters, tool geometries, dynamic tool-workpiece interactions, and material deformation during drilling. This allows the end user of the model to use it as a robust and rapid tool for designing the drilling of FRP process and tool design.
- Can be further utilized to predict subsequent material damage and tool wear.
- The model prediction errors have to be within the acceptable range of the industry.

1.3. Thesis Outline

The aforementioned research objectives will be addressed in the thesis according to the following outline:

1. Chapter 1 presented an orientation on the relevance of the research question in addition to a brief introduction on the scope and the outline of the proposed approach of dealing with the research problem.
2. Chapter 2 will discuss the research work that has been reported in the available literature on drilling of FRPs and drilling induced mechanical and thermal damage in FRP laminates. Furthermore, the chapter will discuss the research work done in the literature on modeling of drilling forces in FRP using different approaches. Such a discussion that encompasses the full picture of the problem will lead to defining the missing links that need to be addressed; hence, the experimental and theoretical research objectives are defined accordingly.
3. Chapter 3 will describe the mechanics of the VAD process from kinematic, mechanical and thermal aspects. This discussion involves information from experimental and analytical analysis from the literature and from the preliminary tests and models that were carried out at the beginning of this research. This is used to develop a deeper understanding of the role of each of the VAD process parameters in controlling the process outputs.
4. Chapter 4 will show the description of the performed experimental analysis on VAD. This includes the experimental setup, the design of the VAD experiments, force and temperature measurement systems, and the methods of process characterization.
5. Chapter 5 will discuss the experimental results of the effect of the VAD process parameters on the drilling forces and temperatures as well as on the produced hole quality attributes. In order to quantify the improvement or deterioration of the VAD outputs, the results of VAD at given conditions will be compared to the results of conventional drilling performed at corresponding conditions.

6. Chapter 6 will show the formulation of the functions and the sub-models incorporated in the generalized mechanistic force model to predict the drilling forces and torques for conventional and vibration assisted drilling of CFRPs.
7. Chapter 7 will show the experimental validation of the model by comparing the model force and torque predictions to the corresponding measured force and torque signals of conventional and vibration assisted drilling. This will be followed by presenting the capability of the validated model of revealing features that are impossible to measure experimentally, e.g., the force distribution along the cutting edges. The final section of the chapter will present the model predictions of the force and torque trends for different combinations of conventional and vibration assisted drilling.
8. In Chapter 8, the main conclusions of the entire research will be presented, as well as the recommendations for the future research work.

CHAPTER 2

Literature Review

2.1. Introduction

Tremendous research efforts have been exerted towards improving the performance of the conventional drilling processes as well as towards introducing new nonconventional drilling processes in order to provide root solutions to the drilling induced material damage. The research done in this regard focused on the experimental characterization and the modeling of the drilling processes of FRPs. The contributions and findings of the research efforts that were reported in the open literature are discussed through the following sections of this chapter.

2.2. Conventional Drilling of FRPs

The conventional drilling process of FRP laminates has been widely investigated in the available literature. The majority of the research work on conventional drilling of FRPs focused on the effect of the process parameters on the drilling forces and the produced hole quality, especially delamination. A few was reported on the thermal aspect of the conventional drilling of FRPs in terms of the effect of the process parameters on the drilling temperature.

The research work carried out by Malhotra et al. in [1] focused on the behavior of the thrust force and torque during dry drilling of woven carbon epoxy laminate using a HSS drill. The reported results showed that the thrust force increased directly with the increase in feed at a constant rotational speed. On the other hand, increasing the cutting speed was found to have less influence on the thrust force compared to that of changing the feed. The torque was found to be changing directly with the change in the feed and inversely with the change in the rotational speed. The findings of the drilling experiments reported in [2] showed thrust force trends similar to those

reported in [1]. The range of rotational speeds and feeds tested in [3] was wider and higher than that used by Malhotra et al. in [1]. Ho-Cheng et al. [3] also confirmed the thrust force trends through dry drilling tests using carbon/epoxy and carbon/acrylonitrile butadiene styrene as workpiece materials and a two-flute HSS twist drill. Similar thrust force and torque trends with the change of the feed were reported in the work done in [4] using woven carbon fiber, and in [5] woven E-glass fiber and epoxy. However, the thrust force and torque were found to have an inverse relationship with the rotational speed for a constant feed rate. The high rotational speed results in higher friction induced temperature rise, which leads to softening of the polymer matrix and hence reduces the axial force and torque [6].

The effect of the drilling parameters on the material entry and exit delamination has been the focus of many research studies, since delamination can deteriorate the mechanical properties of the produced part [5, 7]. The drilling forces (thrust and torque) were found to be the main factor that controls the material entry and exit delamination [8].

The research work carried out by Davim et al. in [8, 9] investigated the effect of the cutting speed and feed on the entry and exit delamination. The delamination was found to increase with higher cutting speed and feed. Tagliaferri et. al. [10], investigated the effect of the aforementioned drilling parameters on the delamination of glass fiber reinforced plastic (GFRP) composites. The reported results in [10] showed that the width of the damage zone (D) around the drilled hole, increased with an increase in feed and decreased with an increase in speed; similar findings were reported by [5, 11, 12] on the experimental investigation of the effect of drilling conditions on the delamination of FRPs.

The previous discussion indicates that the conventional drilling of FRPs in dry conditions tends to require low feeds combined with high rotational speeds for most of the cases in order to reduce mechanical damage. Operating at low feeds compromises the processes productivity and increases the tool-workpiece contact time. This promotes tool wear and thermal damage of the FRP material especially

when drilling is performed at the high range of the so far investigated rotational speeds.

Therefore, a motivation to modify the conventional drilling process in order to untie this conflict was created. By that time, high and ultrahigh speed machining has been exhibiting great enhancements in machining of metallic material. The principle behind the enhancement of the drilling process performance with high speed is based on the relationship between the rotational speed and the axial feed of the drilling tool. The increase in rotational speed of the drilling tool for a fixed axial feed reduces the feed per tooth, which can significantly reduce the cutting energy within a certain range, and accordingly reduces the mechanical and thermal material damage. This effect facilitates operating at a higher axial feed range with low drilling forces, less tool-workpiece contact time and higher productivity. On the other hand, the high rotational speed in many cases is associated with undesirable tool dynamics and friction induced temperature rise that leads to accelerated tool wear and thermal material damage. Moreover, reducing the feed per tooth to extremely low values can reverse the force trend because of high cutting pressures and the process can deteriorate due to dynamic instability.

2.3. High Speed Drilling of FRPs

The work done in [6] on HSD of woven CFRPs investigated the drilling forces at high and very high speed ranges (210 – 850 m/min) in combinations with low feed rates. The reported results showed that the thrust and the cutting forces increased significantly at higher rotational speeds as the feed rate increased. It was explained that as the rotational speed increases, the effect of lateral friction and tool wear become more significant, thus increasing the cutting forces for a fixed feed. Aside from the effect of the feed per tooth on the cutting forces, the increase in cutting forces at higher cutting speeds could be due to the strain rate, lateral friction between the tool and the workpiece or the effect of cutting edge pressing in the soft matrix at higher temperatures [13]. Although the matrix softening is supposed to result in force

reduction, this reduction was not however significant due to the superior effect of the fiber strength compared to the matrix strength.

In [11], Enemuoh *et. al.* developed a multi-objective function optimization one objective of which was to obtain delamination free holes in CFRPs. Their results recommended using high rotational speeds and low feeds for producing delamination free holes. The results shown in [14] confirmed this recommendation for the range of ultrahigh speed drilling, and attributed this behavior to the axial force reduction at low feed and high speed.

The performance of very high speed drilling (higher than 15,000 rpm) of CFRPs was investigated in [14] for high productivity axial feeds of 8 and 12 m/min under dry conditions. The reported results showed that the thrust forces decreased with the increase in the rotational speed, due to the decrease in the feed per tooth. This implies that HSD allows drilling holes at productive axial feeds, which used to be unworkable with lower cutting speed ranges because of thrust force associated defects (e.g. delamination). It was also reported that the higher axial feed resulted in higher thrust forces for this range of rotational speeds. On the other hand, an increase in cutting forces with higher axial feeds was observed, which was attributed to the tool corner wear and the significant lateral friction between the tool and the workpiece at high rotational speeds. In order to assess the effect of the ultra-high speed UHS on the tool wear, the authors in [14] compared the measured flank wear in the case of (>15000 rpm) to the flank wear reported in [15] for HSD (6000 rpm to 15000 rpm). The comparison showed that the flank face wear could experience initial, steady, and ultimate wear stages for drilling over 500 holes in the case of HSD, while in the case of the UHS drilling, the tool reached the ultimate flank wear after 20 holes, which agrees with the rapid tool wear reported in [6] for UHS drilling of woven CFRPs.

The effect of tool wear on the maximum recorded tool and workpiece temperatures for UHSD of 20 holes, which was reported in [14]. The temperature increased with the increase of the rotational speed as a result of the corresponding increase of the friction between the tool and workpiece. The authors could correlate the trend of the increase in the maximum tool temperature to the level of tool wear

experienced at each drilling speed. The reported results showed that although the maximum tool temperature exceeded the material decomposition temperature, the material did not however experience any considerable thermal damage. This was attributed to the very low contact time between the tool and the workpiece due to the high axial feed.

The previous discussion implies that although drilling at high and ultrahigh speeds was able to reduce the axial forces, and hence the exit delamination, the increased tool temperature accelerated the tool wear drastically, in such a way that the tooling cost represents a significant limitation of the process. Moreover, the analysis implies that the temperature rise in UHSD could result in thermal damage if applied to thick composite plates or hybrid metal/composite stacks, where prolonged contact takes place between the hot tool and the workpiece. This directed the sight of researchers towards novel modes of lubrication.

2.4. Intermittent Drilling Processes of FRPs

The intermittent cutting is a process where one or more cutting edges of the tool are not in continuous engagement with the workpiece[16]. Some machining processes have an intermittent nature due to the discontinuity of the contact between the tool cutting edges and the workpiece (e.g. side milling) [17]. On the other hand, the continuous motion in turning or drilling can be modified to be intermittent by the means of superimposing a secondary motion (e.g. axial and elliptical vibration) over the feed motion of the tool. The studies on the cutting temperatures of the intermittent cutting highlight the significant role of the interrupted contact between the tool and the workpiece in temperature is reduction [18-23]. The cutting forces in intermittent cutting of metals were found to be reduced in some cases due to less contact time and length between the chip and the rake face of the tool which reduces the frictional force component [24]. The force and temperature reduction of the intermittent cutting processes attracted many researchers to study the possibility of implementing such technique in drilling of FRPs to in order to reduce or eliminate the drilling induced damage due to excessive forces and temperature rise. The following

subsections discuss the main findings of the research reported on orbital and vibration assisted drilling, which represent two intermittent drilling processes that have shown substantial potential to improve the performance and the quality of the produced FRP parts.

2.4.1. Orbital Drilling of FRPs

Orbital drilling (OD) is an emerging drilling technique that has exhibited a huge potential for eliminating defects associated with drilling of CFRP laminates [25-27]. One explanation of the axial force reduction in OD is the helical motion, which eliminates the axial dwell of the stationary drilling tool center over the uncut material thickness [28, 29]. This is achieved through rotating a cutting tool of a smaller diameter about its own axis and simultaneously about the axis of the desired cylindrical hole, located at an offset distance from the tool axis. The cutting tool used for OD is usually an end-mill or a cutting head with polycrystalline diamond PCD inserts.

The research work published in [25] showed the results of using OD to produce holes in sandwich constructions with aluminum and carbon honeycomb core for aerospace applications. This process produced delamination-free holes with allowable geometric accuracy. The tool experienced considerable chipping on the main cutting edge that was attributed to the lack of tool dynamic stability.

The research work carried out in [30] investigated the unique characteristics of the orbital drilling (OD) process from a new energy perspective. The main factors that reduce the risk of exit delamination in orbital drilling were explained in terms of the eccentric distributed axial load applied by the tool on the hole exit layer, and redirecting the work done by the OD cutting tool in the axial direction towards the tangential direction. The effect of the axial feed, and rotational speed of the OD process on cutting forces, temperature, and the hole quality attributes have been established. It was shown that the reduced axial force component in OD produced delamination-free holes. The thermal performance of the orbital drilling process in terms of the tool cooling effect was shown to be enhanced by the formation of vortices

in an unstable air flow regime in the annular gap. The OD process has shown through this study that it's capable of enhancing the quality of the produced holes in terms of surface quality and geometric accuracy. However, the tool dynamics and deflection at high speeds and high axial feeds were found to be a source of limitation on the produced hole quality. Additionally, the productivity of the OD process was found to be one of the main limitations of the process. This is due to the helical path that the tool has to follow in OD compared to the linear feed in the axial direction in the case of conventional drilling. This is compounded by the limitations on the maximum speed and acceleration that the machine can achieve to deliver the helical tool motion, when OD is performed on a CNC machining center.

2.4.2. Vibration Assisted Drilling (VAD) of FRPs

In the VAD process, a harmonic motion is superimposed over the conventional feed motion in the axial direction [16, 31, 32]. This type of mixed motion is believed to combine the mechanical and thermal benefits of the intermittent cutting state and at the same time preserve the process productivity by maintaining the conventional axial feed motion. The vibration assisted machining in general has exhibited substantial potential for improving different material removal processes in terms of force and temperature reduction, surface integrity, and tool life [33-39].

The VAD process is applied in high frequency low amplitude (HFLA) and low frequency high amplitude (LFHA) regimes [31]. According to the definition in [31], the HFLA is performed in a range of frequency >1000 Hz. The research done by Babitsky et al. in several publications [35, 40-42] used an autoresonant system to control a piezoelectric transducer in order to deliver the vibratory motion to the cutting tool. This system utilizes the resonant modes of vibration of the system and is operated to actively match the oscillating system with the dynamic loads imposed by the cutting process. This method was applied to different metallic materials at different cutting conditions; however, nothing was reported in the work published in [35, 40-42] on using the autoresonant system for HFLA machining of composite materials. The autoresonant system can be operated only at certain combinations of vibration

conditions in order to activate the system resonant modes. This represents a significant limitation on using this system for this present research, which is aiming at investigating the role of each independent parameter of the VAD process.

The research work by Paris et al. and Peigne et al. in [43-45] introduced a new self-vibrating drilling head (SVDH) to superimpose the vibratory motion over the conventional axial feed. The principle of the working of the developed system is based on using the cutting energy to generate the axial vibrations through setting up the cutting conditions in order to create axial drilling chatter, which leads to intermittent cutting and chip breaking due to tool separation. The authors in [43-45] reported that the main challenge in operating their SVDH proposed system is choosing the cutting parameters and the cutting head parameters to obtain the targeted chatter that can deliver the intermittent cutting conditions. Therefore, the SVDH system cannot be employed in the present research since it does not facilitate the control of the independent parameters of the VAD process.

By investigating the low frequency high amplitude (LFHA), several systems were developed in order to produce the required vibratory motion of VAD. The systems developed in the available literature were used to study LFHA of metallic materials.

Chhabra et al [37] developed a new linear drive technology that was used to deliver a combined motion of conventional feed and superimposed low-frequency modulation (< 400 Hz) for VAD. The authors studied the drilling torque, thrust and controlled chip breakage during VAD of ductile aluminum alloys. The research work carried out by Chhabra et al focused also on verifying the VAD kinematic model developed by Toews et al [46] through studying the effect of the ratio of the frequency of modulation "ω_m" to the frequency of tool rotation "ω_T" on the chip breaking during VAD of aluminum alloys. The results reported in [37, 46] showed that chip breakage is obtained by adjusting the VAD conditions to produce an odd integer frequency ratio, under these conditions, the mean torque and mean thrust are decreased in comparison with conventional drilling.

The application of an odd-integer value of the frequency ratio was found to result in broken chips of consistent size, and reduced mean torque and mean thrust compared to conventional drilling [37]. On the other hand, even-integer ratio resulted in continuous chip and the change in torque and thrust was insignificant compared to conventional drilling.

Jallageas et al. [47] developed a model for the commercial Mitis VAD head based on the formula of the kinematics of vibratory drilling developed by Deyuan et al. in [48]. The experimental results of VAD tests of composite/metal hybrid stacks were used to validate the model predictions in terms of chip breaking and geometry. The commercial Mitis system utilizes a mechanical wavy ring cam with rolling elements to generate the vibratory motion at fixed multiples of the spindle rotational speed. Although the Mitis system provides a precise vibratory motion because of its high rigidity, it provides very limited control on the VAD parameters, which makes it an inappropriate choice to achieve the objectives of the present research. The following subsections discuss the findings of the research work reported on the characterization and investigation of the VAD of FRPs.

Effect of VAD Parameters on Drilling Forces

Ramkumar et al. [49, 50] and Arul et al. [32] compared the performance of the vibration assisted and conventional drilling of GFRP composites at low-frequency, high amplitude using high-speed steel (HSS) drills. In both studies, the authors performed online analysis on drilling force, power and acoustic emissions A.E and in addition to offline tool wear monitoring for both drilling techniques. The drilling experiments were carried out using dry conditions and HSS drills.

The results reported in [49-51] agreed in their findings that VAD produced around double the number of drilled holes by conventional drilling before reaching the critical thrust force, cutting power or tool wear. For the used drilling conditions the optimized parameters for drilling were: a speed of 630 rpm, a feed rate of 0.04 mm/rev and a frequency of 220 Hz.

The results reported by Arul et al. [51] showed that the thrust force increased directly with the feed rate. The thrust force of the VAD was reported to be reduced by around 40 % compared to conventional drilling. Arul et al. attributed this reduction in the VAD thrust force to two main factors. First, the impact experienced by the composite in the axial direction, which creates a pulse/intermittent cutting mode that requires less force for chip formation due to the concentration of the cutting energy. Second, the frequent separation and contact between the rake faces and the chips, reduces the contact area between the chip and the rake face of the tool which reduces the frictional force component of the resultant cutting force.

The reported findings of the analysis suggested using the on-line monitoring of thrust for controlling the drilling parameters based on the reported good correlation between thrust and delamination factor. The optimum parameters reported by Arul et al. for the VAD of woven glass fabric/epoxy were found to be 18.85 m/min cutting speed, 0.02 mm/rev. feed rate, 200 Hz frequency and 15μm amplitude of vibration for minimum thrust.

The work done by Wang et al. in [52] compared the thrust forces of conventional and vibration assisted drilling of glass fiber-reinforced plastic composite (GFRP), carbon fiber-reinforced plastic composite (CFRP) and printed circuit board (PCB). Wang et al. superimposed a harmonic motion over the axial tool motion at frequencies 100, 300 and 500 Hz, and amplitudes 2, 6 and 10 μm. The specifications of the used vibration drilling spindle head were not mentioned in the description of the experimental setup. Although the ratio of the frequency to the rotational speed has a major role in controlling the drilling force in VAD [37, 46, 53]; however, all the conventional and vibration drilling tests in [52] were conducted at a constant spindle speed of 22,000 rpm. This was based on the findings reported by [54, 55], which stated that the thrust force is not sensitive to the change of rotational speed in conventional drilling. The effect of vibration frequency and amplitude was investigated at different speeds, and feeds, using carbide and a high-speed steel (HSS) drills. The experimental results showed that the force was controlled by the feed at the first place. The VAD tests conducted at the aforementioned conditions showed a

considerable force reduction of the thrust force compared to conventional drilling forces. The authors attributed this reduction to the generation and the accumulation of material fractures and cracks. The thrust force recorded for drilling of CFRP using HSS tools was higher compared to that recorded for the case of carbide drills. This could be due to the accelerated tool wear because of the higher abrasive effect of the fiber particles on the HSS tools compared to the carbide tools [1, 56].

Force and Temperature Measurement in VAD

Measuring VAD forces using piezoelectric dynamometers is challenging due to the cutting dynamics in addition to its unique process dynamics that adds to the complexity of the problem [44, 57]. The research work published in [58, 59] showed that the dynamics of piezoelectric dynamometers during cutting can interfere with the cutting signal, resulting in significantly erroneous force signals. The research work done in [58] was focused on correcting the milling forces measured by a piezoelectric dynamometer in a large frequency range through developing a correction function that includes the dynamic effect of all the elements interacting significantly with the milling process. A transfer function that serves this objective was developed via experimental modal analysis, and the reported results showed high agreement with a reference sinusoidal system excitation signal. Girardin et al. [60] constructed a system transfer matrix to relate the erroneous signals of the milling force components measured by a piezoelectric dynamometer to the applied known force components. The developed model took into account the effect of cutting conditions including the effect of lubrication for cutting force correction.

The beneficial effect of temperature reduction in LFHA VAD of metallic materials was clearly shown by the results reported by Okamura et al. in [61]. However, for LFHA VAD of FRPs, nothing was reported in the available literature on the effect of VAD parameters on the tool temperature except the work published in [62], which is part of this research that will be discussed in Chapter 5.

Delamination in Holes Produced by VAD

The research work done by Arul et al [51] showed that the vibration drilling increased the number of drilled holes before reaching the critical level of thrust force and delamination factor by 67% compared to conventional drilling. The authors suggested that on-line monitoring of thrust can facilitate defect-constrained drilling according to the reported good correlation between the thrust and the delamination factor.

2.5. Predictive Force Modeling for Machining of FRPs

2.5.1. Predictive Force Modeling for Machining of FRPS Based on Shear Plane Models

The research work done in [63-65] by Takeyama et al , Bhatnagar et al., and Zhang et al. tried applying the shear plane model for chip formation in metal cutting to the chip formation in machining of unidirectional FRPs. This assumption was based on the observation reported by Takeyama in [63] which showed the pattern of chip formation to be close to that of metal cutting where the shear plane direction was controlled by the fiber orientation within the limited range of fiber orientations less than 90º.

The model presented in [63] was based on the assumption that (a) chip formation is performed by quasi-continuous shear, (b) the shearing stress is function of the fiber orientation angle only, (c)the shearing strength obtained via the simple shear test was used to replace the flow stress of the material for cutting power calculation, (d) the model is applicable for two-dimensional orthogonal cutting only for fiber orientations between 0˚ and 90˚, and (e) the model yields merchant's theory of minimum energy of chip formation where shearing is assumed to take place along the direction that will minimize the cutting energy.

The model of chip formation of FRPs presented by Zhang et al in [65] suggested that the total cutting force is a resultant of three components defined as chipping, pressing, and bouncing forces. The model of the chipping force followed the same

approach discussed in [63] for the same range of fiber orientations between 0º and 90º.

The deformation force was described to be because of the tool nose penetration into the workpiece surface. This was modeled as the case of deformation of the FRP material under a cylindrical indenter, which was based on the contact mechanics of elastic deformation. The effect of the microcracks that might take place because of the tool nose penetration was included empirically through a modified force value, which was defined as a function of the fiber orientation.

The third component of the resultant cutting force in Zhang's model was the frictional force between the clearance face and the workpiece, which was caused by the bouncing back (elastic recovery) of the machined surface material. The contact length was determined using the contact mechanics between a wedge and a half-space. The total normal force was computed based on this assumption. The authors mentioned that experimental calibration of the coefficient of friction between the tool flank face and the workpiece was used in order to define the frictional force.

The experimental findings of the research work performed by Bhatnagar et al in [64] showed that for 2D orthogonal cutting of FRPs, chip formation took place due to a macrocrack which propagates along a plane similar to that observed in the Iosipescu shear test specimens. This plane was found to be along the fiber orientation direction between 0º and 90º. Based on these findings the model developed in [64] used the shear plane model for chip formation in which the shear plane angle was always aligned to the fiber orientation angle. The model uses the in-plane shear strength of the CFRP material determined from the Iosipescu shear test to calculate the cutting forces.

The predictions of the models in [63, 65] were compared to the experimental results of the orthogonal cutting of GFRP and CFRP, respectively. The comparison of both models showed that the chip formation of GFRP and CFRP can be modeled using the proposed approach for fiber orientations up to nearly 70º only. The proposed approach was not able to predict the cutting forces for higher fiber orientations.

The model predictions in [64] showed a good match with the experimental results for the fiber orientations between 15º and 60º. However, the model predictions were shown to be sensitive to variations in the rake and friction angles. It was also concluded that using the shear plane approach for prediction of cutting forces of fiber orientations <90º is quite difficult and requires considerable theoretical work, which diminishes the feasibility of this modeling approach.

Accordingly, it can be concluded that there is a major flaw in the concept of using the shear plane approach for modeling the cutting force in the case of FRPs. This is because the chip formation in FRP involves a series of brittle fractures that produce discontinuous chips rather than plastic deformation in the case of metallic materials [54, 66-70]. Furthermore, the limited special cases of fiber orientation less than 90º for which the shear plane models were able to provide good predictions were because the special case of fiber failure along planes that had orientations close to the orientations of the shear plane in the case of plastic deformation of metallic materials. Therefore, such approach failed to maintain the same level of prediction for higher fiber orientations. Hence, it does not represent the appropriate approach to be used for the prediction of the cutting forces in a highly complicated process as drilling of multidirectional FRPs.

2.5.2. Predictive Force Models for Drilling of FRPs

Drilling is one of the highly complicated machining processes due to the complexity of the tool geometry [71-76]. As discussed in chapter 1, there has been an imperative need for developing a force model that can predict the trends of the drilling forces and torques at different drilling conditions for process design and optimization. Using a multidirectional FRP material as a workpiece adds to the complexity of the drilling process due to its anisotropy and laminar structure [13, 54, 66-70, 77-79]. The directionality of the FRP laminates results in a dynamically changing drilling force with the rotation of the tool. This adds to the complexity of the required model, which is expected to capture the principal features of the force signal in terms of the force fluctuation and maximum force value and location.

Research efforts have been exerted in order to develop empirical force models that relate the thrust and cutting forces to the drilling feed and rotational speed [80-88]. The empirical models showed good predictions within the range of the drilling parameters used for calibration; however, the empirical models are not generic models that can be used for advanced process and tool design as well as optimization. Moreover, empirical models require a large number of experimental tests, which excludes this approach for lack of feasibility for many applications. The following sections present the trials that were available in the open literature for developing a generic model for drilling of multidirectional FRP laminates.

Shear Plane Models for Drilling of Multidirectional FRPs

The models presented in [89-91] adopted the shear plane concept, which was reported in [63-65] for modeling the drilling forces of multidirectional FRPs. Therefore, such drilling models inherited the same limitations and sources of errors of the shear plane concept when applied to chip formation in FRPs as discussed earlier. This was obvious from models predictions, which were represented by an average force value rather than predicting the principal features of the force signal.

The model presented by Guo et al in [89] employed the concept of the three deformation regions suggested by Zhang in [65] and implemented it for oblique cutting on discretized sections of the cutting lip. The total drilling force was then obtained by integrating the elemental forces. The model predictions of the average force value showed satisfactory agreement with the experimentally measured forces at different drilling conditions. However, the only case that was shown to compare the predicted and measured force forms showed an error of around 55%. Moreover, no information was reported on the accuracy for predicting the force fluctuation and the maximum force value and location for the rest of the conditions and for the torque predictions.

Elhachimi et al [90, 91] used a similar approach as Guo [89] but applied the oblique cutting model established by Oxley [92] on each element of the cutting lip. Oxley's model was developed for orthogonal machining of metallic materials and was based

on the accurate prediction of the shear plane angle, which was found to be inappropriate for force prediction in machining of FRPs, as discussed earlier. The trends of the average force, torque and power predicted by the model presented in [90, 91] showed good agreement with the corresponding experimentally measured values for different drilling conditions.

Although, the predicted average force values that were reported in [89-91] seem to be in agreement with the experimentally measured average force values, there is no information reported in these models on the accuracy and/or the ability of the model to predict the critical features force signal. This raises serious concerns regarding the concept that was used to build these models, which were purely based on the formulation used for metal cutting via plastic deformation.

Finite Element Modeling of Drilling of Multidirectional FRPs

There have been research efforts on finite element modeling of drilling of FRPs that followed the trials of the empirical modeling of the process [39, 67, 92-97]. The enormous computational cost is the most significant challenge of the FEM approach especially for modeling a highly complex process like drilling of FRPs. Therefore, a relatively very fine mesh of the tool and the workpiece and smaller time steps have to be used to account for the dynamically changing directional properties of the material on the fiber scale. Additionally, the contact problem and friction between the tool and the workpiece requires modeling of very intricate details of the process in order to capture principal features of the force signal. Another major challenge that faced the FE models reported so far in the literature is the insignificance of the ideally defined material properties (e.g. Young's modulus, shear strength, Poisson's ratio, etc) when used to predict chip formation by fracture on the fiber scale.

The reported FE models developed for drilling of FRPs were not able to predict the basic features of the force signal due to the huge difference of the mechanical properties and failure criteria of the fibers and the matrix materials. The proposed solution to this problem was to simplify the problem through using homogenized equivalent material properties [39, 92], which hinders the model's capability of

capturing principal features of the force signals. Therefore, the reported results of the models in [39, 67, 92-96] compared the predicted vs. measured average force only and were not able to compare any other feature of the force signal (e.g. force fluctuation, and maximum force location). The difference between the mechanical properties and failure criteria of the fibers and the matrix materials introduces another source of significant material nonlinearity due to predicted large strain problems. This problem necessitates using higher order elements, which adds to the complexity and the computational cost of the model.

Mechanistic Modeling of Drilling Multidirectional FRPs

The predictive force models developed by Chandrasekharan et al, and Langella et al in [98, 99] adopted the mechanistic approach. This approach utilizes the well-established relationship between the uncut chip geometry and cutting forces, through the experimentally calibrated cutting pressures of the cutting tool and workpiece pair at different cutting conditions.

Chandrasekharan's model [98] aimed at predicting the total thrust force and torque from the partial forces and torques calculated on the primary and chisel cutting edges using the mechanistic modeling approach. The model included the effect of the variation of the rake angle and the cutting speed on the cutting pressures along the primary cutting edges of the tool. This was performed by borrowing a fitted empirical relationship between each of the rake angle and the cutting speed and the cutting pressure from the case of metal cutting and applying it to the case of FRPs. The calibrated cutting pressures were defined in the normal and tangential directions as function of the uncut chip thickness, rake angle and cutting speed. The effect of the fiber orientation angle on the cutting pressures was not included, an equivalent property of an isotropic material was considered instead. The model predictions were validated by comparing the predicted force and torque signals to the corresponding experimentally measured signals for drilling of grey cast iron and CFRP. The model predictions for drilling of metallic materials showed good agreement with the experimental results. In the case of drilling of CFRP, only the primary cutting edge

model could show good predictions of the average force. The model predictions for the case of the engaged chisel edge did not match the experimental data. The authors concluded that the cutting mechanism assumed for the chisel edge was incorrect, and added that there is an additional material removal mechanism that occurs at the chisel edge while drilling CFRPs.

The model developed by Langella et al [99] used a very close approach to that of Chandrasekharan [98] to predict the thrust forces and torque for drilling of unidirectional GFRP laminates. The forces and torques were calculated on elements of the primary and chisel edges then integrated along the length of each edge. The product of the uncut chip thickness and the width difference of each element on the edge defined the elemental area of the uncut chip area. Langella et al assumed orthogonal cutting along the infinitesimal width of each element. Therefore, the cutting pressures at different cutting conditions were defined via a set of orthogonal cutting tests of unidirectional GFRP tube at different fiber orientations. The effects of the rake angle and cutting velocity variation along the primary cutting edges were introduced to the model in the form of an empirical model.

Similar to the limitations of the mechanical models developed in [89-91], the mechanistic models presented in [98, 99] did not provide any information regarding the possibility of predicting the essential features of the force signal. Therefore, the models presented in [98, 99] can be used for the preliminary design of the drilling process based on the average force values, but they can neither be used for process and tool optimization, nor can they be extended for mechanical damage prediction based on the force predictions.

Identification of Cutting Pressures for Mechanistic Modeling of Machining of Multidirectional FRPs

The previous discussion implies that predicting drilling forces using mechanistic modeling of drilling of FRPs has a great potential. Mechanistic models for machining require a set of experimentally calibrated cutting pressures, which represent the directional material property with respect to the fiber orientations. Kala et al presented an approach in [100, 101] for identifying the cutting pressures as a function

of fiber orientation for side milling of multidirectional FRPs. The calibration of the model presented in [100, 101] used 54 milling experiments at 3 speeds, 3 feeds and 6 fiber orientations, which was believed to cover the entire range of the effective fiber orientations. Each milling test gave information on the cutting pressures for one rotational speed, and a range of fiber orientation and uncut chip thickness, which were varying simultaneously with the rotation of the tool. The milling tests were repeated at different depths of cut and different fiber orientations in order to build a huge database of nonsystematic cutting pressures with respect to fiber orientations and uncut chip thickness. In order to build a systematic database of cutting pressures as a function of two major parameters (uncut chip thickness and the fiber orientation), the high density of information was assigned towards the uncut chip thickness instead of the fiber orientation. This represents one major flaw of this approach because the effect of the fiber orientation on the cutting pressure changes drastically from one material to another [102]. Although this approach covers the range of the effective orientations, it can easily miss substantial information like the fiber orientation that possess the maximum cutting pressure value.

The model reported in [100, 101] comprises a correction function that introduces the effect of the rake angle change along the cutting edge to the cutting pressures. This function was developed based on the concept of the effective rake angle presented by Ramulu et al in [103], which defines the rake angle as the angle between the rake face of the tool and the axis of the fiber being cut. The same database of the cutting pressures as a function of fiber orientation was also used in order to feed the rake angle correction function. The force predictions of the model presented in [100, 101] were validated versus experimental force measurements for side milling tests that were carried out on a laminate that had the same fiber orientations as the ones used for calibration.

The methodology presented by Kala et al has introduced useful concepts to define the cutting pressures for edge trimming of FRPs, but it remains limited and tailored to the side milling process and cannot be used as a feasible methodology for defining cutting pressures for other processes especially drilling. For the case of drilling it is

more practical to use the drilling process with certain hole preparation to define the cutting pressures on the primary and chisel edges as function of speed, feed, and fiber orientation.

2.6. Conclusions of the Literature Review

- The results of the experimental investigation of the VAD process reported so far in the available literature show the huge potential of the process in terms of fulfilling the balance between reducing the drilling force and temperature and their consequent damage, while preserving the process productivity.
- The experimental results reported in the available literature on the VAD of CFRP laminates do not provide enough information for process characterization and for understanding the physics of the process. A few nonsystematic research works is available on the experimental investigation of the effect of the LFHA VAD parameters on the produced FRP hole quality attributes and the associated forces and temperatures.
- Analytical modeling of the fundamental mechanics of the chip formation mechanisms during drilling of multidirectional FRPs is a highly complex process and could be infeasible. On the other hand, empirical mechanistic models based on homogenized material properties are unable to capture the principal features of the force signal during drilling of multidirectional FRPs, hence cannot predict consequent physical damage.
- The effect of the parameters of LFHA VAD of FRPs on the tool temperature and the subsequent material thermal damage was not studied in the available literature.
- There is no available accurate analytical force model, in the open literature, which can predict the principal features of the drilling force and torque during the steady state and transient stages of conventional drilling or VAD of multidirectional FRP laminates.

CHAPTER 3

Mechanics of the Vibration Assisted Drilling Process

3.1. Introduction

In the VAD process, the tool and workpiece relative motion follows the combination of the conventional feed motion and the superimposed harmonic motion. The conventional feed motion causes the tool to advance axially through the depth of the workpiece. In a non-resonant VAD process, the superimposed harmonic motion is controlled by the modulation frequency and amplitude, and is responsible for engaging and retracting the tool about the mean path of the feed motion. The resultant relative positions of the workpiece and the tool define the geometry of the formed chip at any given instant of time. The maximum uncut chip thickness 'd' corresponding to the depth of cut (DOC) is achieved when the tool is at the maximum engagement position, whereas 'd' can drop to a value of zero at the position of full separation. The width of the chip is also determined by the duration of the engagement cycle controlled by the modulation frequency. These factors have direct impact on the cutting energy, which is translated to forces and temperatures in the first place. The nature of VAD of fiber-reinforced polymers FRPs is discussed in this chapter, in terms of the mechanisms of force and temperature reduction in relation to the kinematics of the VAD process. This discussion will not focus on the mechanisms of the VAD process relevant to metallic materials. However, it will focus on the VAD mechanisms that are shared by metallic and FRP materials, as well as on the specific mechanisms relevant to FRP materials only.

3.2. Kinematics of Vibration Assisted Drilling

The VAD process is based on creating a state of intermittent cutting, under the action of the superimposed vibratory motion, where a series of periodic separation cycles take place between the cutting edge of the tool and the workpiece. In VAD, the

vibratory motion is superimposed along the primary feed direction, which is the axial direction, to ensure the effective separation between the tool and the workpiece.

In order to explain the basic kinematic features of the vibration assisted machining (VAM) process, Figure 3-1 shows a schematic of a 2D vibration assisted shaping process along the direction of the primary linear feed motion [16]. The tool undergoes a superimposed harmonic linear motion with respect to the workpiece. The tool shown in Figure 3-1 is advancing at an axial feed speed of "f_a" and is vibrating at a linear velocity of "V_h". At time "t_1" the tool is ready to engage with the uncut material since the feed and vibration velocity vectors are of the same direction. At time "t_2" the tool advances to remove the formed chip by reaching the maximum engagement position. At time "t_3", the feed velocity vector maintains its direction while the vibration velocity flips its direction to cause the tool retract towards the maximum disengagement position. Accordingly, the contact of the rake face of the tool with the uncut material surface is interrupted and broken segments of chip are formed [16].

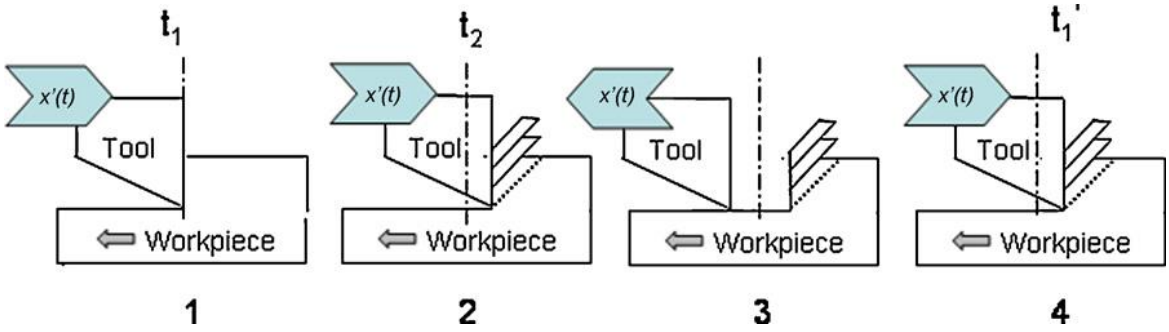

Figure 3-1 Schematic of the idealized vibration-assisted cutting process [16]

The duration of one full vibration cycle of the tool is "τ", which is equal to the reciprocal of the modulation frequency "ω_m". The portion of the cycle in which the tool is engaged with the workpiece is called a duty cycle [16]. The duration of the duty cycle for the case shown in Figure 3-1 is the difference between the time of the end "t_2" and the beginning "t_1" of the tool engagement with the workpiece. The duration of the duty cycle depends on the ratio between the velocities "V_h" and "f_a" and controls the geometry of the produced chips and hence the cutting force and temperature. In

conventional machining the tool rake face remains in continuous contact with the formed chip therefore the duty cycle in that case is equal to the full cutting time.

For the case of drilling, the axial feed and vibration velocities "f_a" and "V_h" of the tool relative to the work piece are defined as follows:

$$f_a = n.f_r \quad \textbf{3-1}$$

$$V_h = 2\pi\omega_m A_m \quad \textbf{3-2}$$

where "n" is the rotational speed of the tool in (rpm), "f_r" is the feed in (mm/rev), "ω_m" is the modulation frequency in (Hz) and "A_m" is the modulation amplitude in (mm).

In order to obtain a state of controlled intermittent cutting, the axial speed ratio "ASR" between the velocities "V_h" and "f_a" has to be greater than or equal to one, as given in Equation 3-3. This conditions guarantees that the velocity of the vibrational motion allows the tool to perform at least one separation cycle while it is advancing to a new vertical position.

$$ASR = \frac{V_h}{V_f} \geq 1 \quad \textbf{3-3}$$

The fulfillment of the periodically interrupted (intermittent) cutting condition given in Equation 3-3 is required in all vibration assisted machining processes including VAD. The beneficial effect of achieving a controlled intermittent cutting state will be discussed in the following sections of this chapter.

The study of the formed chip geometry and chip breakage gives good indication on the interaction between the tool and the workpiece during the cutting process, and helps demonstrating the physical meaning of the process parameters. The study of the geometric features of the formed chips in VAD has to be performed on chips of a metallic material although it is out of the scope of this research, which focuses on VAD of FRPs. This is because the chips of FRP are produced in a dust-like or small fractured particle form. These particles do not possess the geometry of the originally formed chip that reflects the interaction between the tool and the workpiece. Figure 3-2 (a) and (b) show the continuous versus broken chips formed by conventional and vibration assisted drilling of Ti, respectively. Figure 3-2 (b) shows that chip breakage

was obtained at a frequency ratio of 0.72, whereas the findings reported in [37, 46] stated that chip breakage takes place when the frequency ratio is an odd integer based on a study that compared even and odd integer frequency ratios only. This indicates that the effect of other VAD parameters should be considered in addition to the frequency ratio in order to study the chip geometry and breakage.

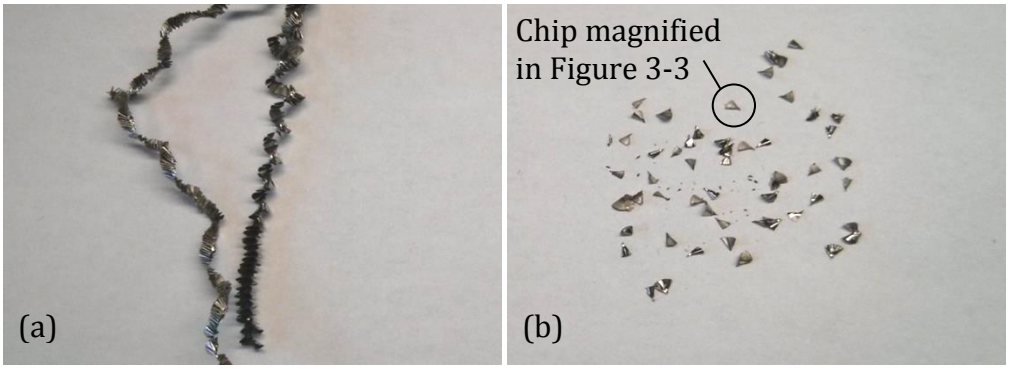

Figure 3-2 Chips of Titanium produced by (a) conventional, and (b) vibration assisted drilling.

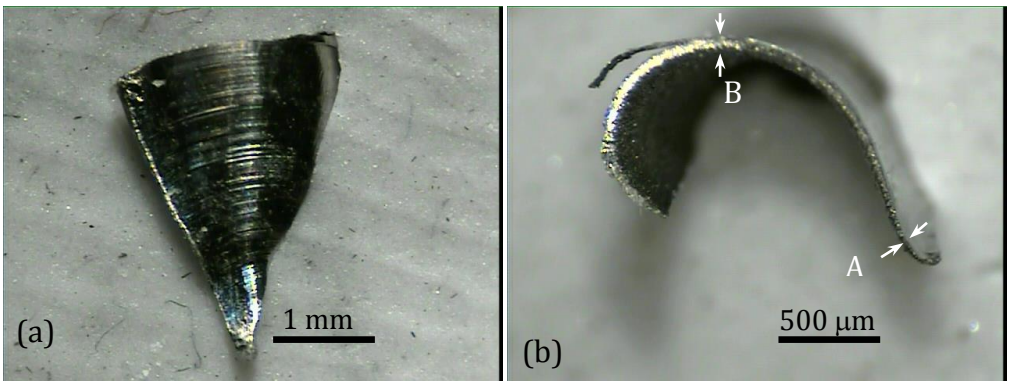

Figure 3-3 Microscopic image of the (a) top plan, and (b) cross section of a broken Ti6Al4V, chip formed by VAD.

Figure 3-3 (a) and (b) show a microscopic image of the geometry of a broken Ti chip formed by VAD. The VAD tests were performed under dry conditions at a drilling feed f_r=0.06 mm/rev, rotating speed n=2500 rpm, modulation amplitude A_m= 0.4 mm and modulation frequency ω_m=30 Hz. Figure 3-3 (a) shows that the broken chip represents a sector of a circular layer of the removed chip. During the drilling process, the center of the sector was adjacent to the chisel edge. The effect of the material extrusion under the chisel edge is shown by the bending of the chip edges near the center. The angle of the chip sector is controlled merely by the duration of the VAD

duty cycle. Figure 3-3 (b) shows that the thickness of the chip is varying from minimum at the beginning of the duty cycle (section A) and reaching the maximum in the middle (section B). The uncut chip thickness during VAD of FRPs is expected to follow the same trend and the drilling force fluctuation is expected to take place in accordance to the fluctuation of the uncut chip thickness during the duty cycle.

The chip geometry in VAD is controlled by the geometry of the surfaces formed according to the trajectory of the first and second cutting edge "E1" and "E2" at the same angular position, assuming a drill with two flutes. Figure 3-4 explains how the trajectory of the cutting edges controls the geometry of the formed chip. Figure 3-4 (a) shows the mean conventional path of the cutting edges in the cylindrical hole. Figure 3-4 (b) shows the combined conventional and vibratory motion of the tool edges in an opened hole presentation. The figure shows that at a certain angular position, the uncut chip thickness "d" is defined by the vertical difference between a point on the previously formed surface and a point on the surface about to be formed at the same angular position. The chip thickness varies according to the phase difference between the variations on the two surfaces, which are controlled by "f_r", "ω_T", "ω_m", and "A_m".

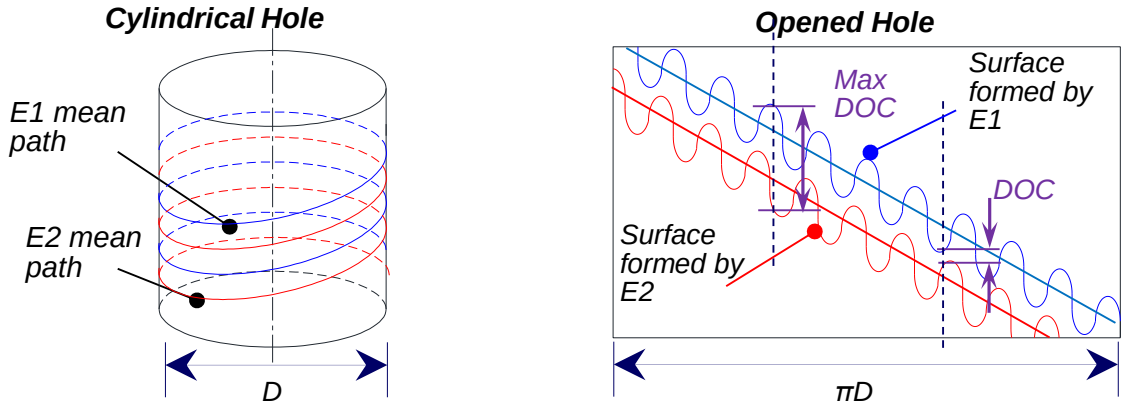

Figure 3-4 (a) Mean paths of the tool cutting edges in the cylindrical hole, (b) the vibratory path of the tool cutting edges represented in the opened hole.

Figure 3-5 shows the positions of the cutting tool during one vibratory cycle as it advances in the axial direction of the hole. The tool is shown to start at the maximum separation position "P1", which is located at the top amplitude position. At position "P2", the tool has advanced to the maximum engagement position corresponding to

traveling the distance of the specified conventional axial feed step and the maximum bottom amplitude. As the tool keeps advancing relative to the workpiece according to the axial feed motion, it retracts simultaneously to the top amplitude position "P3".

Figure 3-6 plots the axial and angular positions of the points on the machined surfaces formed by the cutting edges E1 and E2 according to the combined conventional and vibratory motion of the tool. The uncut chip thickness at each angular position is a result of the vertical difference between the surfaces by E1 and E2. The tool positions P1, P2, and P3 described in Figure 3-5 are marked on the plot in Figure 3-6 showing the maximum disengagement and engagement positions.

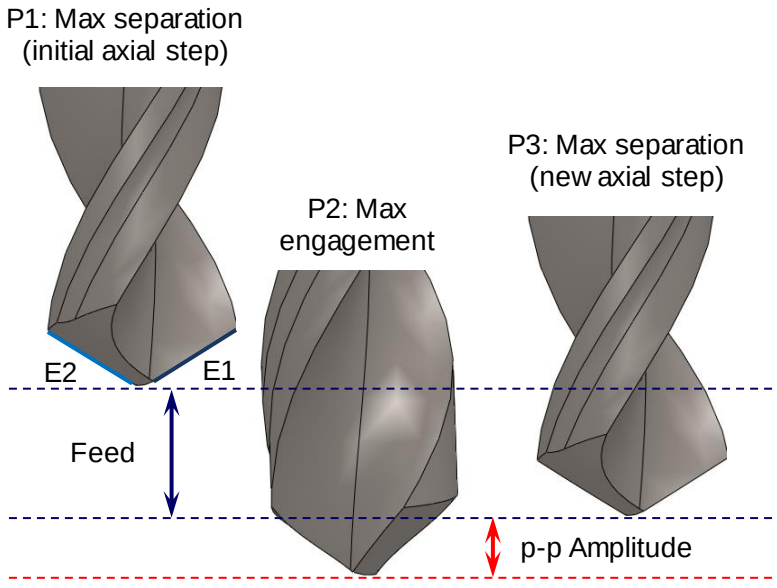

Figure 3-5 Schematic on the positions of the tool edges through the VAD engagement and the separation cycles.

A general formula used to define the uncut chip thickness "d" as a dynamic parameter based on the presented definition was introduced in [46]. The formula relates the uncut chip thickness to the modulation frequency and amplitude of the harmonic motion superimposed on the conventional feed motion. The relationships shown below are generalized for a tool that has a total number of edges "k". The edges are numbered with an index "j", where j= {1,2,..,k}. The axial position "d_j" of a cutting edge "j" at a certain instant of time "t_i", is determined from the resultant motion of the tool (harmonic motion + conventional motion), as follows:

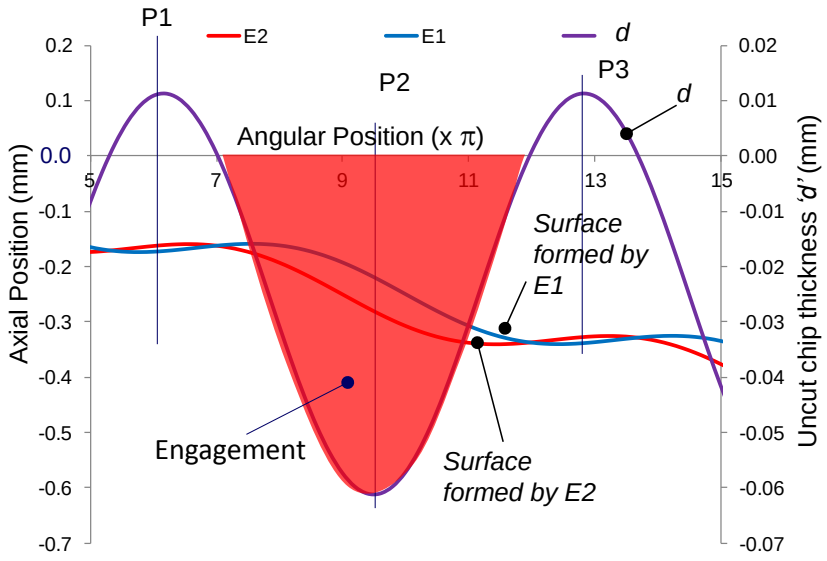

Figure 3-6 Axial and radial positions of the points on the machined surfaces formed by the cutting edges during VAD, and the resultant uncut chip thickness.

$$d_j = f_r . \omega_T . t_i + A_m . \sin(2\pi\omega_m t_i) \quad \textbf{3-4}$$

The edge "*j+1*" is going to reach to the same angular position of the edge "*j*" at time "t_{i+1}" as shown in Equation 3-5.

$$t_{i+1} = t_i + \Delta t \quad \textbf{3-5}$$

where "Δt" is the time required for the edge "*j+1*" to reach to the same angular position of the edge "*j*", and is determined as follows:

$$\Delta t = \frac{1}{k . \omega_T} \quad \textbf{3-6}$$

The axial position of the edge "d_{j+1}"at "t_{i+1}"is determined from Equations 3-4 and 3-5 as follows:

$$d_{j+1} = f_r . \omega_T . t_{i+1} + A_m . \sin(2\pi\omega_m t_{i+1}) \quad \textbf{3-7}$$

The general dynamic thickness of the formed chip at time "*t*" as a result of the overall tool motion "*d(t)*" is given by the difference between the two successive cutting edge locations as follows:

$$d(t) = d_{j+1}(t + \Delta t) - d_j(t) \quad \textbf{3-8}$$

$$d(t) = \left(\frac{1}{k}.f_r\right) + 2A_m cos\left(2\pi\omega_m t + \frac{\pi\omega_m}{k\omega_T}\right)\sin\left(\frac{\pi\omega_m}{k\omega_T}\right) \quad \textbf{3-9}$$

It can be seen that the total uncut chip thickness "*d*" at time "*t*" consists of a conventional term "d_o" and the dynamic term "d_d" where

$$d_o = \frac{1}{k}.f_r \quad \textbf{3-10}$$

$$d_d = 2A_m cos\left(2\pi\omega_m t + \frac{\pi\omega_m}{k\omega_T}\right)\sin\left(\frac{\pi\omega_m}{k\omega_T}\right) \quad \textbf{3-11}$$

From Equation 3-9 [46], it can be noted that the total 'd' for VAD depends on the feed, rotational speed, modulation frequency and modulation amplitude. The phase difference "φ" between the form of the machined surfaces E1 and E2 is controlled by the number of full vibration cycles that the tool is going to perform during one full rotational, which is the physical meaning of the ratio between the modulation and rotational frequencies of the tool shown in Equation 3-9. Figure 3-7 shows the effect of changing the modulation frequency and amplitude on the phase difference and hence on the calculated maximum 'd' using Equation 3-9. In Figure 3-7, 'd' was calculated for n= 6000 rpm and f_r =0.05 mm/rev, combined with A_m=0.04 mm for (a, c, and e), A_m=0.1 mm for (b, d, and f), ω_m=30 Hz for (a and b), ω_m=90 Hz for (c and d), and ω_m=120 Hz for (e and f). The figure shows that increasing the amplitude directly increases 'd' due to the increase in the engagement depth during the duty cycle. In VAD, 'd' at a given instant is defined as the vertical difference between the surfaces E1 and E2 at each radial position. This is controlled by the phase difference "φ" between the peaks of the two successive machined surfaces. Therefore, changing the frequency for the same 'n' and 'f_r' can result in either increasing or decreasing 'd', depending on the location of the peaks and the valley of both surfaces relative to each other. The maximum variation of 'd' can be achieved by adjusting the cutting conditions such that the peak of the first surface coincides with the valley of the following surface at the same radial position.

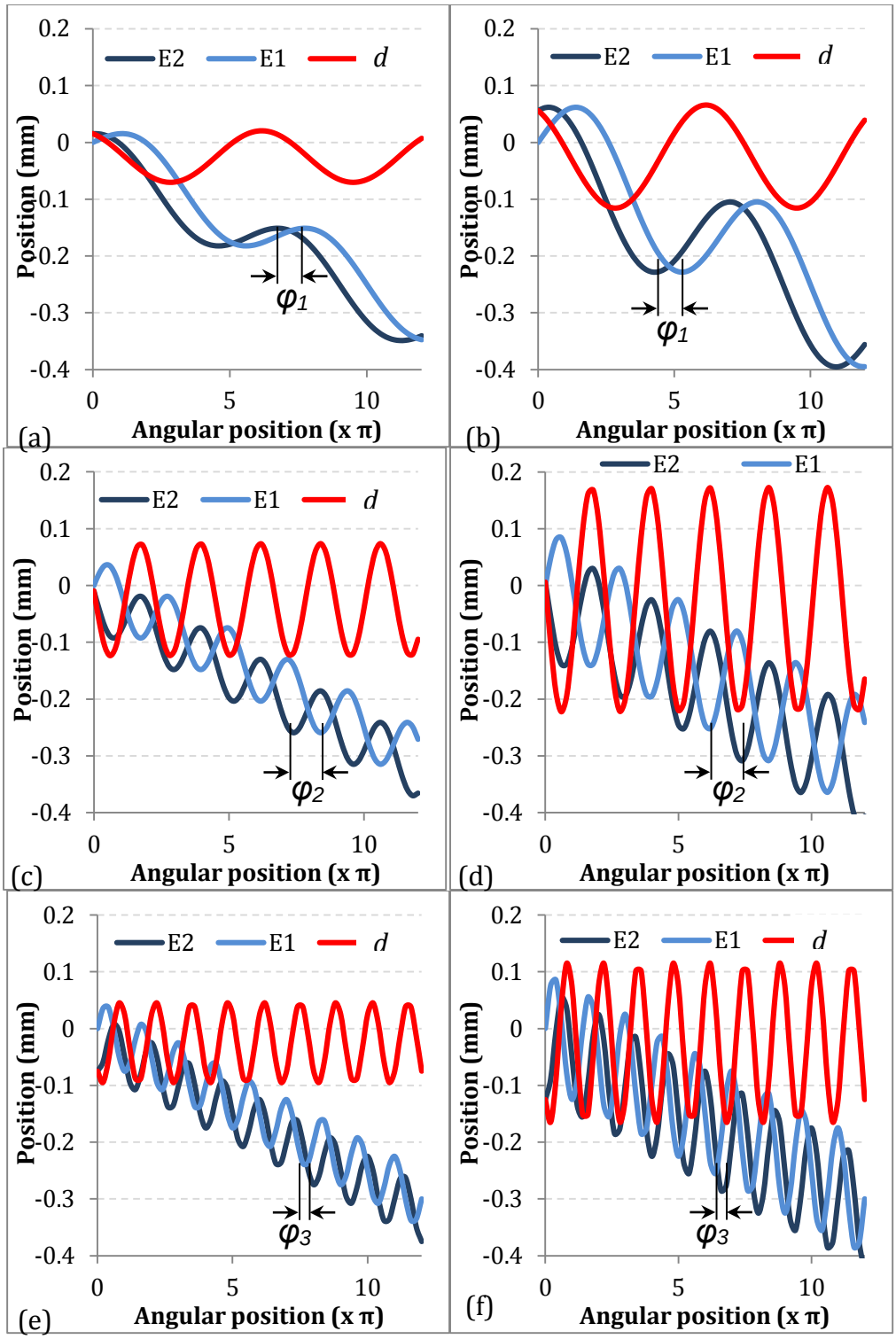

Figure 3-7 Effect of the modulation frequency and amplitude on the uncut chip thickness in VAD based on the difference between the successive machined surfaces E1 and E2 at each radial position. (a, c, and e) A_m=0.04 mm, (b, d, and f) A_m=0.1 mm and (a and b) ω_m=30 Hz, (c and d) ω_m=90 Hz and (e and f) ω_m=120 Hz.

3.3. Mechanisms of Force Reduction in VAD

3.3.1. Progressive Chip Removal

The drilling force in VAD is correlated to the thickness and size of formed chip, which was shown to be varying depending on the cutting conditions ('n' and 'f_r') and the modulation parameters ('ω_m' and 'A_m'). A properly selected combination of the VAD parameters can produce a significant drilling force reduction, compared to the conventional drilling force. For such combination, the large uncut chip thickness produced in conventional drilling is progressively removed in accordance to the small modulation amplitude in the case of VAD, which reduces the maximum force required to cut the maximum uncut chip thickness at each duty cycle. This effect will be further discussed in section 5.2 on the effect of VAD parameters on the cutting forces.

3.3.2. Friction Reduction due to Intermittent Cutting

On the rake face, the frictional force reverses its direction during the tool retraction and separation cycle, which helps to pull the chip away from the workpiece. In addition, the reduced contact area between the broken chip and the rake face of the tool results in reducing the friction force on the rake face [16]. The friction force is further reduced due to the intermittent contact between the flank face of the tool and the machined surface [16].

3.4. Mechanism of Temperature Reduction in VAD

Preliminary experiments and results reported in the open literature [61] showed that the tool temperature in VAD could be lower than that in conventional drilling by as much as 150 K. In this section, an explanation is provided for this favourable effect.

In VAD, as the tool vibrates and moves in a direction opposite to the feed direction, it loses contact with the workpiece, and a conical air gap is created. This configuration resembles a closed enclosure in a rotor-stator system. The air flow regime in the gap depends on the rotational speed 'n' and the gap width 'g' between the tool (rotor) and the workpiece (stator). At low rotational speeds, the basic laminar flow is three-

dimensional and is driven by the imbalance of centrifugal forces in the annulus. As 'n' and 'g' increase, Reynolds number 'Re' reaches a critical value 'Re_{cr}' and toroidal Taylor vortices are formed. The flow regime depends also on the cone vertex angle ϕ. Conical gaps formed by standard twist drills, $\phi \sim 60^{o}$, have flow pattern similar to that between flat discs [104]. This simplifies greatly the thermal modeling of the VAD process.

For laminar flows, the coefficient of heat transfer CHT across the air gap 'h_g' can be expressed in terms of the dimensionless parameters: Nusselt Number 'Nu', Reynolds Number 'Re', and the normalized gap width G, which are determined by the following relations:

$$Nu = \frac{h_g R}{K_a} \quad \textbf{3-12}$$

$$Re = \frac{2\pi n R^2}{60 v} \quad \textbf{3-13}$$

$$G = \frac{g}{R} \quad \textbf{3-14}$$

where 'R' is the rotating tool radius, 'ν' is the air kinematic viscosity and the symbol 'K_a' stands for the thermal conductivity of air. The Nu{Re,G} correlations [105] are plotted in Figure 3-8. The figure shows that at G=0.01, h_g is much higher than that of the free rotor in open space. At intermediate gap widths $0.02 \leq G \leq 0.06$, h_g drops to a minimum at $G \approx 0.02$ and then increases to a maximum level at $G \sim 0.063$ [105]. For the VAD system under consideration, these extrema correspond to gap widths g = 35 and 115 μm, respectively. As the air gap becomes larger than a certain distance, h_g decreases due to the decoupling effect between the tool and workpiece surfaces. Similar effect is expected when the two surfaces are very close, as less mass of cooling air can get and penetrate into the gap [106]. Marked enhancement in the CHT can be achieved when low frequency vibration (40-120 Hz) is imposed on the rotating body, even to the extent of quadrupling the 'h_g' value [107]. This increase is more pronounced at higher amplitudes and frequencies of vibration.

For better understanding of the heat dissipation mechanism due to the interrupted cutting in VAD, a sensitivity analysis was carried out on a simple transient heat transfer model, using the Finite Difference (FD) method. The tool was idealized as a 1D cylindrical body (6 mm diameter and 50 mm long). It is assumed that the cutting energy is applied to the base of the tool during half of the vibration cycle. During the second half of the cycle, heat is dissipated from this plane by forced convection, enhanced by the air flow in the gap between the tool and the workpiece. The CFRP material was idealized as a stack of four annular fin elements of uniform thickness 'w'. The modeled material had an inner diameter D_1=6 mm, outer diameter D_2=18 mm, and w=2 mm. The coefficient of heat transfer 'h_s' at the lateral surface of the rotating tool, outside the hole, was estimated to be 50-70 W/m^{2}K [108], for n= 6,000-12,000 rpm. The thermal resistance of the annular fin element R_{fin} was determined as a function of D_1, D_2, w, the free convection CHT at the workpiece surfaces, h_o, and the thermal conductivity of the CFRP material [109]. The resistance 'R_{fin}' was estimated to be 330 m^{2}K/W. The thermal contact resistance 'R_c' between the tool and the CFRP fin elements was estimated to be 2×10^{-4} m^{2}K/W [110]. The analysis showed that the interrupted cutting in VAD does not allow enough time for the heat generated in the cutting zone to propagate into the tool and the workpiece materials due to their high

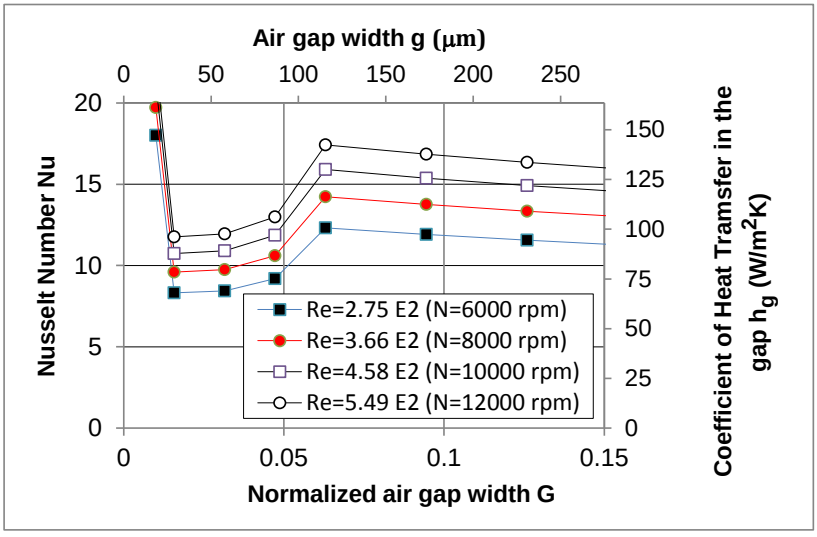

Figure 3-8 Effect of rotational speed and air gap on the CHT h_g

thermal inertia. The FD analysis showed that the rotational speed has a strong effect on the heat dissipation through h_s. It also showed that the contact resistance 'R_c' has an effect on the tool temperature. The FD idealized model was used to predict the temperature of the tool base 'T_b', where the cutting action and heat input are assumed to take place. Figure 3-9 compares the signals predicted by the FD idealized model for conventional and vibration assisted drilling. The figure shows that the predicted maximum 'T_b' for VAD was lower by more than 100 K compared to conventional drilling. The fluctuation in 'T_b' in VAD was also found to be greater than 100 K.

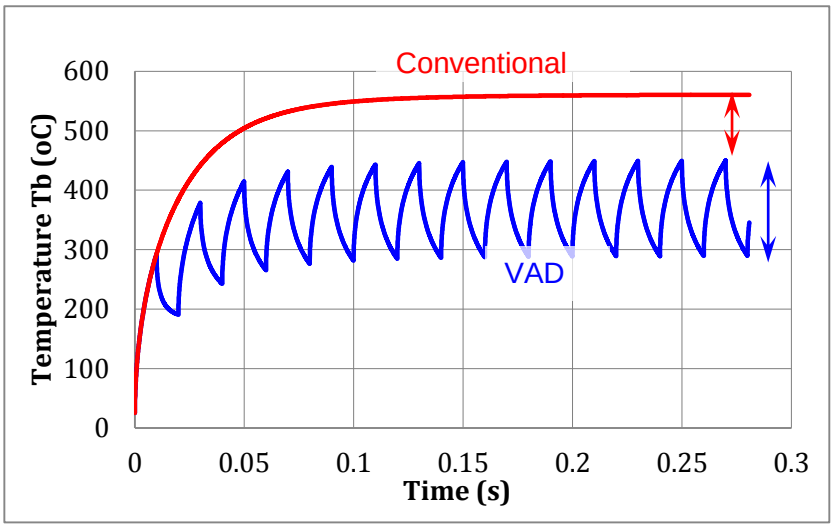

Figure 3-9 Base temperature 'T_b' for conventional and vibration assisted drilling predicted by the FD idealized model

A 3D Finite Element (FE) analysis was also carried out using DEFORM-3D® software in order to estimate the temperature variation along the cutting tool lip. To avoid the uncertainty associated with modeling the anisotropic CFRP material, Ti6Al4V was selected, since its thermal diffusivity is close to that of CFRP. A 6 mm diameter WC tool with two flutes was modeled as a rigid body. The workpiece is modeled as a rigid-plastic material with a size of 25.3×25.3×6.3 mm. Its flow stress constitutive equation is given in DEFORM material library. The drilling feed (f=150 mm/min) and rotating speed (n=2500 rpm) were imparted to the tool. For the VAD simulation, the tool vibration amplitude and frequency were 400 μm and 30 Hz, respectively. A Coulomb friction model with a coefficient of 0.3 was applied at the tool-workpiece interface, where a perfect thermal contact is assumed. The heat

transfer coefficients at various surfaces were similar to those used in the FD model. Figure 3-10 shows the FE predictions for the temperature variation along the primary cutting edges and at the tip of the cutting tool for the cases of conventional and vibration assisted drilling of Ti. The figure shows that the difference between the tip and the mid-edge temperatures is around 125 K for VAD and 75 K for conventional drilling.

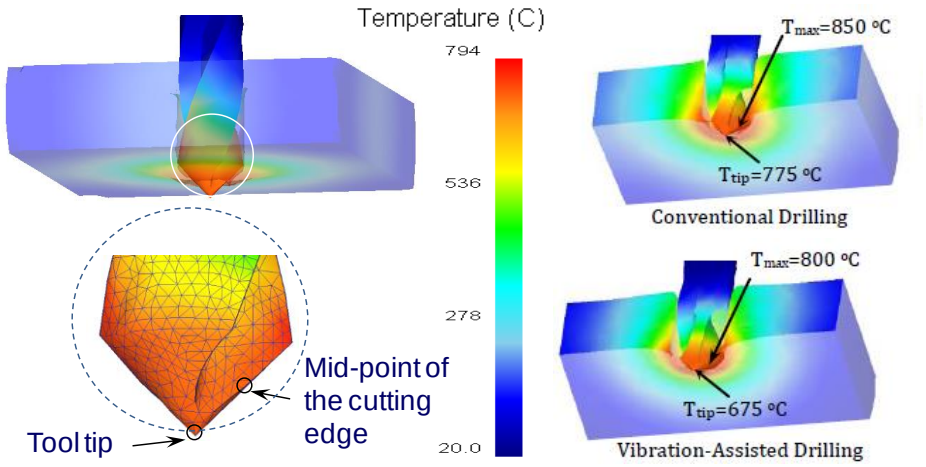

Figure 3-10 Thermal FE model predictions for (a) the temperature variation along the primary cutting edges and at the tip of the cutting tool, and (b) the cross-sectional view of the temperature field in the tool and workpiece at exit, in conventional and vibration-assisted drilling

The FE results showed that at the mid-point of the edge, the maximum temperature in VAD is approximately 50 K less than that of conventional drilling. On the tool tip, the maximum temperature in VAD was found to be 100 K less than that of conventional drilling, which is attributed to the cooling effect associated with the interrupted cutting state in VAD.

Figure 3-11 plots the FE predictions for the conventional and vibration assisted drilling temperatures at the primary edge middle point and at the tip of the cutting tool. The figure shows that the periodic temperature drop in the VAD temperature signal was found to match the modulation frequency of the VAD process. The figure also shows that the temperature variation at the tool tip in VAD was found to be as low as 20 K, while it reached up to 120 K at the mid-point of the primary cutting edge. On the other hand, the temperature variation for conventional drilling was

insignificant at the tool tip and remained within the range of 40 K at the mid-point of the primary cutting edge.

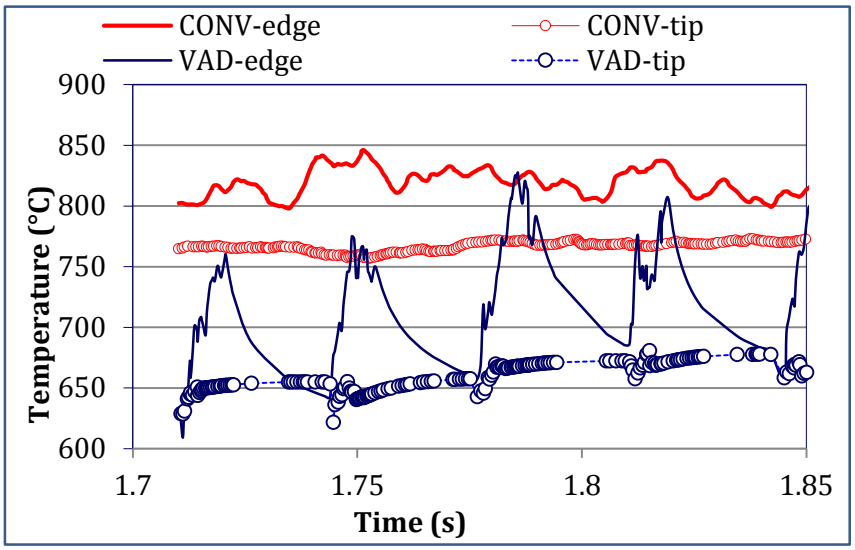

Figure 3-11 Tool Temperature- 3D FEM of VAD and Conventional Drilling

The discoloration is an indication of the undesirable effects of overheating of Titanium (Ti6Al4V) during machining. Visual investigation of the discoloration along the drilled hole edge at the exit plane can be used as an indication of overheating of Ti6Al4V during drilling. Figure 3-12 (a and b) compare the condition of the hole edge at the exit plane of drilled Ti6Al4V using conventional and vibration assisted drilling, respectively for (n=5000 rpm, f=75 mm/min, ω_m=40 Hz and A_m=0.4 mm). The figure shows a clear evidence on the previously described temperature reduction in VAD represented in the significantly reduced intensity of discoloration along the hole edge.

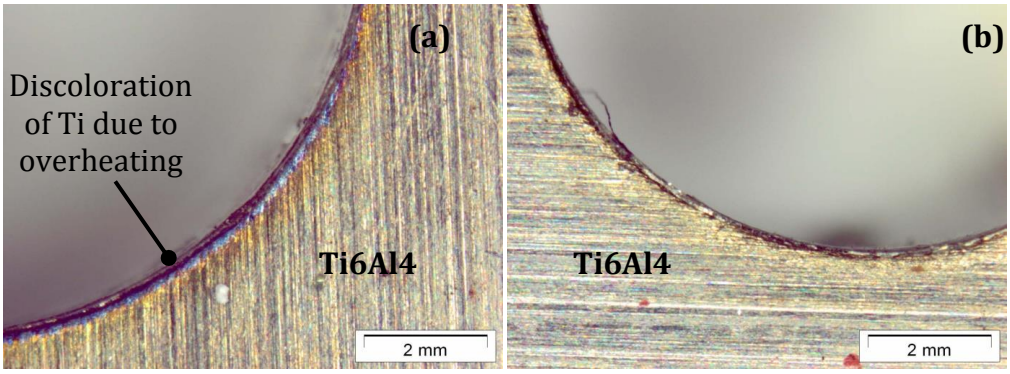

Figure 3-12 Hole edge at the exit plane for drilling of Ti at n=5000 rpm, f=75 mm/min using (a) conventional drilling, and (b) VAD at ω_m=40 Hz and A_m=0.4 mm.

3.5. Summary

This chapter discussed the kinematics of the VAD tool motion relative to the workpiece, which was shown to control the formed chip geometry, which has a significant effect on the drilling forces. The mechanisms of force and temperature reduction in VAD were presented in this chapter as well. In the following chapters of this thesis, experimental and analytical analysis will be presented to further explain the concepts discussed in this chapter on the mechanics of the VAD process in the mechanical and thermal aspects. The understanding of the intrinsic parameters from the experimental analysis will be used to develop an analytical model that incorporates such parameters to predict full signals of axial forces and torques for the VAD of multidirectional CFRPs.

CHAPTER 4

Experimental Investigation of VAD

This chapter provides a description of the setup and the performed tests for the experimental analysis on VAD. In this research work, conventional and VAD experiments were conducted. The conventional drilling tests were conducted for model calibration and validation, and to provide reference data for the corresponding VAD conditions for the sake of comparison. Two sets of VAD experiments were conducted to investigate the effect of the independent and the combined process parameters on the drilling associated forces, temperatures, and hole quality attributes. The independent VAD parameters that were investigated were the feed "f_r", rotational speed "n", modulation frequency "ω_m", and modulation amplitude "A_m". The combined process parameter of interest was the ratio of the maximum modulation speed to the axial speed of the tool, known as the axial speed ratio 'ASR' (refer to Eq. 3-3); this ratio has to be greater than or equal to 1 in order to obtain the required intermittent cutting state. For each of the produced holes, the forces and temperature were measured during the drilling process. The hole quality attributes were also measured using the appropriate measurement techniques. The hole quality attributes of interest were the entry and exit delamination, thermal damage, surface roughness, and hole size and circularity errors.

4.1. Experimental Setup

4.1.1. Machine Tool

All the conventional and vibration assisted drilling tests were performed under dry conditions on a 5-axis Makino A88ε machining center, shown in Figure 4-1. The Makino A88e machining center is featured with a 50 kW spindle power, three linear and two rotary axes, maximum spindle speed of 18,000 rpm and maximum feed rate

of 50 m/min. The working envelope of this machining center is 900 mm x 800 mm x 970 mm which can accommodate the conventional and the VAD setups as will be shown later in this chapter.

Figure 4-1 Makino A88ε machining center used for drilling tests

4.1.2. Drilling tool

All the conventional drilling and VAD tests were performed using a Fullerton-15107 Micro-grain tungsten carbide (WC) 2- flute right hand twist drill shown in Figure 4-2. The drilling tools used for all drilling tests were uncoated and had a 6 mm diameter with a 25° helix angle, 118° point angle, a fluted length of 51 mm and an overall length of 83 mm. The diameter tolerance limits specified by the tool manufacturer are +0.000, -0.013 mm.

Figure 4-2 Fullerton-15107 WC 2- flute 6.0 mm twist drill

4.1.3. Workpiece Materials

The prepreg used to build the workpiece material was a flame retardant unidirectional modified epoxy prepreg L-930(GT700) manufactured by J.D Lincoln composites. The test material used was a cross-ply laminate comprising 42 plies of graphite epoxy. The laminates were autoclave-molded with a cure time of 60 min at 127 °C and 516.75 kPa autoclave pressure. The final cured laminate thickness was 8.6 ± 0.02 mm.

Table 4-1 shows the mechanical properties of the L-930(GT700) epoxy prepreg standard sample as provided by the manufacturer. Figure 4-3 shows a schematic of the unidirectional and cross ply laminates that have been used in this research work. The laminates had layup configurations of $[0^{\circ}]_{42}$ and $[90^{\circ}, (0^{\circ}/90^{\circ})_{10}]_{s}$.

Table 4-1 Mechanical properties of the L-930(GT700) epoxy prepreg standard sample as provided by the manufacturer

Property at 690 MPa cure condition	Property at Test temperature		Test method
	25˚C	71˚C	
Ultimate tensile (0˚) strength	1.6 GPa	1.4 GPa	ASTM D 3039
Tensile (0˚) modulus	117 GPa	118 GPa	ASTM D 3039
Compression (0˚) strength	1.2 GPa	N/A	SACMA SRM IR94
Compression (0˚) modulus	111 GPa	N/A	SACMA SRM IR94
Ultimate flexural (0˚) Strength	1.0 GPa	0.97 GPa	ASTM D 790
Flexural (0˚) modulus	103 GPa	103 GPa	ASTM D 790
Short beam (0˚) strength	83 MPa	N/A	ASTM D 2344

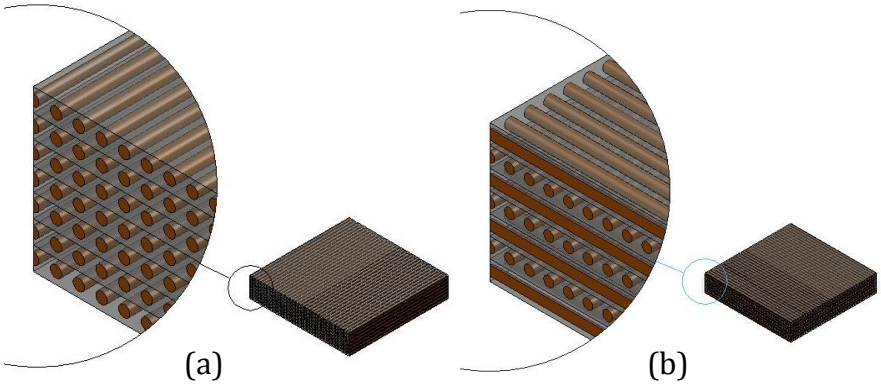

Figure 4-3 (a) Unidirectional CFRP, (b) multidirectional (cross ply)

4.1.4. Workpiece Fixture

This subsection describes the means by which the CFRP workpiece was fixed to the conventional drilling and VAD setups. The design of both setups accounted for the required force measurement during the drilling process as well as for the attachments used for chip evacuation, and temperature measurement at the exit of the hole.

Workpiece Fixture for Conventional Drilling

Figure 4-4 shows the experimental set-up used for the conventional drilling experiments. Fixture (1) was used to hold the CFRP laminates to the face of the dynamometer (2). The dust-like CFRP chips were evacuated using a special vacuum arrangement (3). The maximum drilling temperatures were measured using a FLIR ThermoVision A20M Infrared camera (4) at the hole exit plane. Figure 4-4 (b) shows a detailed view of the temperature measurement attachment of the drilling setup, where a special reflective mirror surface was used to allow the IR camera receive the IR rays in a direction parallel to the hole exit surface. This reduces the compartment needed to accommodate the camera between the dynamometer and the workpiece, which promotes more accurate force measurements. Further details on the drilling temperature measurements will be discussed later in this chapter.

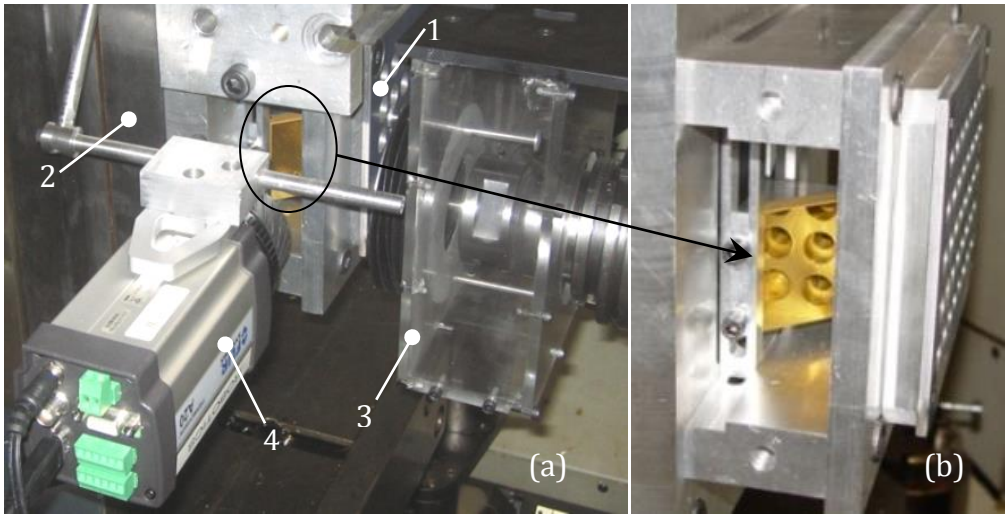

Figure 4-4 Experimental setup used for conventional drilling of multidirectional CFRP laminates

Figure 4-5 shows a schematic representation of the temperature measurement using the IR camera in the conventional drilling setup. The temperature at the point of interest (point A) is monitored, which is the intersection of the axis of the hole to be drilled and the outermost layer on the exit side of the CFRP laminate. The maximum temperature takes place when point (A') on the tool tip coincides with point (A) at the instant of the exit penetration of the tool tip.

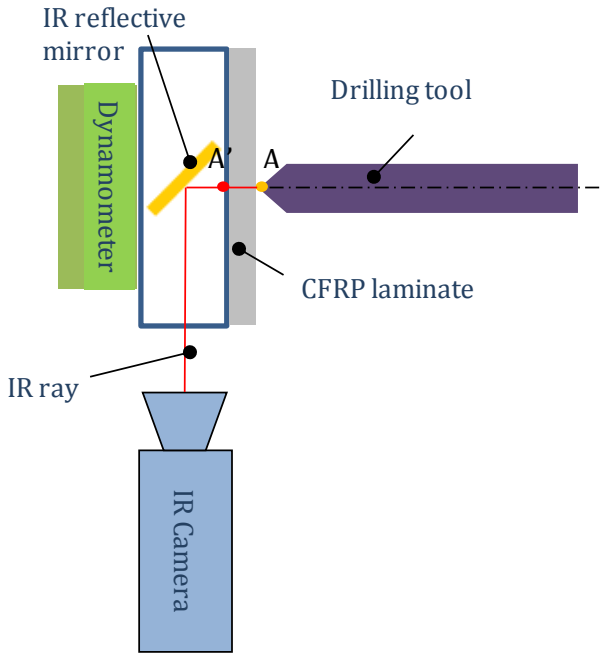

Figure 4-5 Schematic of temperature measurement using the IR camera for the conventional drilling experiments

Workpiece Fixture for Vibration Assisted Drilling

As shown in Figure 4-6 (a), the low frequency high amplitude (LFHA) modulation was provided using a Brüel & Kjaer (B&K) 4805 electro-magnetic shaker body and a (B&K) 4812 General Purpose head (1). The VAD force signals were recorded using a Kistler 9272 4-component piezoelectric dynamometer (2), and a 5019B Kistler charge amplifier. The system vibrations in axial and tangential directions are measured at the base and face plates of the dynamometer, using PCB 356A01 ICP® tri-axial accelerometer (3) and a B&K 4381 charge accelerometer (4), respectively. The CFRP plate (5) was bolted on a fixture plate (6) mounted on the face of the dynamometer.

The setup used for the VAD drilling tests does not allow mounting the camera on the side of the workpiece mounted on the vibrating shaker. This can significantly affect the temperature and force measurements and can damage the IR camera. Therefore, in the VAD setup, the FLIR ThermoVision A20M Infrared camera was attached to the spindle and located above the tool tip to measure the temperature at the instant of the tool exit from the hole, as shown in Figure 4-6(b).

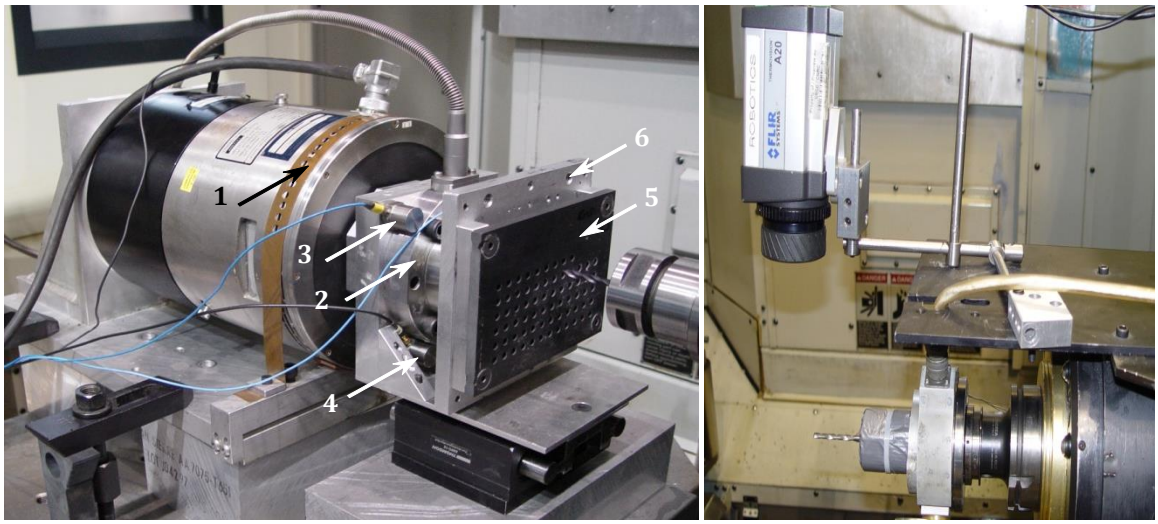

Figure 4-6 (a) The LFHA VAD setup mounted on the Makino A88e machining center bed facing the spindle, (b) setup used for temperature measurement using IR camera in VAD tests

A (B&K) 1050 vibration exciter control unit and the (B&K) 2707 power amplifier were used to control and operate the electro-magnetic shaker. The combination of the electromagnetic shaker and the controller setup described earlier possess the capabilities of delivering a wide range of independently controlled frequencies and amplitudes within the domain of the LFHA regime. Figure 4-7 depicts the ranges of frequencies and amplitudes that the VAD setup can provide under the loaded and unloaded conditions. The operation range of the VAD tests is highlighted within the loaded range in order to avoid system stoppage by the drilling forces. Table 4-2 shows the specifications of the electromagnetic shaker setup used for VAD tests.

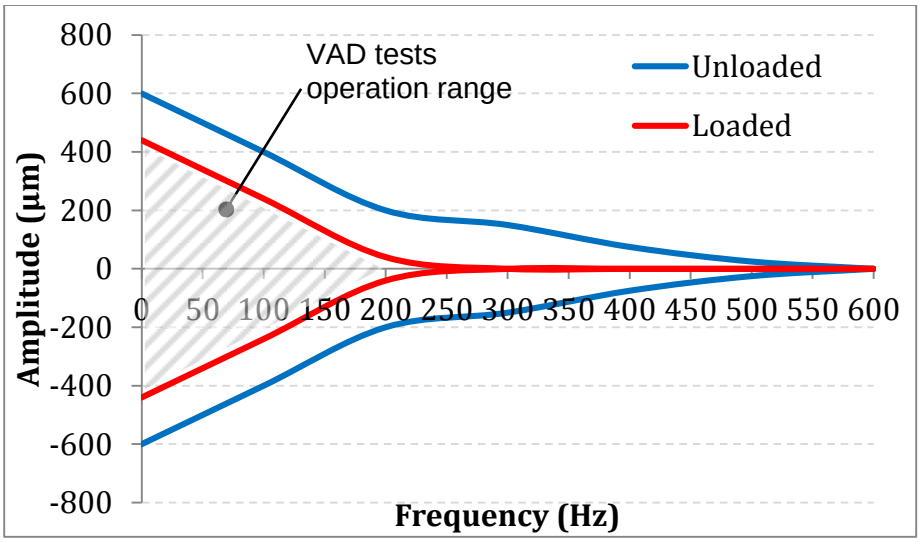

Figure 4-7 Operation range of the VAD setup under loaded and unloaded conditions

Table 4-2 Specifications of the electromagnetic shaker setup used for VAD tests

Shaker specifications	
Average working force (N)	310
Stiffness (floating) K (N/mm)	21
Speed limit (m/s)	1.14
Frequency operation range(Hz)	20-300
Displacement limit (mm)	12.7
Moving element dynamic mass (kg)	0.454
Resonance frequency unloaded (Hz)	1.1
Magnetic shields (gauss)	68

4.2. Design of Experiments

4.2.1. Experimental Test on the Effect of Independent VAD Parameters

The VAD conditions used for testing the effect of the modulation frequency and amplitude at different feeds and rotational speeds are shown in Table 4-3 and Table 4-4, respectively. According to the operation range of the VAD system shown in Figure 4-7, the testing conditions shown in Table 4-3 and Table 4-4 were selected to test multiple levels of the widest range of the system operation conditions. The effect of the modulation frequency was investigated through four frequencies (30, 60, 90 and 120 Hz) at two amplitudes (low: 0.04mm and high: 0.1 mm). Similarly, the effect of

the modulation amplitude was investigated through four amplitudes (0.04, 0.1, 0.2 and 0.4 mm) at low frequency (30 Hz) mm and high frequency (60 Hz). The total number of VAD experiments was 270 experiments performed for the combinations of the conditions shown in Table 4-3 and Table 4-4 with at least 2 replicates for each condition. For the purpose of comparison, the same feeds and speeds were tested under conventional drilling.

Table 4-3 Test matrix of VAD conditions for testing the effect of the frequency

Frequency (Hz)	Feed (mm/rev)	0.05			0.10			0.15		
	Rotational speed (rpm)	6000	9000	12000	6000	9000	12000	6000	9000	12000
30	Amplitude (mm)	0.04								
		0.10								
60		0.04								
		0.10								
90		0.04								
		0.10								
120		0.04								
		N/A								

Table 4-4 Test matrix of VAD conditions for testing the effect of the amplitude

Amplitude (mm)	Feed (mm/rev)	0.05			0.1			0.15		
	Rotational speed (rpm)	6000	9000	12000	6000	9000	12000	6000	9000	12000
0.04	Frequency (Hz)	30								
		60								
0.1		30								
		60								
0.2		30								
		60								
0.4		30								
		60								

4.2.2. Experimental Tests on the Effect of Combined VAD Parameters

As shown in Table 4-5, full factorial VAD experiments were conducted (3 speeds × 3 feeds × 2 frequencies × 3 axial speed ratios 'ASR'), with at least 2 replicates for each condition. For comparison, conventional drilling tests were also carried out for the same feeds and speeds. The combinations of the modulation amplitudes and frequencies in Table 4-5 were designed to maintain a fixed ASR value for each feed and rotational speed.

Experimental Tests for the Calibration of Conventional Drilling Cutting Pressures

Table 4-6 shows the set of conventional drilling test conditions that were conducted in order to identify the cutting pressures used for the predictive model calibration. The selected ranges of process parameters (4 speeds × 4 feeds), with at least three replicates for each condition cover the full practical range of the drilling speeds and feeds. Moreover, the range of fiber orientations is fully covered for each set of conditions through the nature of the drilling of unidirectional FRP laminate as will be described later in chapter 5.

Table 4-5 Test conditions for experiments conducted to establish the effect of combined VAD parameters

Feed (mm/rev)		**0.025**		**0.05**		**0.075**	
Frequency (Hz)		**30**	**60**	**30**	**60**	**30**	**60**
n (rpm)	**ASR**	**Peak-to-Peak Amplitude (mm)**					
6,000	**3.3**	0.045	0.025	0.090	0.045	0.135	0.070
	6.7	0.090	0.045	0.180	0.090	0.270	0.135
	10	0.135	0.070	0.270	0.135	0.400	0.200
9,000	**3.3**	0.070	0.035	0.135	0.070	0.200	0.100
	6.7	0.135	0.070	0.270	0.135	0.400	0.200
	10	0.200	0.100	0.400	0.200	0.600	0.300
12,000	**3.3**	0.090	0.045	0.180	0.090	0.270	0.135
	6.7	0.180	0.090	0.360	0.180	0.535	0.270
	10	0.270	0.135	0.535	0.270	0.800	0.400

Table 4-6 Drilling conditions for defining the cutting pressures

Feed 'f_r' (mm/rev)	Rotational speed 'n' (rpm)			
	6,000	8,000	10,000	12,000
	Axial feed (mm/min)			
0.05	300	400	500	600
0.1	600	800	1,000	1,200
0.15	900	1,200	1,500	1,800
0.2	1,200	1,600	2,000	2,400

4.3. Hole Quality Assessment

4.3.1. Delamination

All the produced holes were investigated for entry and exit delamination using a stereo optical microscope (Olympus Model GZX 12). As shown in Figure 4-8, the delamination damage was quantified by a delamination factor as follows:

$$\emptyset_d = \frac{(D_m - D_h)}{D_h} \quad \textbf{4-1}$$

where "D_m" is the maximum diameter of the circle encompassing the observed delamination, and "D_h" is the nominal hole diameter. The delamination factor "$\emptyset_d$" quantifies the level of delamination in the exit or entry planes only and does not account for the depth of the delamination. It also does not also measure the internal delamination that might take place between the inner layers of the hole wall. This is justified since the maximum delamination is always expected to take place at the exit or the entry planes. The first layer of the material at the hole entry plane is more susceptible to the peel delamination because of the tensile cutting forces applied by the cutting edges. The last layers are, however, susceptible to the push out delamination because the thickness of the remaining material is small and the effect of the axial forces is maximum before the tool tip exit [111-115].

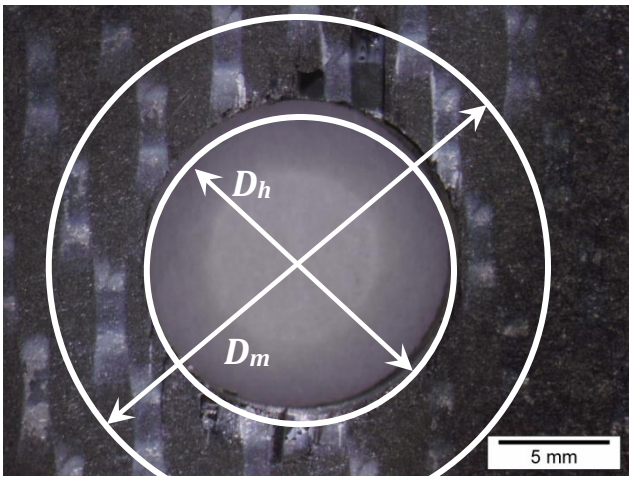

Figure 4-8 Delamination factor definition

4.3.2. Surface Roughness

The mean surface roughness parameter "Ra" is an indicator on the average absolute value of the surface peaks and valleys. The mean surface roughness Ra of the hole walls was measured using a Taylor-Hobson 2 profilometer (Series S4C). The surface roughness measurement was performed over a sampling length of 4 mm along the depth of the hole parallel to the hole center axis, and a cutoff length of 0.8 mm was used. The hole surface was scanned along the hole depth at the 4 quadrant points. The reported "Ra" roughness of the hole surface is taken as the average value of the 4 measurements.

4.3.3. Geometric Accuracy

All the geometric features of the drilled holes were measured using the horizontal-arm Mitutoyo- Mach 806 CMM machine shown in Figure 4-9.

Hole Size Error

The hole size error is defined by the ratio of the difference between the actual hole diameter "D_{actual}", and the nominal hole diameter "$D_{nominal}$" to the nominal hole diameter as follows:

$$Hole\ Size\ Error\% = \frac{100.(D_{actual} - D_{nominal})}{D_{nominal}} \quad \textbf{4-2}$$

A negative error indicates that the produced hole size is smaller than the nominal size. The limits of allowable tolerance were defined based on the aerospace manufacturing standard for low load carrying holes.

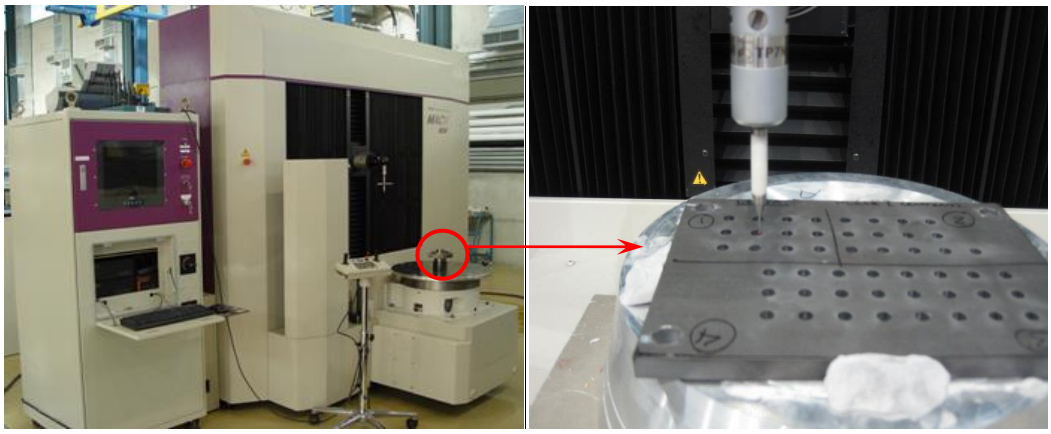

Figure 4-9 Horizontal-arm Mitutoyo- Mach 806 CMM

Hole Circularity Error

The hole circularity error is represented by the radial distance between two concentric circles that encompass the minimum and maximum point positions that define the circle measured by the CMM probe [116]. A high circularity error represents large difference between the radii of the minimum and maximum circles, which means that the probe located points on the circle of measurement are scattered within a larger distance. The circularity error is caused by the tool run out in the first place. Holes with high circularity errors can experience uneven bearing pressure under the load applied by the fastener.

4.4. Rectification Model for VAD Forces

As explained in chapter 2, obtaining accurate force measurements during VAD operations has been a challenging process due to the dynamic force errors. The challenge becomes more significant in systems where the force transducer is part of the vibrating mass mounted on the shaker head. In this case, the undesirable VAD dynamic force components exist in the measured force signals at the same frequency of the superimposed harmonic motion. Therefore, the conventional signal filtering and compensation techniques were found to be not applicable for attenuating such

dynamic force errors. This section presents a corrective dynamic model that rectifies the erroneous VAD tangential and axial force signals measured by a commercial piezoelectric dynamometer mounted on electro-magnetic shakers for the LFHA regime.

4.4.1. Description of the Dynamic Model

An experimental modal analysis in tangential and axial directions was conducted in order to define the transfer function of a multiple degrees of freedom VAD system mounted on a vibrating base (shaker). The rectified force is then obtained by plugging the relative motion between the dynamometer base and face measured during cutting into the system transfer function.

In the current research work, the dynamic behavior of the system in the axial and tangential directions was decoupled. In each direction, the masses of the dynamometer face plate assembly and the dynamometer base plate were modeled as a 2-DOF dynamic system mounted on the vibrating shaker head. Figure 4-10 shows the schematic of the 2-DOF model in the axial direction only. A similar model was used for studying the dynamic behavior in the tangential direction.

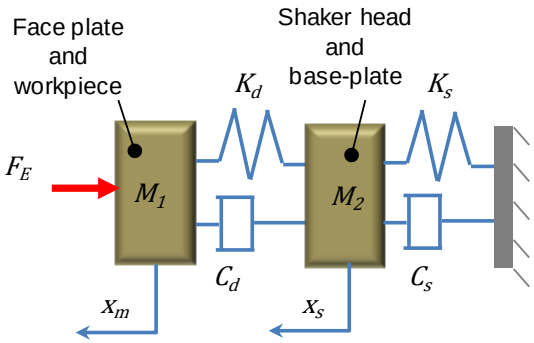

Figure 4-10 Two degree of freedom dynamic model for vibrating shaker and dynamometer mass

The piezoelectric dynamometer comprises piezoelectric oriented discs that produce a charge proportional to the externally applied pressure, along the direction of the relative displacement between the face and base plates of the piezoelectric dynamometer. The stiffness of the dynamometer is controlled by the stiffness of the intermediate discs between the two dynamometer plates. The values of the dynamic

mass, stiffness, and damping of the system elements were defined via experimental modal analysis as will be explained in a coming section.

The equation of the 2-DOF dynamic system is given by:

$$\boldsymbol{M\ddot{x} + C\dot{x} + kx = F} \quad \textbf{4-3}$$

where "$\boldsymbol{M}$" is the matrix of dynamic masses of the dynamometer face plate and workpiece "M_1" and the dynamometer base and shaker head "M_2". "$\boldsymbol{C}$" is the matrix of the damping coefficients of the dynamometer "C_d" and the shaker "C_s". "$\boldsymbol{K}$" is the matrix of dynamic stiffness of the dynamometer "K_d" and the shaker "K_s". "$\boldsymbol{F}$" is the vector of external forces acting on the shaker head, and on the dynamometer face "F_E", which is the drilling force to be predicted. The vector of displacement "$\boldsymbol{x}$" comprises the displacements of the dynamometer base and shaker head mass "x_s" and the displacement of the mass on the dynamometer face "x_m".

The predicted rectified drilling force is determined by defining the transfer function of the described system relating the external force "F_E" and the force measured by the dynamometer "F_d". The calibrated dynamic stiffness of the dynamometer is used to link the measured dynamometer force signal "F_d" and the relative displacement between the dynamometer base and face plates, as shown below:

$$F_d = K_d(x_m - x_s) \quad \textbf{4-4}$$

where "x_s" is the displacement measured on the dynamometer base plate during drilling. Hence, the displacement on the dynamometer face plate could be determined as follows:

$$x_m = \frac{F_d}{K_d} + x_s \quad \textbf{4-5}$$

The external force "F_E" can be computed from the following equation:

$$\begin{pmatrix} F_E \\ 0 \end{pmatrix} = [M]\begin{pmatrix} \ddot{x}_m \\ \ddot{x}_s \end{pmatrix} + [C]\begin{pmatrix} \dot{x}_m \\ \dot{x}_s \end{pmatrix} + [k]\begin{pmatrix} x_m \\ x_s \end{pmatrix} \quad \textbf{4-6}$$

where ($\ddot{x}_s$ and $\dot{x}_s$) are the acceleration and velocity of the dynamometer base plate, respectively, and ($\ddot{x}_m$ and $\dot{x}_m$) are the acceleration and velocity of the dynamometer face plate, respectively.

The motion of the base of the dynamometer and the shaker head is introduced to Equation 4-6 as an input in the form of the real measured displacement of the system masses. Therefore, the force signal obtained by the dynamometer is interpreted in terms of more reliable inputs, which are the measured displacement of the base plate and the calculated displacement of the face-plate (from Equation 4-5) based on the calibrated dynamometer dynamic stiffness. This procedure bypasses the dynamic errors of the dynamometer and defines the measured force based on the full motion of the system elements.

4.4.2. Modal Analysis

In order to determine the transfer function of the system, the spatial parameters of the LFHA VAD system were obtained via experimental modal analysis using a MetalMax® impact hammer system with TXF processing software.

The MetalMax® setup was used to excite the system via a known impact force, and measure the free vibration of the MDOF system. The TXF software then was used for signal processing in order to define the frequency response function (FRF) of the MDOF system, and to extract the system parameters matrices namely dynamic stiffness "$\boldsymbol{K}$", mass "$\boldsymbol{M}$" and damping properties "$\boldsymbol{C}$". Table 4-7 shows the dynamic parameters of the VAD system obtained by modal analysis in the X, Y and Z directions.

The main challenges of achieving reliable system parameters from a modal test are the system mounting conditions, and the selection of an appropriate excitation technique, in addition to the system errors (e.g. misalignment) [117]. For the LFHA VAD system used in the current research, the best mounting condition was found to be by rigid clamping on the bed of the CNC machine tool, in order to achieve the required support rigidity. The noncontact system excitation took place using an impact hammer with a plastic tip.

Table 4-7 Dynamic parameters of the VAD system obtained by modal analysis

Parameter	Element	Direction		
		Z	X	Y
Frequency (Hz)	ω_1	2.73E+03	9.52E+02	7.85E+02
	ω_2	4.62E+03	4.06E+03	1.26E+03
Stiffness (N/m)	K_d	3.78E+08	2.15E+11	2.89E+11
	K_s	2.03E+08	1.47E+12	6.02E+10
Damping Coefficient (N.s/m)	C_d	5.70E+02	9.97E+04	1.46E+05
	C_s	2.21E+02	1.14E+05	4.12E+04
Mass (Kg)	M_1	1.29E+00	1.56E+01	3.08E+01
	M_2	2.42E-01	5.85E+00	2.49E+00

4.4.3. Experimental Validation

In order to validate the developed model, impact and sinusoidal excitations were employed in the axial and the tangential directions. The impact and sinusoidal excitation tests were applied to the force measurement system while vibrating at different combinations of the modulation frequencies "ω_m" and amplitudes "A_m" used for the VAD experiments. A sampling rate of 8 kHz was used for all the validation experiments. Table 4-8 shows the range of the modulation conditions for the experimental validation of the axial and the tangential force components. The VAD system was tested through its entire range of operation; however, the conditions shown in Table 4-8 were selected as representative cases for the modulation conditions that cause significant force errors in each direction.

Table 4-8 Modulation conditions used for experimental validation of the rectification model in the axial and tangential directions

Direction	Frequency (Hz)	Amplitudes (mm)
Axial	30,40, and 50	0.2,0.4, and 0.6
Tangential	40,60, and 100	0.04,0.1,0.2, and 0.4

Experimental Setup for Model Validation

For the LFHA system used in this study (Figure 4-6), the assembly of the workpiece and its fixture was mounted on the piezoelectric dynamometer. This assembly was then mounted on the vibrating shaker head. The electromagnetic shaker was properly fixed on the machine-tool bed in order to deliver the required vibratory motion to the workpiece while the drilling tool performs the conventional axial feed motion. The frequency of the vibratory motion of the piezoelectric dynamometer in a LFHA regime falls fairly below its natural frequency excluding the possibility of force measurement errors due to the dynamometer excitation.

For the experimental validation, impact and sinusoidal excitation modes were employed in each of the axial and the tangential directions. A PCB impact hammer (PCB 086D05) with a plastic tip was used for system impact excitation. The known sinusoidal axial force input to the system was the force required to compress an external coaxial spring due to the displacement of the vibrating shaker. In order to apply that, a calibrated helical spring (1) with a rate of (36.7 N/mm) was compressed and mounted coaxially with the shaker head, as shown in Figure 4-11. The spring (1) was mounted against a rigid structure (8) from one end and against a spring seat (2), which was attached on the face-plate mass (4) of the dynamometer at the other end. The spring force was verified by the readings of a B&K 4381 unidirectional force transducer (7), which was mounted on the rigid structure (8). The displacement of the base plate mass (3) was measured using a B&K 8200 accelerometer (5). The displacement of the face-plate mass (4) was verified using a triaxial PCB 356A25 accelerometer (6).

Figure 4-12 shows the setup used to excite the system in the tangential direction with a known sinusoidal force. A Step motor (1) (4023-830 Applied Motion Products) was mounted on the face-plate of the dynamometer (5) and was used to rotate an eccentric mass (2) located at an eccentricity arm (3). The excitation force in the tangential direction was calculated from the relation of the rotating eccentric mass at a given rotation speed. The displacement of the dynamometer base (4) in the tangential direction was measured using a triaxial PCB 356A25 accelerometer (6).

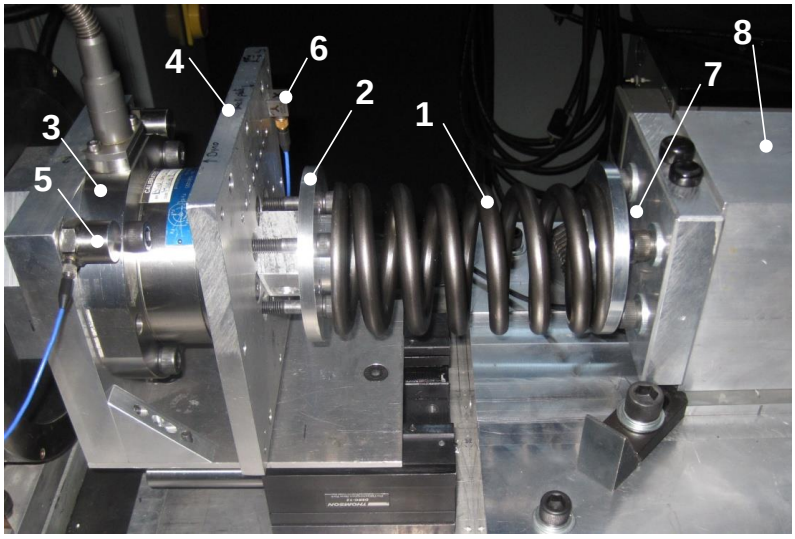

Figure 4-11 Setup for sinusoidal system input in the axial direction

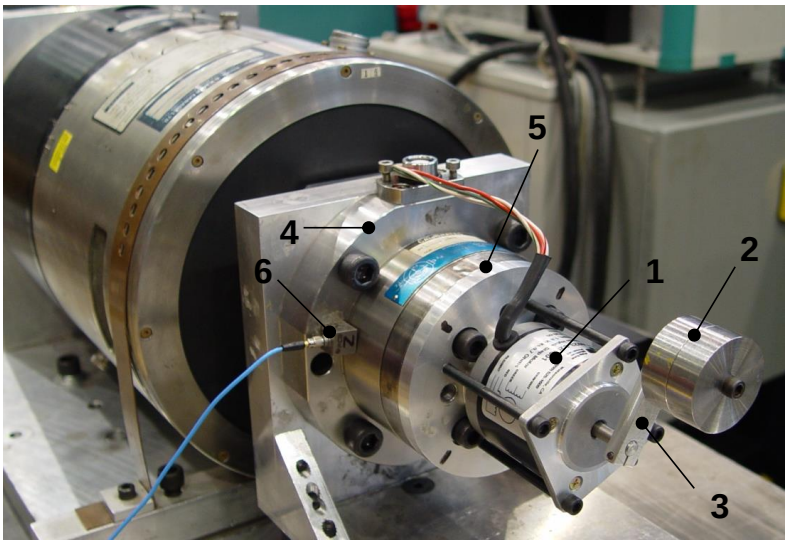

Figure 4-12 Setup for sinusoidal system input in the tangential direction

Validation of Impact Excitation

Figure 4-13 depicts the large error (41%) of the axial impact force measured by the dynamometer mounted on the shaker head compared to the known reference force of the impact force recorded by the reference impact hammer transducer. This error is due to the very low stiffness of the electromagnetic shaker in the axial direction which provides a non-rigid support to the dynamometer's base. This allows the dynamometer base to perform displacement under the action of the impact force, which results in a smaller relative displacement between the dynamometer's base and

face-plates. This in turn, imposes less pressure on the piezoelectric ring, which results in producing a smaller charge output, and hence a lower force is measured. By rectifying the measured force signals using the developed model in the axial direction, the effect of the relative displacement of the plates of the dynamometer is compensated for, which produces a rectified force with a maximum error of 14.5 %.

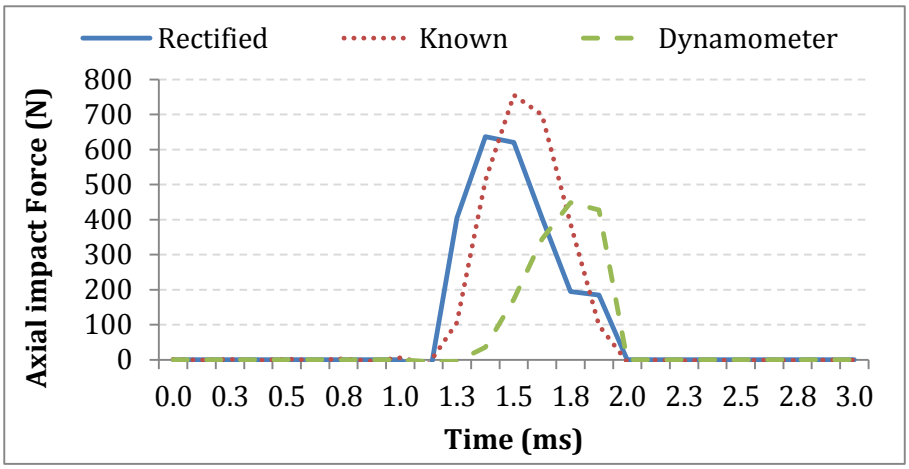

Figure 4-13 Comparison of the rectified, reference, and measured axial impact force signals at ω_m=50 Hz, A_m=0.6 mm.

The errors of the axial impact rectified forces and the forces measured by the dynamometer at different vibration frequencies and amplitudes are compared in Figure 4-14. The errors of the measured forces (without rectification) varied from 22% to 41%, with no specific trend with respect to either modulation frequency or amplitude. On the other hand the errors of the predicted rectified forces varied from 0.5% to 14.5% which is within an acceptable range of measurement errors.

Figure 4-15 compares the tangential force signals of the impact excitation measured by the dynamometer and the rectified force signal compared to the force recorded by the reference (known) impact hammer transducer. The measured force showed an error of 30%, while the rectified force showed a very close prediction with an error of 8%. In the tangential direction, the stiffness of the thin strips supporting the shaker's head is much higher than that in the axial direction. However, the errors of the impact forces measured by the dynamometer in the tangential direction are still exceeding the acceptable range of experimental measurement errors.

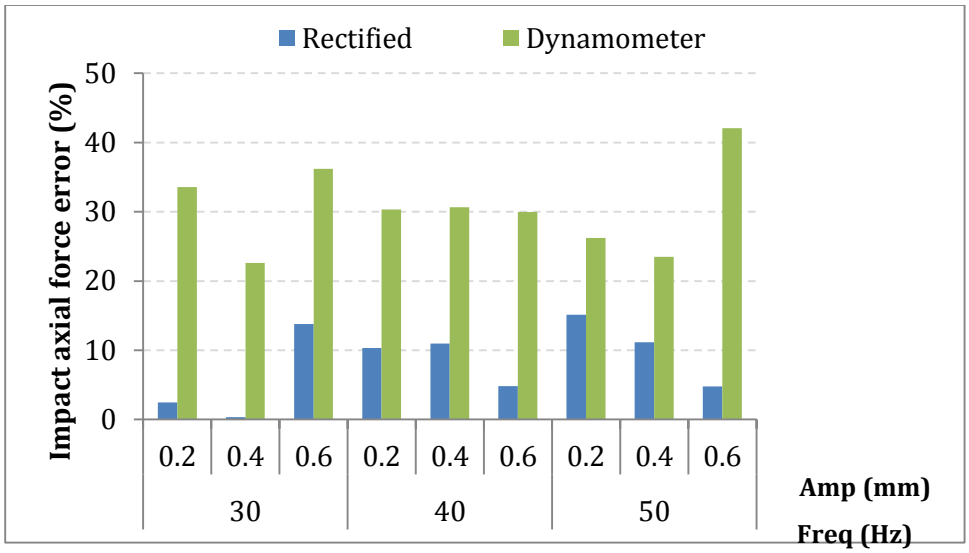

Figure 4-14 Errors of the measured and the rectified axial forces for impact excitation at different modulation conditions

Figure 4-16 compares the errors of the tangential impact rectified forces and the forces measured by the dynamometer at different vibration frequencies and amplitudes. The errors of the measured forces (without rectification) varied from 13% to 40% with no specific trend. The errors of the predicted rectified forces showed an average error of 9% with a minimum error of 4% and a maximum error of 17% compared to the reference force signal of the impact hammer.

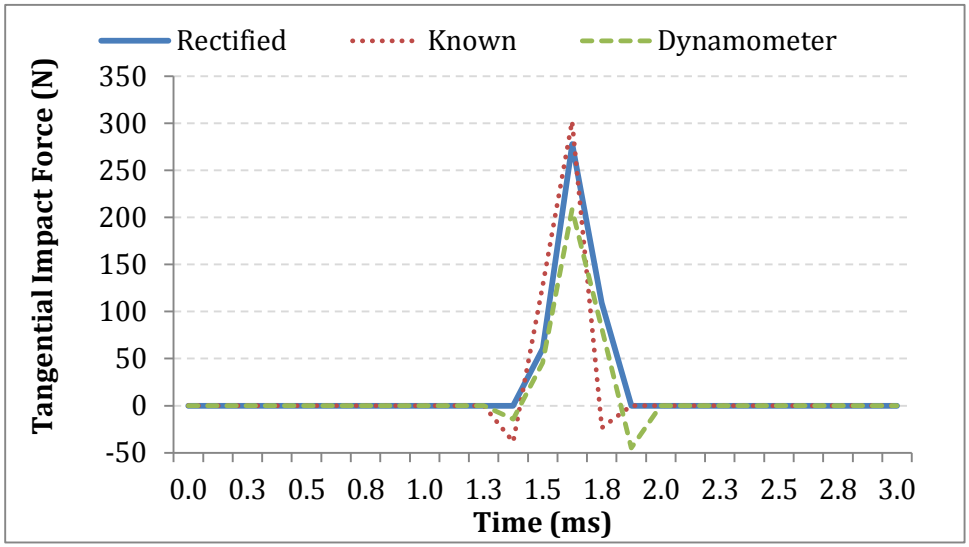

Figure 4-15 Comparison of the rectified, reference, and measured tangential impact force signals at ω_m=40 Hz, A_m=0.2 mm.

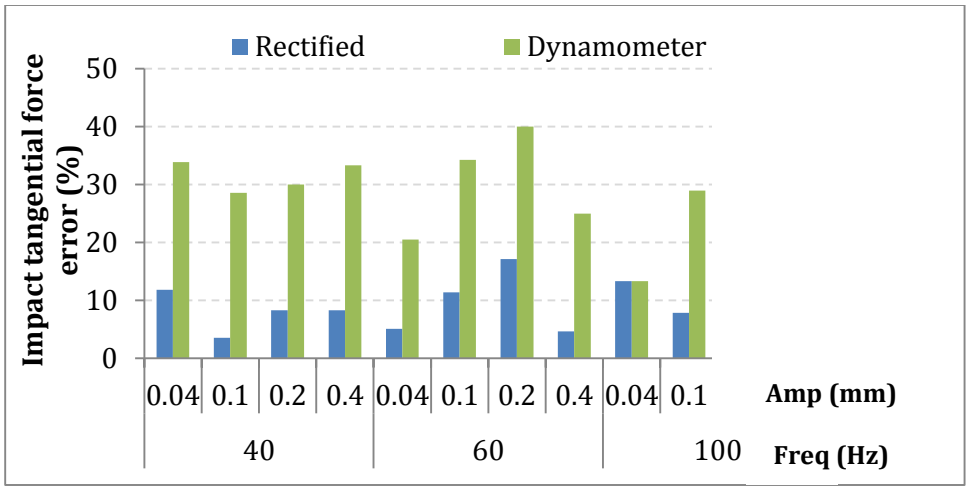

Figure 4-16 Errors of the measured and the rectified tangential forces for impact excitation at different modulation conditions.

Validation of Sinusoidal Excitation

Figure 4-17 compares the axial force signals of the sinusoidal excitation measured by the dynamometer and the rectified force signal compared to the reference known spring force computed from the relationship of the spring rate and the measured displacement. The dynamometer showed a highly erroneous force signal with an error of 180%, while the rectified force showed a very close signal compared to the spring reference force with an error of 9%.

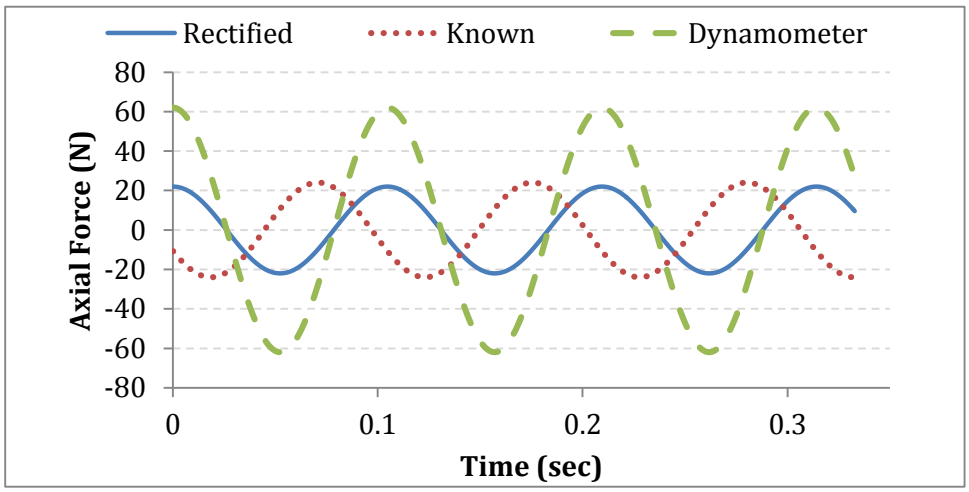

Figure 4-17 Comparison of the rectified, reference, and measured axial sinusoidal force signals at ω_m=50 Hz, A_m=0.6 mm.

The errors of the axial sinusoidal rectified forces and the forces measured by the dynamometer at different vibration frequencies and amplitudes are compared in Figure 4-18. The errors of the measured forces showed an average error of 50% with frequencies 30 Hz and 40 Hz, the error then grew significantly higher at modulation frequency of 50 Hz. However, the model was capable of predicting forces with a maximum error of 15% in all ranges of frequency and amplitude.

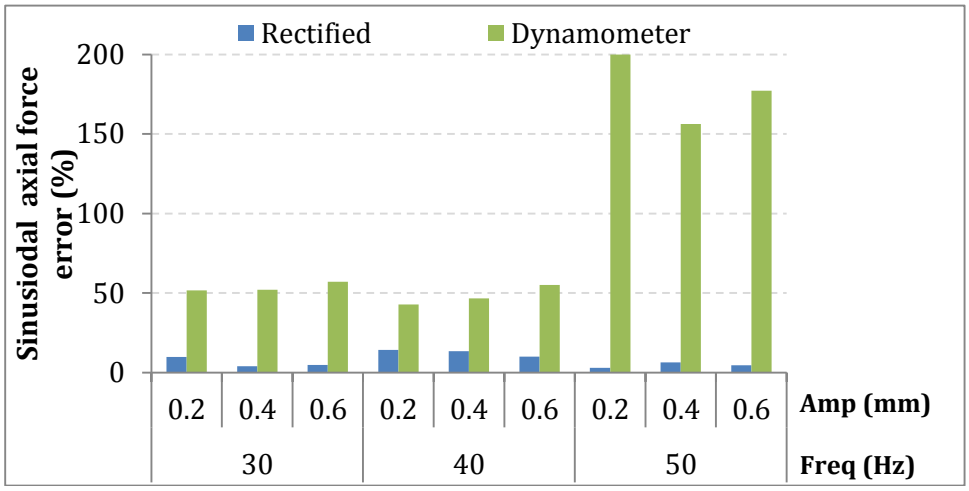

Figure 4-18 Errors of the measured and the rectified axial forces for sinusoidal excitation at different modulation conditions.

Figure 4-19 compares the rectified, reference, and measured sinusoidal tangential force signals corresponding to the sinusoidal excitation input mentioned above. The figure shows slight differences between the three plotted force signals. This shows that the model is effective in rectifying the significantly erroneous measured signals while it does not alter the measured force signals that fall within the acceptable range of errors.

Figure 4-20 compares the errors of the dynamometer measured and the rectified forces at different modulation conditions with respect to a reference sinusoidal excitation force applied in the tangential direction of the system. The reference excitation force was generated using the setup shown in Figure 4-12 by rotating an eccentric mass of (0.13 kg) at an excitation frequency of 12 Hz (750 rpm). Figure 4-20 shows that the measured and the rectified sinusoidal tangential forces at different modulation conditions exhibited errors within the error range of 12.5%. The low

errors of the measured forces could be due to the limited range of excitation of the rotating eccentric mass setup used for system sinusoidal excitation in the tangential direction.

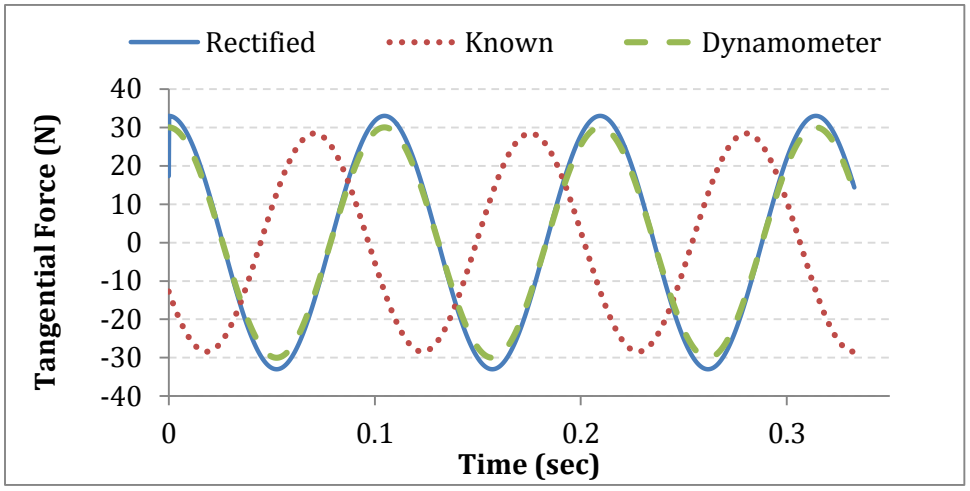

Figure 4-19 Comparison of the rectified, reference, and measured tangential sinusoidal force signals at ω_m=40 Hz, and A_m=0.1 mm, and tangential excitation frequency 12 Hz.

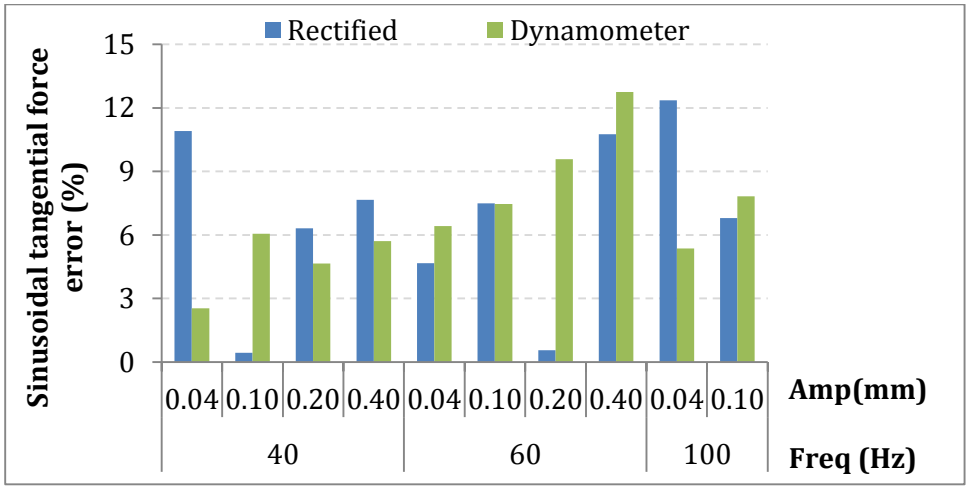

Figure 4-20 Errors of the measured and the rectified tangential forces for sinusoidal excitation at 12Hz for different modulation conditions

CHAPTER 5

Experimental Characterization of Vibration Assisted Drilling of CFRP

5.1. Introduction

This chapter discusses the results of two sets of experiments, which were conducted for the characterization of the effects of the parameters of LFHA VAD on the mechanics of the process and on the produced hole quality attributes. The first set of experiments studies the direct effect of independent process parameters (frequency, amplitude, feed and speed). The second set of experiments was carried out to examine if the combined parameter of the axial speed ratio (ASR) acts as an intrinsic property that can uniquely control the cutting forces and temperatures in VAD. By investigating the effect of independent and combined parameters of the VAD process on the process outputs, a comprehensive understanding of the mechanics of the LFHA VAD is provided. Additionally, this investigation defines the process capabilities and limitations within a wide range of independently controlled process parameters. The results shown in this chapter for conventional and vibration assisted drilling are obtained for drilling of the cross ply laminate described in section 4.1.3.

5.2. Effect of VAD Process Parameters on the Cutting Forces

In machining processes, most of the material and tool damage types could be explained through investigating the drilling forces generated during the machining process. Therefore, it is essential to establish a thorough understanding of the forces of the LFHA VAD process and the parameters controlling the features and the trends of the LFHA VAD force signals. The maximum force value is always of interest because it indicates the possibility of occurrence of the physical material and tool damage during the drilling process. Therefore, this section focuses on the effect of the LFHA

VAD parameters on the maximum force value obtained under different operating conditions.

As discussed in the previous chapter, the measured force signals were rectified using the dynamic rectification model described in chapter 3. Figure 5-1 shows the full signals of the measured and the rectified VAD axial force performed at n=12000 rpm, f_r= 0.075 mm/rev, A_m=0.1 mm, and ω_m=60 Hz. The axial force signal shown in Figure 5-1 (b) experiences major fluctuations (10 N to 120 N) due to the superimposed harmonic motion, and minor fluctuations (100 N to 120 N) due to the dynamic change of the angle between the cutting edge and the fiber as the tool rotates. Figure 5-1 (b) shows also that the percentage of force rectification is within 13% of the original unrectified signal. This is a small range compared to the range of force error in the case of system impact and sinusoidal excitation shown in section 4.5.3. This is due to the significantly lower range of the drilling forces compared to that of the impact test. The following sections will focus on the effect of the VAD parameters on the axial forces, rather than the cutting torque due to the significant role of the axial force in developing and propagating interlaminar cracks, which are the most serious type of mechanical damage that can affect the mechanical properties of the machined part.

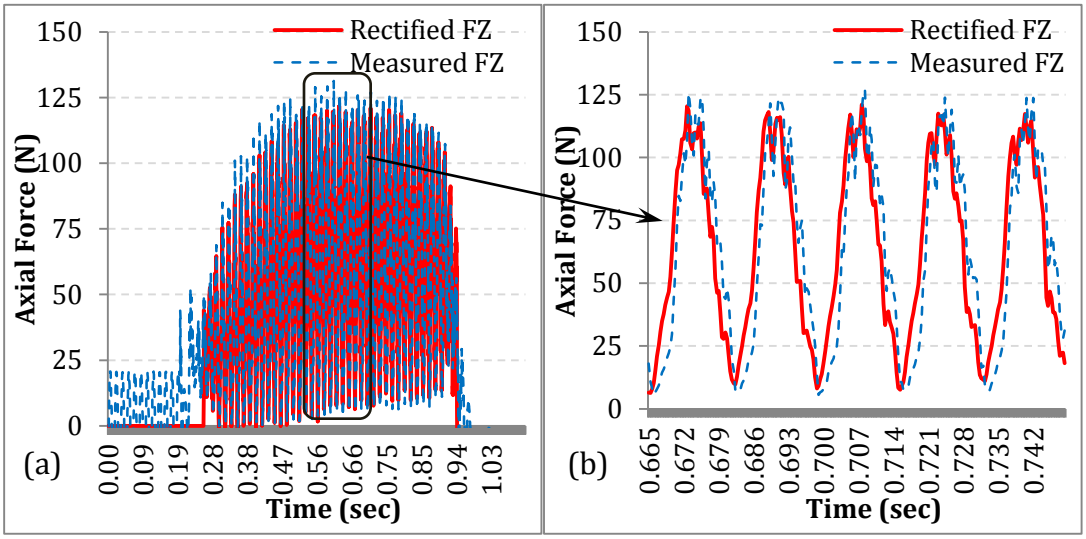

Figure 5-1 The VAD axial force performed at n=12000 rpm, f_r= 0.075 mm/rev, A_m=0.1 mm, and ω_m=60 Hz (a) full signals, and (b) detailed measured and rectified signals

5.2.1. Effect of the VAD Modulation Frequency on the Axial Forces

As explained in the previous chapter, due to the limitation on the VAD system capacity, it was hard to test the force trends at frequencies higher than 120 Hz for the 0.04 mm amplitude or higher than 90 Hz at 0.1 mm modulation amplitude. Figure 5-2 shows the effect of the modulation frequency 'ω_m' on the VAD maximum axial force at different feeds, speeds and modulation amplitudes. Changing the modulation frequency was found to have different effects on the maximum force value depending on the rotational speeds. This can be seen by comparing the plots in Figure 5-2 (a, c, and e) for A_m=0.04 mm and rotational speeds of 6000 rpm, 9000 rpm, and 12000 rpm, respectively. For the three plots, the axial force increased directly with the increase of the frequency until the frequency of 90 Hz. At frequency of 120 Hz, the axial force declined at the speeds of 6000 rpm, while kept increasing at 9000rpm, and 12000 rpm. At A_m=0.1 mm, the plots in Figure 5-2 (b, d, and f) show a clear direct relationship between the maximum axial force and the full range of the feed and the modulation frequency at the three levels of 'n'.

Figure 5-2 also depicts the dominant direct relationship between the drilling feed and the maximum axial force value. This is attributed to the direct effect of the feed on the uncut chip thickness where large feeds require high forces for chip formation. The effect of the rotational speed was found to be of the least independent effect on the maximum axial force. The trend of the axial force values matched the trend of the theoretical maximum uncut chip thickness with the change of the rotational speed shown in Figure 5-3. The axial force declined with the increase of the rotational speed, which promotes progressive chip removal for the same frequency because the cutting edge of the rotating tool will perform more rotational cycles for the same number of vibration cycles, which results in removing smaller uncut chip thickness per rotation.

The observations of the previously discussed behavior of the maximum force values can be explained by investigating the effect of the same ranges of VAD conditions on the calculated maximum uncut chip thickness. The values of the maximum 'd' were calculated using equation (3-9). Figure 5-3 shows the effect of the VAD parameters on the calculated maximum 'd' at a single feed level of f_r=0.1

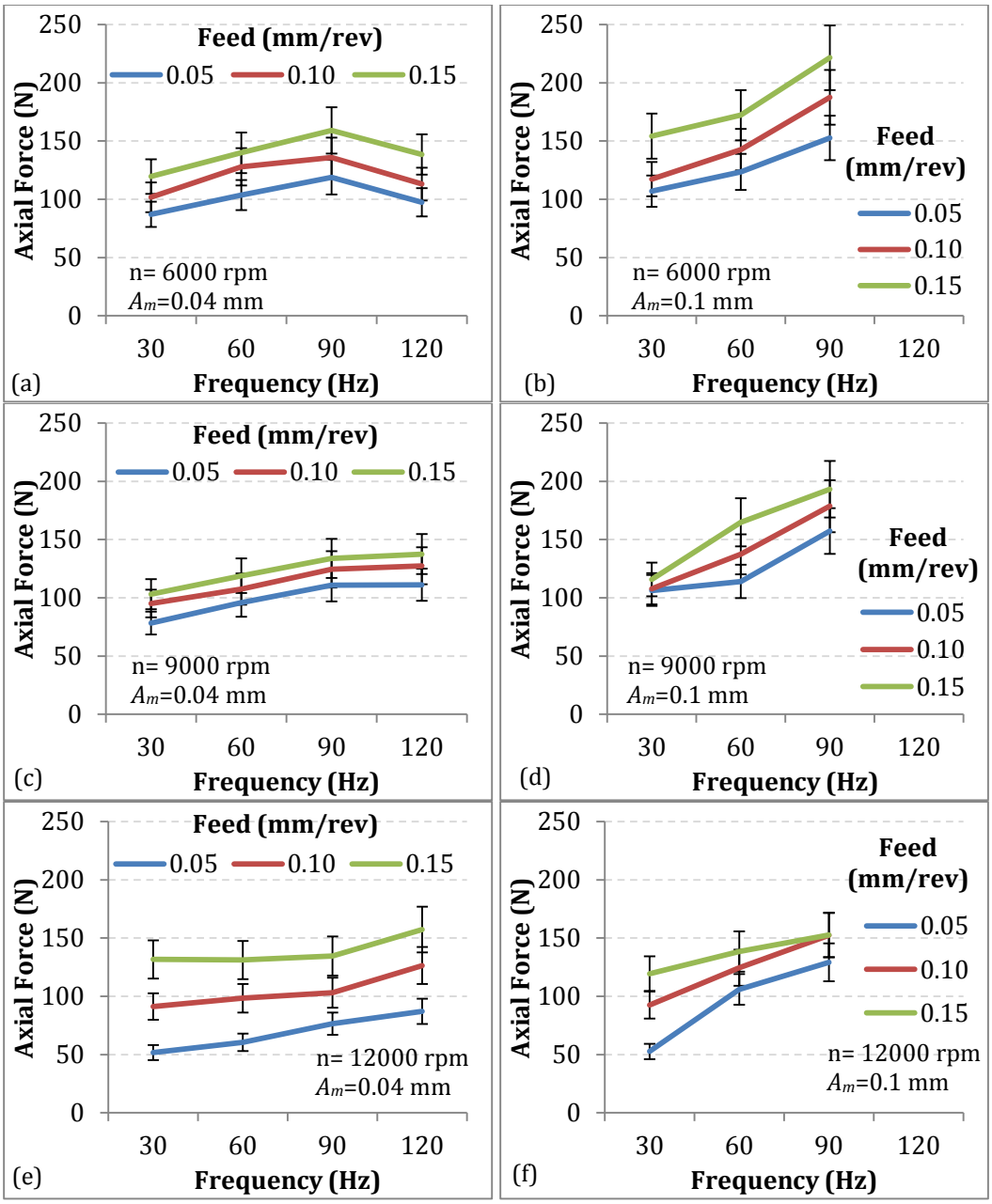

Figure 5-2 Effect of the modulation frequency "ω_m" and the feed on the VAD maximum axial force, at rotational speeds (a,b) n=6000 rpm, (c,d) n=9000 rpm, and (e,f) n=12000 rpm and modulation amplitudes (a,c,e) A_m=0.04 mm, and (b,d,f) A_m=0.1 mm.

mm/rev as a representative case. Figure 5-3(a) shows that at A_m=0.04 mm, the calculated maximum 'd' experienced the same trend of the axial forces that was shown in Figure 5-2 (a, c, and e). As explained in Chapter 3, the value of 'd' is determined from the normal distance between two successive machined surfaces formed by each of the cutting tool's cutting edges at the same angular position. Such normal distance

is controlled by the feed, amplitude and the phase difference between the peaks of the machined surfaces formed by the cutting edges due to the superimposed vibration.

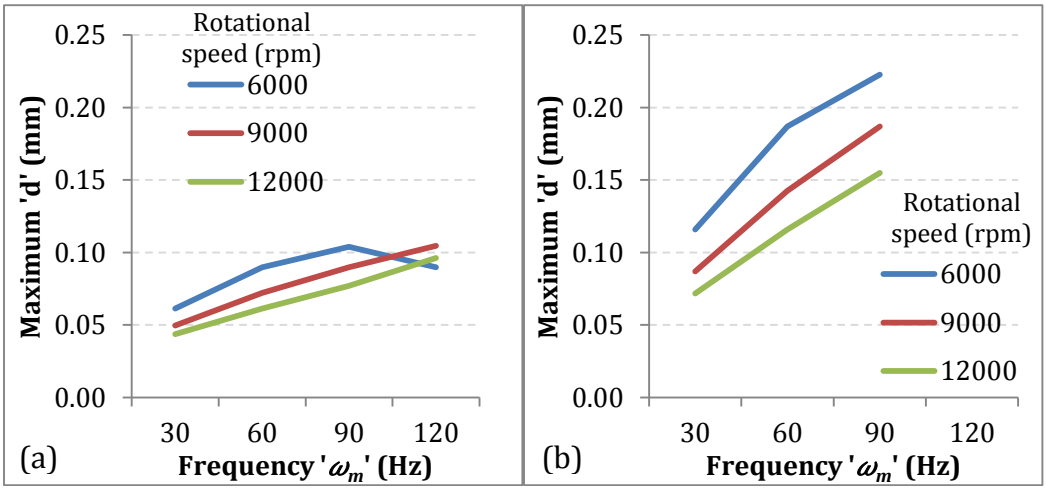

Figure 5-3 Effect of the modulation frequency "ω_m" on the theoretical VAD maximum uncut chip thickness value at different speeds, f_r = 0.05 mm/rev, and (a) A_m = 0.04 mm and (b) A_m = 0.1 mm.

Figure 5-4 is focusing on the effect of 'ω_m' on the percentage of the axial force reduction (negative percentage) or increase (positive percentage) in VAD compared to conventional drilling. The figure shows that the force reduction was found to be more significant at the lower amplitude A_m=0.04 mm (Figure 5-4 (a, c, and e)), which is represented by the higher percentage of force reduction (negative percentage). The figure also indicates that the VAD process has a higher potential for force reduction through the combination of high rotational speed, at low frequency and low amplitude where the maximum axial force of conventional drilling can be reduced by up to 40 %. This beneficial effect was found also to be more effective with higher feeds. This is because the low amplitude reduces the maximum 'd' in each duty cycle through the progressive removal of the larger 'd' corresponding to the high feed. This beneficial effect is enhanced by the increase of the rotational speeds, which was shown in Figure 5-3 to reduce the maximum 'd' during the duty cycles.

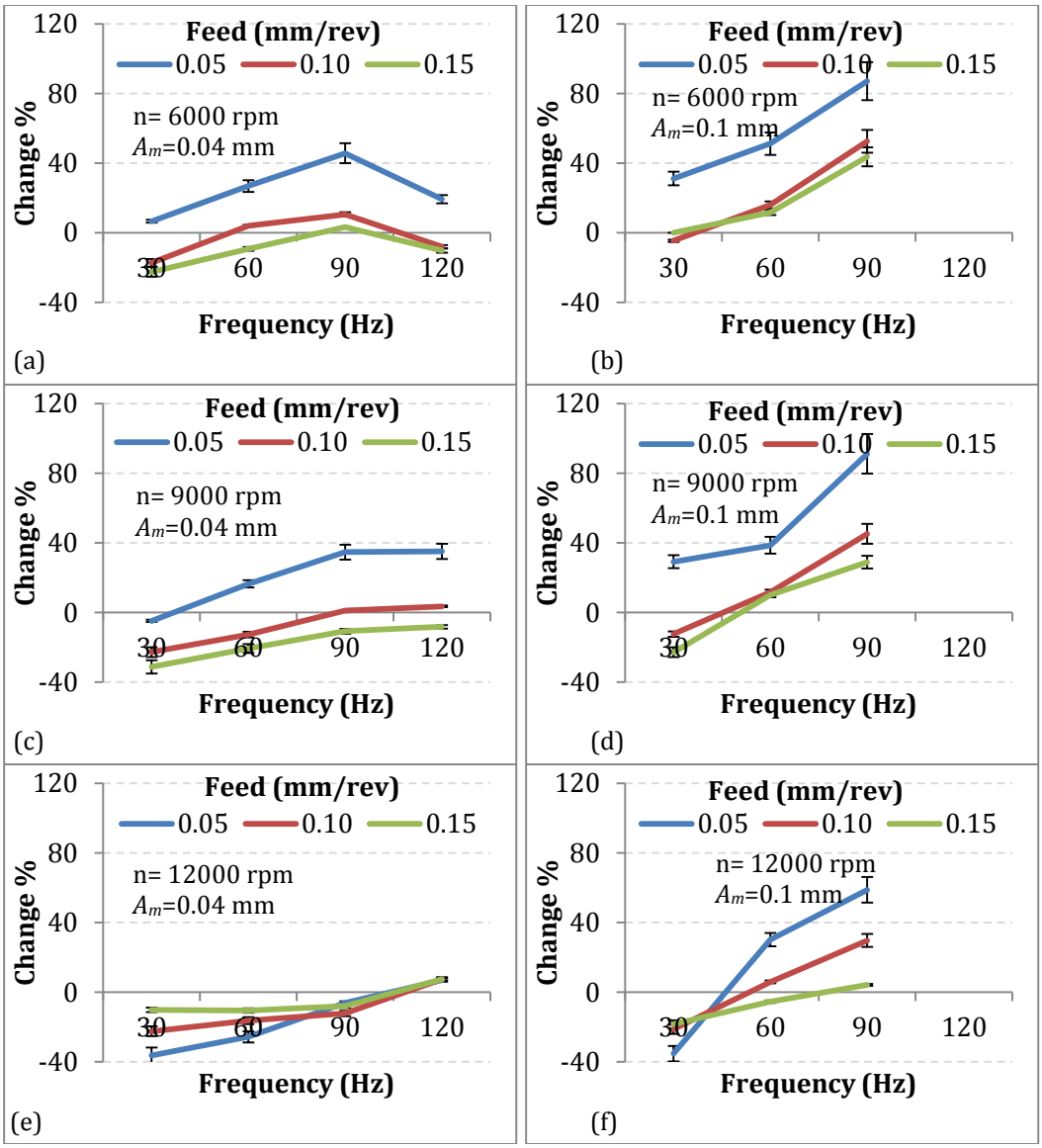

Figure 5-4 Effect of the modulation frequency "ω_m" and the feed on the change % of the VAD maximum axial force compared to conventional drilling, at rotational speeds (a,b) n=6000 rpm, (c,d) n=9000 rpm, and (e,f) n=12000 rpm and modulation amplitudes (a,c,e) A_m=0.04 mm, and (b,d,f) A_m=0.1 mm.

5.2.2. Effect of Modulation Amplitude on the Axial Forces

Figure 5-5 shows the effect of a wide range of modulation amplitude "A_m" (0.04 mm – to 0.4 mm) on the VAD maximum axial force at different feeds, speeds and modulation frequencies. The figure shows a consistent direct relationship between the maximum axial force value and both the amplitude and the feed. This is attributed to the direct effect of increasing the feed or the amplitude on the maximum 'd', which

increases the axial force due to the higher energy required to remove a larger uncut chip thickness.

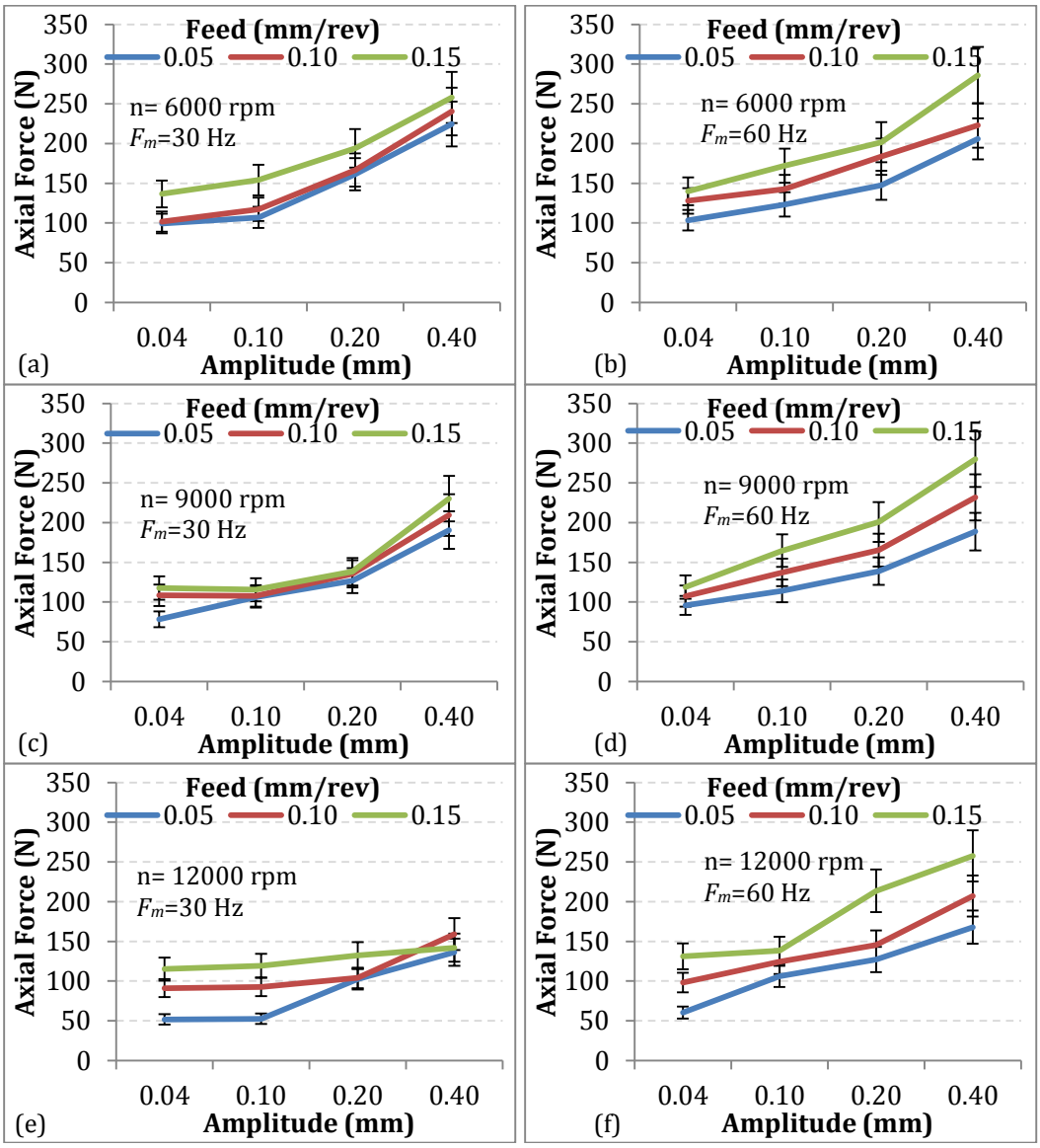

Figure 5-5 Effect of the modulation amplitude "A_m" and the feed on the VAD maximum axial force, at rotational speeds (a,b) n=6000 rpm, (c,d) n=9000 rpm, and (e,f) n=12000 rpm and modulation frequencies (a,c,e) ω_m=30 Hz, and (b,d,f) ω_m=60 Hz.

Comparing Figure 5-5 (a,c,e) and (b,d,f) shows the higher slope of the axial force-amplitude relationship as the frequency increases from 30 Hz to 60 Hz. This is attributed to the larger increase in 'd' with the increase in frequency if other VAD conditions were kept fixed. As previously explained, the axial force was found to be declining with the increase of the rotational speed for the same frequency and

amplitude due to the decrease in 'd' determined by the difference between the two successive machined surfaces. This is evident by the results shown in Figure 5-5.

Figure 5-6 shows the percentage of reduction (negative percentage) or increase (positive percentage) of the VAD maximum axial force compared to conventional drilling. The results in Figure 5-6 show that the higher force reduction could be achieved at the low modulation amplitude when combined with low frequency, high speed and high feed. At low frequency of 30 Hz (Figure 5-6 a, c and e), the axial force reduction (negative percentage) was found to be achievable for n=6000 rpm with f_r=0.1 and f_r=0.15 mm/rev, for vibration amplitudes below 0.1 mm. As the speed was increased, the force reduction was extended to a higher range of amplitudes. At n=12000 rpm, the axial force reduction was observed within the entire range of amplitudes, ($0.04<A_m<0.4$mm) at f_r=0.15 mm/rev. At higher frequency of 60 Hz (Figure 5-6 b, d and f), the axial force reduction was only observed for the range of low amplitudes A_m=0.04 mm through the entire range of feeds and speeds. The aforementioned behavior of force reduction can be explained through the mechanisms of force reduction discussed in Chapter 3. The low amplitude with high feed promotes the progressive chip formation, where the larger uncut chip thickness is divided into sections of smaller thicknesses corresponding to the small value of the amplitude, which reduces the maximum axial force value. The increase of the rotational speed for the same frequency leads to changing the phase difference between the forms of the successive machined surfaces. For the cases shown in (Figure 5-6 a, c and e), the phase difference was reduced with the increase in the rotational speed, which reduced the maximum uncut chip thickness 'd'. At f_r=0.1 mm/rev, ω_m=30Hz and A_m=0.04 mm, the maximum calculated uncut chip thickness was d=0.086, 0.075 and 0.069 mm for n=6000, 9000 and 12000 rpm, respectively. For higher frequency (Figure 5-6 b, d and f), the tool performed double the number of the separation cycles compared to the low frequency and hence contributed to increasing the uncut chip thickness compared to that of the conventional drilling.

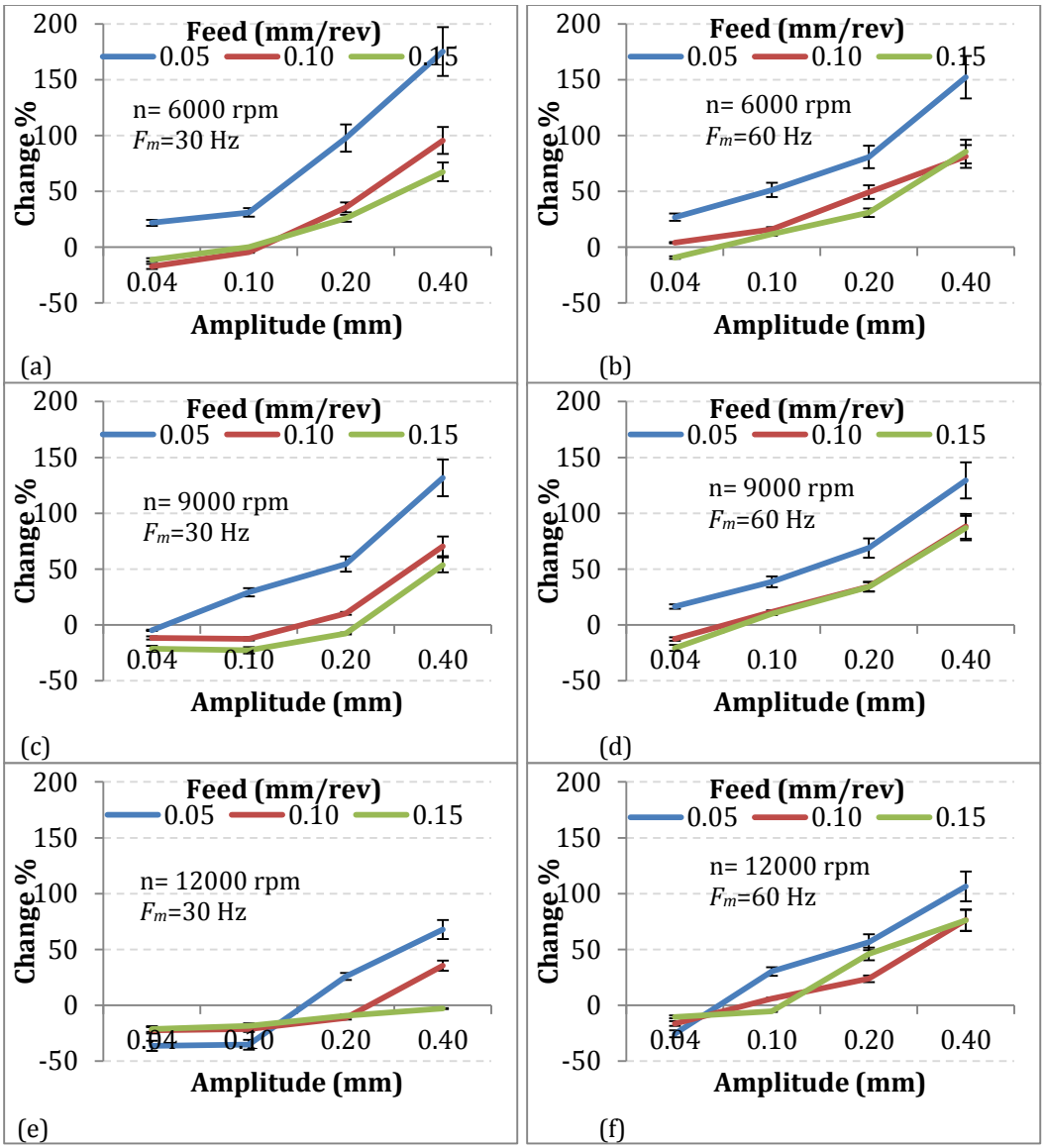

Figure 5-6 Effect of the modulation amplitude "A_m" and the feed on the change % of the VAD maximum axial force compared to conventional drilling, at rotational speeds (a,b) n=6000 rpm, (c,d) n=9000 rpm, and (e,f) n=12000 rpm and modulation frequencies (a,c,e) ω_m=30 Hz, and (b,d,f) ω_m=60 Hz.

5.2.3. Testing the Hypothesis of the Independent ASR Effect on the VAD Forces

Figure 5-7 shows the effect of the VAD feed, rotational speed, and ASR on the VAD maximum measured axial force, and the theoretical maximum 'd'. As shown in Figure 5-7 (a), for a given rotational speed, the axial forces were found to be higher at the higher ASR values with low frequency. This is because the higher amplitudes used in order to achieve higher ASR values resulted in a larger 'd'.

(a)

Feed		0.025 mm/rev		0.05 mm/rev		0.075 mm/rev	
rpm	ASR	Frequency (Hz)					
		30	60	30	60	30	60
6000	3.3	75 N to 125 N		>125 N		>125 N	75 N to 125 N
	6.7						
	10.0						
9000	3.3		<75 N	>125 N			
	6.7						
	10.0						
12000	3.3			75 N to 125 N			
	6.7						
	10.0	75 N to 125 N					

(b)

Feed		0.025 mm/rev		0.05 mm/rev		0.075 mm/rev	
rpm	ASR	Frequency (Hz)					
		30	60	30	60	30	60
6000	3.3					0.13 to 0.26 mm	
	6.7			0.13 to 0.26 mm		>0.26 mm	
	10.0	<0.26 mm		>0.26 mm		>0.39 mm	>0.26 mm
9000	3.3	0.00 to 0.13 mm				0.13 to 0.26 mm	
	6.7			0.13 to 0.26 mm		0.26 to 0.39 mm	
	10.0	0.13 to 0.26 mm		>0.26 mm		>0.39 mm	
12000	3.3	0.00 to 0.13 mm				0.13 to 0.26 mm	
	6.7			0.13 to 0.26 mm		0.26 to 0.39 mm	
	10.0	0.13 to 0.26 mm		0.26 to 0.39 mm		>0.39 mm	

Figure 5-7 Effect of the VAD feed, rotational speed, and ASR on (a) VAD maximum axial force, and (b) calculated maximum uncut chip thickness.

In the horizontal direction, Figure 5-7 (a) shows that increasing the feed and/or the frequency of vibration, for a fixed ASR value, resulted in a significantly varying force level, which was controlled mainly by the feed. This indicates that the ASR factor does not represent an intrinsic parameter that has a unique effect on the VAD maximum axial force. Comparing Figure 5-7(a) and (b) depicts the strong correlation between the axial force and the corresponding uncut chip thickness for each of the VAD conditions. This confirms that the independent process parameters namely feed, amplitude, frequency and speed are the key factors that control the uncut chip thickness and hence the value of the maximum force.

5.3. Effect of the VAD Process Parameters on the Tool Temperature

Reinforced polymer composites are sensitive to thermal damage that causes material deterioration and decomposition at the machined surface and/or within the heat affected zones. Therefore, the thermal damage associated with any machining process is a critical aspect to be considered for the characterization of such process.

The thermal damage is expected to take place when the temperature at the cutting zone exceeds the decomposition temperature of the polymer matrix. The occurrence of the thermal damage is also controlled by whether there was enough time during the cutting process for the heat to build up and propagate through the material. The measured maximum tool temperature at the exit plane of the drilled hole can give an indication on the possibility of the occurrence of thermal damage associated with the drilling process.

5.3.1. Effect of the Modulation Frequency on the Tool Temperature

Figure 5-8 shows the effect of the modulation frequency "ω_m" on the maximum tool temperature measured at the hole exit plane at different feeds, speeds and modulation amplitudes. For all VAD conditions in Figure 5-8, the measured tool lip temperatures were found to be below the material decomposition temperature (T_{cr}=320°C). The figure shows the marginal effect of frequency on the temperature for the range of frequencies of this set of experiments.

Figure 5-8 shows that for VAD, the tool temperature generally was reduced with the increase in feed. Although increasing the feed results in an increase in the cutting energy, it reduces the time required for the heat to propagate into the tool and workpiece. The only exception to this trend was observed at low speed (Figure 5-8 (a) and (b)), where the highest temperature was associated with the medium feed (f_r =0.1 mm/rev). This could be attributed to the relatively shorter cutting time and the less heat dissipation associated with the high and the low feeds, respectively. This behavior was observed at the low speed only, which creates a relatively low 'Nu' number, and hence not enough heat could be dissipated in the air gap during the separation cycle. At medium and high speeds, although low feed generates less heat it allows enough time for heat to build up and hence the temperature increases. On the other hand, while high feed generates more heat during cutting, the short cutting duration does not allow the temperature to increase. For the two levels of amplitude (A_m= 0.04 and 0.1 mm) shown in Figure 5-8, the effect of the amplitude on the maximum temperature seems to be marginal. Therefore, the effect of the amplitude in a wider range of amplitudes is further investigated in the following sub-section.

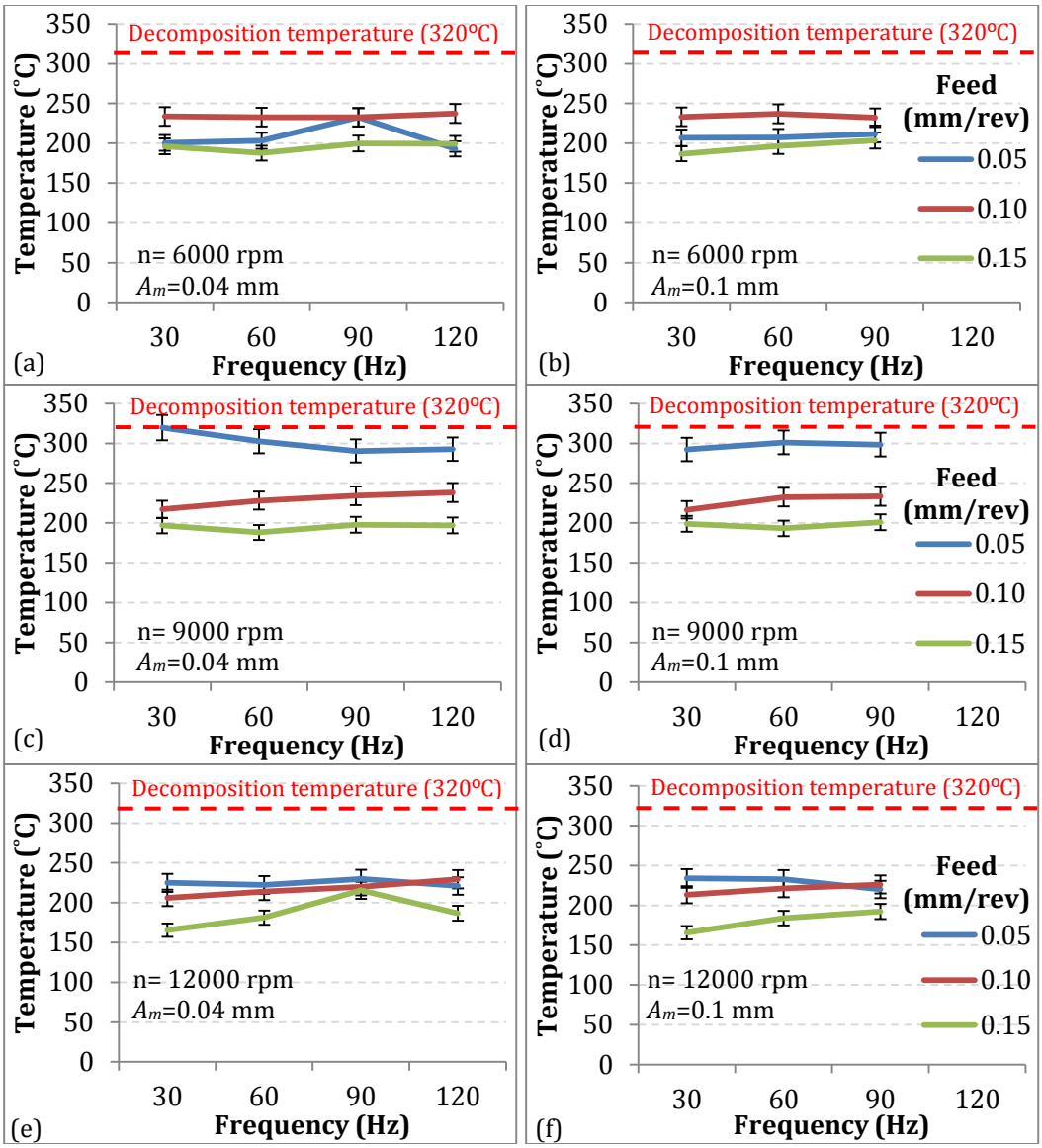

Figure 5-8 Effect of the modulation frequency "ω_m" and the feed on the VAD maximum tool temperature, at rotational speeds (a,b) n=6000 rpm, (c,d) n=9000 rpm, and (e,f) n=12000 rpm and modulation amplitudes (a,c,e) A_m=0.04 mm, and (b,d,f) A_m=0.1 mm.

As seen in Figure 5-8, the temperature was found to be maximum at the medium rotational speed (n=9000 rpm) compared to the low and high speeds of 6000 and 12000 rpm, respectively. This is because low speed is accompanied by low heat generation and dissipation, while with medium speed the heat generation increases due to the higher cutting energy; however, the speed of rotation is not high enough to cool the tool down via the generated vortices in the air gap. As the rotational speed increases to 12000 rpm, the cutting energy increases further, which increases the

temperature of the tool, however, the high speed effectuates the source of heat dissipation through increasing the 'Nu" number as explained in section 3.4.

Figure 5-9 shows the effect of the modulation frequency and the feed on the increase (positive percentage) or reduction (negative percentage) of the maximum tool temperature in VAD compared to conventional drilling, at different rotational speeds and modulation amplitudes. The figure shows trends similar to the trends shown in Figure 5-8 with respect to the modulation frequency. In general, the VAD

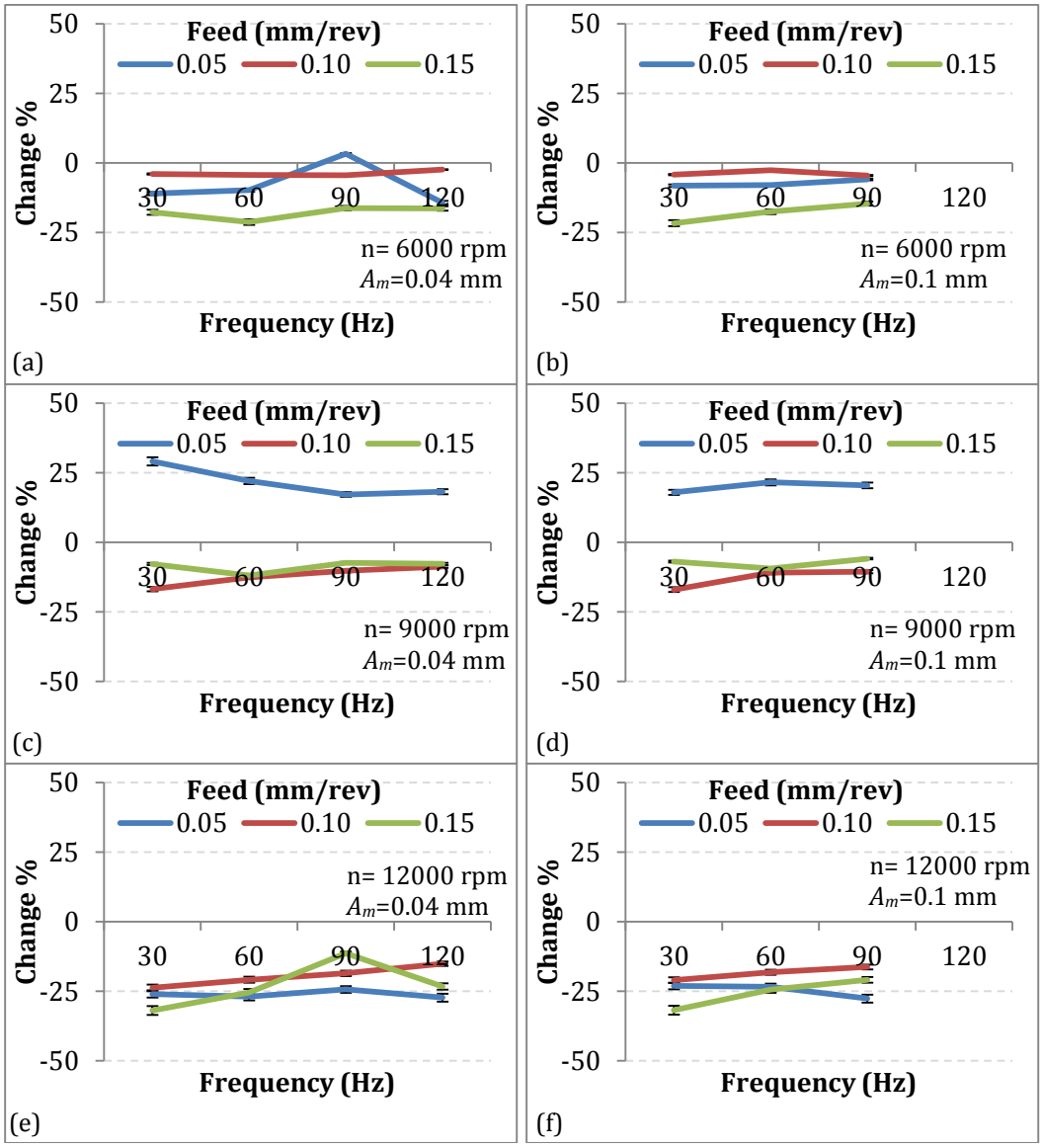

Figure 5-9 Effect of the modulation frequency "ω_m" and the feed on the percent change of the VAD maximum tool temperature, at different rotational speeds and modulation amplitudes "A_m".

temperature was found to be reduced by up to 30%, except for the case of n=9000 rpm with f_r=0.05, where the VAD temperature was higher than that of the conventional drilling by an average of 20%.

5.3.2. Effect of the Modulation Amplitude on the Tool Temperature

Figure 5-10 shows the maximum tool temperature measured at the hole exit plane for a wider range of modulation amplitudes at different feeds, speeds and modulation

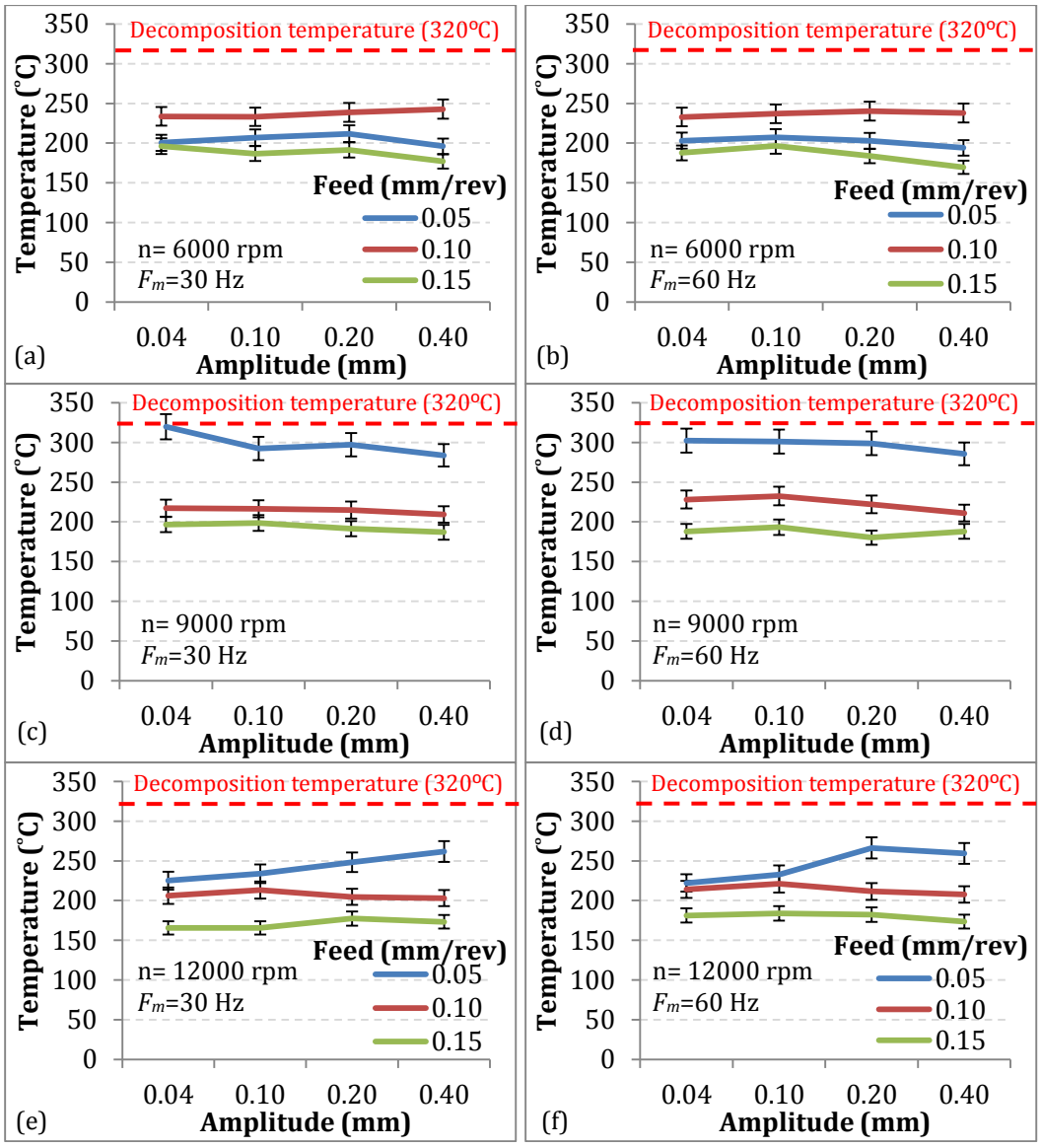

Figure 5-10 Effect of the modulation amplitude "A_m" and the feed on the VAD maximum tool temperature, at different rotational speeds and modulation frequencies "ω_m".

frequencies. For all VAD conditions in Figure 5-10, the measured tool lip temperatures were found to be below the material decomposition temperature (T_{cr} = 320°C).

Figure 5-10 shows a slight effect of the modulation amplitude on the maximum tool temperature. This could be either because the sources of heat generation and dissipation are balanced so none of them shows a dominant effect, or that the range of the large amplitudes is larger than the range of the effective gap size for effective cooling. The figure also shows the marginal effect of frequency on the temperature. As

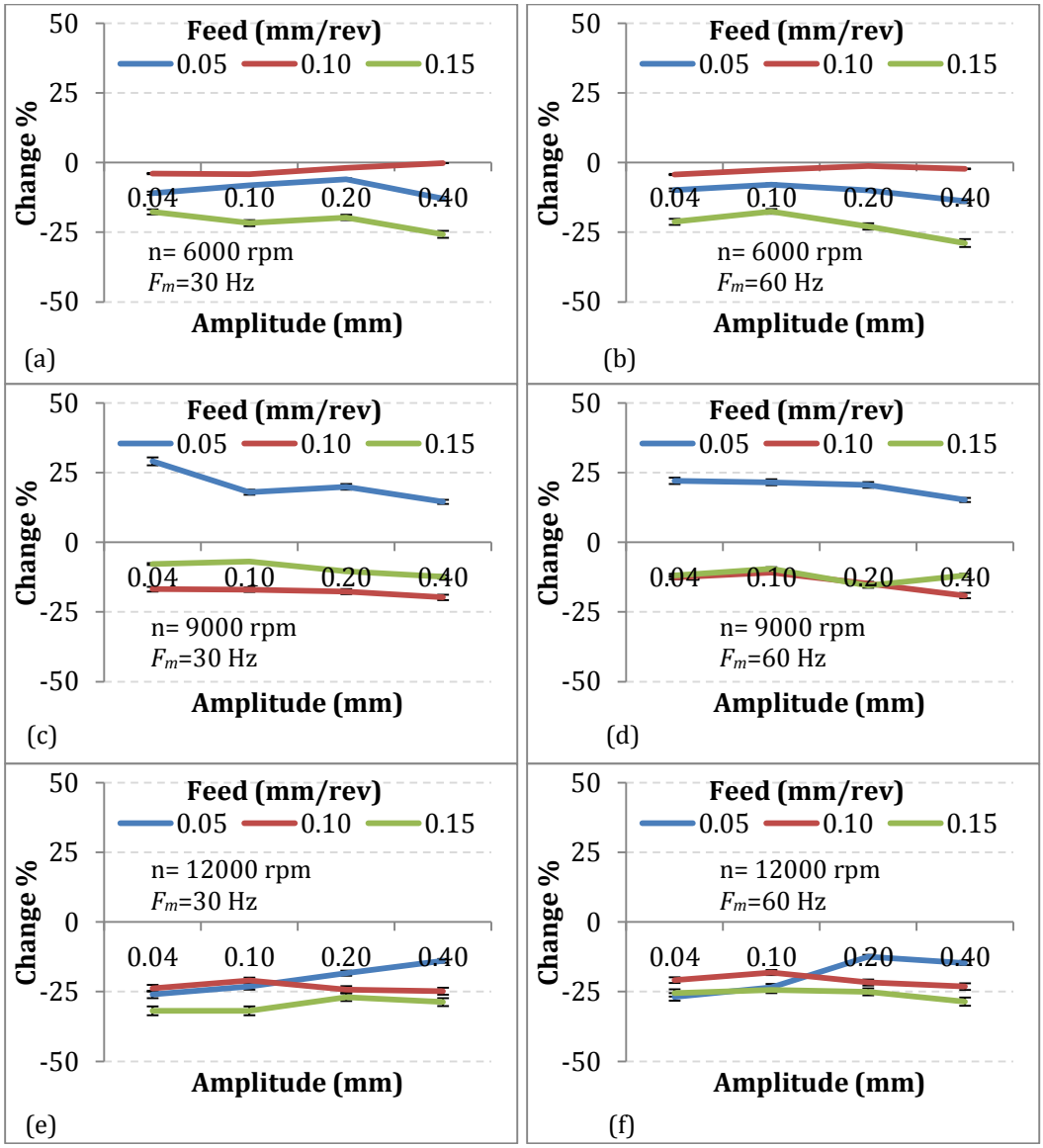

Figure 5-11 Effect of the modulation amplitude "A_m" and the feed on the percent change of the VAD maximum tool temperature compared to conventional drilling, at different rotational speeds and modulation frequencies "ω_m".

indicated earlier, although increasing the feed results in an increase in the cutting energy, it reduces the time required for the heat to propagate into the tool and workpiece. Figure 5-10 shows that feed, at all levels of the rotational speed, has the most significant effect.

Figure 5-11 shows the percentage of change of the VAD maximum temperature compared to conventional drilling relative to the same VAD conditions discussed in Figure 5-10. For all the plots in Figure 5-11, the VAD tool temperature was found to be reduced by up to 30%, except for the case of n=9000 rpm with f_r= 0.05 where the VAD temperature was higher than that of the conventional drilling by up to 25%.

5.3.3. Testing the Hypothesis of the Independent Effect of the ASR on the VAD Tool Temperature

Figure 5-12 shows the effect of the VAD feed, rotational speed, and ASR on the maximum tool lip temperature measured at the hole exit. The figure confirms the previously observed trend of the inverse relationship of the tool temperature in VAD with the feed. The measured tool lip temperatures in Figure 5-12 were found to be below the material decomposition temperature (T_{cr}=320°C), except at low feeds when combined with (i) low speed and high frequency of vibration, (ii) medium speed and low/medium ASR, or (iii) high speed and high ASR. In contrast, the lowest measured temperatures (<200°C) were found also at low feed, but in combination with (iv) high rotational speed and low ASR. Comparison of the worst and best combinations, (iii) and (iv), respectively, demonstrates the competing mechanisms of heat generation and dissipation in VAD. Both combinations involve high spindle speed of 12,000 rpm. While this translates into high cutting energy, it also promotes heat dissipation in the gap between the tool and the workpiece during disengagement as shown in Figure 3-8. With combination (iv), where ASR=3.3, the average air gap is in the range of 15 to 45 μm, where the CHT h_g offers the highest cooling capacity. Combination (iii), on the other hand, correspond to ASR=10 (with average air gap width of 75-160 μm), where the air gap thickness is sub-optimal and hence the heat dissipation capacity of the VAD system is impaired.

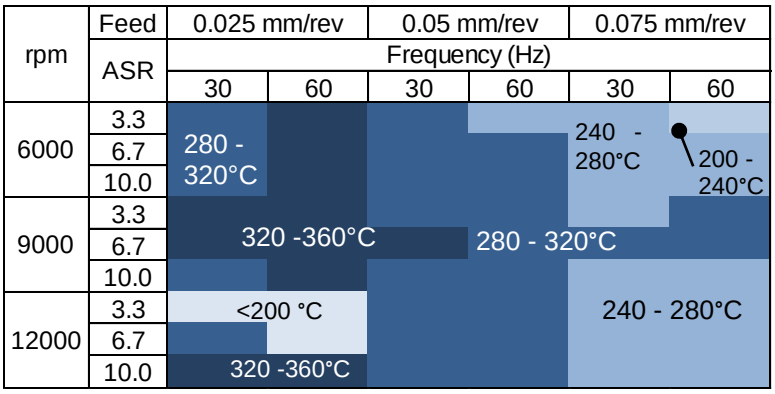

Figure 5-12 Effect of the VAD feed, rotational speed, and ASR on the maximum tool lip temperature measured at the exit plane of the hole.

5.4. Effect of the VAD Process Parameters on the Delamination

All the holes produced by VAD were investigated for entry and exit delamination damage. None of the holes produced by the entire set of experiments has shown noticeable entry delamination. On the other hand, the exit delamination for the VAD conditions varied from cases where VAD produced delamination-free holes to cases where VAD has introduced considerable levels of exit delamination. The delamination damage at the exit or entry plane could be quantified by a delamination factor 'ϕ_d' as described in section 4.3. The delamination factor 'ϕ_d' quantifies the level of delamination in the exit plane only and does not account for the depth of the delamination nor for the internal delamination that might take place between the inner layers of the hole wall. However, using 'ϕ_d' for delamination assessment is justified since the maximum push out delamination is expected to take place at the exit plane where the remaining material thickness is small and the axial forces are maximum before the tool tip breaks through the last layer of the material. Based on the specification provided by leading aerospace manufacturers, the acceptable range of the delamination factor is between ϕ_d = 0.0 and ϕ_d =0.5.

5.4.1. Effect of the Modulation Frequency and Amplitude on the Exit Delamination

Figure 5-13 shows the effect of the modulation frequency "ω_m" and amplitude "A_m" on the exit delamination factor "ϕ_d" at the hole exit plane within the entire range of feeds, and speeds of the first experiment set. As indicated in Table 4-3, the capacity of

the LFHA VAD system could not provide a modulation frequency of 120 Hz with modulation amplitude of 0.1 mm. Therefore, this set of conditions is labeled in red as (N/A) in Figure 5-13 (a). The figure shows that VAD produced delamination free holes at mainly at low feed. On the other hand, the exit delamination factor did not follow a clear trend with respect to the modulation frequency and amplitude. The feed has exhibited the most dominant effect, where the low feed of 0.05 mm/rev resulted in holes with acceptable levels of delamination while as the feed went larger this limit was exceeded. Although the highest exit delamination factor took place at the low rotational speed, the entire range of high rotational speed combined with high feed resulted in delamination factors beyond the acceptable limit because of the high axial feed that increases the chances of push out delamination.

(a)

Feed (mm/rev)		0.05		0.10		0.15	
rpm	Freq. (Hz)	Amplitude (mm)					
		0.04	0.10	0.04	0.10	0.04	0.10
6000	30	0.0 – 0.50	0.5-1.5		0.0-0.5	>1.5	
	60						
	90						
	120		N/A		N/A		N/A
9000	30	0.0 – 0.50					
	60						
	90						
	120		N/A		N/A		N/A
12000	30		1.0 – 1.5				
	60						
	90						
	120		N/A		N/A		N/A

(b)

Feed (mm/rev)		0.05		0.10		0.15	
rpm	Amp. (mm)	Frequency (Hz)					
		30	60	30	60	30	60
6000	0.04	0.5 – 1.5		0.5-1.5		>1.5	
	0.10		0.0 – 0.50				
	0.20						
	0.40						
9000	0.04	0.0 – 0.5		0.5 – 1.5			
	0.10						
	0.20						
	0.40						
12000	0.04						
	0.10	0.5 – 1.5					
	0.20		0.0-0.5		0.0-0.5		
	0.40						

Figure 5-13 Effect of the VAD modulation (a) frequency and (b) amplitude, at different feeds and rotational speeds on the exit delamination factor "ϕ_d" measured on the hole exit plane.

Figure 5-14 shows the exit delamination for the holes produced by VAD at a rotational speed 9000 rpm, modulation frequency 30 Hz, modulation amplitude 0.2 mm, and feeds (a) 0.05 mm/rev, (b) 0.10 mm/rev, and (c) 0.15 mm/rev. The figure shows that the hole produced at feed 0.05 mm/rev was found to be free of any delamination while the exit delamination increased directly with the increase of the feed.

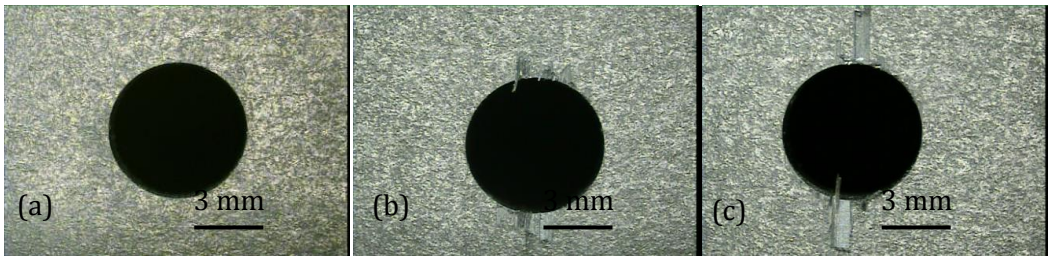

Figure 5-14 Exit delamination for the holes produced by VAD at a rotational speed 9000 rpm, ω_m=30 Hz, A_m=0.2 mm, and (a) f_r=0.05 mm/rev, (b) f_r=0.10 mm/rev, and (c) f_r=0.15 mm/rev.

5.4.2. Testing the Hypothesis of the Independent Effect of the ASR on the Exit Delamination

Figure 5-15 depicts the marginal effect of the ASR at different feeds and rotational speeds on the exit delamination factor "ϕ_d" measured on the hole exit plane. The figure confirms the dominant effect of the feed on delamination as shown in Figure 5-13 and Figure 5-14. The feeds of 0.025 mm/rev and 0.05 mm/rev exhibited delamination factors within the acceptable range of $\phi_d = 0.0$ to $\phi_d = 0.5$.

Feed		0.025 mm/rev		0.05 mm/rev		0.075 mm/rev	
rpm	ASR	Frequency (Hz)					
		30	60	30	60	30	60
6000	3.3	0.0 -0.5					
	6.7						
	10.0						
9000	3.3					0.5 -1.5	
	6.7						
	10.0						
12000	3.3						0.5 - 1.5
	6.7						
	10.0						

Figure 5-15 Effect of the ASR at different feeds and rotational speeds on the exit delamination factor "ϕ_d" measured on the hole exit plane.

5.5. Effect of the VAD Process Parameters on the Hole Surface Roughness

5.5.1. Effect of Frequency and Amplitude on the Hole Surface Roughness

Figure 5-16 shows the effect of the modulation frequency "ω_m" and amplitude "A_m" on the mean surface roughness "R_a" of the hole walls within the entire range of feeds, and speeds of the first experiment set. Figure 5-16 shows that the modulation frequency and amplitude did not yield the surface roughness to a certain trend. On the other hand, the figure shows that the surface roughness was controlled mainly by the interactions of the rotational speed and the feed. The maximum surface roughness (>3.0 µm) was associated with the 9000 rpm and 12000 rpm rotational speeds at low feed. This could be attributed to the effect of tool dynamics at high speeds and low damping at low feeds.

(a)

Feed (mm/rev)		0.05		0.10		0.15	
rpm	Freq. (Hz)	Amplitude (mm)					
		0.04	0.10	0.04	0.10	0.04	0.10
6000	30	1.5 µm - 3.0 µm					
	60						
	90	1.5 µm - 3.0 µm					
	120		N/A		N/A		N/A
9000	30						
	60					<1.5µm	
	90						
	120	<1.5µm	N/A		N/A		N/A
12000	30	>3.0					
	60			1.5 µm - 3.0 µm			
	90						
	120	>3.0	N/A		N/A		N/A

(b)

Feed (mm/rev)		0.05		0.10		0.15	
rpm	Amp. (mm)	Frequency (Hz)					
		30	60	30	60	30	60
6000	0.04	1.5 µm – 3.0 µm					
	0.10						
	0.20	1.5 – 3.0					
	0.40						
9000	0.04					<1.5 µm	
	0.10	<1.5 µm					
	0.20		1.5 µm – 3.0 µm				
	0.40				1.5 µm – 3.0 µm		
12000	0.04	> 3.0 µm					
	0.10						
	0.20	<1.5 µm					
	0.40						

Figure 5-16 Effect of the VAD modulation (a) frequency and (b) amplitude, at different feeds and rotational speeds on the hole surface roughness "Ra".

5.5.2. Testing the Hypothesis of the Independent Effect of the ASR on the Surface Roughness

Figure 5-17 shows the effect of the ASR at different feeds and rotational speeds on the hole surface roughness (Ra). In general, the surface roughness increased with the increase of the rotation speed and ASR. This could be due to the dynamic and the geometric effects of the high tool rotational speed and the high modulation amplitude associated with high ASR, respectively. Compared to the Ra value obtained in conventional drilling, which ranged from 1.5 to 3 µm, the surface quality in VAD was improved by up to 40% at low speed when combined with (i) low feed and low ASR, (ii) medium feed, or (iii) high feed and low/medium ASR. On the other hand, at the highest rotational speed with the highest ASR, the VAD surface roughness was deteriorated by up to 200% especially at low feed. Although the low feed is expected to produce high surface quality, this was not the case since the tool does not have enough damping to hinder the tool dynamics effect at high speeds.

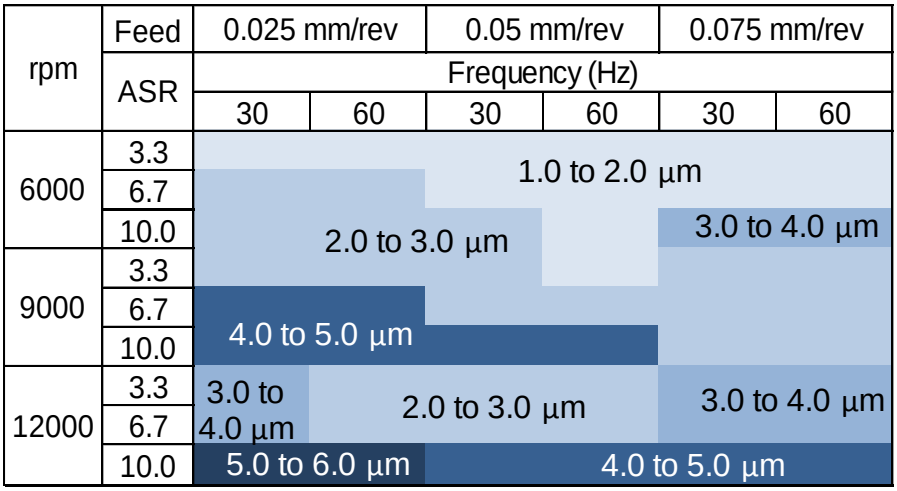

Figure 5-17 Effect of the ASR at different feeds and rotational speeds on the surface roughness (Ra) of holes produced by VAD

High feeds produced high surface roughness due to the geometric effect of the large uncut chip thickness. The surface roughness produced at high feeds was better than that produced at low feeds because of the considerable damping of the large uncut chip thickness, which attenuates the effect of tool dynamics. The medium range of feed in Figure 5-17 exhibited a wider area of low surface roughness compared to the low and high feeds. This is attributed to the higher damping of the tool dynamics at

the medium feed compared to that of the low feed, in addition to the geometric effect of the medium feed, which is lower than that of the high feed.

5.6. Effect of the VAD Process Parameters on the Geometric Accuracy of the Produced Holes

5.6.1. Effect of the VAD Process Parameters on the Hole Size Error

As indicated in section 4.4, the hole size error can be defined by the percentage of the difference of the actual hole diameter compared to the nominal hole diameter. A negative error indicates that the produced hole size is smaller than the nominal size. Based on the specification provided by leading aerospace manufacturers, the allowable tolerance limits of the hole size errors for low load carrying holes are -0.7% to 0.4%.

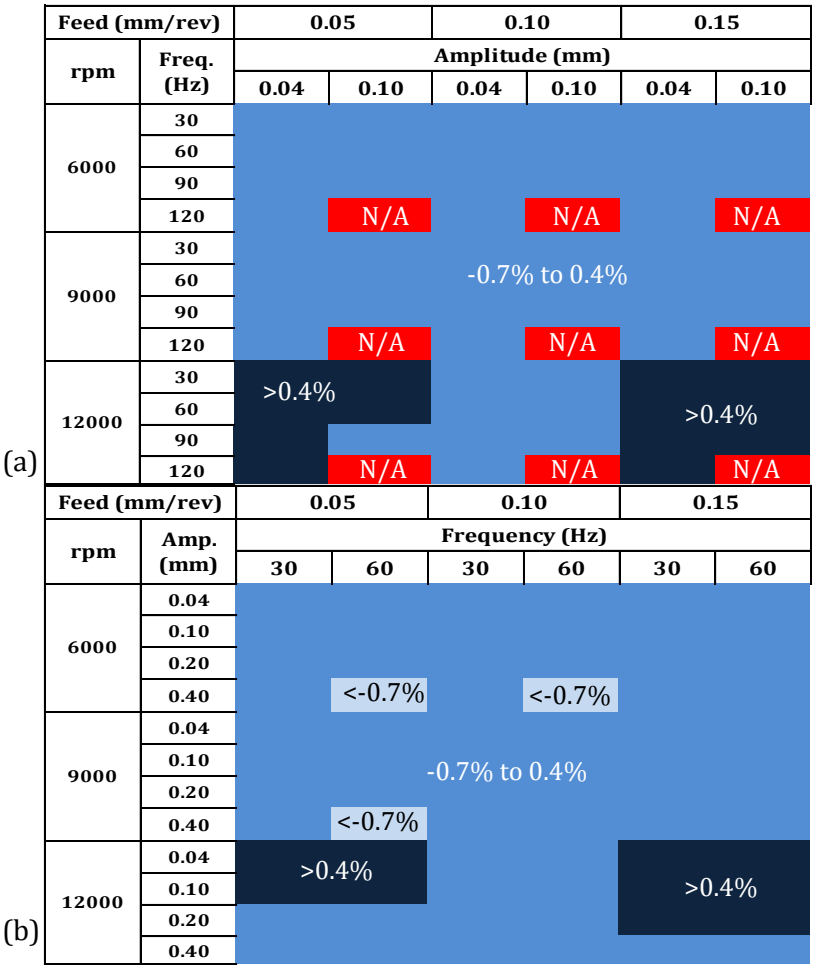

Figure 5-18 Effect of the VAD modulation (a) frequency and (b) amplitude, at different feeds and rotational speeds on the VAD hole size error %.

Figure 5-18 shows the effect of the modulation amplitude and the feed on the VAD hole size error %, at different rotational speeds and modulation frequencies. The figure shows that the majority of the holes produced by VAD were within the acceptable hole size tolerance limit. Hole produced at high speed combined with low and high feeds were over the upper tolerance limit. This could be due to the effect of tool dynamics at high speeds combined with low damping at low feed and excessive tool deflection in the case of high feed.

5.6.2. Effect of the VAD Process Parameters on the Hole Circularity Error

Figure 5-19 shows the effect of the modulation amplitude and the feed on the VAD hole circularity error, at different rotational speeds and modulation frequencies. The circularity tolerance limit specified by the aerospace standards is 0.0 mm to 0.02 mm.

(a)

Feed (mm/rev)		0.05		0.10		0.15	
rpm	Freq. (Hz)	Amplitude (mm)					
		0.04	0.10	0.04	0.10	0.04	0.10
6000	30	0.01 to 0.02			<0.01		>0.02
	60						
	90		<0.01				
	120		N/A		N/A		N/A
9000	30		<0.01			<0.01	
	60			0.01 to 0.02			
	90						
	120	<0.01	N/A		N/A		N/A
12000	30	>0.02					
	60	0.01 to 0.02		<0.01			
	90						
	120	>0.02	N/A		N/A		N/A

(b)

Feed (mm/rev)		0.05		0.10		0.15	
rpm	Amp. (mm)	Frequency (Hz)					
		30	60	30	60	30	60
6000	0.04						
	0.10			<0.01		>0.02	
	0.20		<0.01		<0.01		
	0.40						>0.02
9000	0.04						
	0.10	<0.01					
	0.20			0.01 to 0.02			0.01 to 0.02
	0.40						
12000	0.04	>0.02					
	0.10				<0.01		
	0.20						0.01 to 0.02
	0.40				>0.02		

Figure 5-19 Effect of the VAD modulation (a) frequency and (b) amplitude, at different feeds and rotational speeds on the VAD hole circularity (mm).

Figure 5-19 shows that the majority of the holes produced by VAD were within the acceptable circularity tolerance limit. The holes with an intermediate range within the acceptable limit of circularity errors were the ones produced at low feed with all rotational speeds and low speed combined with all feeds. The holes that exceeded the circularity tolerance limit were scattered but remained within the ranges of high rotational speed or high feed. This could be due to the tool run out due the dynamic effect at high speeds, or due to the tool deflection under the action of higher forces at high feeds.

5.7. Optimization of the Investigated Range of LFHA VAD of the Cross-ply CFRP Laminates

This section shows an example of using the developed hole quality attribute maps as a tool for selecting the optimum ranges of the LFHA VAD parameters. Figure 5-20 shows the maps of four hole quality attributes (a) exit delamination factor, (b) hole size error, (c) surface roughness and (d) hole circularity plotted at different VAD process parameters (feed, speed, amplitude and frequency). The maps in Figure 5-20 depict allowable and unallowable regions of each of the quality attributes of interest indicated by light and dark colors, respectively. The objective of this optimization processes is to determine the optimum set of conditions that can produce holes in the allowable ranges of all the quality attributes at the maximum process productivity. Therefore, the selected region should fall at the maximum possible feed and speed, which produce the maximum axial feed. This condition is indicated on each map by the shaded area highlighted in a red square. The conditions that satisfy the maximum productivity and the allowable range of all four quality attributes shown in Figure 5-20 is corresponding to f_r=0.1 mm/rev, n=12,000 rpm speed, ω_m=60 Hz, and A_m = 0.2 mm. In Figure 5-20 (a, b and c), the amplitude A_m =0.4 mm was shown to be a satisfactory condition when combined with the aforementioned speed, feed and frequency. However, it was excluded from the set of optimum conditions because it is intersecting with the unacceptable circularity range in Figure 5-20 (d).

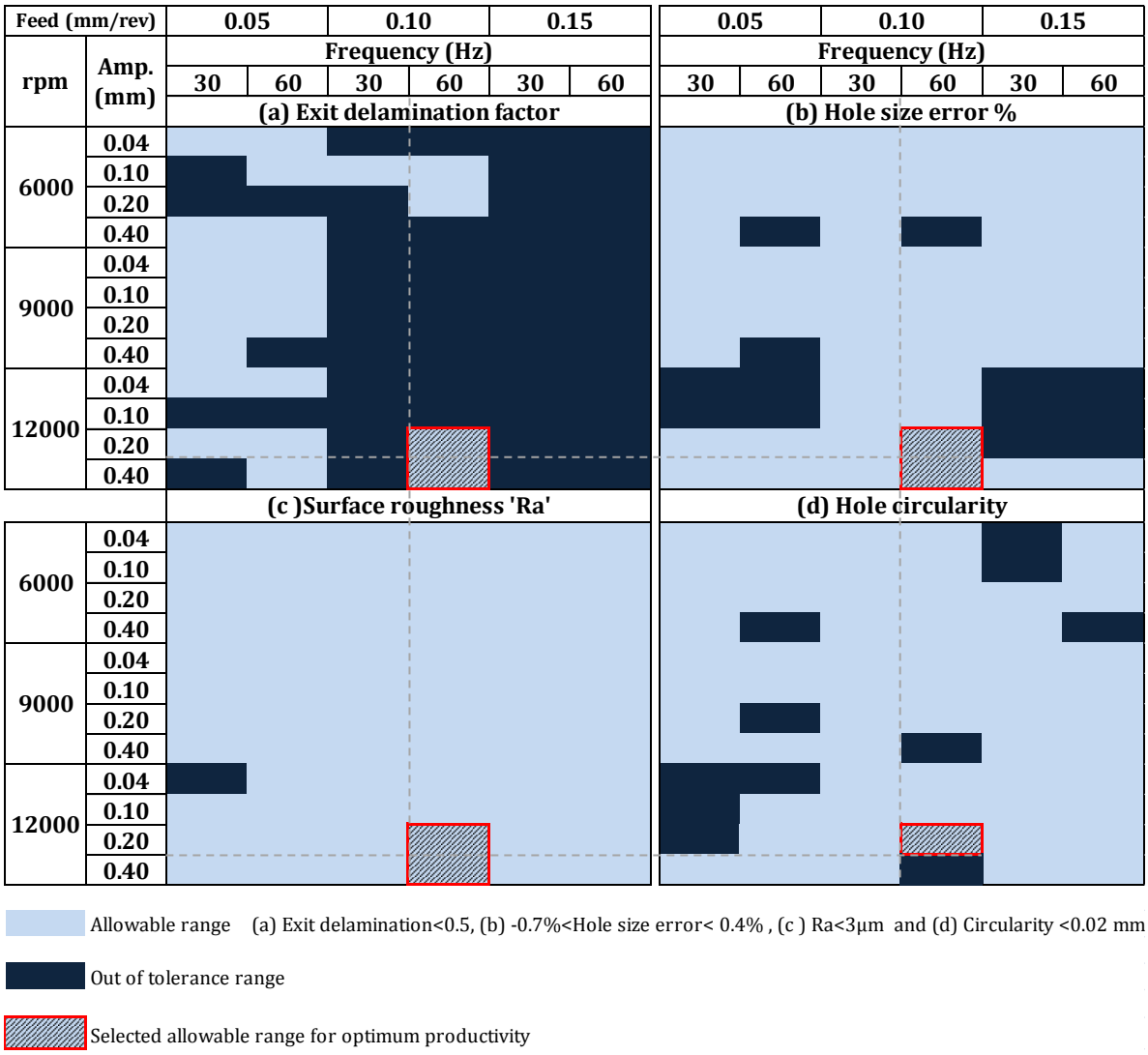

Figure 5-20 Experimental optimization of VAD parameters using hole quality map plots

5.8. Summary

Significant axial force reduction of up to 40 % could be achieved by VAD compared to conventional drilling at the low modulation amplitude when combined with low frequency and high feed. The possibility of achieving the beneficial effect of force reduction in VAD at lower feeds and higher amplitudes was found to be increasing with the increase in the rotation speed.

All the measured VAD temperatures were found to be below the material decomposition temperature. The measured VAD tool temperature in most of the cases was reduced by up to 30% compared to the conventional drilling. This is attributed to

the cooling effect of the formed vortices in the air gap created by the separation between the tool's flank face and the machined surface during cutting. The amount of temperature reduction in VAD is controlled by the competing factors of heat generation and dissipation.

The investigation of the produced hole quality showed that the VAD could eliminate and reduce the exit delamination factor to values within the desirable range of exit delamination, commonly specified by the aerospace manufacturers. The feed was found to have the dominant effect on the exit hole delamination. The low feed resulted in acceptable levels of exit delamination while as the feed went larger this limit was exceeded.

As for the geometric accuracy of the produced holes, the tested VAD conditions resulted in hole sizes within the desirable tolerance limits of the low load carrying holes according to the standards of the aerospace applications. However, the conditions of high speed with low and high feed produced hole sizes over the specified upper tolerance limit which could be due to the effect of tool dynamics at high speed. The tested VAD conditions produced holes within the circularity tolerance limits. Only few holes have exceeded the allowable circularity tolerance limit, but there has been no fixed trend that can explain such measurements.

The results of the forces and temperatures of VAD confirmed that the axial speed ratio ASR is not an intrinsic property that can uniquely control the cutting temperature and force in VAD. This was demonstrated by the considerable variation of forces and temperatures as a result of changing the VAD independent parameters for a constant ASR value.

CHAPTER 6

Development of Mechanistic Model for Force and Torque Prediction

6.1. Introduction

Developing a predictive force model for drilling of FRP laminates is required in order to achieve a comprehensive understanding of the physics of the VAD and conventional drilling processes of FRP laminates. As indicated in Chapter 2, the results reported in the available literature on analytical modeling of the machining of FRPs showed limited predictive capabilities of models that require a relatively huge number of calibration experiments. This makes such techniques extremely complex and unfeasible. On the other hand, empirical mechanistic models based on homogenized FRP material properties are easier to build but they are only valid within a very limited range of operating conditions and for a specific CFRP architecture. They are also unable to capture the important variations of the drilling forces of FRPs. Hence this approach cannot predict consequent physical damage. Finite element models developed for simulating the drilling of FRPs face the challenges of high computational cost, and large errors due to employing the overall macro scale material properties and failure criterion for the prediction of microscale fractures on the level of a single fiber (of the order of 7 to 10 μm). This highlights the importance of developing a modeling methodology that employs the feasibility of the mechanistic modeling techniques and at the same time respects the fundamental mechanics of the different chip formation mechanisms at different FRP fiber orientations and for any architecture structure.

6.2. Nature of the Problem

Unlike the case of chip formation by plastic deformation during machining of ductile metals, chips are formed by a series of consecutive fractures of matrix and

fibers during the machining of FRPs [13]. Moreover, the mechanical properties are theoretically homogenous and isotropic for metals, while they are known to be dependent on the fiber orientation for FRP laminates. These two major differences in the principles of machining of metals versus FRPs justify the importance of introducing a new model that gives in depth understanding of the mechanics of the drilling process of FRP laminates. The model needs to consider the tool geometry and to recognize that the fibers are the main component of the composite material that control its machinability due to their significantly higher strength compared to that of the matrix [13].

The geometrical features of the cutting lip of the drilling tool are highly complex. As Figure 6-1 shows, the flute surface and the flank surface of the tool have curved profiles that form a 3D curve at their intersection, forming the primary cutting edge. The curvature of the flank surface controls the relief angle of the cutting edge while the helix of the curved flute surface controls the rake angle, which varies along the cutting edge. Sections A, B, and C in Figure 6-1 show that the rake angle α of the primary cutting edge is high near the outer diameter and decreases towards the inner tool diameter; $\alpha_1 > \alpha_2 > \alpha_3$. The intersection of flank faces of each of the tool primary cutting edges forms the chisel edge, which is featured by a constant negative rake angle along its length. The developed model is aiming at including the effect of the aforementioned geometric features of the drilling tool on the drilling force and torque. This should enhance the accuracy of the model predictions and allow the model to be used for the optimization of the drilling tool geometry.

The FRP laminates are classified as anisotropic materials because their properties are dependent on the orientation of the load carrying elements, which are the fibers. The material is formed of a layup of unidirectional plies of fibers pre-impregnated in the matrix polymer resin. The orientations of the plies in the laminate are designed in order to give strength to the material in the required directions of loading in service. The FRP material designer can produce an infinite number of material layup configurations comprising different combinations of fiber orientations and laminate thicknesses in order to fulfill the design requirements. Figure 6-2 illustrates the

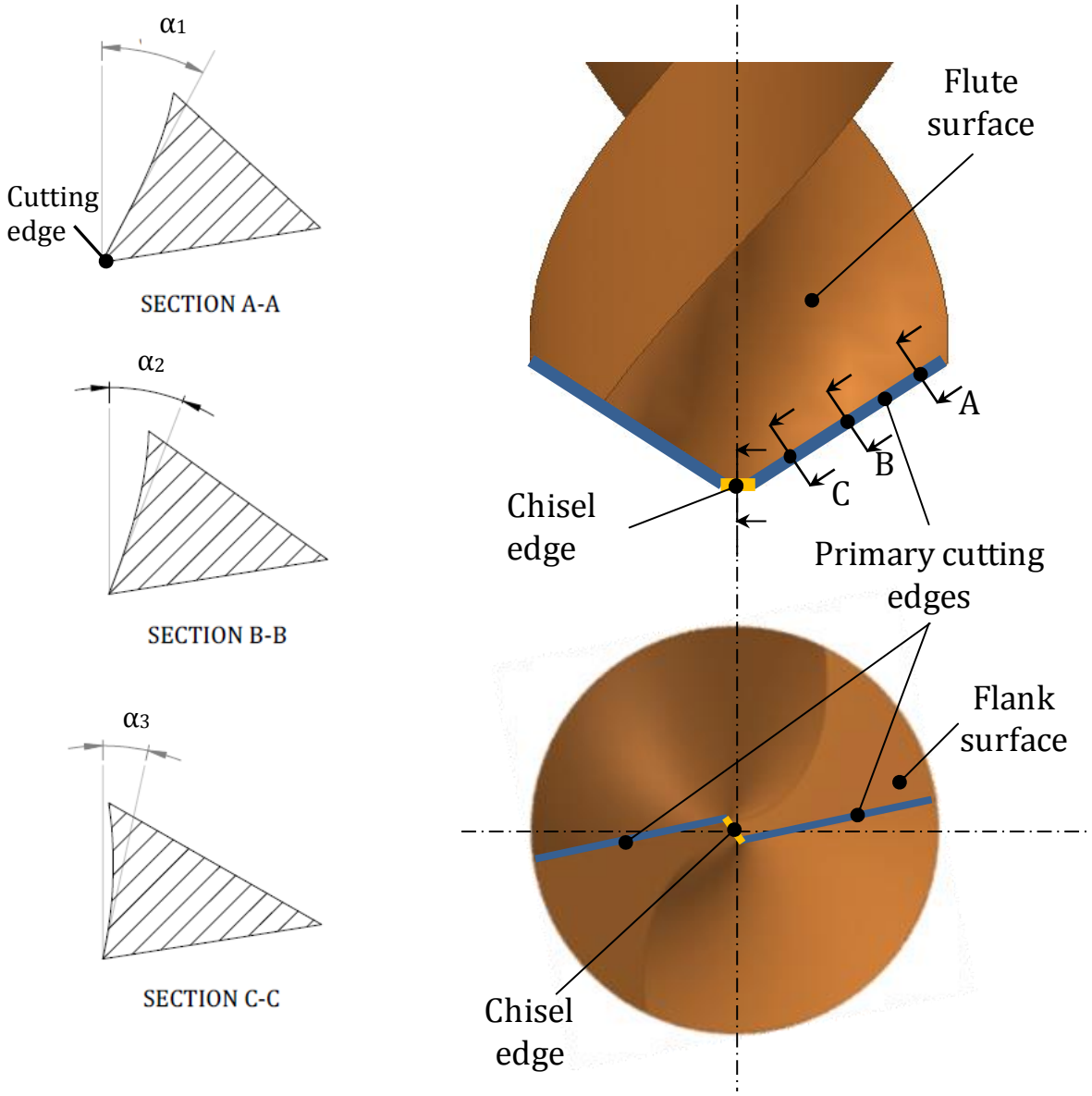

Figure 6-1 Main features of the drilling tool geometry

architecture of the most widely used families of FRP layups, namely unidirectional, cross-ply, and quasi-isotropic laminates. In order to introduce a predictive force model for drilling of FRPs that can be used for real life applications it has to be formulated to deal with any multidirectional layup configuration for any FRP material. This represents another challenge for modeling the drilling of FRP materials. This is due to the compounded complexity of the interaction between the drilling tool

geometry and the multidirectional FRP material architecture in the angular and axial directions.

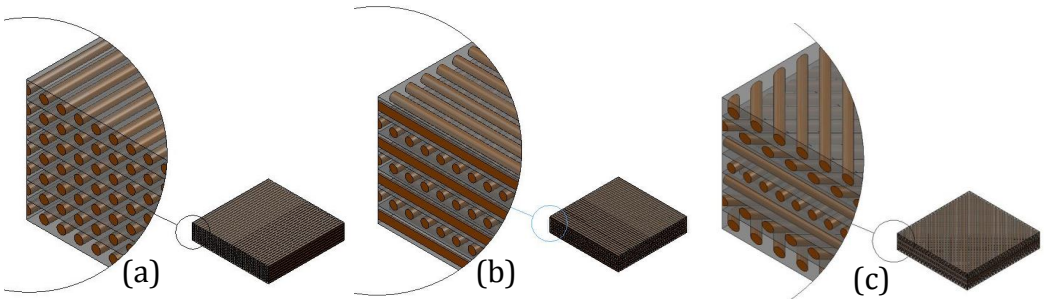

Figure 6-2 (a) Unidirectional CFRP, (b) multidirectional (cross ply), and (c) multidirectional (quasi-isotropic ply)

Furthermore, there are several defined modes of chip formation in machining of composites that depend merely on the effective fiber orientation and the rake angle of the cutting edge. The fiber orientation angle "θ" in the laminate layup is defined with respect to the coordinate system of the laminate, whereas the effective fiber orientation angle 'θ_e' is dynamically changing with respect to the angular position of the rotating cutting edge during drilling [103]. As shown in Figure 6-3, the effective fiber orientation angle 'θ_e' is the enclosed angle between the line of the cutting direction and fiber axis in the clockwise direction. The figure also depicts the significant role of the effective fiber orientation angle in defining the different modes of chip formation during cutting. For the case of the primary cutting edge, the fibers at effective orientation angles θ_e<90 are cut by shearing under the action of a cutting edge with a positive rake angle. Fibers at effective orientation angles θ_e>90 are, however, cut by bending under the action of a similar cutting edge. The chisel edge of the drilling tool is featured by a highly negative rake angle, which causes the side of the edge to press and bend the formed chip until it fractures.

The model presented in this chapter is based on a novel approach that employs the feasibility of the mechanistic modeling techniques and at the same time respects the fundamental mechanics of the different chip formation modes at different FRP fiber orientations. In addition to the considerably low computational cost of the adopted modeling approach, it also increases the efficiency of the calibration experiments to

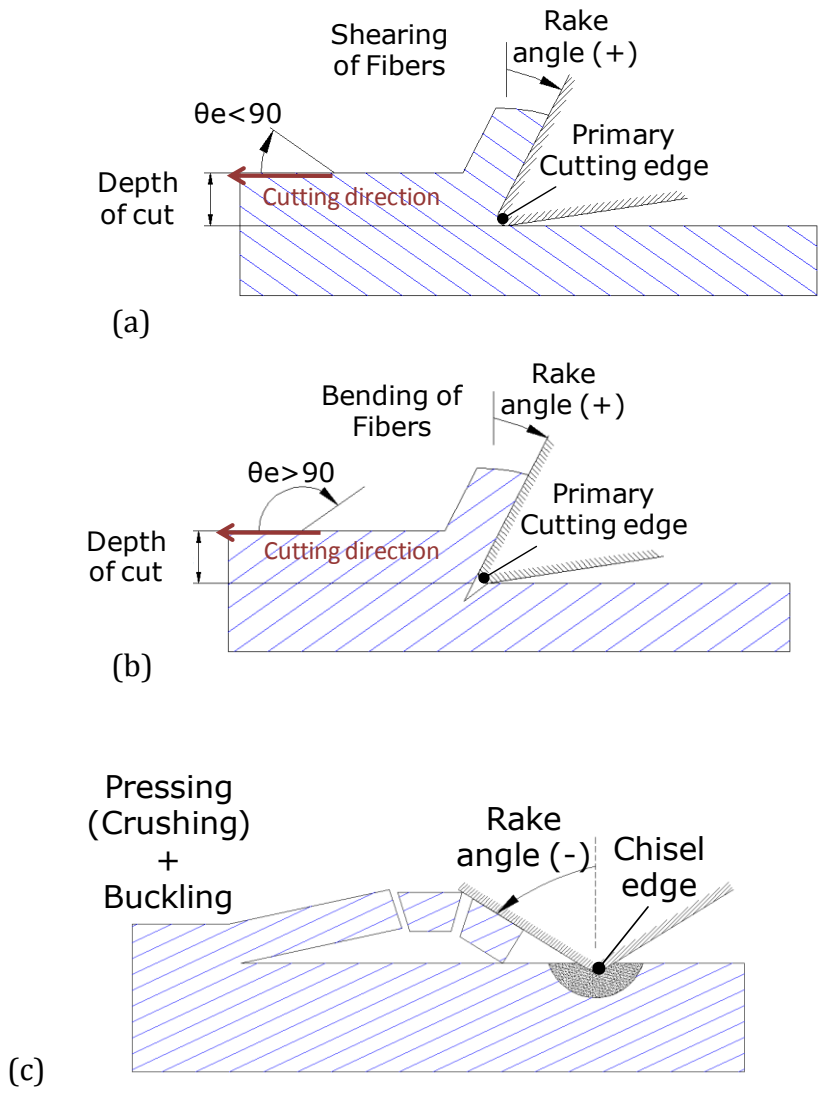

Figure 6-3 Chip formation mechanisms by (a) shearing of fibers (θ_e <90) on the primary cutting edge, (b) bending of fibers (θ_e >90) on the primary cutting edge, and (c) pressing and buckling under the chisel edge

provide maximum information using a limited number of experiments. The developed model, based on this approach, represents a reliable, flexible and generic prediction capability that can deal with a wide range of variability in FRP material layup configurations, process parameters, tool geometries, dynamic tool-workpiece interactions, and material deformation during drilling. This allows the end user of the model to use it as a robust and rapid tool for optimizing the drilling process of FRP and establishing a physics-based approach for tool design.

6.3. Conceptual Development of the Modeling Approach

A mechanistic modeling approach is adopted in this research work, where the cutting force components are related to the uncut chip geometry through a process-dependent property. This property is known as the cutting pressure or the specific cutting energy when defined with respect to the uncut chip area or the uncut chip volume, respectively. Figure 6-4 shows a schematic of the mechanistic modeling principle for oblique and orthogonal cutting. In the case of orthogonal cutting, the cutting edge is normal to the vector of the cutting direction. For oblique cutting, the edge is inclined to the vector of the cutting direction by an angle 'λ'. The ratio of the cutting force to the normal projected area of the uncut chip defines the cutting pressure of the pair of the tool and workpiece. The normal projected area of the uncut chip is defined by the product of the depth 'd' and the width 'b' of cut. The defined cutting pressures of a mechanistic model vary according to the process parameters but they are specific to the tool and the workpiece material. The experimentally defined cutting pressure "K_c" can then be used for the prediction of the cutting force "F_c" if the uncut chip area "A_{chip}" is known through the relationship ($F_c = K_c \, . \, A_{chip}$). For isotropic materials like metals, the cutting pressures depend on the workpiece material, the cutting velocity, the uncut chip thickness, and the tool geometry. In highly anisotropic materials, like multidirectional FRPs, the cutting pressures depend on the aforementioned parameters in addition to the effective fiber orientation, which controls the mode of chip formation.

The adopted technique is based on experimentally defining the drilling torque and axial force cutting pressures for the primary and chisel edges. The defined cutting pressures are functions of the cutting velocity "v_c", the uncut chip thickness 'd', the effective fiber orientation angle 'θ_e', and the rake angle of the cutting edge "α". This enables the model to account for the effect of the drilling process parameters, the material fiber orientations, the dynamic uncut chip thickness for the case of VAD, and the tool geometry on the drilling forces. As discussed earlier, the primary and chisel cutting edges of the drilling tool produce different chip formation modes that vary as the cutting edge engages with different fiber orientations during the drilling process.

Therefore, the cutting pressures for the cutting torque and the axial force of each fiber orientation on each type of edge has to be defined separately.

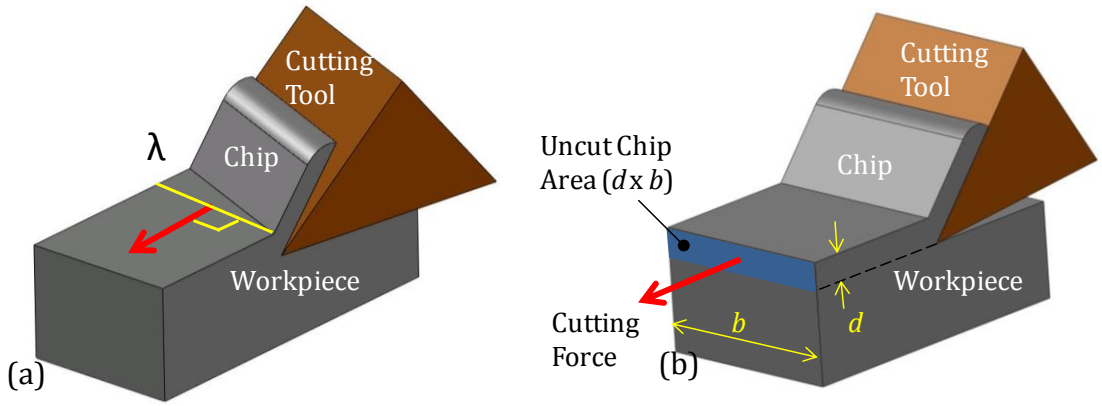

Figure 6-4 Schematic of the mechanistic modeling for (a) oblique and (b) orthogonal cutting

Figure 6-5 shows an outline of the modules and functions to be incorporated in the developed generalized model that deals with VAD and conventional drilling of multidirectional FRPs. The inputs of the model are the process parameters (v_c, f_r, ω_m *and* A_m), the tool geometry, the material layup, and the experimentally identified and calibrated cutting pressures. The model is structured to compute the drilling axial forces and torques in an incremental fashion for each time increment in the time loop.

The first step shown in block (1) starts with determining the relative angular and axial positions of the tool and the workpiece based on the input drilling axial feed and rotational speed. For each instant of time, the intersection between the positions of the cutting edges and the interfaces of the material layers divide the active length of the cutting edges into sections, each of which is engaged with a certain layer of the material. This determines the length (3) and the uncut chip thickness (4) of each of these sections. The product of (3) and (4) defines the uncut chip area (5) required to calculate the force and torque on this edge section. For each section of the chip area that has a certain fiber orientation, the effective fiber orientation (2) is defined from the angular position of the cutting edge relative to the fiber orientation of the section. The uncut chip thickness (3) and the effective fiber orientations (2) for each section are used to determine the corresponding axial force and torque cutting pressures (7)

using the input cutting pressures database. The effect of the rake angle (10) and the cutting velocity (11) on the cutting pressures of each of the primary cutting edge sections can be determined from the input tool geometry and drilling rotational speed. The instantaneous axial force and torque (9) are obtained using the function (8), which sums the products of the chip area of each section of the cutting edges and its corresponding force and torque cutting pressures. Based on the instantaneous frictional area of contact between the lateral tool surface and the hole walls calculated in (12), function (8) incorporates the effect of the frictional force predicted from function (13) and the material softening predicted from function (14) on the predicted cutting torque and force. The predicted axial force in (9) is fed into function (15) that calculates the level of deflection of the remaining material thickness, which is used to modify the actual uncut chip thickness (3) of the following time step. The aforementioned procedure is applied to the primary and chisel cutting edges separately due to their different geometrical, kinematic, and mechanistic features. The predicted forces and torques on each edge in each instant of time are superimposed to form the total drilling force and torque.

The following sections will discuss the concept behind including the effect of the main elements of the model shown in Figure 6-5. The detailed formulation of incorporating such elements and other modules will be presented and discussed under section 6.5 of this chapter.

6.3.1. Relative Tool and Workpiece Positions

The instantaneous relative position between the tool and the workpiece controls the dimensions of the active sections of the cutting edges and the corresponding geometry of the chip formed by each of these sections. The effective fiber orientation angles at each of the cutting edge sections at any instant of time are also determined based on the angular position of the cutting edge relative to the fiber orientation of the material layer. Attaining an accurate prediction of the geometry of the uncut chip and the effective fiber orientation is a key factor for accurate prediction of the drilling force and torque.

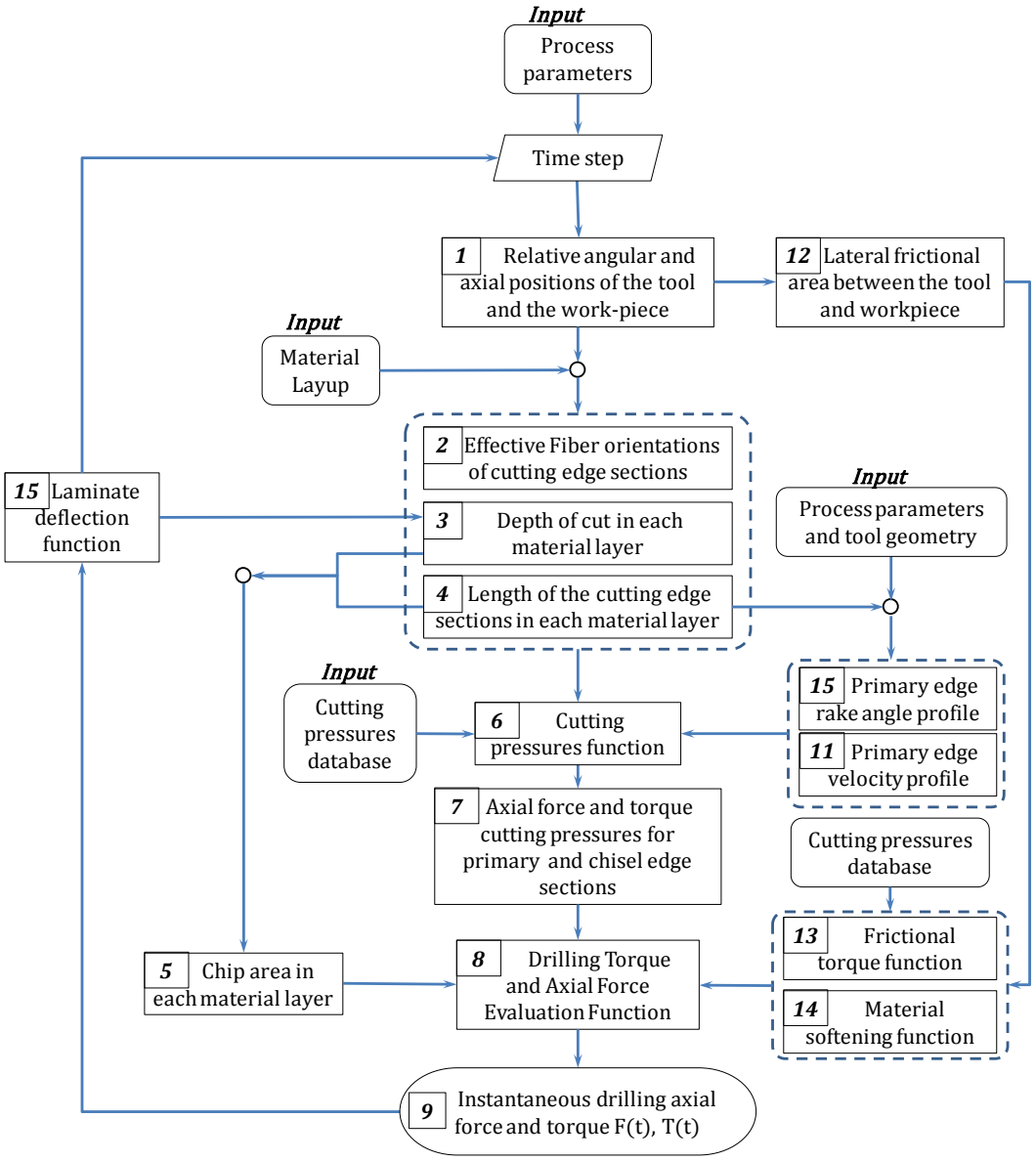

Figure 6-5 Outline of the modules and functions to be incorporated in the developed model

The model is formulated to be a generalized one allowing the prediction of the general case of dynamic chip geometry to deal with the case of (VAD). The case of conventional drilling of static chip geometry becomes, therefore, a special case of the dynamic generalized model. In order to predict the correct relative positions between the tool and the workpiece in the presence of relative axial vibration, the model formulation has to account also for any undesirable relative motion between tool and workpiece (e.g. laminate deflection), which can alter the nominal uncut chip thickness.

The material layers displacement due to deflection results in a shallower engagement between the cutting lip and the workpiece compared to the ideal uncut chip thickness.

6.3.2. Cutting Pressures Input to the Model

A calibrated database of the cutting pressures for the drilling of FRPs represent the material properties input required by the predictive model in order to calculate the drilling forces and torques. It is important in this section to mention the conceptual considerations of identifying the process cutting pressures. This is because the model structure depends on the method with which the cutting pressures are obtained.

Identification of the Cutting Pressures for Primary and Chisel Cutting Edges

As explained earlier, the primary and chisel edges of the cutting tool exhibit different behaviors during the drilling of FRPs. The cutting pressures of each type of these cutting edges have to be identified separately. This presents a challenge, since the measured total force and torque during the calibration drilling tests correspond to the entire cutting lip, which comprises both edges. Therefore, a special preparation has to be applied to the hole being drilled in order to be able to split the effect of each of the cutting edges during the calibration test. Figure 6-6 shows a schematic for the hole preparation used for all the cutting pressures calibration tests. A blind pilot hole of a diameter slightly larger than the chisel edge encompassing circle diameter was predrilled from the top plane of the FRP laminate until the middle plane. This assures that the effect of the chisel edge is completely isolated during the first half of the hole thickness and what is being measured is purely the effect of the full primary cutting edges in the steady state. This is represented by the first portion of the force signal shown in Figure 6-7, where the measured axial force was lower due to the existence of the pilot hole. During the second half of the drilling pass, the measured force increases as a result of the engagement of the chisel edge. The effect of the chisel edge only can then be determined via subtracting the signal of the primary edge from the signal obtained when the full cutting lip was engaged.

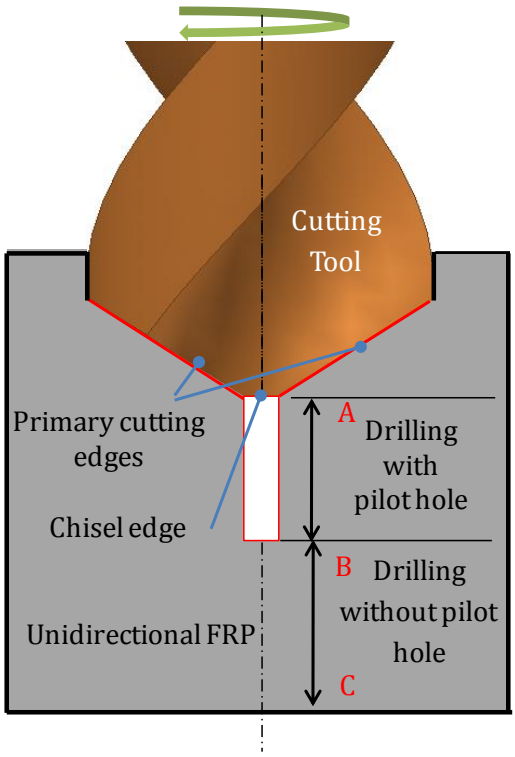

Figure 6-6 Hole preparation for the calibration experiment to split the behavior of the primary and chisel cutting edges during drilling of FRP

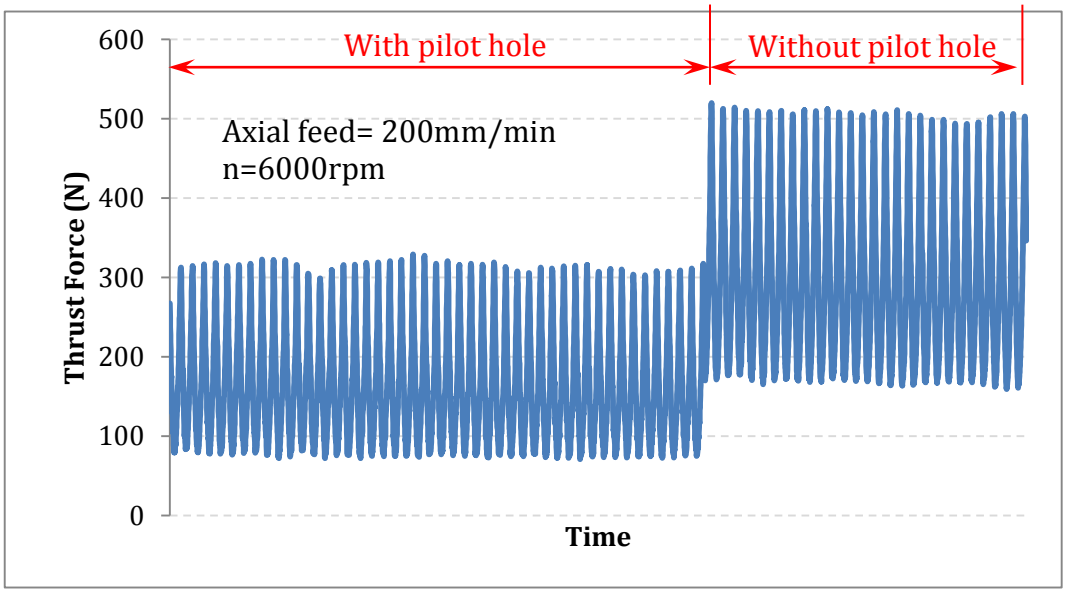

Figure 6-7 The measured force signal showing the effect of the engagement of the chisel edge after drilling through the air gap of the pilot hole.

Effect of the Fiber Orientation on the Cutting Pressures

After splitting the effects of the cutting lip edges, the second step is establishing the effect of the effective fiber orientation on the cutting pressures on each of the cutting edges from the measured drilling force and torque signals. This can be achieved by assuring that the cutting edges are engaged with only one fiber orientation at each instant of time. The most practical way to fulfill this condition is to use a unidirectional FRP laminate as a workpiece material and a symmetric two-flute drill for the cutting pressures calibration tests. This setup facilitates acquiring information on the cutting torque and axial force continuously at every effective orientation angle during the engagement with the primary and chisel edge separately.

From the definition of the effective fiber orientation mentioned earlier, the effective fiber orientation angle is dynamically changing with the angular position of the rotating cutting edge during drilling, as shown in Figure 6-8 (a). The figure demonstrates a conventional drilling process of a unidirectional CFRP laminate using a 2-flute drill bit. During drilling with this setup, the chips are formed at each instant either by bending of fibers when the cutting takes place in the first and third quadrants of the hole, or by shearing of fibers while cutting in the second and fourth quadrants.

The cutting lip of the drill shown in Figure 6-8 (a) consists of two primary cutting edges (labeled P) and a chisel edge (labeled C). The shearing and bending modes of chip formation are experienced on the primary cutting edges of the drilling tool. The chip formation along the chisel edge comprises mixed modes of fiber buckling and/or crushing. This is attributed to the inability of either of the thermoset matrix or the fibers to perform plastic deformation and hence the material is not extruded under the action of the chisel edge, unlike the case of drilling of ductile metals.

Figure 6-8 (b) shows the thrust force signal obtained during conventional drilling of a unidirectional CFRP laminate at speed n=3,000 rpm, and axial feed f_a=200 mm/min using a 2-flute (tool diameter =9.53 mm) drill bit. The shown curve demonstrates the distinct variation of thrust force with the effective angle 'θ_e'

between the fiber and the primary cutting edge through one revolution of the tool. The maximum thrust force was recorded at the shearing zone at an effective angle θ_e = 45˚, while a minimum thrust force was recorded at the bending zone at θ_e = 135˚. Such distinct variation of the measured thrust force with "θ_e" for the same hole drilling pass gives information on the effect of the entire range of the fiber orientation angles "θ_e" on the cutting pressures for a specified set of drilling condition. Therefore, the required information on the drilling torques and axial forces as functions of the effective fiber orientation can be defined for each cutting condition from a single drilling experiment. This maximizes the utilization of the measured information, while reducing the effort and cost required for experimental calibration of the cutting pressures of the model. Based on this concept, the cutting pressure of the FRP material can easily and efficiently be determined as a function of the cutting speed, feed, and the effective fiber orientation angle. The details of calculating the cutting pressures are discussed further in section 6.4 of this chapter.

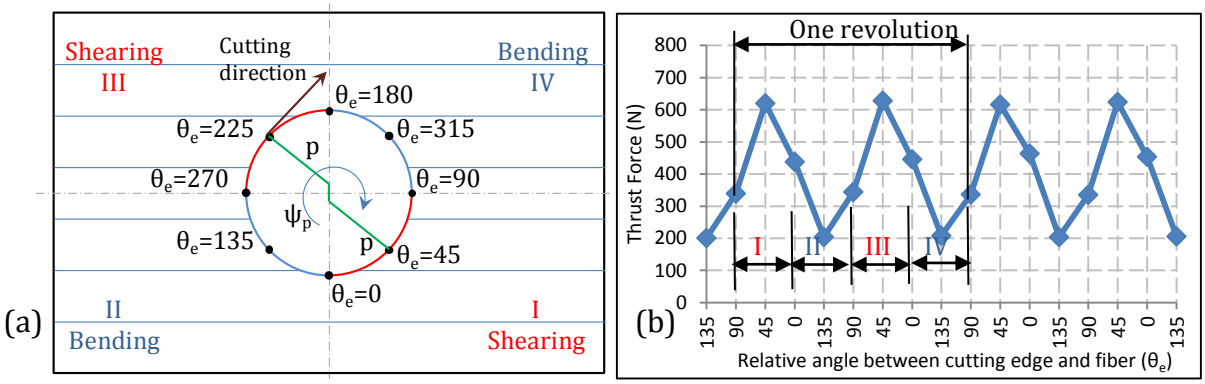

Figure 6-8 Shearing and bending modes corresponding to (a) variable effective fiber angles "θ_e", (b) Thrust force fluctuation during drilling of unidirectional laminates

6.3.3. Effect of the Primary Edge Rake Angle on the Cutting Pressure

As shown in Figure 6-1, the rake angle is variable along the length of the tool primary cutting edges. The effect of the rake angle on the cutting forces for the case of the highly heterogeneous FRP materials was found to be dependent on the fiber orientation angle [118]. Based on the experimental results reported by Wang et al. [118], Figure 6-9 (a) and (b) shows the effect of the change of the rake angle on the normalized horizontal and vertical cutting pressures in orthogonal cutting of different

orientations of carbon epoxy laminates. The cutting pressures of all the effective fiber orientations at a given rake angle were normalized with respect to the value of the cutting pressure at the rake angle of the middle section of the edge.

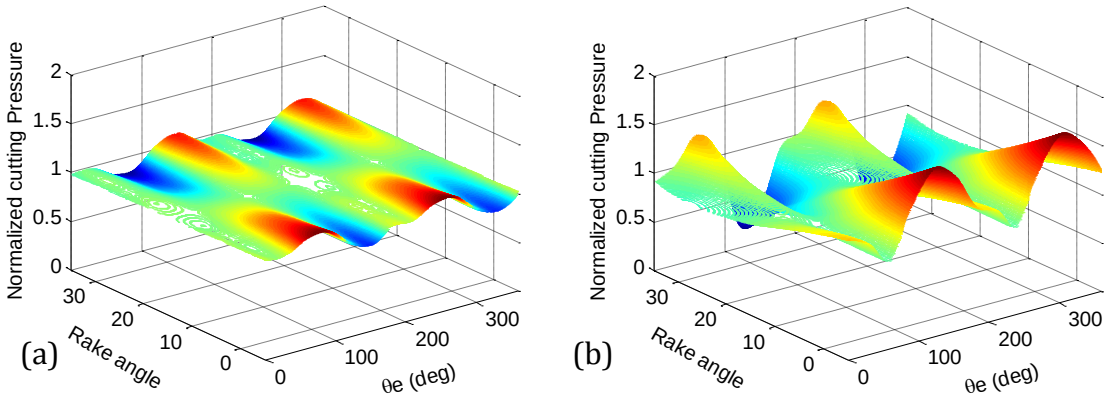

Figure 6-9 The effect of the change of rake angle and effective fiber orientation angles on the normalized (a) horizontal and (b) vertical cutting pressures of orthogonal cutting.

The variable behavior of the cutting pressures at different rake angles and fiber orientations can affect the accuracy of the predicted forces on the primary cutting edge. In order to include the effect of this variability on the predicted forces, the cutting pressure of each section of the primary cutting edge is defined as a function of the rake angle of this section based on the fiber orientation it is engaged with, at any instant of time.

The information shown in Figure 6-9 (a) and (b) is used to define the effect of the rake angle on the cutting pressures in the vertical and the horizontal directions, for various fiber orientations. In the developed model, the predicted force and torque values along the primary cutting edges are based on the average cutting pressures at a given effective fiber orientation. This predicted value does not account for the effect of the rake angle. Therefore, the normalized rake angle cutting pressure values are multiplied by the predicted average cutting pressures in order to include the effect of the rake angle at each of the cutting edge sections. The challenge of directly using the information in Figure 6-9 (a) and (b) is that it was obtained for the case of 2D

orthogonal cutting while drilling is an oblique cutting process. Figure 6-10 shows a diagram of the directions of the oblique drilling forces which was introduced in [119].

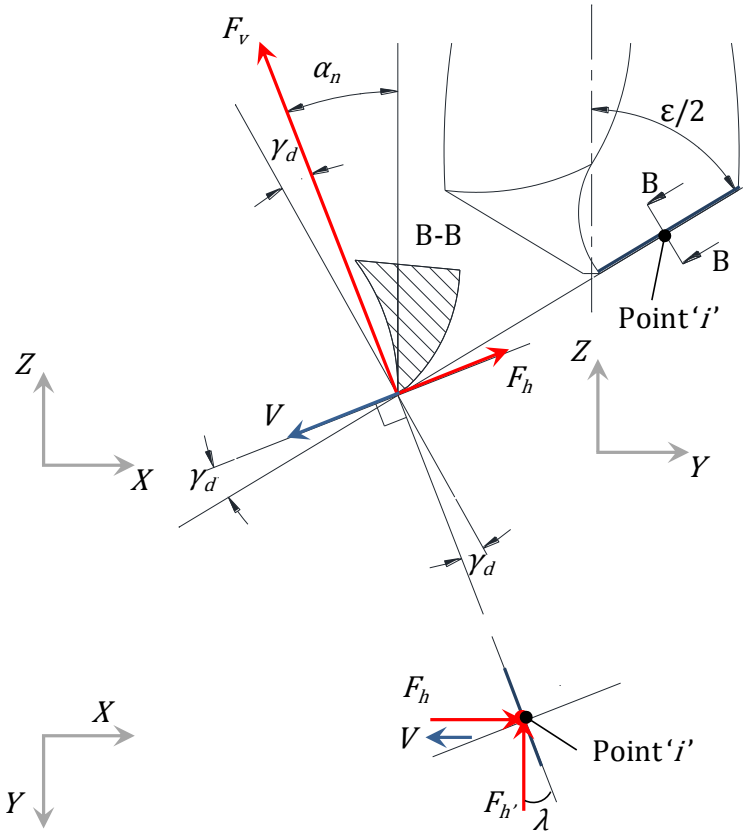

Figure 6-10 Schematic of the forces of the oblique cutting process using (a) a simple turning tool and (b) the complex drilling tool

In order to apply the normalized rake angle cutting pressures (orthogonal) to the predicted forces (F_z, F_x, and F_y) on each section (oblique). These forces should be calculated from the predicted torque then transformed to the orthogonal system (F_v, F_h, and $F_{h'}$) using the following transformation matrix based on the formulation introduced in [119] .

$$\begin{bmatrix} F_x \\ F_y \\ F_z \end{bmatrix} = [\boldsymbol{T}] \begin{bmatrix} F_h \\ F_{h'} \\ F_v \end{bmatrix} \qquad \textbf{6-1}$$

$$[\boldsymbol{T}] = \begin{bmatrix} sin\gamma_d & -cos\,\Theta & -sin\,\lambda \\ -cos\gamma_d . cos\varepsilon & -sin\,\Theta & sin\lambda . sin\gamma_d . cos\varepsilon \\ cos\gamma_d . sin\varepsilon & 0 & -(cos\lambda . cos\varepsilon + sin\lambda . sin\gamma_d . sin\varepsilon) \end{bmatrix} \qquad \textbf{6-2}$$

where 'λ' is the oblique cutting angle defined between the cutting velocity direction and the normal to the cutting edge. The following relationship defines 'λ' in terms of the cutting velocity angle 'Θ' in the horizontal plane and the tool point angle 'ε'.

$$sin\lambda = sin\,\Theta\,.\,sin\,\varepsilon \qquad \textbf{6-3}$$

The cutting velocity angle 'Θ_i' in the horizontal plane at a point 'i' on the cutting edge is defined from the following relationship between the cutting web thickness 't_w' and the radius 'r_i' of the point 'i'

$$\Theta_i = \sin^{-1}\frac{t_w}{2r_i} \qquad \textbf{6-4}$$

The angle between the cutting velocity components '$\gamma_{d,i}$' at a point 'i' in plane ZX shown in section B-B in the Figure 6-10 is defined as follows.

$$tan\gamma_{d,i} = tan\Theta_i.cos\,\varepsilon \qquad \textbf{6-5}$$

6.3.4. Effect of the Variation of the Linear Cutting Speed along the Primary Cutting Edge

As shown in Figure 6-11, the linear cutting speed "$v_{c,i}$" of any point "i" on the cutting tool lip has a direct relationship with the rotational speed "n" and the distance "r_i" of the point from the center of tool with an outer radius 'R'. The velocity of the middle section (section B in Figure 6-11) is considered as the reference average velocity "v_r"

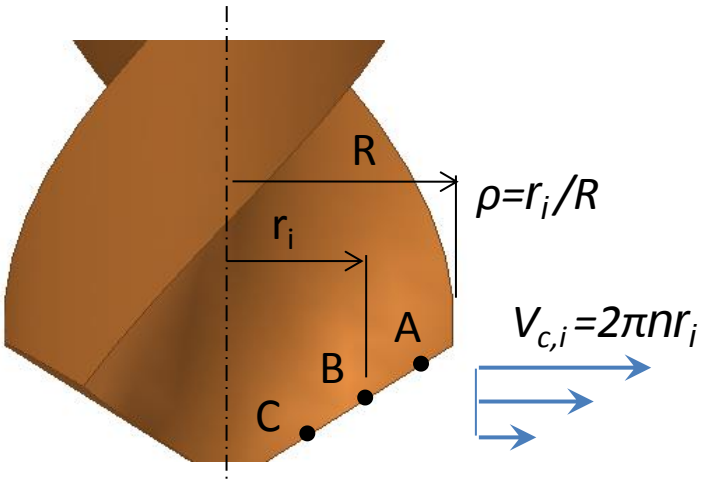

Figure 6-11 Linear cutting velocities on the primary cutting edge of the drilling tool

of the primary cutting edge. The effect of the average linear velocity on the cutting pressures of the axial force and torque is shown in Figure 6-12 (a) and (b), respectively. The figure depicts a slight effect for the change of cutting velocity on the axial cutting pressures, which yields an inverse linear relationship. On the other hand, Figure 6-12 (b) shows that the increase in the average linear velocity led to a considerable decrease in the torque cutting pressures.

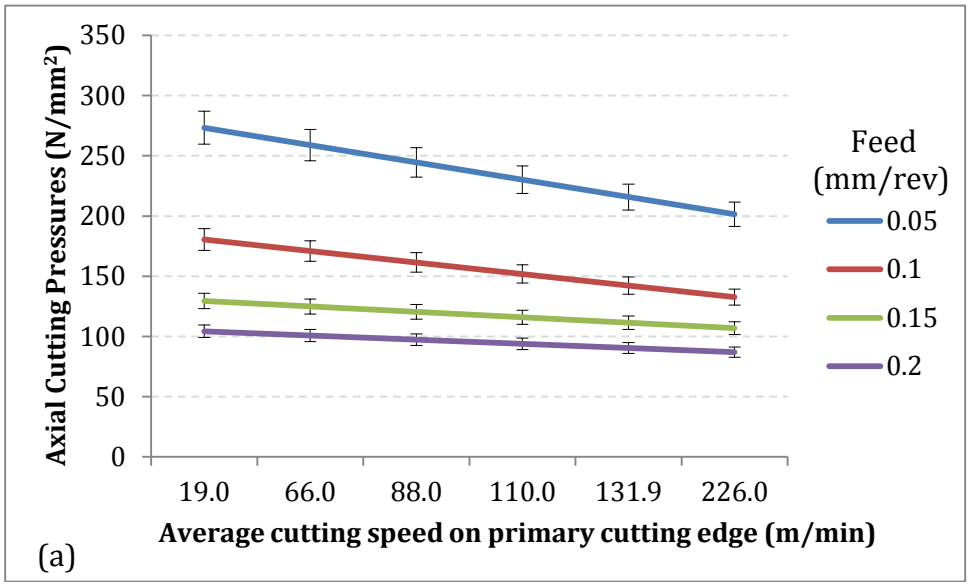

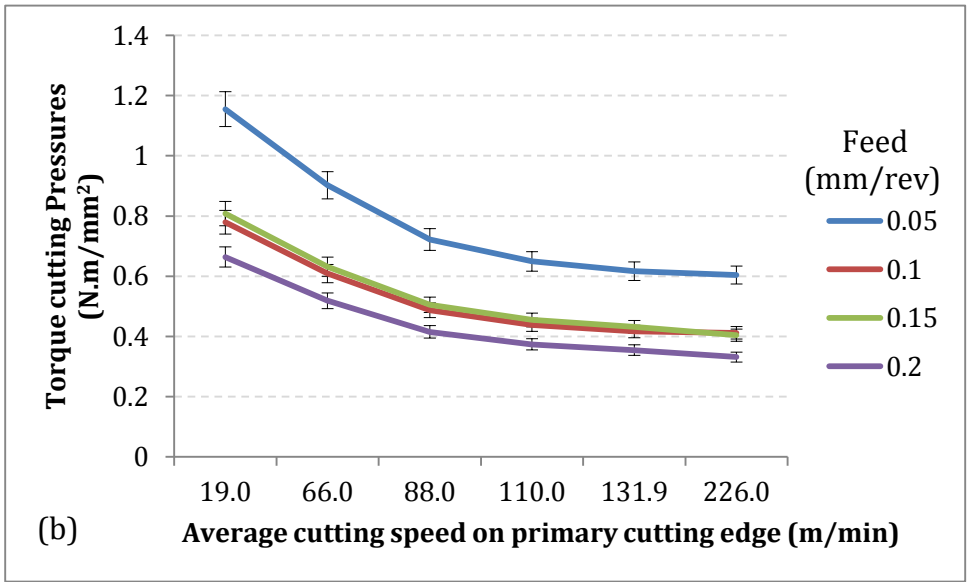

Figure 6-12 Effect of linear cutting velocity on the (a) axial and (b) torque cutting pressures at different feeds per rev.

In the prediction model, a function is developed to determine the cutting velocity of each section of the primary cutting edge and calculate the corresponding cutting pressure from the database established by the calibration tests. When dealing with the cutting pressures as function in the cutting velocity 'v_c', it is assumed that the same velocity will give the same cutting pressure for the same effective fiber orientation and 'd', even if the radius and the rotational speeds were different, but their combined effect produces the same 'v'. Based on this assumption, the database of the cutting pressures as function of the cutting velocity is expanded and used to give information on the change of the cutting velocity along the primary cutting edge.

6.3.5. Effect of the Frictional Torque on the Total Drilling Torque

Figure 6-13 shows the full torque signal for a typical calibration test of conventional drilling of unidirectional CFRP laminate at rotational speed n=10,000 rpm, and feed f_r=0.2 mm/rev. The region (E) shown on Figure 6-13 represents the part of the signal after the cutting lip has exited the hole. Throughout the region (E), the value of the torque kept fluctuating at a value above zero. This is because of the frictional torque, which tends to resist the rotation of the tool while the lateral surface of the tool is in contact with the hole surface after the cutting lip exits the hole. This feature was found to be marginal in the measured axial force signals, which indicates a marginal or negligible axial component of the frictional force.

The arrow (AB) in Figure 6-13 indicates an increasing trend of the average torque as the tool advances in the axial direction. This is due to the increasing lateral area of contact between the tool and the hole wall until the cutting lip exits the hole [120]. The values of the maximum frictional torques in Figure 6-14 represent the case where the maximum lateral area of the tool is in contact with the hole wall along the entire hole depth. The value of the frictional torque at any instant during the drilling pass is assumed to be proportional to the ratio of the lateral tool area at this instant to the maximum lateral area.

Figure 6-14 shows the effect of the rotational speed and feed on the maximum frictional torque measured after the exit of the cutting tool lip. The figure shows a

linear inverse relation between the frictional torque and rotational speed. On the other hand, the frictional torque exhibited a nonlinear direct relationship with the feed.

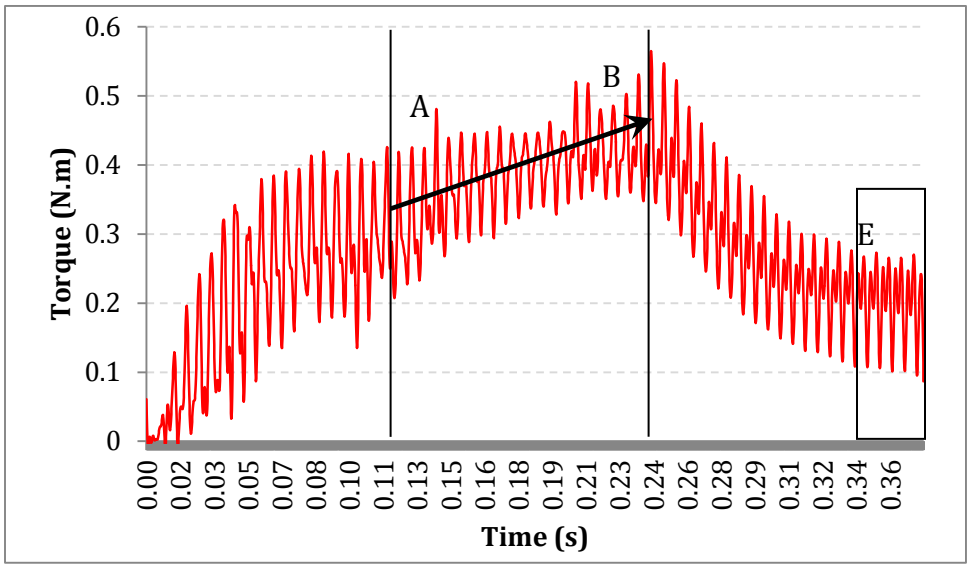

Figure 6-13 Typical torque calibration signal for drilling of unidirectional CFRP at n=10,000 rpm, f_r=0.2 mm/rev

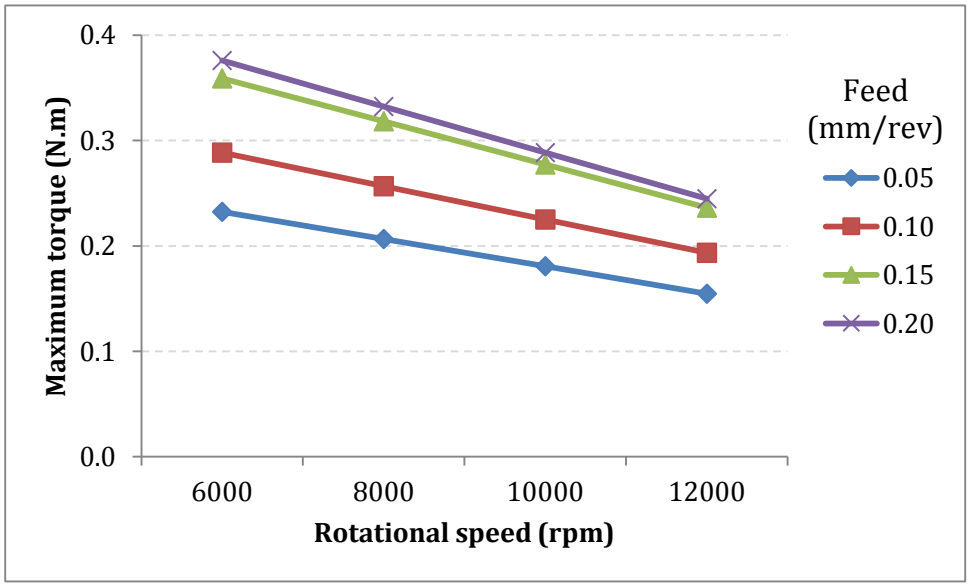

Figure 6-14 Effect of the rotational speed and feed on the maximum frictional torque values due to the friction between the tool lateral surface and the hole wall measured after the exit of the cutting tool lip

6.3.6. Effect of Material Softening on the Axial Force

Figure 6-15 shows the full axial force signals for the calibration test of conventional drilling of a unidirectional CFRP laminate, using a pilot hole at rotational speed n=10,000 rpm, and feed f_r=0.2 mm/rev. The arrow (AB) in Figure 6-15 indicates a declining trend of the average axial force as the tool advances in the axial direction through the steady state stage of the drilling pass. This is due to the building up cutting temperature until the chisel edge exits, which causes the thermoset matrix to soften and hence require less force to be cut. The average slope of arrow AB for all the calibration cases was found to be 0.8.

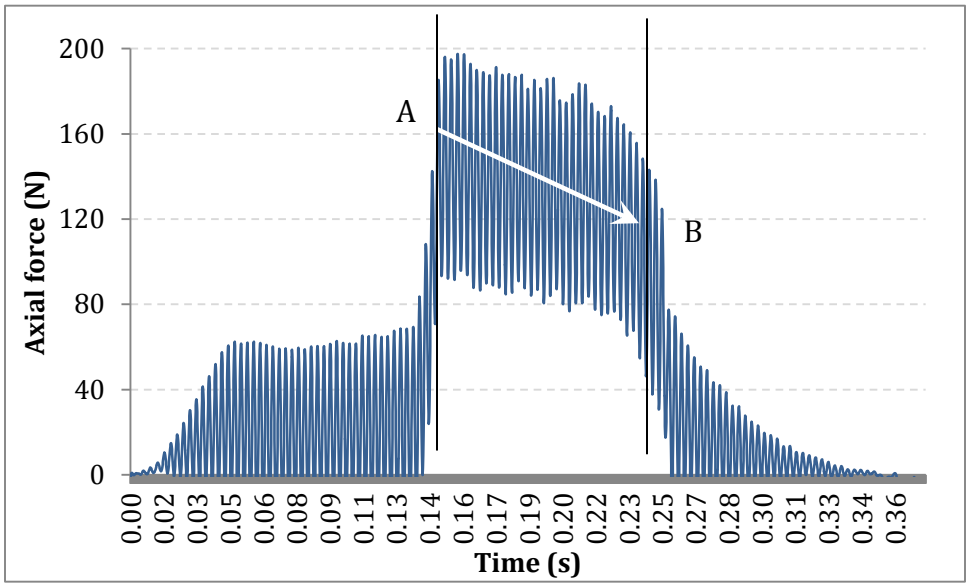

Figure 6-15 Typical axial force calibration signal for drilling of unidirectional CFRP at n=10,000 rpm, f_r=0.2 mm/rev

6.3.7. Effect of the Laminate Deflection on the Uncut Chip Thickness

The material deflection takes place under the action of the axial drilling force at every instant of time. The level of laminate deflection starts from a very low value in the beginning of the drilling pass where the laminate has the maximum thickness and the drilling axial force is still very low. The level of deflection increases as the tool advances axially towards the steady state stage of the drilling pass. This is because the axial force reaches its maximum level in the steady state drilling stage and the thickness of the remaining material ahead of the tool keeps decreasing as a result of

the material removal. As the tool approaches the exit transient stage of the drilling pass, the deflection keeps increasing because the thickness of the remaining material keeps decreasing while the average axial force is still high. Once the chisel edge breaks through the exit plane of the hole, the force decreases rapidly and the level of deflection is significantly reduced although the remaining material thickness is very small.

In the prediction model, the critical role of the material deflection takes place near the moment the chisel edge breaks through the exit plane of the laminate. This is because, if the deflections were not taken into consideration at this stage, an idealized model would predict a chisel edge breakthrough and hence will predict no forces on the chisel edge. In reality, due to the deflection of the last layers, the exit plane is displaced, keeping the chisel edge engaged with the material. Therefore, a considerable value for the force components of the chisel edge can be observed. As shown in Figure 6-16, the actual chisel uncut chip thickness is different from the ideal 'd' by the amount of material deflection "δ" at a given instant of time. Based on the aforementioned reasons, it is very important to include the effect of the material deflection on the relative position of the chisel edge and on the chisel edge uncut chip thickness.

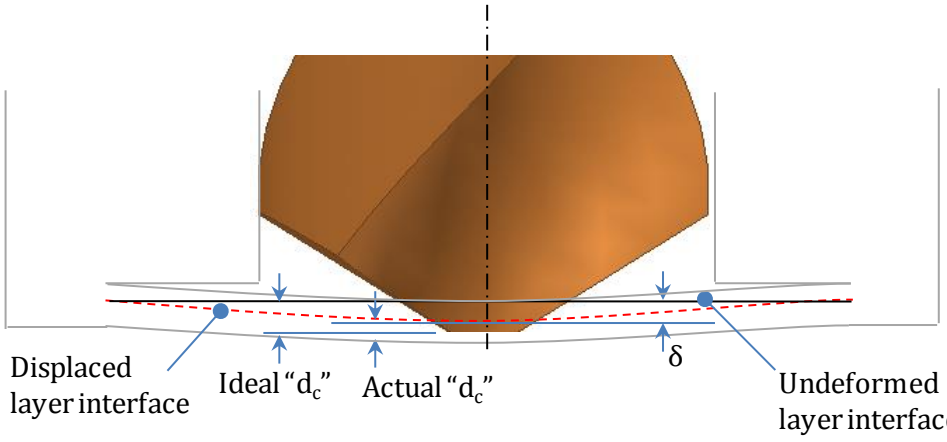

Figure 6-16 Effect of material deflection on the chisel uncut chip thickness

6.4. Predictive Model Assumptions

The formulation of the prediction model is based on the following assumptions:

a. The effect of the change of the linear cutting velocity along the chisel edge is negligible due to the relatively small radius of the circle encompassing the chisel edge.
b. The fibers are assumed to be uniformly distributed and equi-spaced in the matrix, and the spacing between the fibers is the same for the unidirectional and multidirectional FRP laminates. This is based on the fact that the layups of both materials are produced using the same unidirectional prepreg ply.
c. The tool geometry is assumed to be of a sharp tool in order to exclude the effect of tool wear. This condition has been maintained throughout all the calibration and validation experiments of the model, by limiting the number of holes produced by a new sharp tool to be < 5.
d. Based on the findings of the extensive experimental analysis in the previous chapter, the maximum drilling temperature does not exceed the decomposition temperature of the material, which was found to be 318°C from the thermogravimetric analysis.
e. The axial frictional force component is negligible; this assumption is based on the explanation given in section 6.3.

6.5. Model Formulation

This section presents the formulation of the elements and functions of the predictive model that have been justified in the previous sections. The formulation of the functions used to predict the drilling axial force and torque of FRPs follow the procedure shown in Figure 6-5.

6.5.1. Model Inputs

Input of the Process Parameters

The input process parameters are all the parameters required to define the tool-workpiece relative positions and the chip geometry. In any of the drilling processes that the developed generalized drilling model is dealing with. The scope of this research work covers the conventional and the vibration assisted drilling processes.

The axial feed "f_a" of the tool in conventional drilling and VAD controls the axial position of the tool at each instant of time. The axial feed is defined in mm/min units from the following relationship.

$$f_a = n.f_r \quad \textbf{6-6}$$

where "n" is the spindle rotational speed in rpm, and "f_r" is the feed in mm/rev. For the VAD process the modulation parameters, namely frequency "ω_m" and amplitude "A_m" have to be input to the model to define the instantaneous position of the tool resulting from its combined harmonic and axial motion.

The accuracy of the model predictions depends significantly on the size of the time increment used to update the tool and workpiece relative positions. The time increment used in this model was chosen to correspond to the sampling rate "Ω_s" used in all of the experimental drilling tests. This assures that the prediction is capturing all the detail of the actual force and torque signals. Moreover, this creates consistency between the predicted and the measured force signals for comparison and validation purposes. As shown below, the time increment "Δt" is defined as the reciprocal of the sampling rate. The defined time increment and axial feed determine the axial position increment of the tool lip 'ΔZ_c'.

At an instant "t" of time, the instantaneous axial position of the tool tip '$Z_c(t)$', and the angular positions of the primary cutting and chisel edges edge '$\psi_p(t)$' and '$\psi_c(t)$' are determined as follows:

$$\Delta t = \Omega_s^{-1} \quad \textbf{6-7}$$

$$Z_c(t) = Z_c(t-1) + \frac{\Delta t \,.\, f_a}{60} \quad \textbf{6-8}$$

$$\Psi_p(t) = \frac{360.\, t \,.\, n}{60} \quad \textbf{6-9}$$

$$\Psi_c(t) = \Psi_p(t) + \Psi_c' \quad \textbf{6-10}$$

where 'ψ'_c' is the chisel edge angle as shown in Figure 6-17. The determined axial and angular positions of the tool can be used with the axial locations of the layer interfaces to determine the relative tool-workpiece positions.

Input of the Tool Geometry

The employed modeling approach is capable of dealing with drilling tools that have similar geometric features, i.e. the cutting lip consists of primary and chisel edges. Within this family of tools, the model can deal with the variations of tool diameter, number of flutes, point angle, chisel edge size and angle, and rake angle profile along the primary cutting edge. Figure 6-17 shows the tool diameter "$2R$", chisel length "L_c", point angle "ε", chisel angle "ψ_c' " and web thickness "t_w" of a 2–flute drilling tool.

The length of the primary cutting edge "L_p" and the vertical height of cutting lip "H_v" are two indirect parameters that are defined using the trigonometric relationships between the main tool dimensions as follows. The "L_p" and "H_v" parameters are very important in defining the axial positions and the lengths of the sections of the cutting edge during the simulation of the drilling process.

$$L_p = \frac{1}{2}\frac{(2R - t_w).\cos(\Psi'_c)}{\sin\left(\frac{\varepsilon}{2}\right)} \qquad \textbf{6-11}$$

$$H_v = L_p.cos\left(\frac{\varepsilon}{2}\right) \qquad \textbf{6-12}$$

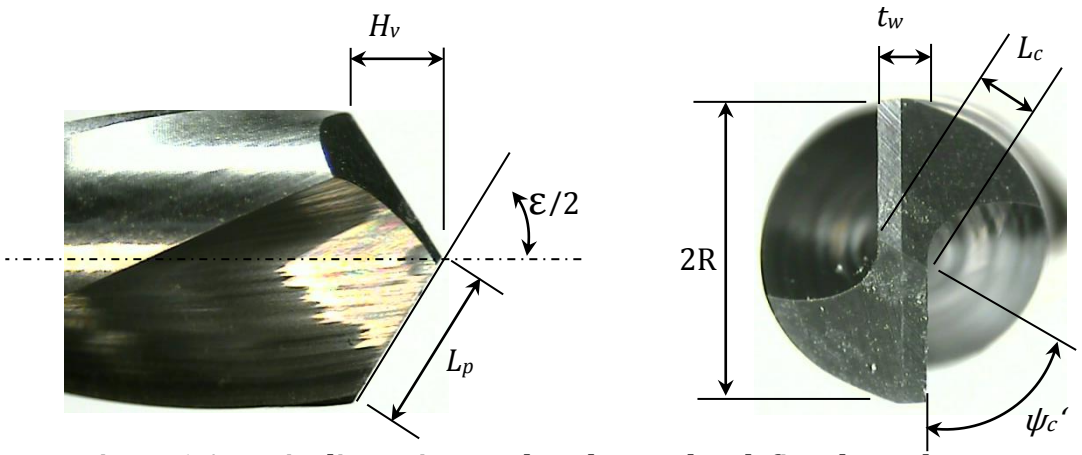

Figure 6-17 Main dimensions and angles used to define the tool geometry of a 2-flute drill bit

Input of the Material Layup

The developed model is formulated to deal with any multidirectional layup configuration for any FRP material. However, the scope of this current work is focusing on unidirectional and cross-ply layups of carbon fiber reinforced epoxy shown in Figure 6-2 (a) and (b), respectively. As shown in Figure 6-18, the material architecture is input to the model in terms of the total number of plies "N", the thickness of a single cured ply "t_p", and the orientation of each ply "θ_i". The total laminate thickness "H_l" is determined from the following relationship:

$$H_l = N.t_p \qquad \textbf{6-13}$$

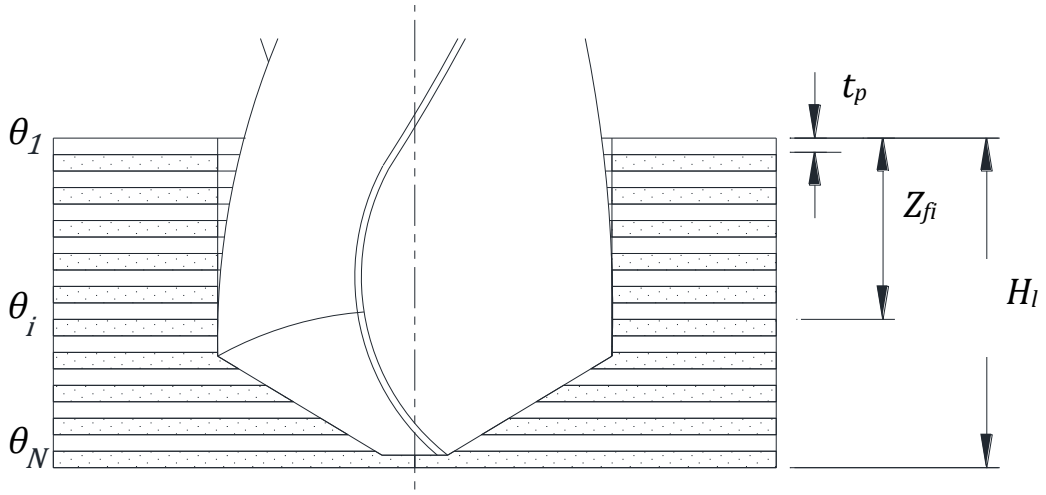

Figure 6-18 Schematic of the axial coordinates of the layers of the material layup and their fiber orientations

The interface between a general layer of fiber orientation "θ_i" and the preceding layer "θ_{i-1}"is defined by its vertical position "Z_{fi}" from the hole entrance plane of the laminate. During the drilling process simulation, the intersection of layer interfaces with the cutting edges at each time increment defines the sections of these cutting edges. The lengths of these sections along the primary cutting edge represent the width of the cut in each of the layers of fiber orientation, while 'd' is determined mainly by the feed. The vertical height of the sections of the chisel edge represents the sections of 'd' in each of the layers of fiber orientation, while the width of cut is always

fixed on the chisel at a value equal to the length of the chisel edge. The details of the geometry of the formed chip are further explained in the following sections.

6.5.2. Modeling of the Formed Chip Geometry

The geometry and the fiber orientation of the uncut chip are the main two parameters that control the required drilling force to remove the chip. This section presents the method of modeling the geometry and the fiber orientation of the formed chip based on the interaction between the tool and workpiece through the different drilling stages. This section also shows the criteria of modeling the beginning and end of the transient and steady state drilling stages. Moreover, the method of modeling the dimensions of the cutting edge sections is shown, based on the intersection of the coordinates of the cutting edge and material layer at a given instant of time. The effective fiber orientation is determined from the relative angular position of the cutting edge with respect to the layup fiber orientation. The area of the formed chip is defined by the length and uncut chip thickness of each of the cutting edge sections. This information will be used in further steps of the model to predict the time variation of the drilling force and torque.

Effective Fiber Orientation Angle

The effective fiber orientation angle is defined as the clockwise angle between the line of the cutting direction and fiber axis, as shown in Figure 6-3. For retrieving the cutting pressures into the prediction model, it is essential to use the same convention of the effective fiber orientation angles used for the calibration of the cutting pressures. Figure 6-9 (a) shows that the cutting pressures for drilling of FRPs using a two-flute drilling tool are symmetric about the central axis of the tool and can be defined in a range from 0˚ to 180˚. However, in order to make the model capable of dealing with multiple cutting flute tools, the effective orientation angles are defined in a range from 0˚ to 360˚ according to the following relationships:

$$For\ 0 \leq \psi < \frac{\pi}{2} \qquad \theta_{e,i}(t) = \theta_i + \pi - \psi(t) \qquad \textbf{6-14}$$

$$For\ \frac{\pi}{2} \leq \psi < \frac{3\pi}{4} \qquad \theta_{e,i}(t) = \theta_i + 3\pi - \psi(t) \qquad \textbf{6-15}$$

$$For\ \frac{3\pi}{4} \leq \psi < 2\pi \qquad \theta_{e,i}(t) = \theta_i + \psi(t) \qquad \textbf{6-16}$$

where "$\theta_{e,i}(t)$" is the instantaneous effective orientation angle on the cutting edge section engaged with a layer "i", "θ_i" is the fiber orientation angle of the layer "i" in the material layup, and "$\psi(t)$" is the instantaneous angular position of the cutting edge in a range from 0° to 360°. Equation 5-9 is applied to each of the cutting lip sections to determine the effective fiber orientation at each of these sections. The output of this step at any given instant of time is a set of effective fiber orientations for each of the primary and the chisel edge. The elements of these sets correspond to the sections of each of the cutting edges. Each value of these sets will be used to determine the corresponding cutting pressure at the same section of the cutting edge.

$$\boldsymbol{\theta_{e,c}(t)} = \begin{bmatrix} \theta_{e,j} \\ \vdots \\ \theta_{e,N_c} \end{bmatrix} \qquad \boldsymbol{\theta_{e,p}(t)} = \begin{bmatrix} \theta_{e,i} \\ \vdots \\ \theta_{e,N_p} \end{bmatrix} \qquad \textbf{6-17}$$

where "N_p" and "N_c" are the numbers of layers engaged with the primary and chisel edges at a given instant of time, respectively. The values "N_p" and "N_c" are determined from the intersection of the edge vertical height with the layers interface. The sets "$\boldsymbol{\theta_{e,c}(t)}$" and "$\boldsymbol{\theta_{e,p}(t)}$" represent the instantaneous effective fiber orientation angles of the engaged layers with the chisel and primary cutting edges, respectively. Length of cutting edge sections

During drilling of multidirectional FRP, the lengths of the sections of the cutting edges keep changing as they engage with different material layers of fiber orientations. In the transient entrance stage, the cutting lip engages with the workpiece progressively as the tool advances in the axial direction, until the full length of the edge is engaged. This is accompanied by the change in the length of the edge sections engaged with different fiber orientation angles because of the combined rotary and axial motions of the tool. The inverse of this trend takes place in the transient exit stage. Therefore, the transient stage condition is given by:

$$\sum_{i}^{N_p} L_{p,i} < L_p \qquad \textbf{6-18}$$

where "$L_{p,i}$" is the length of the primary edge section engaged with layer "i ". The entrance and exit transient stages are determined as follows:

$$Z_c(t) < H_v \qquad \textbf{6-19}$$

$$Z_c(t) > H_l \qquad \textbf{6-20}$$

The steady state stage begins when the primary edge is fully developed and its engaged length becomes constant, however, the length of the edge sections engaged with different fiber orientation angles keep changing because of the combined rotary and axial motions of the tool. Figure 6-19 shows a general position of the engagement of the primary cutting edge with different layers of fiber orientation "θ_i". The length of the general primary cutting edge section "$L_{p,i}$" is given as follows:

$$L_{p,i} = \frac{Z_c - \left(Z_{f,i} - \sum_i^N Z_{f,i \le i-1}\right)}{\sin\left(\frac{\varepsilon}{2}\right)} \qquad \textbf{6-21}$$

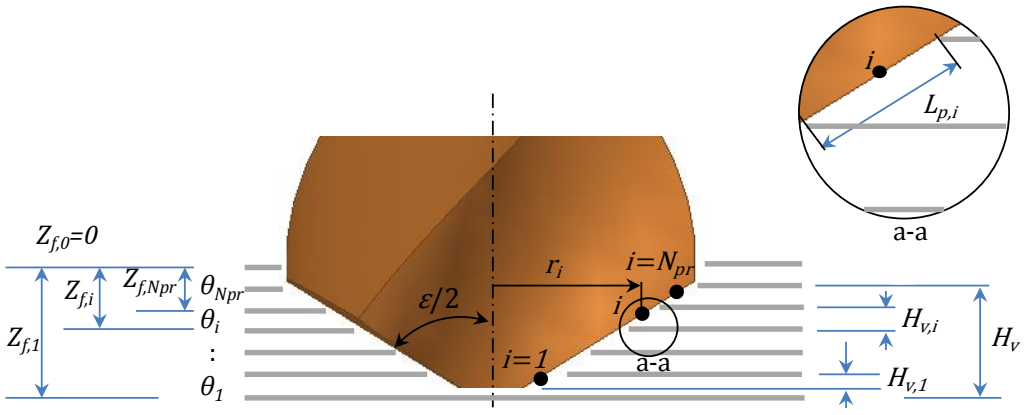

Figure 6-19 Sections of the primary cutting edge engaged with different layers of fiber orientations during the steady state stage

The relationship described by equation 6-17 is applicable for calculating the lengths of the active primary cutting edge sections, while the unengaged sections will have a value of ($L_{p,i}$=0). The chisel edge is located in a plane normal to the axial

direction of the tool motion, and the full length of the edge does not have any projection on the vertical plan. Therefore, the chisel edge has a constant length "L_c" at each axial position step throughout the stages of the drilling process. The lengths of the primary cutting edge sections "$\boldsymbol{L_p(t)}$" at each incremental instant of time are determined in the following form:

$$\boldsymbol{L_p}(\boldsymbol{t}) = \begin{bmatrix} L_{p,i} \\ \vdots \\ L_{p,N_p} \end{bmatrix} \quad \textbf{6-22}$$

Modeling of the Dynamic Uncut Chip Thickness

In the generalized drilling model that can deal with conventional and vibration assisted drilling process, the nominal dynamic uncut chip thickness of the chisel and primary cutting edges '$d_{c,n}(t)$' and '$d_{p,n}(t)$ ', respectively, are determined as follows.

$$d_{c,n}(t) = (f_r) + 2Acos\left(2\pi\omega_m t + \frac{\pi\omega_m}{\omega_T}\right)\sin\left(\frac{\pi\omega_m}{\omega_T}\right) \quad \textbf{6-23}$$

$$d_{p,n} = \left(\frac{1}{2}.f_r\right) + 2Acos\left(2\pi\omega_m t + \frac{\pi\omega_m}{2\omega_T}\right)\sin\left(\frac{\pi\omega_m}{2\omega_T}\right) \quad \textbf{6-24}$$

Equations 6-23 and 6-24 are based on the analysis presented in Chapter 3, which was developed in [46].

In the transient exit stage, as the tool advances in the axial direction towards the exit plane, the remaining material becomes thinner and experience higher deflection under the action of the axial forces. As shown in Figure 6-16, the deflection of the remaining material layers near the exit plane of the hole "δ_l" alters 'd' compared to the ideally defined uncut chip thickness for the case of a perfectly rigid plate.

The remaining thickness deflection "δ_l" is calculated at a given instant of time "t" based on the predicted axial force at the time step before "$F_z(t\text{-}1)$". The thickness of the remaining material layers 'H_r' at a given instant of time is determined as follows:

$$H_r(t) = H_l - Z_c(t) \quad \textbf{6-25}$$

The material plies are assumed to have the same orientation (θ=0), where they form a 2D beam under a centric point load with fully clamped ends. The modulus in the fiber direction 'E_x' is assumed to be the same for all the plies. At a given instant of time the total modulus of the beam '$E_T(t)$'.

$$E_T(t) = \frac{H_r(t)}{t_p} E_x \qquad \textbf{6-26}$$

$$I_r(t) = \frac{2R.H_r^3(t)}{12} \qquad \textbf{6-27}$$

$$\delta_l(t) = \frac{F_z(t-1).(2R)^3}{48.E_T(t).I_r(t)} \qquad \textbf{6-28}$$

The modified uncut chip thickness 'd_p' and 'd_c' of the primary and chisel edges, respectively, are calculated based on the calculated deflection as follows:

$$d_p(t) = d_{p,n}(t-1) - \delta_l(t) \qquad \textbf{6-29}$$

$$d_c(t) = d_{c,n}(t-1) - \delta_l(t) \qquad \textbf{6-30}$$

The output of the function discussed in this section are two sets that represent the uncut chip thickness '$\boldsymbol{d_p}$' and '$\boldsymbol{d_c}$' of the formed chip on the sections of the primary and chisel cutting edges for each instant of time "t" as follows:

$$\boldsymbol{d_p}(\boldsymbol{t}) = \begin{bmatrix} d_{p,i} \\ \vdots \\ d_{p,N_p} \end{bmatrix} \qquad \boldsymbol{d_c}(\boldsymbol{t}) = \begin{bmatrix} d_{c,j} \\ \vdots \\ d_{c,N_c} \end{bmatrix} \qquad \textbf{6-31}$$

Each value of the above sets is used to determine the corresponding cutting pressure. The product of the sets of the cutting width and depth on each of the primary and chisel cutting edges at each instant of time gives a set of chip areas for the sections of each cutting edge.

6.5.3. Cutting Pressures

Identification of the Cutting Pressures

Using the approach discussed in section 6.3.2, the force and torque cutting pressures "$K_{F,p}$", and "$K_{T,p}$" of the primary cutting edge are obtained by dividing the

measured axial force "$F_{p,m}$" and torque "$T_{p,m}$" for the primary edge by the chip area. The area of the formed chip by the primary cutting edge is the product of the length of the cutting edge "L_p" and the uncut chip thickness "d_p". Similarly, the force and torque cutting pressures "$K_{F,c}$" and "$K_{T,c}$" for the chisel edge are obtained by dividing the measured force "$F_{c,m}$" and the torque "$T_{c,m}$" by the area of the formed chip under the chisel edge "$L_c.d_c$", the expressions for the cutting pressures is expressed as follows:

$$K_{F,p}\left(d_p,\theta_e,v_r,\alpha_m\right)=\frac{F_{p,m}\left(d_p,\theta_e,v_r,\alpha_m\right)}{L_p d_p} \quad \textbf{6-32}$$

$$K_{T,p}\left(d_p,\theta_e,v_r,\alpha_m\right)=\frac{T_{p,m}\left(d_p,\theta_e,v_r,\alpha_m\right)}{L_p d_p} \quad \textbf{6-33}$$

$$K_{F,c}\left(d_c,\theta_e,v_r\right)=\frac{F_{c,m}\left(d_c,\theta_e,v_r\right)}{L_c d_c} \quad \textbf{6-34}$$

$$K_{T,c}\left(d_c,\theta_e,v_r\right)=\frac{T_{c,m}\left(d_c,\theta_e,v_r\right)}{L_c d_c} \quad \textbf{6-35}$$

The cutting pressures "$K_{F,p}$", and "$K_{T,p}$" obtained from equations 6-32 and 6-33 are functions of the uncut chip thickness "d_p", the effective orientation angle "θ_e", the reference cutting velocity "v_r", and the mean rake angle of the primary cutting edge "α_m" . The values of "$K_{F,p}$", and "$K_{T,p}$" represent mean values that cannot be used directly for force and torque predictions. They need to be distributed according to the rake angle and cutting velocity profile along the sections of the primary cutting edge at each instant of time as will be shown in the following section. The chisel edge cutting pressures "$K_{F,c}$", and "$K_{T,c}$" obtained from equations 6-34 and 6-35are functions of the uncut chip thickness "d_c", the effective orientation angle "θ_e", and the reference cutting velocity "v_r". The "$K_{F,c}$", and "$K_{T,c}$" values are considered final and can be used directly for force and torque predictions. This is because the cutting velocity variation is assumed negligible and there is no rake angle change along the length of the chisel edge.

Cutting Pressures Calculations for Force and Torque Predictions

The variation of the cutting pressures through the sections of the chisel edge results from the variable uncut chip thickness of its sections as they engage with different material layers. The variation of the cutting pressures through the sections of the primary cutting edges takes place due to three main factors (v_c, α *and* θ_e). The sections of the primary cutting edge engage with different effective fiber orientations corresponding to different material layers. This takes place while the rake angle and the cutting velocity of the primary cutting edge sections are variable. This section shows the procedure of obtaining the sets of cutting pressures corresponding to the aforementioned sources of variation through the sections of the primary and chisel cutting edge.

For each time step in the prediction model, the axial force and torque cutting pressures for a cutting edge section can be determined based on the reference cutting velocity, uncut chip thickness, and the effective fiber orientation of the this section. Using the cutting pressure database obtained by equations 6-32 to 6-35, the following sets of cutting pressures can be determined for the sections of the chisel and primary cutting edge.

$$\bar{\boldsymbol{K}}_{\boldsymbol{F,c}}(t) = \begin{bmatrix} K_{F,c,j}(v_r, d_{c,j}, \theta_{e,j,c}, t) \\ \vdots \\ K_{F,N_c}(v_r, d_{c,i}, \theta_{e,N_c}, t) \end{bmatrix} \quad \textbf{6-36}$$

$$\bar{\boldsymbol{K}}_{\boldsymbol{T,c}}(t) = \begin{bmatrix} K_{T,c,j}(v_r, d_{c,j}, \theta_{e,j,c}, t) \\ \vdots \\ K_{T,N_c}(v_r, d_{c,j}, \theta_{e,N_c}, t) \end{bmatrix} \quad \textbf{6-37}$$

$$\bar{\boldsymbol{K}}_{\boldsymbol{F,p,r}}(t) = \begin{bmatrix} K_{F,p,r,i}(v_r, d_p, \theta_{e,i,p}, t) \\ \vdots \\ K_{F,p,r,N_{pr}}(v_r, d_p, \theta_{e,N_p}, t) \end{bmatrix} \quad \textbf{6-38}$$

$$\bar{\boldsymbol{K}}_{\boldsymbol{T,p,r}}(t) = \begin{bmatrix} K_{T,p,r,i}(v_{c,i}, d_p, \theta_{e,i,p}, t) \\ \vdots \\ K_{T,p,r,N_p}(v_{N_p}, d_p, \theta_{e,N_p}, t) \end{bmatrix} \quad \textbf{6-39}$$

where $\boldsymbol{K_{F,c}(t)}$, and $\boldsymbol{K_{T,c}(t)}$, are the sets of axial force and torque cutting pressures acting on the sections of the chisel edge at time "t", respectively. Similarly, $\boldsymbol{K_{F,p,r}(t)}$, and

$K_{T,p,r}(t)$ are the sets of the axial force and torque cutting pressures acting on the sections of the primary edge at time "t", respectively.

The determination of the cutting pressures of a section "j" of the chisel edge at a given instant of time is based on the reference cutting speed, the uncut chip thickness, and the effective fiber orientation angle.

For the primary cutting edge, the cutting pressures "$K_{F,p,r,i}$" and "$K_{T,p,r,i}$" for a section "i", are obtained for an average rake angle of the middle section of the full primary cutting edge. A set of correction factors is obtained to represent the distribution of the cutting pressures corresponding to the rake angle variation through the sections of the primary cutting edge. The factor for each section is obtained from the database of the normalized effect of rake and effective fiber orientation angles on the cutting pressures shown in Figure 6-9. In order to be able to use the rake angle database, the predicted off-axis cutting pressures for forces and torques on each section of the primary cutting edge have to be transformed to on-axis vertical and horizontal components. Correction factors are applied to the transformed cutting pressures, then they are inverse transformed to the off-axis components after correction.

The uncorrected off-axis components "$K_{x,r,i}$" and "$K_{y,r,i}$" of the tangential cutting pressures on the primary cutting edge are resolved from the following equations:

$$K_{X,r,i} = K_{T,p,r,i}\cos(\Theta) \quad \textbf{6-40}$$

$$K_{Y,r,i} = K_{T,p,r,i}\sin(\Theta) \quad \textbf{6-41}$$

The uncorrected on axis components "$K_{h,r,i}$", "$K'_{h,r,i}$", and "$K_{v,r,i}$" of the cutting edge section are obtained from the transformation of the uncorrected off-axis components "$K_{x,r,i}$", "$K_{Y,r,i}$", and "$K_{Z,r,i}$" as follows:

$$\begin{bmatrix} K_{h,r,i} \\ K'_{h,r,i} \\ K_{v,r,i} \end{bmatrix} = [\boldsymbol{T}]^{-1} \begin{bmatrix} K_{X,r,i} \\ K_{Y,r,i} \\ K_{Z,r,i} \end{bmatrix} \quad \textbf{6-42}$$

The effect of the rake angle variation is introduced using the corresponding correction factors "$C_{h,i}$", and "$C_{v,i}$" from the database of the normalized effect of rake

and effective fiber orientation angles on the cutting pressures. The corrected on-axis cutting pressures "$K_{h,i}$", and "$K_{v,i}$" are obtained from the following relationship:

$$\begin{bmatrix} K_{h,i} \\ K'_{h,i} \\ K_v, i \end{bmatrix} = \begin{bmatrix} K_{h,r,i} \\ K'_{h,r,i} \\ K_{v,r,i} \end{bmatrix} \begin{bmatrix} C_{h,i} \\ 1 \\ C_{v,i} \end{bmatrix} \quad \textbf{6-43}$$

The corrected on axis force components are inverse transformed to give the corrected off-axis force components using the inverse of the transformation matrix as follows:

$$\begin{bmatrix} K_{X,i} \\ K_{Y,i} \\ K_{Z,i} \end{bmatrix} = [\boldsymbol{T}] \begin{bmatrix} K_{h,i} \\ K'_{h,i} \\ K_{v,i} \end{bmatrix} \quad \textbf{6-44}$$

The corrected off-axis components are then used for force and torque predictions using the relationship with the formed chip area at each section of the cutting edge as will be shown in the following section.

6.5.4. Force and Torque Computation

The total axial forces and torques on each of the primary and chisel cutting edges during the drilling process of multidirectional laminates are predicted by summation of the elemental forces predicted at each section of the cutting edges:

$$F_p(t) = k \sum_{i}^{N_p} K_{F,p,i}\left(v_r, d_p(t), \theta_{e,p,i}\right). d_p(t). L_{p,i}(t) \quad \textbf{6-45}$$

$$F_c(t) = \sum_{j}^{N_c} K_{F,c,j}\left(v_r, d_c(t), \theta_{e,c,j}\right). d_{c,j}(t). L_c \quad \textbf{6-46}$$

$$T_p(t) = k \sum_{i}^{N_p} K_{T,pr,i}\left(v_{c,i}, d_p(t), \theta_{e,p,i}\right). d_p(t). L_{p,i}(t) \quad \textbf{6-47}$$

$$T_c(t) = \sum_{j}^{N_c} K_{T,c,j}\left(v_r, d_c(t), \theta_{e,c,j}\right). d_{c,j}(t). L_c \quad \textbf{6-48}$$

where $F_P(t)$ *and* $T_P(t)$ are the instantaneous axial force and torque on the primary cutting edge at a certain time (t), respectively. Similarly, $F_c(t)$ *and* $T_c(t)$ are the instantaneous axial force and torque on the chisel cutting edge at time (t), respectively. The total number of layers engaged with the primary cutting edge at a given time (t) is denoted as "N_p", while "i" is the rank of each of the engaged layers. "$L_{p,i}$" is the length of segment "i" of primary cutting edge sections. Similarly, the total number of layers engaged with the chisel cutting edge at time (t) is denoted by "N_c", while "j" is the rank of each of the engaged layers, and "L_c" is the length of the chisel edge.

The frictional torque is computed for each incremental instant of time knowing the ratio between the lateral area of the tool in contact with the hole wall "$A'_L(t)$" and the maximum lateral tool area "$A_L(t)$" after the cutting lip exits the hole. The value of the frictional torque at a given instant is the product of the area ratio and the maximum frictional torque "$T_{f,m}$" value obtained from the database shown in Figure 6-14. The instantaneous frictional torque is calculated using the following equation:

$$T_f(t) = \frac{A''_L(t)}{A_L} T_{f,m} \qquad \textbf{6-49}$$

The total instantaneous axial force and torque are then obtained from the summation of the axial and torque components on each of the chisel and the primary cutting edges:

$$F_Z(t) = F_{Z,p}(t) + F_{Z,c}(t) \qquad \textbf{6-50}$$

$$T(t) = T_p(t) + T_c(t) + T_f(t) \qquad \textbf{6-51}$$

CHAPTER 7

Experimental Validation of the Mechanistic Model

7.1. Introduction

This chapter demonstrates the capability of the mechanistic model developed in Chapter 6 to predict the drilling forces and torques for different process parameters, in addition to the effect of the tool geometry and material deflection. To quantify the accuracy of the model predictions, the errors of the predicted maximum and average forces and torques in the transient and steady state stages will be shown. This is presented by comparing the full signals of the predicted force and torque to the corresponding experimentally measured signals during the drilling experiment.

The accuracy of the procedure followed in order to define the cutting pressures of the process is the main factor that controls the accuracy of the model prediction. This chapter also shows the procedure of determining the cutting pressures and the results of their experimental validation.

7.2. Identifying the Cutting Pressures

The experiments of defining the cutting pressures were designed to accommodate two main considerations. First, the primary and cutting edges have different chip formation mechanisms; therefore, their effects have to be isolated in order to define their corresponding cutting pressures separately. This was achieved by preparing the hole used for the calibration experiment as shown in section 6.3.2. A blind pilot hole of a diameter slightly larger than the circle that encompasses the chisel edge is predrilled from the top plane of a unidirectional FRP laminate until half the thickness of the specimen. This assures that the effect of the chisel edge is completely isolated during the first half of the drilling operation and what is being measured is purely the effect of the full primary cutting edges in the transient and the steady states. During

the second half of the drilling operation, the measured force increases as a result of the additional engagement of the chisel edge. The effect of the chisel edge only can then be determined via subtracting the signal of the primary edge from the combined primary and chisel signal.

The second consideration is that each cutting edge has to be engaged with only one fiber orientation at each time instant, because the effective fiber orientation is the key factor that controls the cutting pressures. In order to achieve that, a two-flute symmetric drill was used for the drilling of a unidirectional FRP laminate in order to assure that the measured torques and forces are symmetric on each of the primary cutting edges while the chisel edge is defined separately.

7.2.1. Experiments Drilling Tests for Cutting Pressures Calibration

Table 7-1 shows the set of conventional drilling test condition that were conducted in order to identify the cutting pressures. The selected ranges of process parameters (4 speeds and 4 feeds), with at least three replicates for each condition cover the full range of drilling speeds and feeds considered in this research. Moreover, the range of fiber orientations is fully covered for each set of conditions through the nature of the drilling of unidirectional FRP laminate as described in chapter 6. The comprehensive and high-resolution information that can be extracted from the small number of experimental tests shown in Table 7-1 represent an important source of strength and originality of the proposed calibration approach.

Table 7-1 Conventional drilling conditions for defining cutting pressures

Feed 'f_r' (mm/rev)	**Rotational speed 'n' (rpm)**			
	6,000	**8,000**	**10,000**	**12,000**
	Axial feed (mm/min)			
0.05	300	400	500	600
0.1	600	800	1,000	1,200
0.15	900	1,200	1,500	1,800
0.2	1,200	1,600	2,000	2,400

For the conditions shown in Table 7-1, a new drilling tool was used to drill four holes only in order to exclude the effect of tool wear. The descriptions of the experimental setup, test material, and drilling tool used for the calibration tests were given in Chapter 3.

7.2.2. Effects of Process Parameters on the Cutting Pressures

Figure 7-1 (a) and (b) show the maximum axial force values of the measured axial forces during the engagement of the primary cutting edges, and the full cutting lip, i.e. primary and cutting chisel edges, respectively.

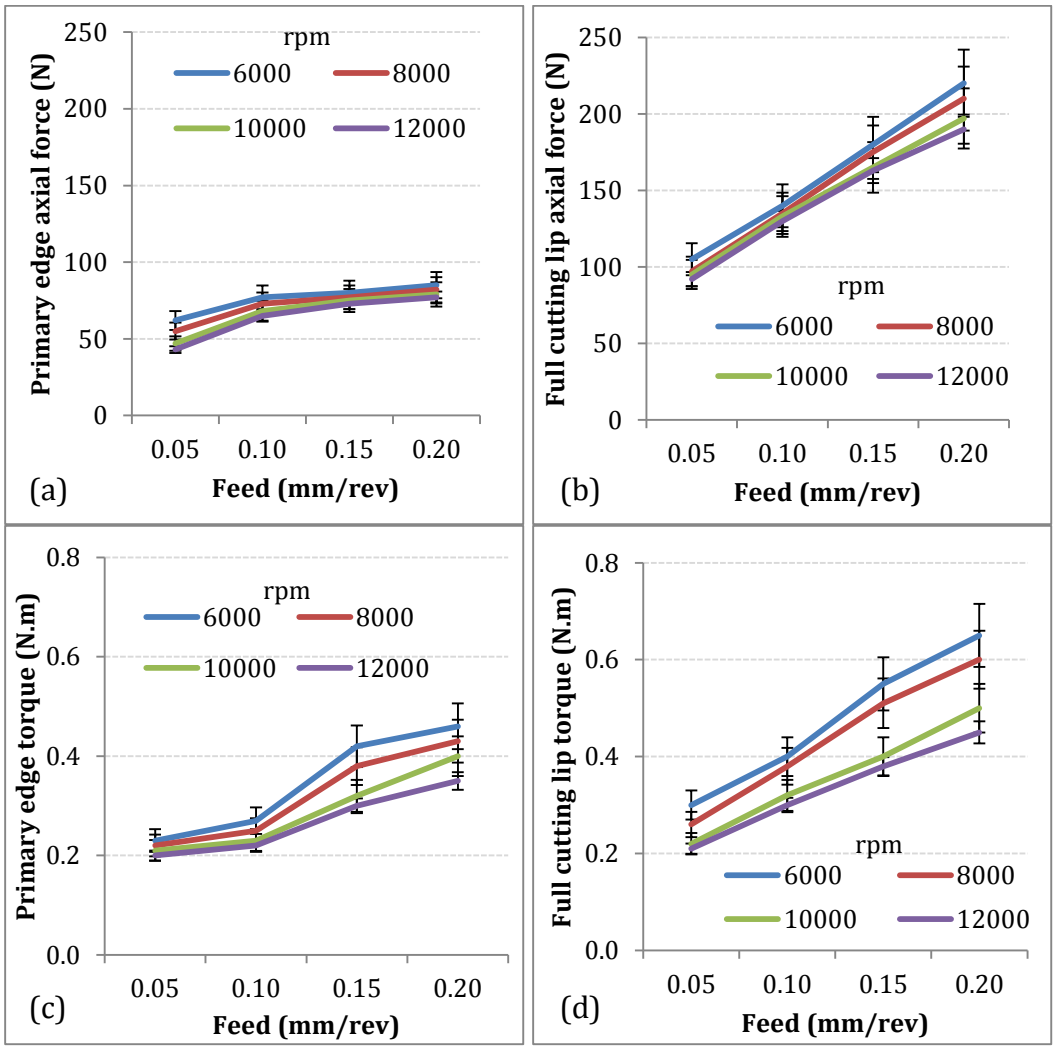

Figure 7-1 Maximum values of the measured (a) primary edge axial force, and (b) full cutting lip axial force, (c) primary edge torque, and (d) full cutting lip torque.

The figure shows that the axial force on the full cutting lip is higher than that on the primary cutting edges only, due to the effect of the chisel edge. One can observe that the axial force increased with the increase in the feed and decreased with the increase of the rotational speed. Figure 7-1 (c and d) show a similar trend for the measured maximum torques on the primary cutting edges and the full cutting lip, respectively. The measured signals of the described conventional drilling tests of unidirectional CFRP laminate will be used to identify the force and torque cutting pressures of the primary and chisel edges. Figure 7-2 shows the full measured axial force and torque signals during the steady state drilling of the unidirectional laminate, at n=6,000 rpm, and f_r=0.15 mm/rev. The obtained force and torque signals for this set of drilling conditions are going to be used through this section as a representative case to show the procedure of identifying the cutting pressures.

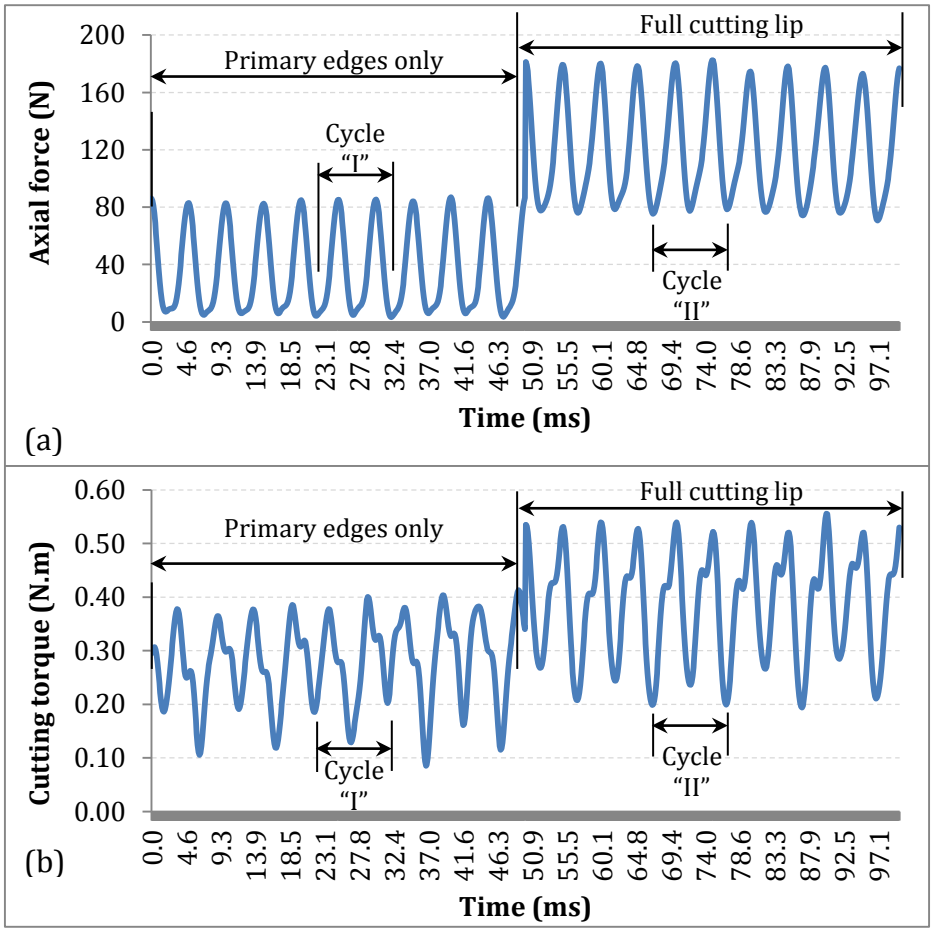

Figure 7-2(a) Axial force and (b) cutting torque signals for the drilling stages with and without the chisel edge engagement (n=6,000 rpm, and f_r=0.15 mm/rev)

The first section of the signals shown in Figure 7-2 (a) and (b) represent the axial force and torque on the primary cutting edge only. This is corresponding to the portion of the hole where the predrilled pilot hole exists. In the second part of the signals, the chisel edge is engaged and the signals show the axial force and torque measured on the full cutting lip. The force and torque fluctuations due to the variation of the fiber orientations as the tool rotates can be obviously seen. A full cycle of the tool in each of the signal sections can be identified, where "cycle I" is for the primary edges, and "cycle II" is for the full cutting lip. Each of these cycles gives information on the value of the force and torque at every fiber orientations that the cutting edges have engaged with during cutting. As shown in Figure 7-3 (a) and (b), the axial force and torque on the chisel edge at each instant of time can be identified separately by subtracting the primary edge cycle from the full lip cycle.

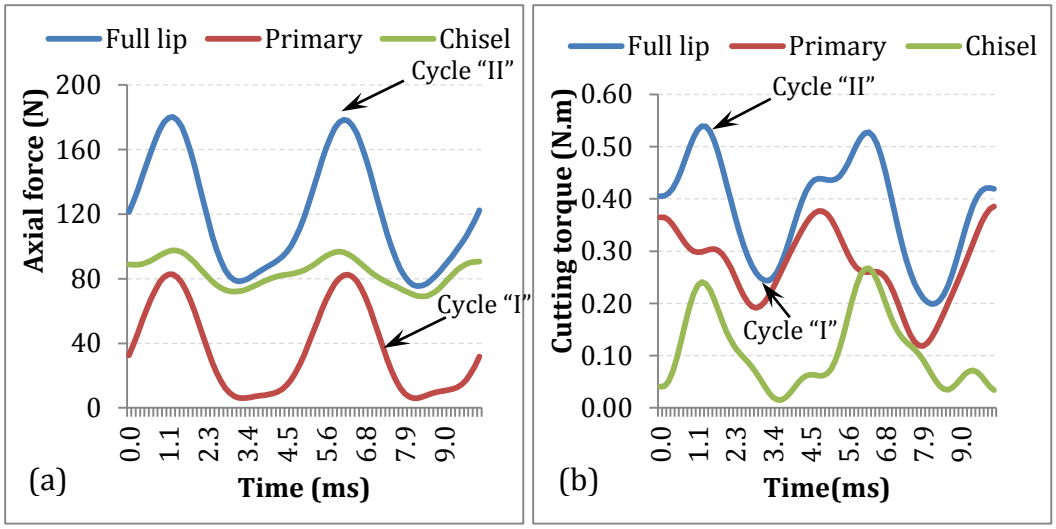

Figure 7-3 Separated behavior of the (a) axial force and (b) cutting torque of the full cutting lip, the primary cutting edges and the chisel edge during the defined cycles of tool rotation at (n=6,000 rpm, and f_r=0.15 mm/rev).

The angular positions corresponding to the time span of each cycle are defined through the relationship between the rpm and the time increment. For all the drilling conditions specified in Table 7-1, each of the cutting edges has shown a typical form of axial force and torque fluctuation with the variation of the effective fiber orientations. The measured axial force and torque signals of the primary and chisel cutting edges were normalized with respect to the maximum value of the signal. Figure 7-4 (a) and

(b) show the variation of the normalized axial force with the variation of the effective fiber orientation angles on the primary and chisel edges. The error bars show the variations of all the cases from the average plotted curve. Figure 7-5 (a) and (b) shows similar trends for the variation of the normalized torque with the variation of the effective fiber orientation angles on the primary and chisel edges.

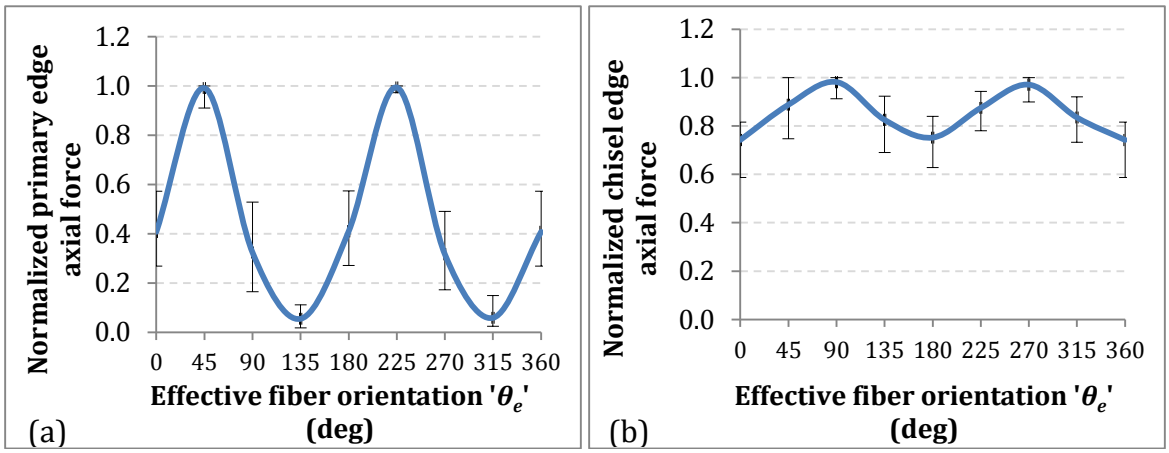

Figure 7-4 Effect of the effective fiber orientation angle on the normalized axial forces on the (a) primary cutting edges, and (b) chisel edge.

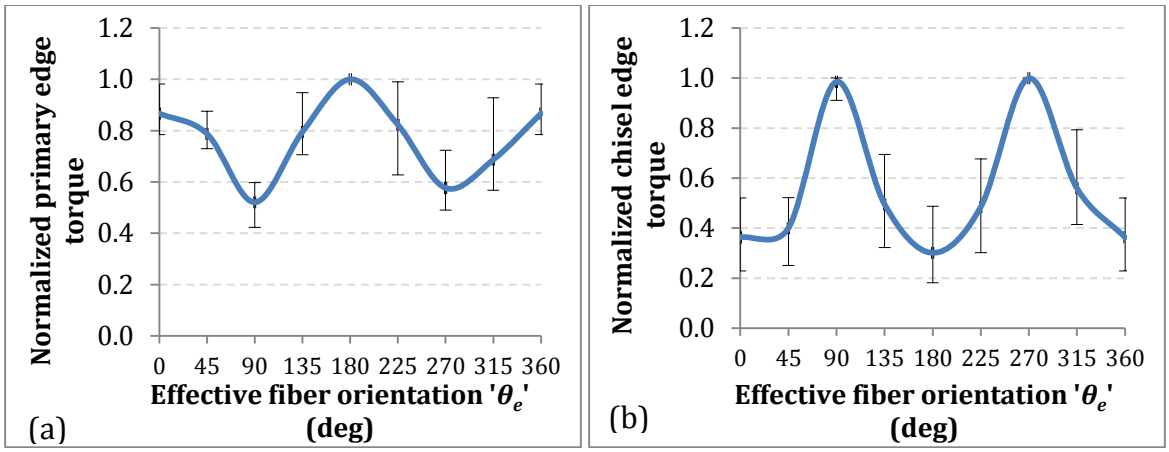

Figure 7-5 Effect of the effective fiber orientation angle on the normalized torques on the (a) primary cutting edges, and (b) chisel edge

Based on the plots shown in Figure 7-4 and Figure 7-5 for each of the cutting edges, the value of the axial force and torque at every effective fiber orientation can be identified as a ratio of the cutting pressure at each fiber orientation to the maximum value. Based on this step, only the maximum force and torque for each feed and speed on each of the cutting edges is required in order to identifying all the cutting pressures

as function of the effective fiber orientation "θ_e". The axial force and torque cutting pressures on the primary and chisel edges are defined for each cutting speed "v_r", uncut chip thickness 'd', and the effective fiber orientation "θ_e" using Eq. 6-32 to Eq. 6-35 in Chapter 6.

Figure 7-6 (a) and (b) show the identified axial cutting pressures of the primary and chisel cutting edges for all the feeds, and effective fiber orientations at a rotational speed of 6000 rpm. The figure shows the fluctuation of the cutting pressures as the fiber orientation varies from 0˚ to 360˚ according to the trend shown in Figure 7-4 (a) and (b). The maximum value of cutting pressures is located at the angles 45˚ for the primary cutting edge and at angle 95˚ for the chisel, which reflects the lead angle of the chisel edge by 50˚ degrees. Although the axial force is lower for the case of a smaller uncut chip thickness corresponding to low feed, the cutting pressures are shown to be decreasing with the increase in the feed, because the force is divided by the uncut chip area, which increases with the increase of the feed.

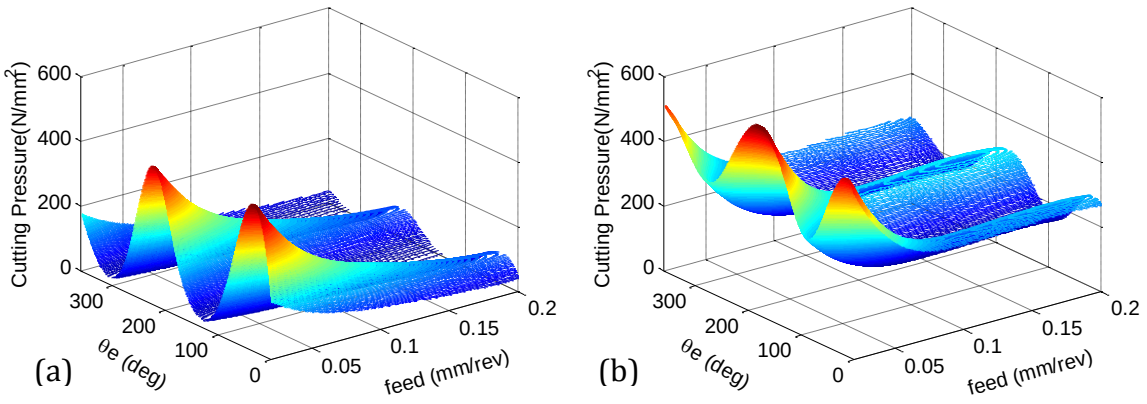

Figure 7-6 Axial cutting pressures of the (a) primary and (b) chisel cutting edges for all the feeds, and effective fiber orientation at a rotational speed of 6000 rpm.

Figure 7-7 (a) and (b) show the identified torque cutting pressures of the primary and chisel cutting edges for all the feeds, and effective fiber orientations at the same rotational speed of 6000 rpm. The figure shows the fluctuation of the cutting pressures as the fiber orientation varies from 0˚ to 360˚ according to the trend shown in Figure 7-5 (a) and (b). The maximum value of the cutting pressures is located at the angles 180˚ for the primary cutting edge and at angles 90˚ and 270˚ for the chisel. For

other cutting speeds n= 8000, 10000 and 12000 rpm, the same trends of cutting pressures were observed.

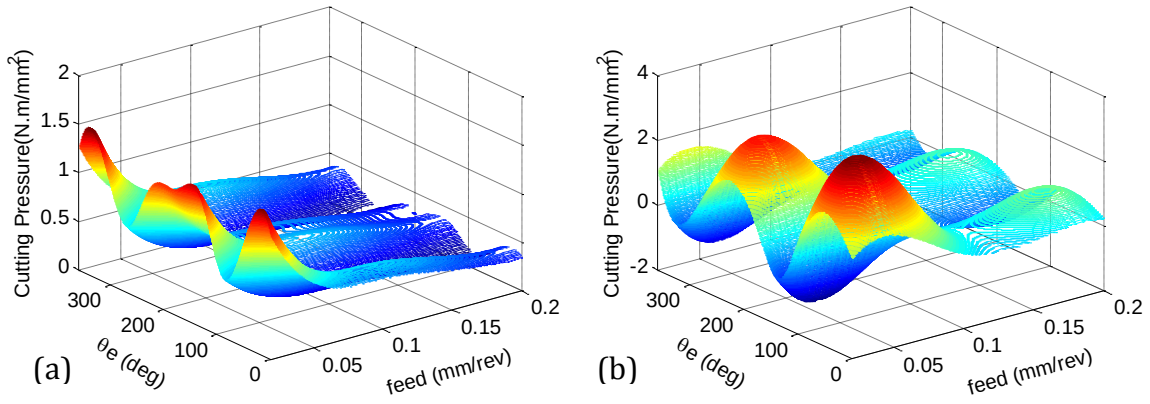

Figure 7-7 Torque cutting pressures of the (a) primary and (b) chisel cutting edges for all the feeds, and effective fiber orientation at a rotational speed of 6000 rpm.

7.2.3. Rake Angle Profile Identification

Figure 7-8 shows the profiles of the main angles of the primary cutting edge of the drilling tool measured using a profilometer. As discussed earlier the change of the rake angle along the cutting edge is the expected to have the most important effect on the predicted forces and torques. The figure shows that the rake angle starts at low value for a section "*i*" at a radius "r_i" from the tool center. The rake angle increases as the radius "r_i" increases towards the outer tool radius "*R*". The effect of the change of the rake angle on the cutting pressures was incorporated in the model as discussed in Chapter 6. As shown in section 6.5, the value of the rake angle and the effective fiber orientation at each section of the primary cutting edge were used to identify a correction factor that was applied to the obtained averaged cutting pressures. The rake angle varies from a value of 25° near the outer radius of the tool and decreases to a value of 1.8° near the chisel edge. The junction of the primary cutting edge with the chisel edge experiences a sharp drop of the rake angle until it reaches a negative constant value at the chisel edge. This region is not included in the plotted profile because it is very challenging to measure such a sharp variation using the profilometer. The change of the rake angle within the intersection between the

primary cutting edge and the chisel edge is assumed to be ideally sudden and the rake angle is assumed to drop suddenly from the minimum value of the primary cutting edge to the constant negative value of the chisel edge.

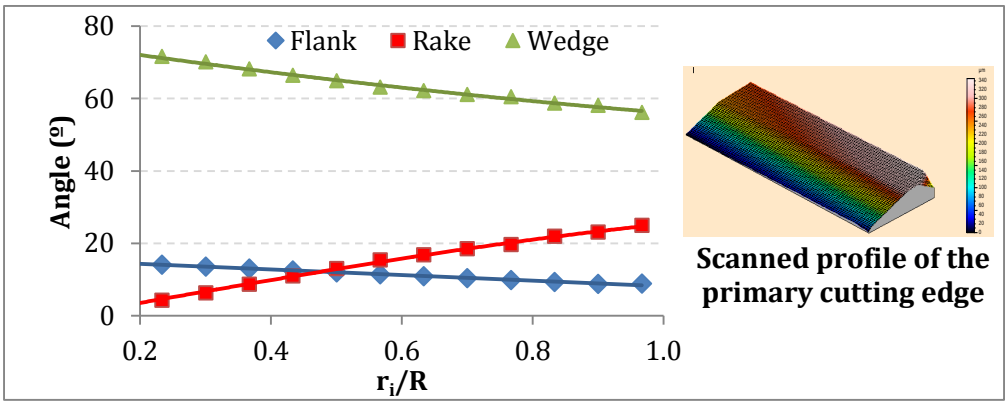

Figure 7-8 Measured profile of the flank, rake and wedge angles along the primary cutting edge

7.3. Experimental Validation of the Multidirectional CFRP Generalized Drilling Model

This section shows the results of using the previously identified cutting pressures in order to predict the forces and torques during conventional and vibration assisted drilling of a multidirectional CFRP laminate. In general, the validation points were selected within the same range of the process parameters used for model calibration. Some of the validation points were chosen to be between two or four calibration points in order to test the model capability of predicting forces and torques at any set of conditions within the specified range. The validation points for each of the conventional and vibration assisted drilling processes will be specified under each relevant section.

For presenting the results of the model predictions for each of the two processes, a representative drilling case was selected to illustrate the details of the predicted force and torque full signals compared to the experimentally measured signals. The accuracy of the model predictions for all the validation cases is shown by presenting the errors of the maximum forces and torques in the different stages of the drilling

operation compared to their corresponding experimentally measured forces and torques.

7.3.1. Conventional Drilling of Multidirectional Laminates

Table 7-2 shows the drilling conditions used for the validation of the model predictions in conventional drilling. In order to validate the model predictions within the range of the process parameters specified in Table 4-6, the same set of rotational speeds were used with 2 feeds that have been used for calibration (0.1 mm/rev and 0.2 mm/rev) and 2 new feeds (0.08 mm/rev and 0.18 mm/rev).

Table 7-2 Conventional drilling conditions used for model validation

Feed 'f_r' (mm/rev)	**Rotational speed 'n' (rpm)**		
	6,000	**8,000**	**10,000**
	Axial feed (mm/min)		
0.08	480	640	800
0.1	600	800	1000
0.18	1080	1440	1800
0.2	1200	1600	2000

Figure 7-9 (a) and (b) compares the predicted and measured force and torque for drilling of the multidirectional CFRP laminate specified in chapter 3, at a rotational speed of 10,000 rpm and a feed rate of 0.18 mm/rev. This case was selected as it represents one of the new feed points selected for validation in the middle of the range of the drilling conditions.

Figure 7-9 (a) and (b) shows the excellent matching between the predicted and the measured axial force and torque signals. The main four drilling stages, namely entrance transient, steady state, chisel edge breakthrough, and primary edges exit stages are identified on the axial force signal plotted in Figure 7-9 (a).

As shown in Figure 7-9 (a), the axial force starts with a relatively rapid increase at the beginning of the drilling operation due to the engagement and axial advancement of the chisel edge. As shown in Figure 6-3, the chisel edge is pressing rather than cutting the fibers as it advances in the axial direction.

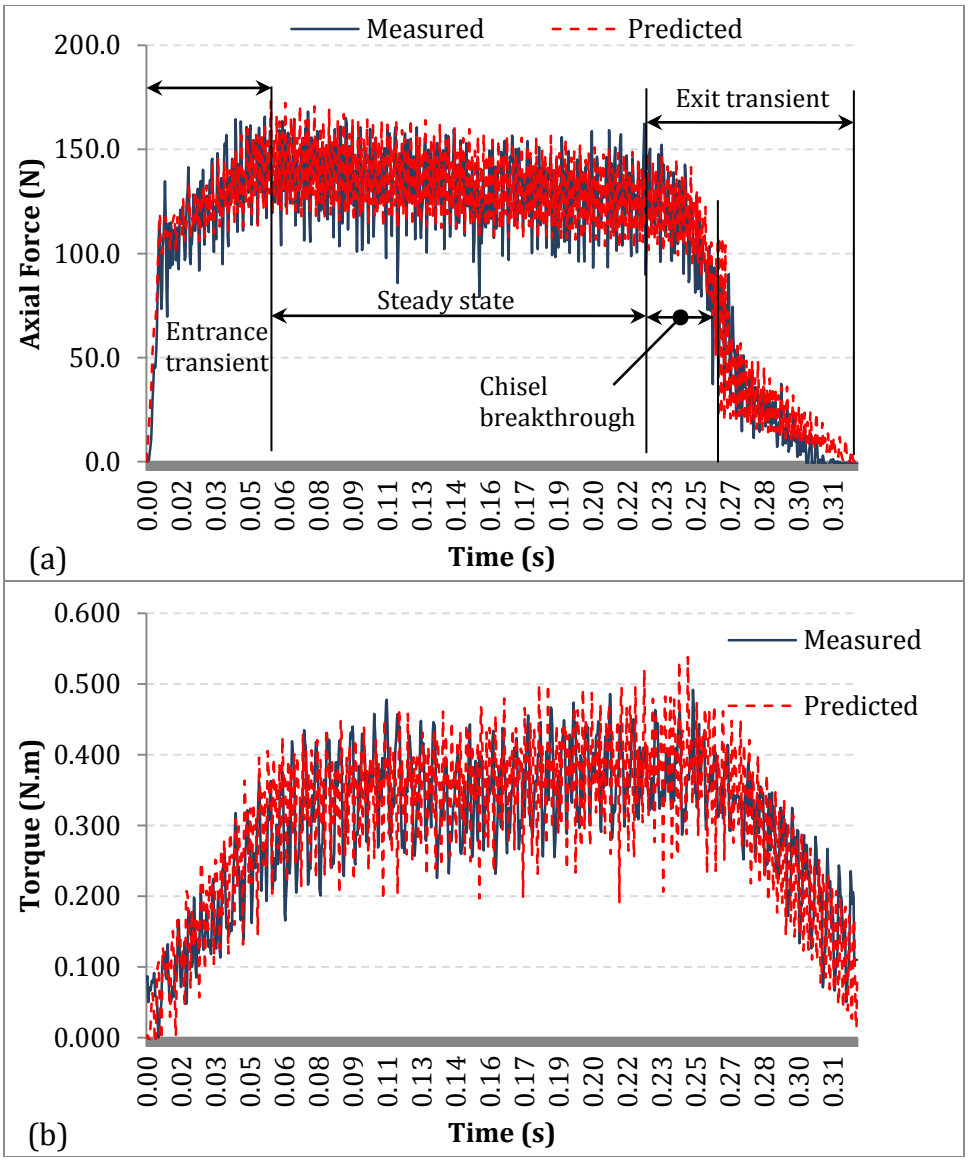

Figure 7-9 Predicted vs. measured signals of (a) axial force, and (b) torque during the full drilling operation drilling at (n=10,000 rpm, and f_r=0.18 mm/rev)

Therefore, the rapid increase in this stage does not show considerable axial force fluctuation. On the other hand, the torque fluctuations took place immediately at the beginning of the drilling operation, because the chisel edge always performs orthogonal cutting of fibers in the tangential direction. As the primary cutting edges engage, the slope of the axial force declines to follow the rate of the progressive engagement of the primary cutting edges. In addition, the force fluctuations start to build up because the cutting edges are forming chips of different fiber orientations as they rotate and advance in the axial direction. Similar build-up of fluctuations takes

place in the case of the drilling torque signal, but at much lower slope compared to that of the axial force. The steady state stage starts when the cutting lip of the tool is fully engaged with the material. Ideally, the slope of the axial force and torque should be unchanged. However, the axial force starts to decline due to the effect of material softening, while the torque keeps increasing due to the frictional torque increase with the increase of the lateral contact area between the advancing tool and the hole walls. Both effects were considered in the developed model as described in Chapter 6.

In the case of a perfectly rigid workpiece material and fixture, a sudden breakthrough of the chisel edge at the exit plane of the hole should take place. In the case of a CFRP laminate, the last layers experience some level of deflection, as shown in Figure 6-16, which causes a gradual chisel edge breakthrough. The considered effect of the material deflection was able to provide the model with the rectified relative positions between the cutting lip and the workpiece. After the chisel edge exits the hole, a significant drop in the axial force level takes place before it starts approaching zero as a result of the final exit of the primary cutting edges. The torque signal experiences a similar drop after the exit of the chisel edge. However, the torque value remains fluctuating and does not reach zero because of the remaining frictional torque on the lateral surface of the tool.

The error in the predicted drilling time can take place because of one or more of the following factors. The possible variation between the idealized estimated axial feed of the tool in the model, compared to the actual axial feed during the drilling process. The error in the calculated level of material deflection could be another factor, which affects the actual length of the axial cutting path. All the tested drilling conditions maintained an acceptable cutting time signal error within 12% compared to the experimentally measured drilling time.

Force and Torque Predictions in the Entrance Transient Stage

Figure 7-10 (a) and (b) demonstrates the predicted and measured signals of the axial force, and torque, respectively, during the entrance transient drilling stage of drilling. The figures show the capability of the model to accurately predict the

increase in the axial force and torque at a rate that highly matches the experimentally measured slope. The slopes of the signals at entrance for all the tested conditions showed a similar level of conformance with the measured signals. The frequency of the force fluctuation of the predicted axial force and torque signals also match very well the frequency of the corresponding measured fluctuations.

This level of matching of the features of the signals shows the validity of the adopted criteria of selecting the time increment of the model calculations to be corresponding to the sampling rate "Ω_s" used in all of the experimental drilling tests, as discussed in section 6.5. The performance of coarser time increments was tested and was found to result in undesirable sudden increases in the force and torque values in the entrance stage.

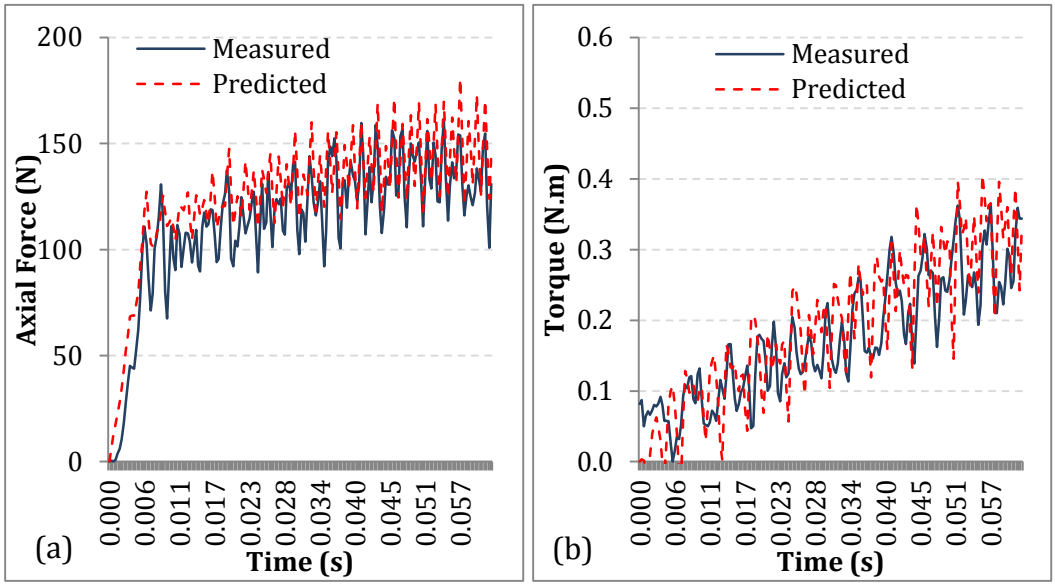

Figure 7-10 Predicted vs. measured signals of (a) axial force, and (b) torque during the entrance transient drilling stage of drilling at (n=10,000 rpm, and f_t=0.18 mm/rev)

The values of the maximum errors of the predicted axial forces, and torques in the entrance transient stage for all the validation conditions are shown in Figure 7-11 (a) and (b), respectively. For the tested cases shown in Figure 7-11(a), the axial forces prediction errors in the entrance stage were within the range of ±10 %.

Figure 7-11 (b) shows a wider range of -8% to +19 % for the torque prediction errors in the entrance transient stage. Within this error range, the predicted torque

values are shown to be higher than the measured values in most of the tested cases. This could be due to the over prediction of the frictional torque at the entrance, which takes place mainly due to the contact between the tool flank face and the adjacent machined surface, while the frictional torque prediction module was calibrated according to the contact between the lateral surface of the tool and the hole walls. No comparison is provided with other models' predictions since these models are not capable of capturing the transient force and torque behavior.

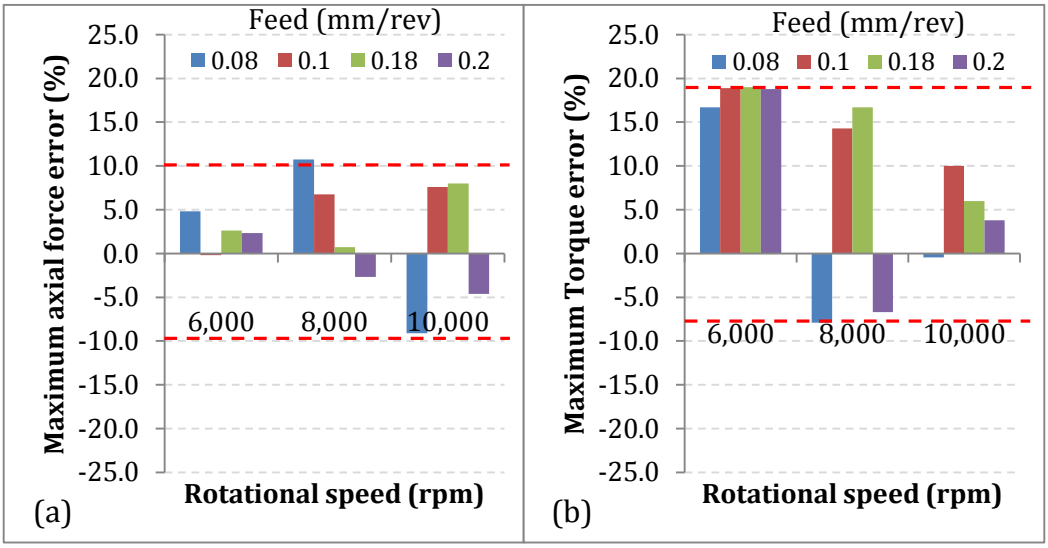

Figure 7-11 Maximum errors of the predicted (a) axial force, and (b) torque in the entrance transient stage for different validation conditions

Force and Torque Predictions in the Steady State Stage

Figure 7-12 (a) and (b) demonstrates the predicted and measured axial force and torque, respectively, during the steady state of the drilling operation. The figure shows that the predicted axial force and the torque are matching the features and magnitudes of the corresponding measured signals to a great extent. The form of the predicted force signal of all the tested cases could capture the exact frequency of the measured force fluctuations due to the varying fiber orientations.

The predicted torque captured the maximum and minimum magnitudes as well as the frequency content of the torque fluctuations associated with the changing fiber orientations during the tool rotation. However, some differences between the

predicted and measured torques can be observed at some locations in Figure 7-12 (b). This could be due to the high variability between the random and systematic patterns of the actual and the predicted frictional torques, respectively.

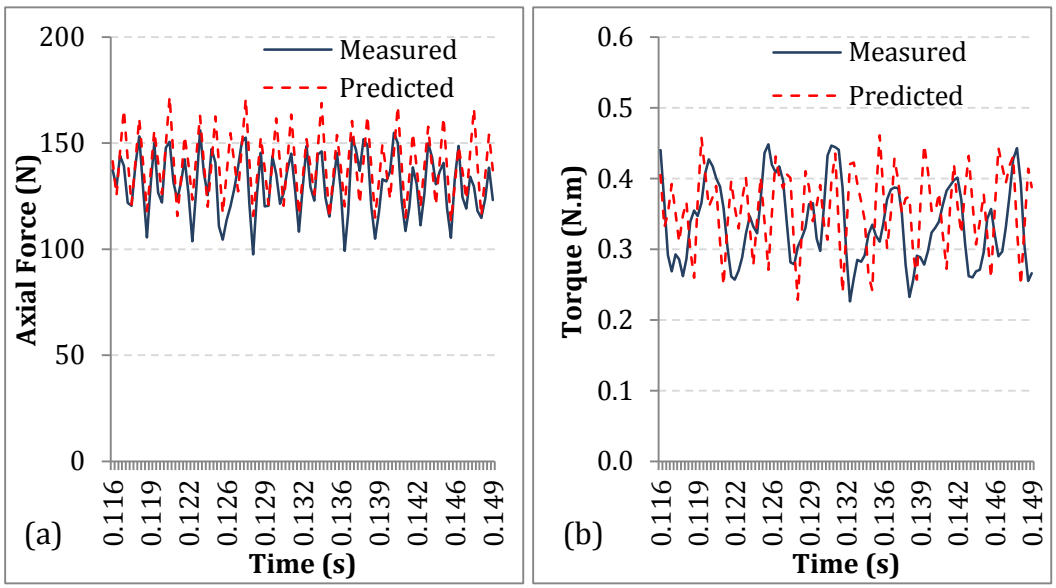

Figure 7-12 Predicted vs. measured signals of (a) axial force, and (b) torque during the steady state drilling stage of drilling at (n=10,000 rpm, and f_r=0.18 mm/rev)

Figure 7-13 (a) and (b) shows the maximum axial force, and torque prediction errors, respectively. The figure shows that for the steady state stage, the force prediction errors were between +4% and +13%, while the torque prediction errors ranged between -12% and +18%. The positive errors in Figure 7-13 (a) could be due to multiplying the averaged cutting pressures on each of the cutting edge sections are by the vector of the rake angle effect along the length of the primary cutting edge as shown in section 6.5. The higher value of correction factors near the chisel edge can result in a higher, yet within allowable error range, predicted total axial force compared to the measured axial force in the steady state stage.

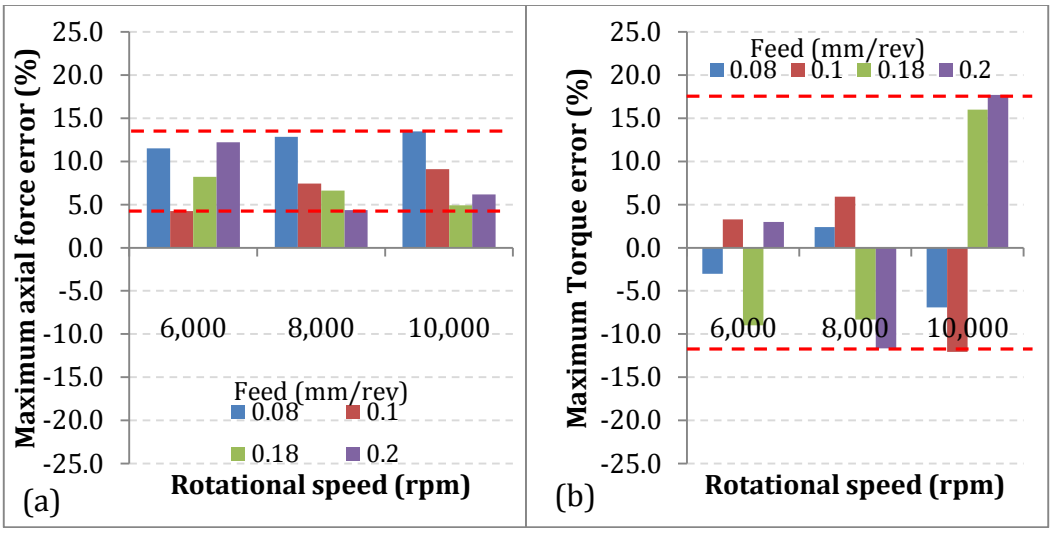

Figure 7-13 Maximum errors for different validation conditions of the predicted (a) axial force, and (b) torque during the steady state stage

Force and Torque Predictions in the Chisel Edge Breakthrough Stage

In the case of drilling of FRP laminates, the last layers experience some level of deflection, which causes a gradual chisel edge breakthrough and alters the value of the uncut chip thickness due to the displacement of the material layers. Figure 7-14 depicts the matching of the predicted variation, form and features of the force and torque to those of the reference measured signals. The effect of material deflection in this stage on 'd' and the consequent force and torque prediction grows to be more significant than in the previous stages. This is due to the relatively small remaining material thickness and the high axial forces near the hole exit plane. This effect can be clearly seen in portion "A" of the force signal shown in Figure 7-14 (a). In this portion, the model predicts material deflection values that cause a significant drop in 'd' and consequently a reduction in the force. This in turn reduces the level of deflection in the following time step. The predicted low deflection increases 'd' again to its original value, which increases the force again. This cyclic behavior results in a different force fluctuation form within the portion "A" of the breakthrough stage, which ends by the full exit of the chisel edge. The aforementioned behavior is not significant in the case of torque prediction because the total predicted torque in this stage is composed mainly by the frictional torque component, which does not depend on the uncut chip thickness variations.

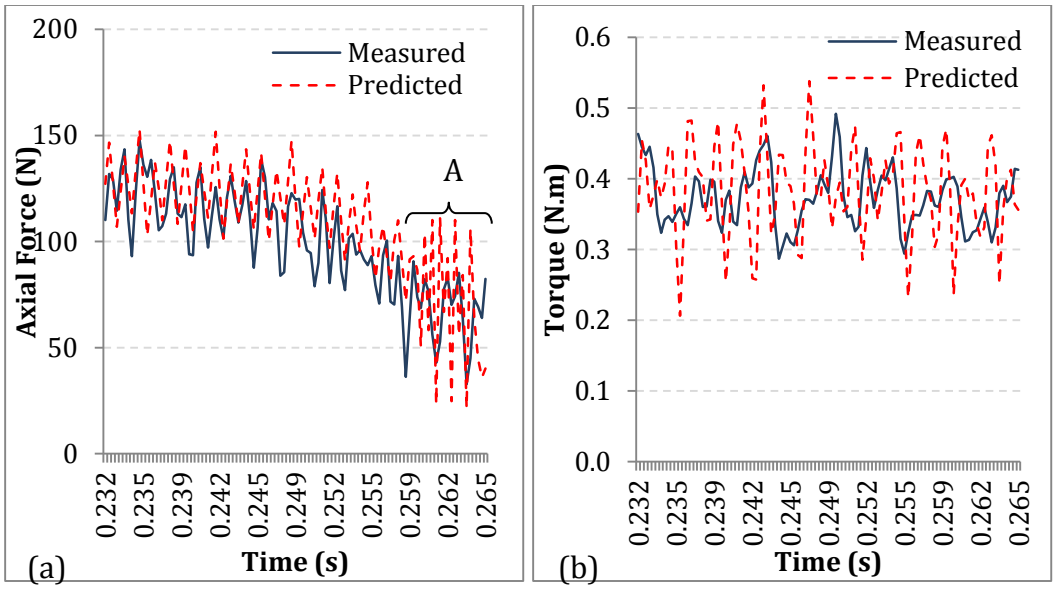

Figure 7-14 Predicted vs. measured signals of (a) axial force, and (b) torque during the chisel edge breakthrough stage of drilling at (n=10,000 rpm, and f_r=0.18 mm/rev)

Figure 7-15 (a) and (b) shows prediction error ranges of +4% to +17% and -18% to +14% for the maximum axial force and torque, respectively, for the chisel breakthrough stage. Accurate force prediction in this drilling stage is essential for further prediction of the possible subsequent exit delamination caused by the axial forces. The obtained level of prediction accuracy for the force features in this critical stage of drilling of FRPs was not achieved before by any of the models reported in the open literature.

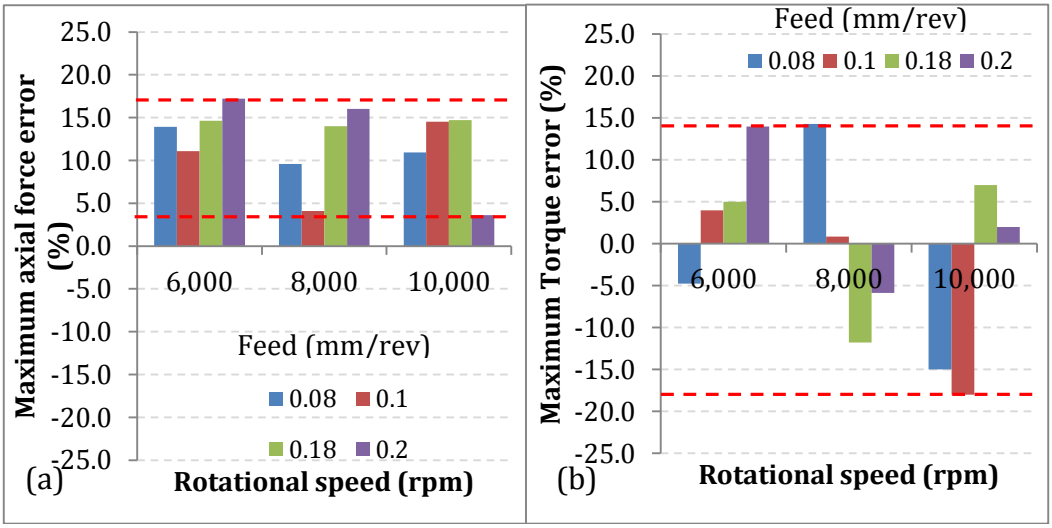

Figure 7-15 Maximum errors for different validation conditions of the predicted (a) axial force, and (b) torque during the chisel edge breakthrough stage of drilling

Force and Torque Predictions in the Primary Edges Exit Stage

Figure 7-16 (a) and (b) shows the gradual decrease of the axial force and torque during the exit of the primary cutting edges after the exit of the chisel edge. The axial force reaches a value of zero while the torque value remains fluctuating and does not reach zero because of the remaining frictional torque on the lateral surface of the tool in contact with the drilled hole. The figure shows that the frequency of the predicted force and torque fluctuations are reasonably matching that of the measured signals. The maximum values of the torque predictions for all of the tested cases showed very good match with the experimental results. However, a mismatch was observed in most of the tested cases between the values at the middle of the cycle denoted as " T " and " T' " on the measured and predicted signals, respectively. This is due to the phase difference that can take place in some cases between the predicted and measured frictional torque fluctuations.

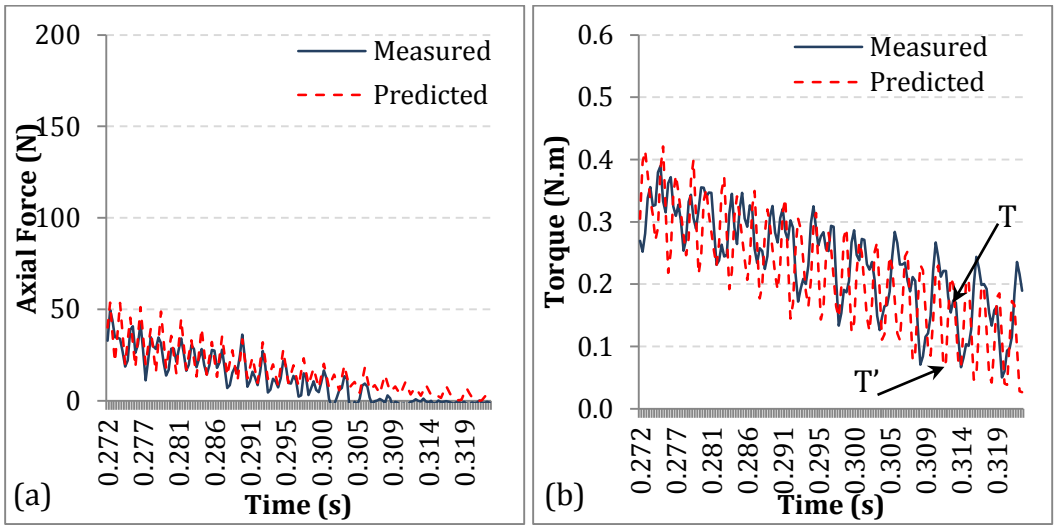

Figure 7-16 Predicted vs. measured signals of (a) axial force, and (b) torque during the primary edges exit stage of drilling at (n=10,000 rpm, and f_r=0.18 mm/rev)

For all the tested conditions, the maximum force and torque prediction errors in the exit transient stage are shown in Figure 7-17 (a) and (b), respectively. The figure shows error ranges of -13% to +22% for the maximum axial forces and -20% to +22% for the maximum torque.

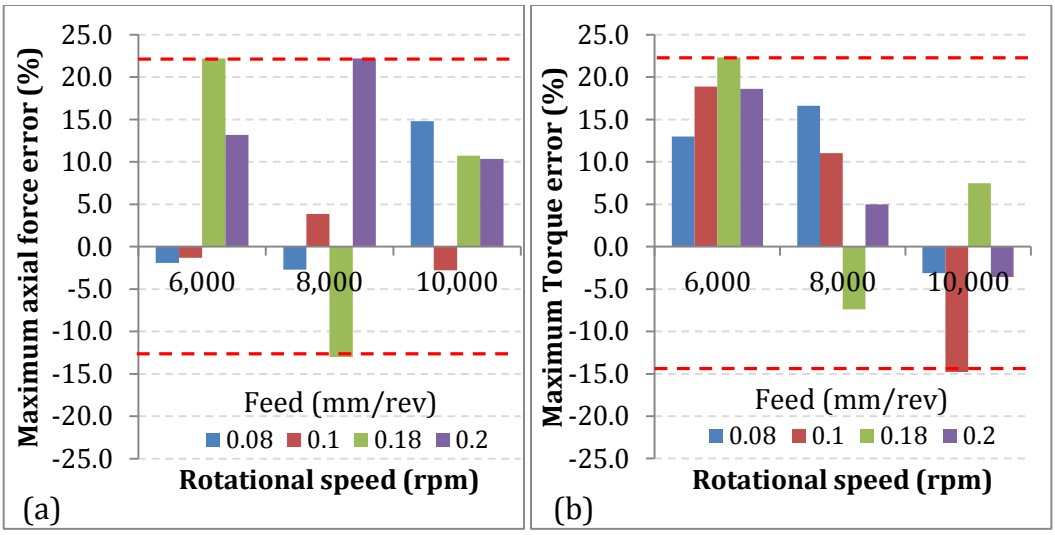

Figure 7-17 Maximum errors for different validation conditions of the predicted (a) axial force, and (b) torque during the primary edges exit stage of drilling

7.3.2. Vibration Assisted Drilling of Multidirectional Laminates

Figure 7-18 (a) and (b) demonstrates the predicted and measured signals of the axial force, and torque, respectively, for the vibration assisted drilling of the multidirectional laminate. The figures show the capability of the model to predict the actual form of the force and torque signals through the VAD operation. The gradual increase in the maximum force and torque takes place over a larger time span compared to the conventional drilling. This is due to the displacement of the shaker head under the action of the axial force. This system dependent motion was taken into account in the prediction model, as described in Chapter 6.

A detailed view of the force and torque features in the entrance, steady state and exit stages of VAD are shown in Figure 7-19 (a) to (f). The figure shows the match between the predicted and measured force and torque features. The model was able to accurately capture the frequency content and the magnitude of the major force and torque variations due to dynamic uncut chip thickness. It was also able to accurately predict the secondary variations due to the dynamic change of the angle between the cutting edge and the fiber as the tool rotates during the duty cycle. For the force and torque in the transient stages, a very good match can be seen between the predicted and measured rate of increase in the entry and decrease in the exit.

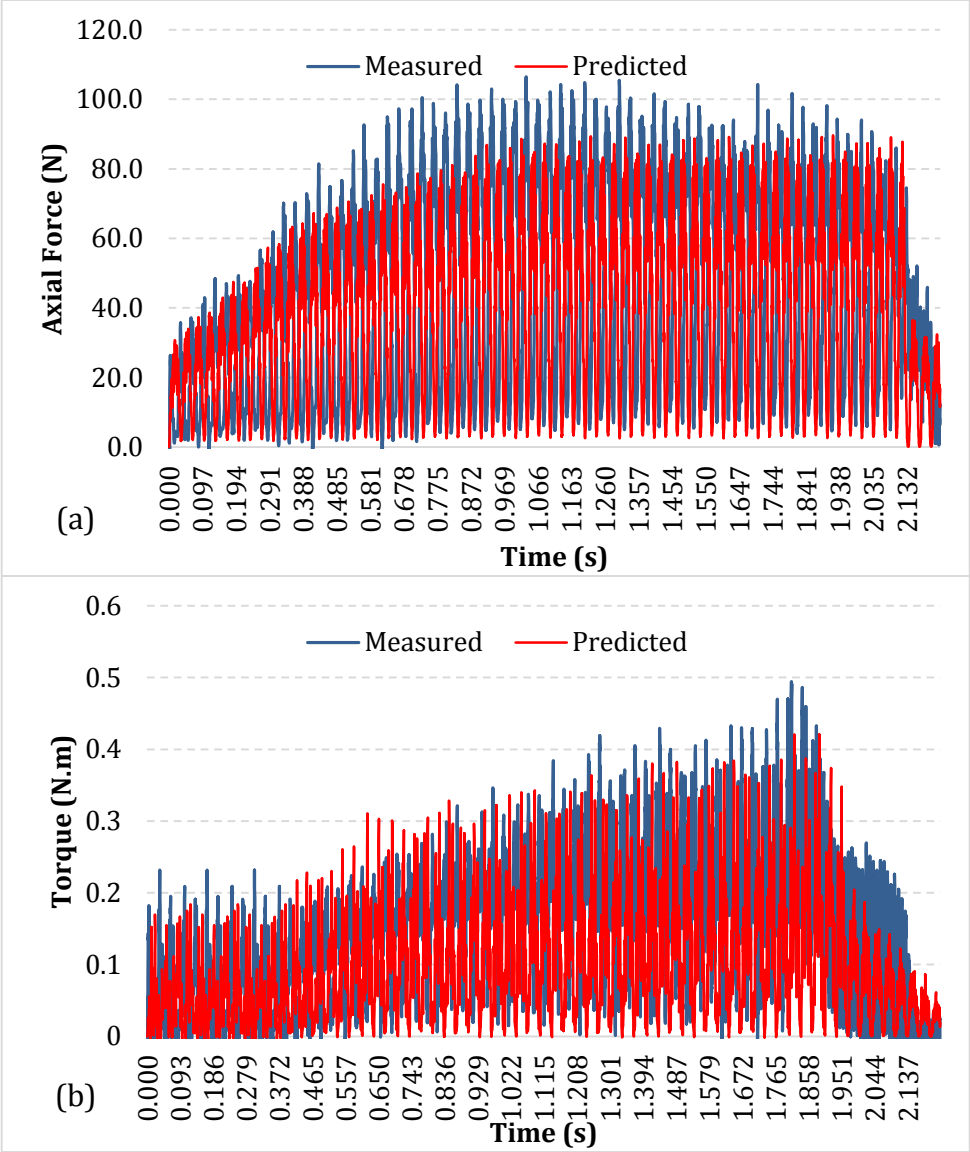

Figure 7-18 Predicted vs. measured signals of (a) axial force, and (b) torque during the full VAD operation at (n=6,000 rpm, and f_r=0.05 mm/rev, ω_m=30Hz, and A_m = 0.09 mm)

Figure 7-19 (d) shows slight torque fluctuations during the separation cycle where the torque value is almost zero, this is due to the frictional torque between the lateral surface of the tool and the walls of the hole. Figure 7-19 (f) shows a different frequency content for the measured torque at the end of the drilling process that could be due to the dominant frictional torque component compared to the small cutting torque at the final layers of the laminate. On the other hand, the predicted torque maintained the ideal vibrational motion till the location of the laminate thickness was detected.

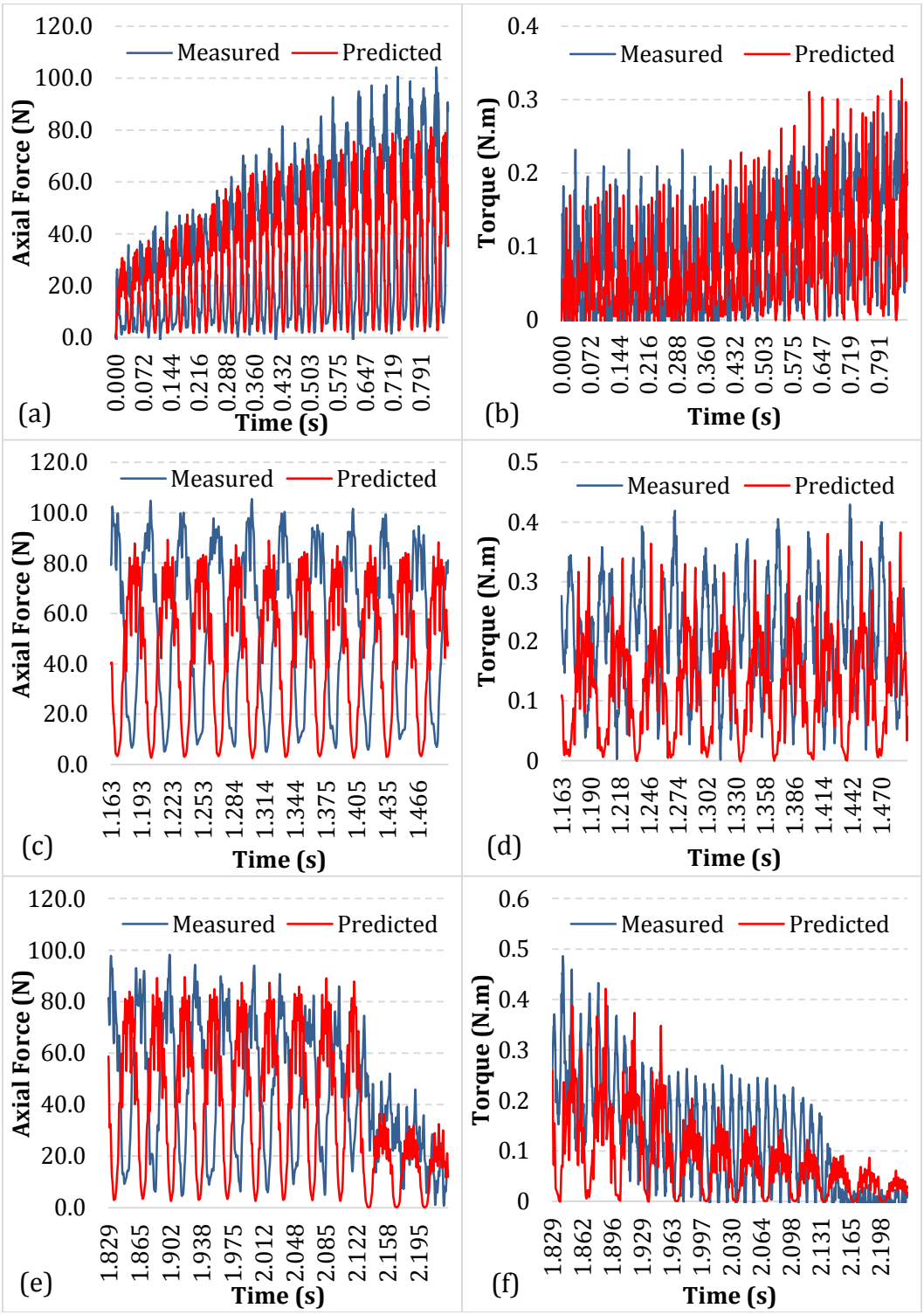

Figure 7-19 Predicted vs. measured signals of (a) entrance, (c) steady state, and (e) exit axial force and (b) entrance, (d) steady state and (f) exit torque of the VAD operation at (n=6,000 rpm, and f_r=0.05 mm/rev, ω_m=30Hz, and A_m = 0.09 mm)

The performance of the generalized model for predicting VAD axial forces and torques has been validated against a wide range of the workable VAD parameters as determined by the experimental characterization of the VAD process in Chapter 4. The validation tests comprised 2 speeds, 2 feeds, and 2 frequencies, and 4 amplitudes, as shown in Table 7-3.

Table 7-3 VAD conditions used for model validation

Feed 'f_r' (mm/rev)	0.05		0.075	
Frequency (Hz)	30	60	30	60
Rotational speed 'n' (rpm)	**Amplitude (mm)**			
6000	0.09		0.135	
9000	0.135		0.2	

The maximum VAD axial forces prediction errors in the steady state and transient (entry and exit) stages are shown in Figure 7-20 (a) and (b) for the VAD conditions listed in Table 7-3 for model validation. The figure shows that the maximum axial force prediction errors were within -22% to +23%. The errors shown in Figure 7-20 did not follow a clear trend with respect to the tested VAD conditions.

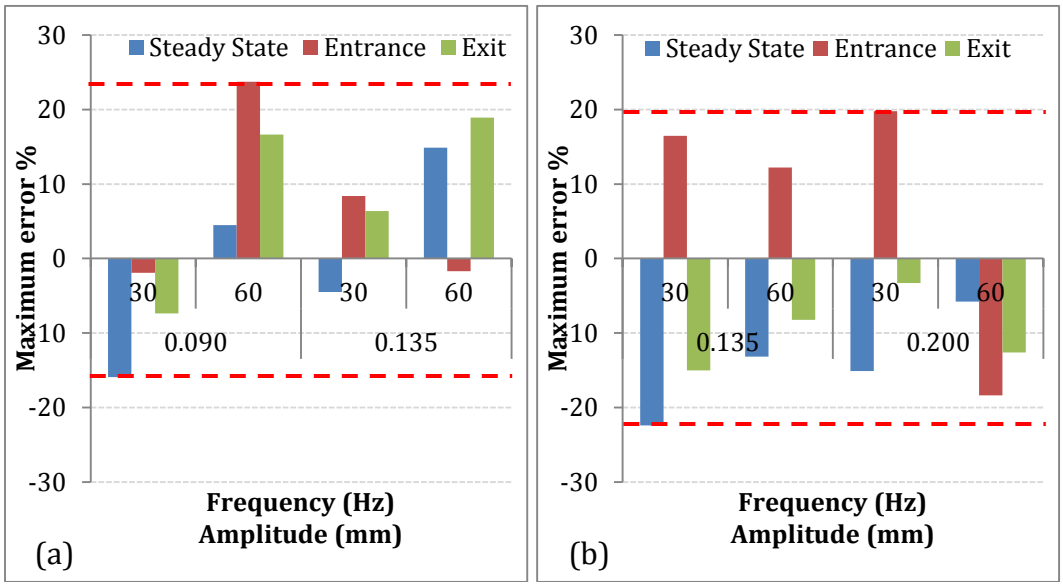

Figure 7-20 Effect of the VAD amplitude and frequency on the maximum predicted axial force errors for VAD at feed (a) 6,000 rpm and (b) 9,000 rpm

The maximum torque prediction errors in the steady state and the transient stages of all the tested conditions shown in Figure 7-21 (a) and (b) were within -26% to +23%.

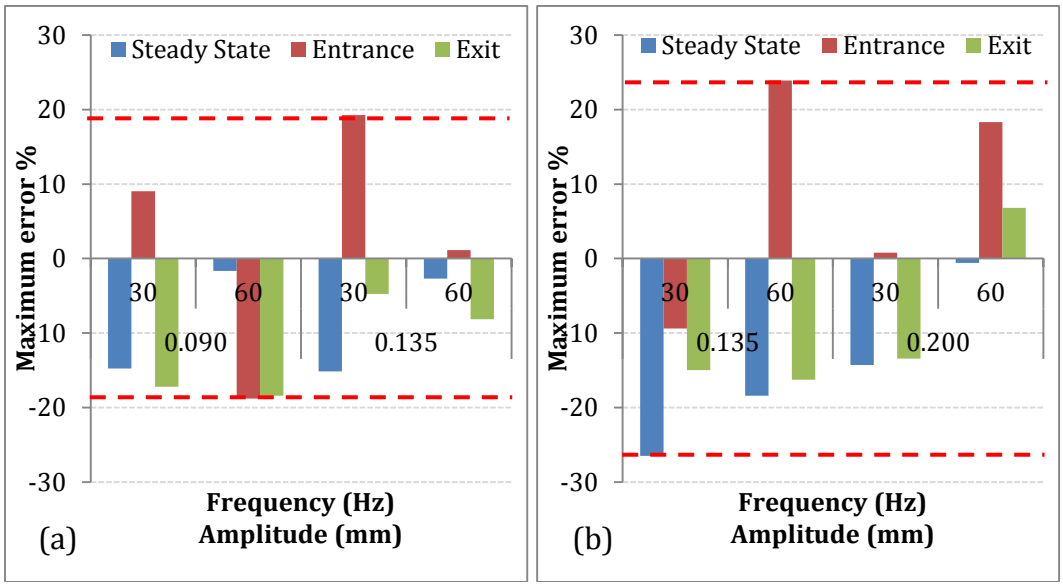

Figure 7-21 Effect of the VAD amplitude and frequency on the maximum predicted torque errors for VAD at feed (a) 6,000 rpm and (b) 9,000 rpm

Through the previous sections, the model predictions for the forces and torques features have been compared to experimentally measured signals that covered the wide ranges of the conventional and the vibration assisted drilling process parameters. Statistical analysis of the prediction error of the generalized model for conventional drilling was shown to be in the range of -5% to +16% for forces and -10% to +20% for torques, with a confidence interval of 95%. For VAD, the error in the generalized model prediction of forces and torques is within ±20 %, with a confidence interval of 95%.

7.4. Predictions of the Effect of the Process Parameters using the Generalized CFRP Drilling Model

This section presents the results of the analysis performed using the validated model to show trends and features of the process that are either infeasible or impossible to be experimentally studied or measured. This analysis can replace the experimental analysis in determining the drilling forces and torques at numerous

levels of the different process parameters for the conventional and vibration assisted drilling processes ('n', 'f_r', 'A_m' and 'ω_m'), which is infeasible to perform experimentally. It also can be performed on a deeper level of exposing intricate features of the predicted force and torque signals, e.g., the force distribution along the cutting edges. This kind of analysis demonstrates the ability of using the model predictions for further future analysis on tool wear prediction, material damage prediction, and thermal analysis of the drilling process.

7.4.1. Predicting the Effect of the Conventional Drilling Parameters on the Drilling Force and Torque.

Effect of the Laminate Deflection on the Force and Torque Predictions

Figure 7-22 shows the variation of the ideal uncut chip thickness, material layers deflection, and the resultant 'd' with time at the chisel edge breakthrough stage of drilling. As described in Chapter 6, the modified 'd' is obtained by subtracting the instantaneous deflection from the ideal 'd' at each instant of time. The figure shows the change in the deflection as the axial force increases and the thickness of the remaining material decreases near the end of the hole. The cyclic behavior within portion "A" explains the behavior observed in the predicted axial force in this drilling stage (Figure 7-14 (a)). In this portion, the predicted material deflection values cause a reduction in the modified 'd', leading to the force reduction at this instant of time. Accordingly, the level of deflection is reduced in the following time step as can be seen in Figure 7-22. The predicted low deflection increases 'd' again to its original value, which increases the force again. This closed loop of the cyclic effects of the force and the displacement leads to the nonlinear behavior of the force fluctuation form within the portion "A" of the signal, which ends by the full exit of the chisel edge.

Figure 7-23 depicts the difference between the predicted axial force with and without the effect of deflection. The predicted force without the effect of material deflection remained at the same level of the steady state force and experienced a rapid drop afterwards as a result of the sudden breakthrough of the chisel edge. As shown in Figure 7-23, when the effect of deflection is considered in the model, a better prediction of the force trend was achieved during the chisel edge exit. The force

predicted without the effect of the laminate deflection was higher, which can lead to a conservative assessment of the performance of the simulated process parameters. By including the effect of the laminate deflection on the predicted forces, a reasonable assessment of the impact of the process parameters can be performed within the known acceptable prediction error. This leads to a more realistic prediction of the consequent damage in that critical stage of the drilling operation.

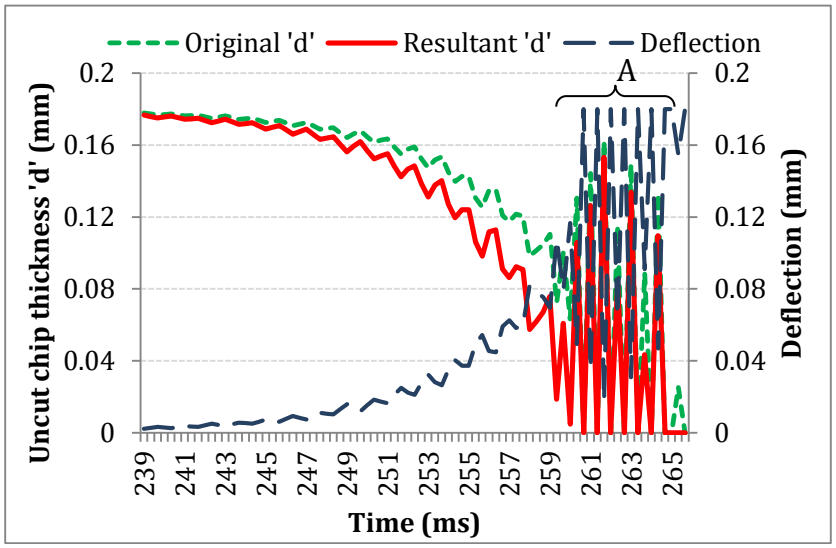

Figure 7-22 The variation of the original 'd', material layers deflection, and the resultant 'd' with time at the chisel edge breakthrough stage of drilling at (n=10,000 rpm, and f_r=0.18 mm/rev)

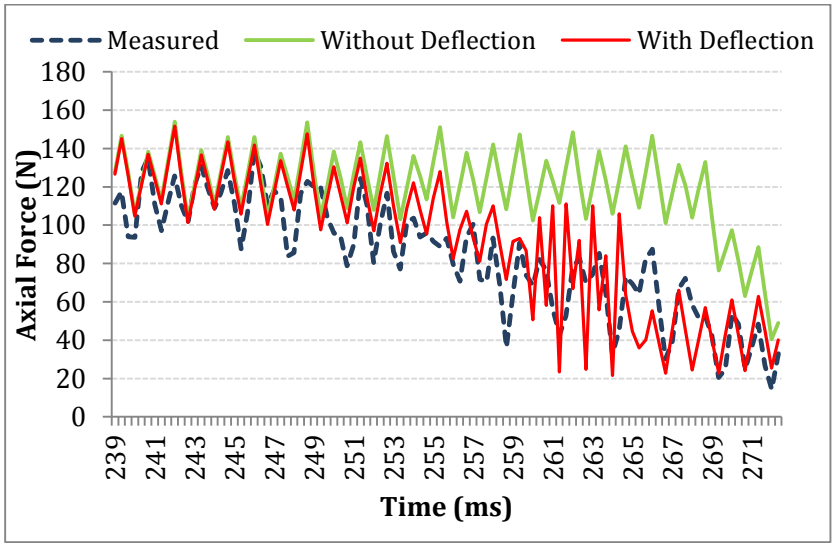

Figure 7-23 Comparison of the enabled and disabled effect of the material deflection on the predicted axial force signal at the chisel edge breakthrough stage of drilling at (n=10,000 rpm, and f_r=0.18 mm/rev)

Effect of the Rake Angle Variation along the Primary Cutting Edges

Figure 7-24 (a) to (d) shows the difference between the predicted axial force signals with and without the effect of the rake angle variation along the primary cutting edge in the drilling operation stages. Figure 7-24 (a), (b) and (c) shows that considering the effect of the rake angle variation can lead to an over-prediction of the maximum force value, especially in the entrance transient stage where the cutting pressures are multiplied by high correction factors corresponding to the low rake angle. During the steady state stage, the primary edges are fully engaged with the workpiece and the correction factors assigned to the sections of the cutting edge are high because of the

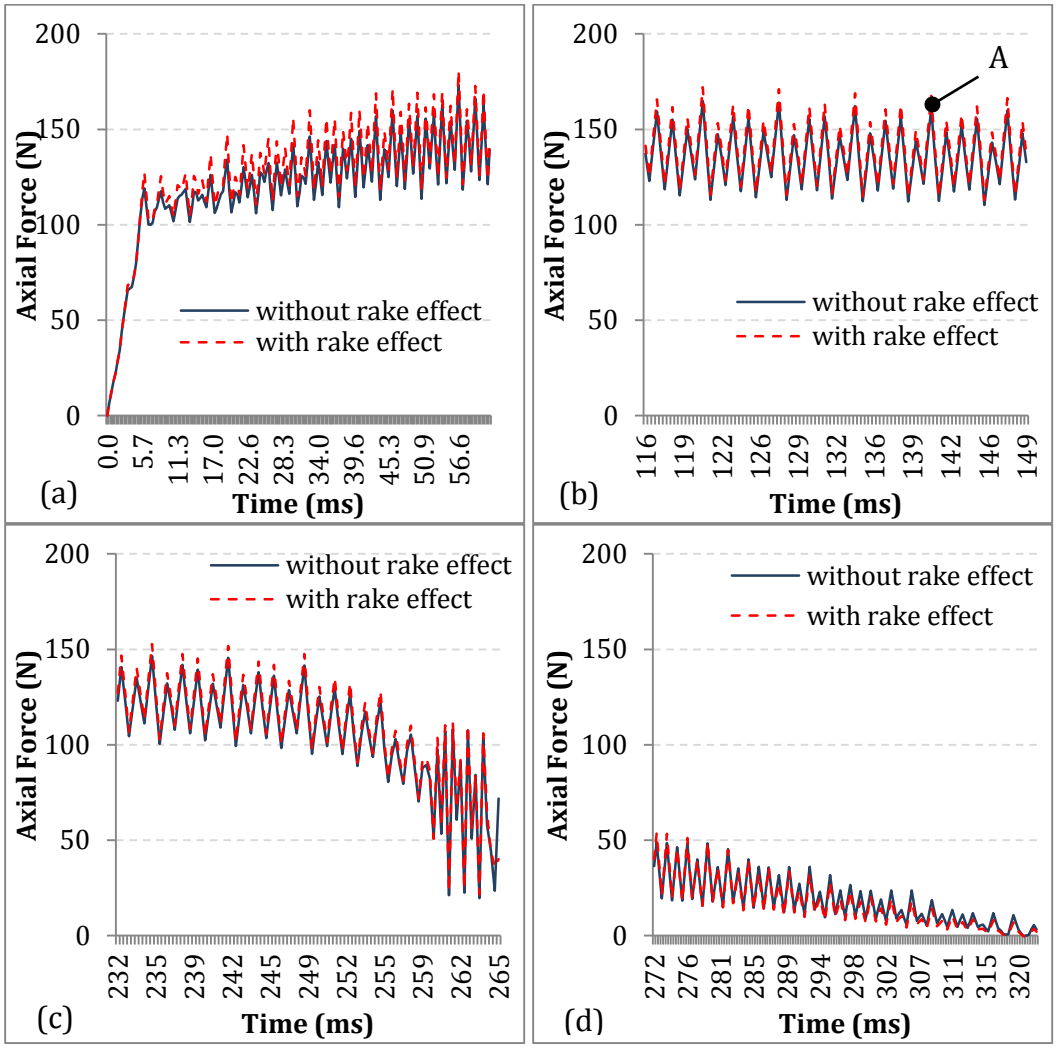

Figure 7-24 Comparison of the enabled and disabled effect of the rake angle variation along the primary cutting edge on the predicted axial force in (a) entrance transient, (b) steady state, (c) chisel edge breakthrough, and (d) primary edges exit stages

very small rake angle near the chisel edge. This in turn leads to an increase in the total axial force on the primary cutting edge compared to the case where the effect of rake is not included. This behavior explains the positive axial force errors (i.e. over predicted force) that were observed for most of the tested cases, although they were all within the allowable range of errors. On the other hand, Figure 7-24 (d) shows that including the effect of the rake angle led to a slightly lower predicted axial force. Figure 7-24 shows also that including the effect of the rake angle variation in the prediction model has a marginal impact, and using the averaged primary edge cutting pressures is a valid assumption.

Figure 7-25 shows the profiles of the effective fiber orientation angles 'θ_e', rake factors 'C_r', predicted axial forces, and lengths of the primary cutting edge sections at point (A) marked in Figure 7-24. Although the primary cutting edge has a single angular position at point (A), the profile shown in Figure 7-25 (a) depicts the variations of the effective fiber orientation angles 'θ_e' at each of the primary cutting edge sections because it is engaged with different layers of fiber orientations $\theta\epsilon\{0,90\}$.

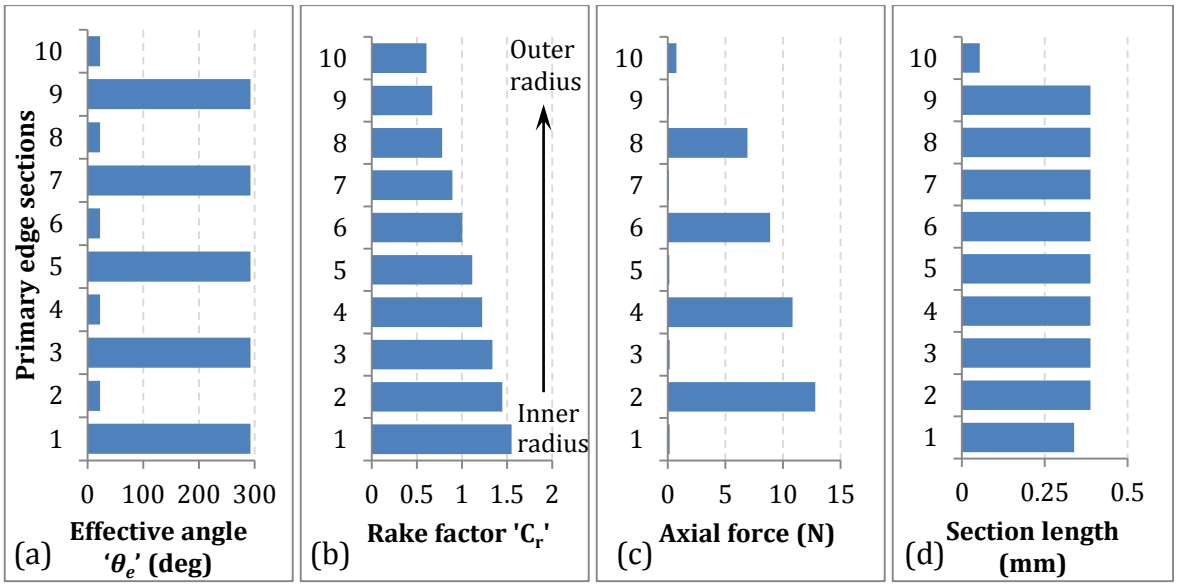

Figure 7-25 Detailed distribution of (a) effective angles, (b) rake factor, (c) axial forces, and (d) lengths of the primary cutting edge sections at point (A) . Conventional drilling at (n=10,000 rpm, and f_r=0.18 mm/rev)

The variation of the rake angle along the sections of the primary cutting edge produced the profile shown in Figure 7-25 (b) for the rake correction factor

0.6<C_r<1.55. This corresponds to the high rake angle near the outer tool radius and the very low rake angle near the chisel edge as shown in Figure 7-8. The force increases towards the chisel edge because of the effect of the low rake angle . The low force value at section 10 is due to the small section length determined from the position of the cutting edge relative to the material layer interfaces.

Effect of the Cutting Speed Variation along the Primary Cutting Edges

Figure 7-26 (a) to (d) shows the difference between the predicted torque with and without the effect of the cutting speed variation along the primary cutting edge. The figure shows that neglecting this effect results in over-predicted torque.

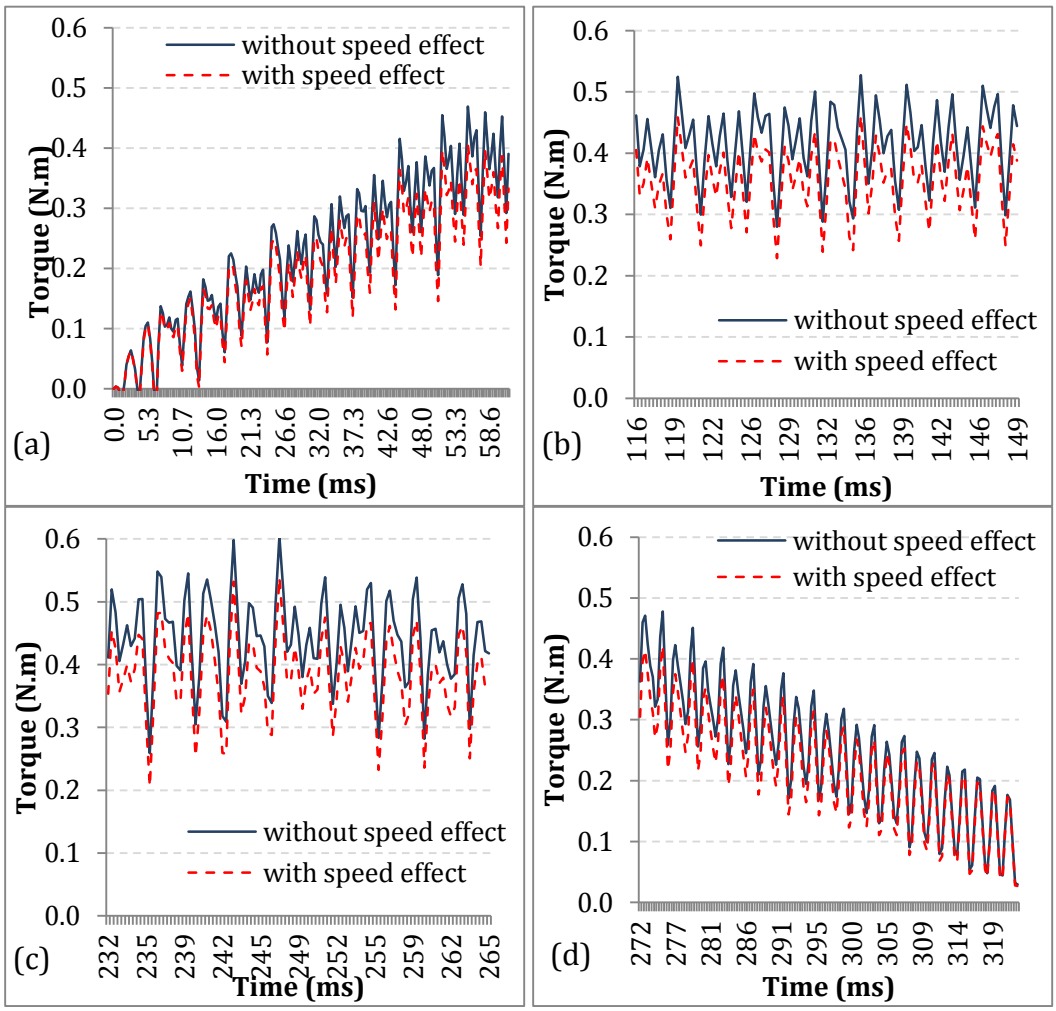

Figure 7-26 Effect of the cutting speed variation along the primary cutting edge on the predicted drilling torque in the (a) entrance transient, (b) steady state, (c) chisel edge breakthrough, and (d) primary edges exit transient

Effect of Conventional Drilling Speed and Feed

Figure 7-27 (a) and (b) shows the model predictions for the axial force and the cutting torque at different rotational speeds and feeds. This analysis is carried out for a wide range of process parameters including feeds and speeds that are different from the ones used for the calibration or the validation of the model. As shown in Figure 7-27 (a), the maximum predicted axial force is significantly dependent on the feed and is to a lower extent indirectly proportional to the rotational speed. Figure 7-27 (b) shows an increase in the predicted maximum torque with the increase in feed, due to the increase in 'd'. The predicted torque increases with the rotational speed up to 9000 rpm. However, this trend is reversed for higher rotational speeds. This is due to the effect of the frictional torque that decreases as shown in Figure 5-13 with the speed.

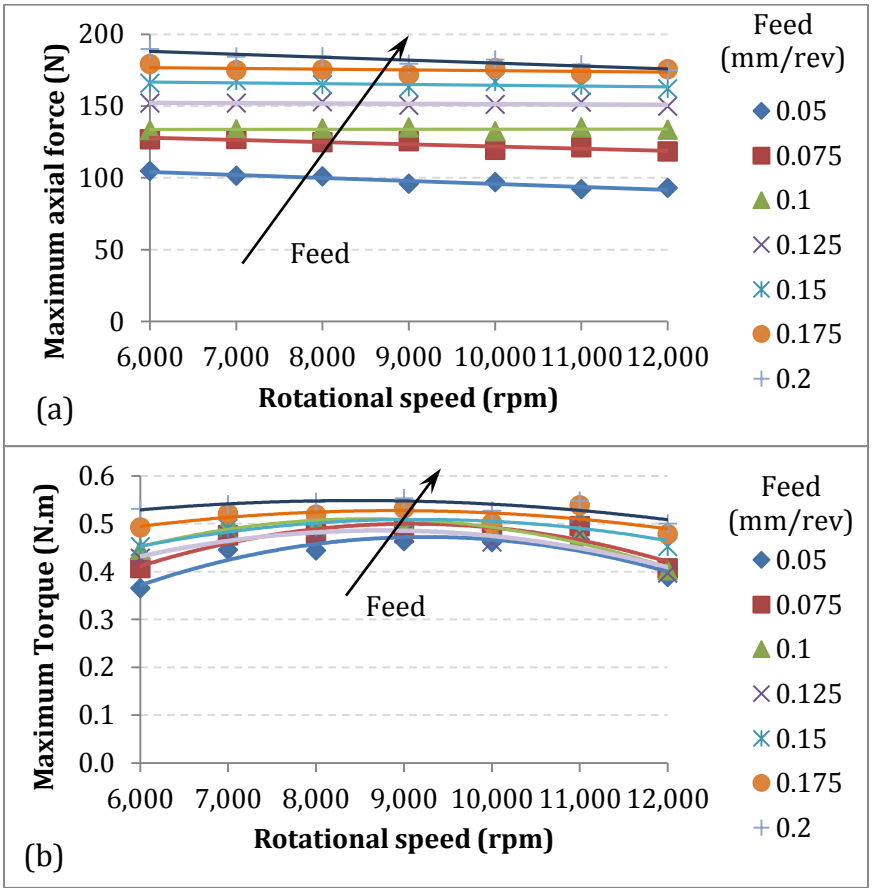

Figure 7-27 Effect of conventional drilling parameters on the predicted maximum (a) axial force, and (b) torque

7.4.2. Model Predictions of the Effect of the VAD Parameters

Figure 7-28 shows the effect of the modulation amplitude at different feeds and speeds on the predicted maximum axial force and torque of VAD at ω_m=90 Hz. The figure shows that the predicted force and torque increase with the amplitude and the feed, due to the increase of the uncut chip thickness at the maximum engagement positions. The predicted axial force was found to decrease with the increase in the rotational speed. The predicted trends strongly agree with the trends shown for the experimental analysis in chapter 5. Figure 7-29 shows the effect of the modulation frequency on the predicted maximum torque obtained in VAD at the rotational speeds n=6000 rpm, and n=12000 rpm, for feeds of f_r= 0.05 mm/rev and f_r= 0.1 mm/rev. The figure shows a clear direct correlation between the predicted force and the amplitude, feed and frequency. The figure shows a trend similar to that of the axial force, which also agrees with the experimental findings of the experimental analysis shown in chapter 5.

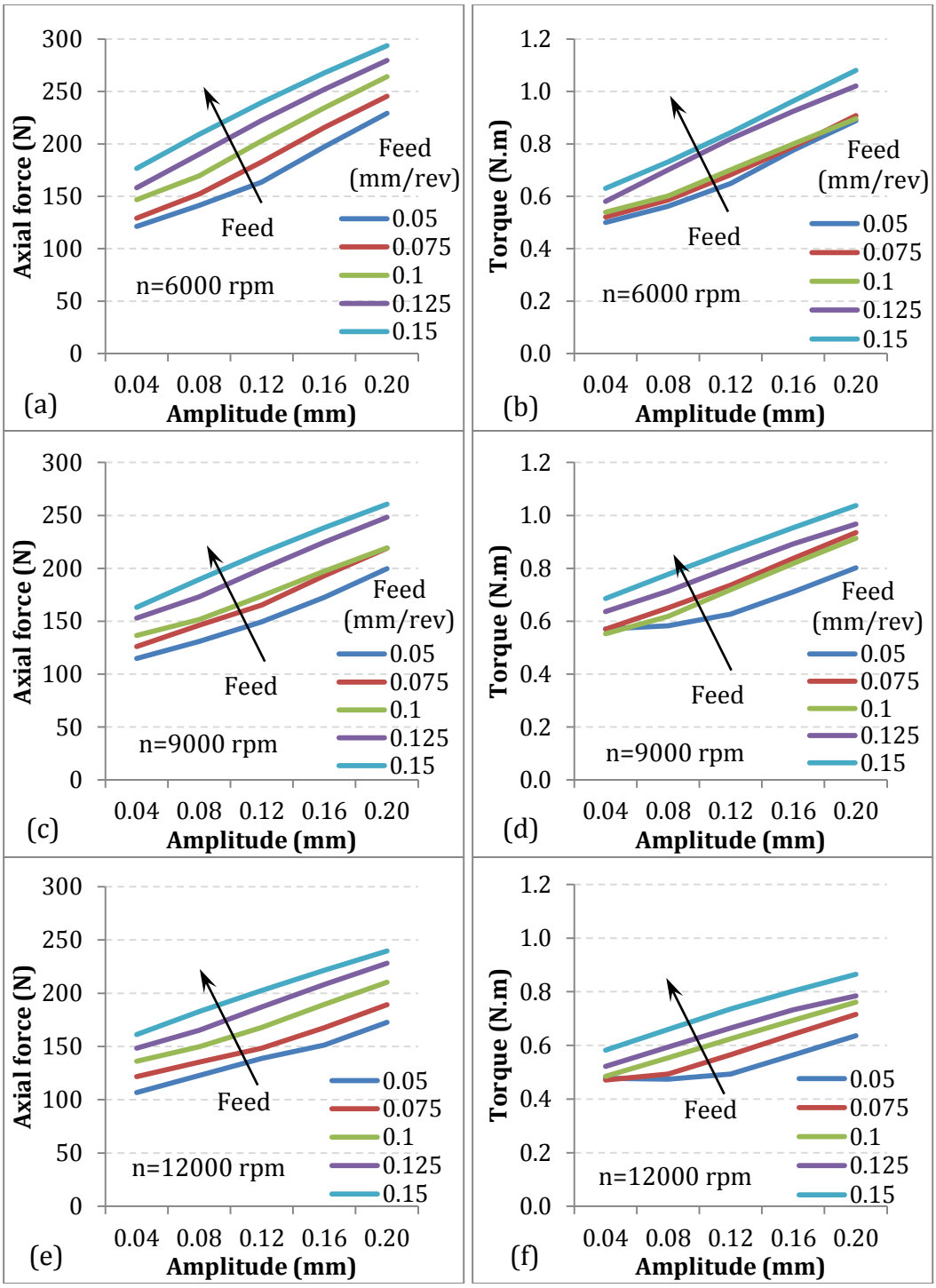

Figure 7-28 Effect of amplitude on the maximum predicted VAD axial force and torque at (a), (b) n=6000 rpm, (c), (d) n=9000 rpm, and (e), (f) n=12000 rpm, at different feeds and ω_m = 90 Hz.

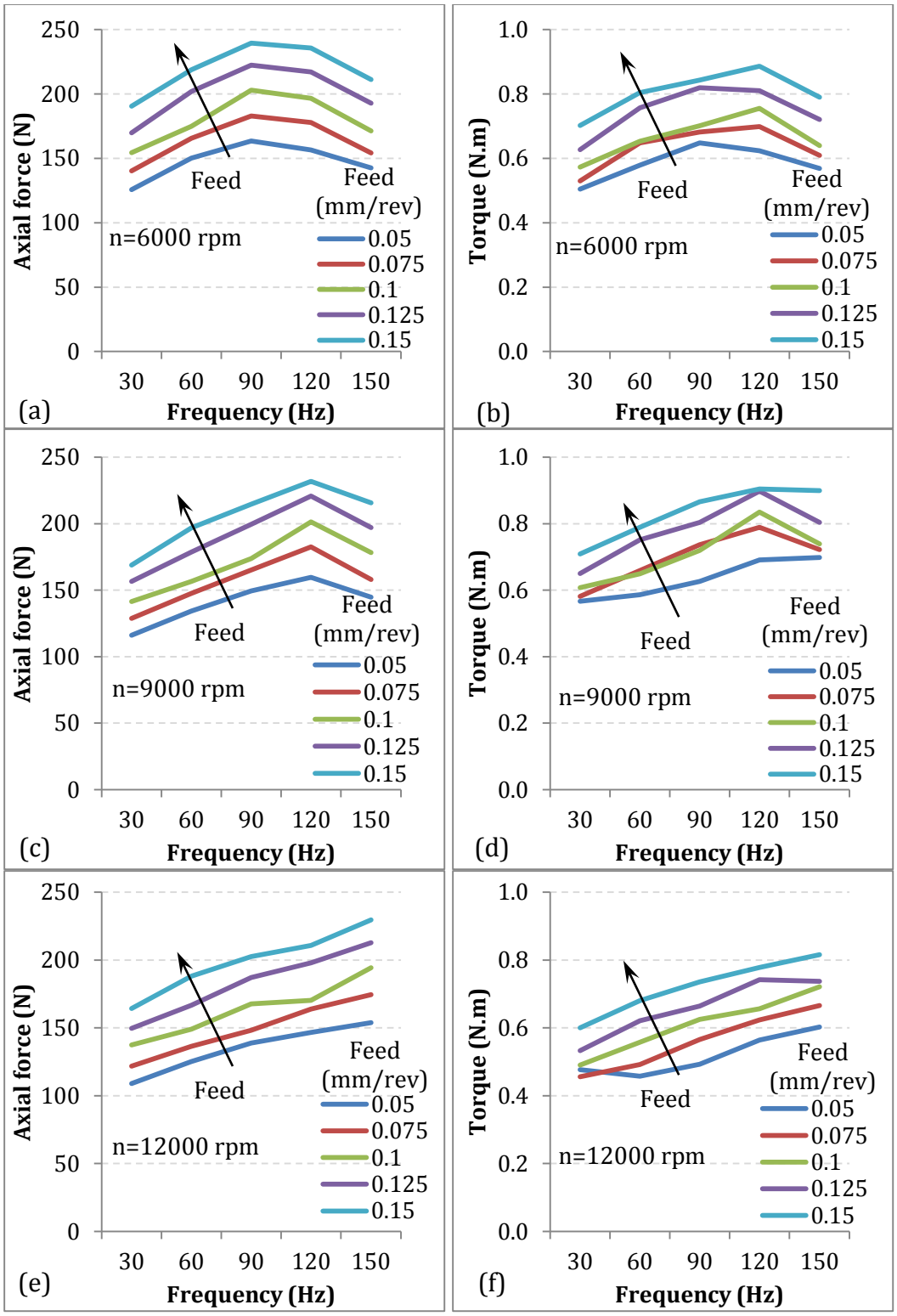

Figure 7-29 Effect of amplitude on the maximum predicted VAD axial force and torque at (a), (b) n=6000 rpm, (c), (d) n=9000 rpm, and (e), (f) n=12000 rpm, at different feeds and A_m = 0.12 mm.

CHAPTER 8

Conclusions and Recommendations for Future Research Work

8.1. Conclusions

The following conclusions could be drawn from the experimental and analytical investigation that has been performed in this research

Conclusions from the experimental investigation of VAD

1. The feed 'f_r' and the modulation amplitude 'A_m' were found to have the most dominant effect on the maximum axial force due to their direct effect on the maximum uncut chip thickness, which was shown to have a strong correlation with the maximum force.
2. For constant 'f_r' and 'A_m', the effect of the modulation frequency 'ω_m' on the maximum axial force was found to be non-monotonic. The critical modulation frequency at which the axial force is maximum depends on the tool rotational speed 'n'. This is due to the resultant effect of 'ω_m' and 'n' on the phase difference between the trajectories of the cutting edges of the vibrating tool, which controls the maximum uncut chip thickness.
3. The hypothesis that the axial speed ratio (ASR) has an intrinsic effect on the VAD process outputs was tested for different ASR values that fulfil the intermittent cutting condition of ASR>1. The results showed that the ASR is not an intrinsic property that can uniquely control the cutting force, temperature and the hole quality attributes. Therefore, the investigation has rejected the proposed hypothesis.
4. The range of low vibration amplitude (A_m<0.1 mm) leads to more effective force reduction, especially with high feed (0.1≤f_r≤0.15 mm/rev) and rotational speed

(n=12,000 rpm), where 40% of axial force reduction can be achieved due to the lower maximum uncut chip thickness in each duty cycle compared to conventional drilling. On the other hand, high amplitudes (A_m=0.4 mm) lead to an increase in the uncut chip thickness, which can increase the axial force by up to 150% compared to conventional drilling.

5. The feed and rotational speed were found to have the most dominant effect on the maximum VAD tool tip temperature at the hole exit, which was found to be reduced by up to 30% compared to conventional drilling in most of the tested VAD conditions. Such significant reduction is due to the formation of vortices in the air gap created during the separation between the tool's flank face and the machined surface. However, for the combined conditions of low feed (f_r=0.05 mm/rev) and medium speed (n=9,000 rpm), the sources of heat generation can be dominant over the sources of heat dissipation. Therefore, the max VAD temperature at these conditions can be increased by up to 25% compared to conventional drilling.
6. The drilling feed was found to have the most dominant effect on the hole exit delamination factor 'ϕ_d'. The experimental investigation showed that the exit delamination could be eliminated or reduced to an allowable range of ($0.0 \leq \phi_d \leq 0.5$) at low and medium feeds (f_r=0.05 mm/rev and f_r=0.1 mm/rev) of VAD compared to conventional drilling. However, this beneficial effect was not achieved at feeds higher than 0.1 mm/rev due to the excessive axial forces.
7. In general, the tested VAD conditions resulted in hole sizes within the allowable tolerance limits (-0.7% to 0.4%) according to the standards followed in the aerospace applications. The conditions of high speed and low or high feed produced hole sizes that exceeded the upper tolerance limit, which could be attributed to the effect of tool dynamics at high speed.
8. The developed hole quality maps for the tested material, tool and cutting conditions were used for selecting the optimum ranges of LFHA VAD parameters based on the objective function of maximum productivity within the constraints of allowable hole quality attributes. The optimum conditions were found to be in a

range that has not been investigated in any previous research; feed f_r=0.1 mm/rev, speed n=12,000 rpm, frequency ω_m=60 Hz, and amplitude A_m =0.2 mm.

Conclusions from the developed generalized force model

A new generalized mechanistic model was developed for conventional and vibration-assisted drilling of multidirectional FRPs. The model can deal with a wide range of process parameters, material configurations and drilling tool geometries, while respecting the fundamental mechanics of the different chip formation mechanisms. It accounts also for the workpiece deformation and the dynamic tool-workpiece interaction during drilling. The following conclusions could be drawn from the results of the developed model:

9. For all tested conditions in the transient and steady state of *conventional* drilling, the predicted force and torque features (variation due to fiber orientation and location of the maximum value) showed a good agreement with the experimental measurements. The force prediction errors ranged from –5% to +16% while the torque prediction error ranged from -10% to +20%, with a confidence interval of 95%. Such an accurate prediction is essential for further assessment of the possible subsequent material and tool damage, whereas the models reported in the open literature could only predict the average force and torque values for the whole drilling process at a certain condition.
10. For all tested conditions of *VAD*, the predictive model was able to capture the force and torque features associated with the dynamic uncut chip thickness, and the changing fiber orientations in the transient and steady state stages. The VAD force and torque prediction errors were in the range of ±20%, with a confidence interval of 95%.
11. The effect of the material deflection due to the axial force on the predicted uncut chip thickness was considered throughout the drilling process. The material deflection was found to have a significant effect on the predicted force and torque at the exit transient stage, where the remaining laminate thickness is small and the axial forces are high. The comparison of the predicted and measured forces at

the exit transient stage showed better agreement when the effect of laminate deflection was accounted for.

12. Considering the effect of the cutting speed and rake angle variation along the primary cutting edge on the predicted forces was shown to be essential for predicting the force distribution along the edge, while it didn't have a significant effect on the accuracy of the total predicted force.

8.2. Recommendations for Future Research Work

The following recommendations are proposed for future research work:

1. Developing an experimental setup for the characterization of the high frequency low amplitude (HFLA) VAD regime, to define the LFHA and HFLA process capabilities and limitations.
2. Developing a multi-objective optimization algorithm to integrate various quality maps with the multi-objective functions of maximum productivity and tool life in VAD, which has a large number of independent process parameters. This can be achieved by extending the work published by the author on evolutionary multi-objective optimization of the orbital drilling process.
3. Developing a semi-analytical model for predicting the tool and workpiece temperatures, knowing the cutting energy from the drilling forces predicted by the analytical model developed in this research work. A CFD model needs to be developed to simulate the formation of vortices in the continuously changing air gap during the VAD separation cycles. This allows define the coefficient of heat transfer from the tool during drilling.
4. Modeling of the tool life based on the predictions of the existing force model and the recommended provisional thermal model.
5. Experimental validation of the model predictions for different geometric features of the drilling tool, namely tool size, point angle, helix angle, number of flutes, web thickness and cutting edge profile. This will allow utilizing the model for tool design optimization.

References

1. S. K. Malhotra, *Some studies on drilling of fibrous composites.* Journal of Materials Processing Technology, 1990. **24**: p. 291-300.
2. D. Bhattacharyya and D. P. W. Horrigan, *A Study of Hole Drilling in Kevlar Composites.* Composites Science and Technology, 1998. **58**(2): p. 267-283.
3. H. Hocheng and H.Y. Puw, *On drilling charachteristics of fiber-reinforced thermoset and thermoplastics.* International Journal of Machine Tools & Manufacture, 1991. **32**(4): p. 592-601.
4. C.C. Tsao, *Experimental study of drilling composite materials with step-core drill.* Journal of Materials and Design, 2008. **29**: p. 1740-1744.
5. U. A. Khashaba, *Delamination in drilling GFR-thermoset composites.* Composite Structures, 2004. **63**(3-4): p. 313-327.
6. S. C. Lin and I. K. Chen, *Drilling carbon fiber-reinforced composite material at high speed.* Wear, 1996. **194**(1-2): p. 156-162.
7. H. Ho-Cheng and C. K. H. Dharan, *Delamination during drilling in composite laminates.* Journal of Engineering for Industry, 1990. **112**(3): p. 236-239.
8. J.P. Davim and P. Reis, *Drilling carbon fiber reinforced plastics manufactured by autoclave--experimental and statistical study.* Materials & Design, 2003. **24**(5): p. 315-324.
9. J. P. Davim and P. Reis, *Study of delamination in drilling carbon fiber reinforced plastics (CFRP) using design experiments.* Composite Structures, 2003. **59**(4): p. 481-487.
10. V. Tagliaferri, G. Caprino, and A. Diterlizzi, *Effect of drilling parameters on the finish and mechanical properties of GFRP composites.* International Journal of Machine Tools and Manufacture, 1990. **30**(1): p. 77-84.
11. E. U. Enemuoh, A. S. El-Gizawy, and A. C. Okafor, *An approach for development of damage-free drilling of carbon fiber reinforced thermosets.* International Journal of Machine Tools and Manufacture, 2001. **41**(12): p. 1795-1814.
12. G. Caprino and V. Tagliaferri, *Damage development in drilling glass fibre reinforced plastics.* International Journal of Machine Tools and Manufacture, 1995. **35**(6): p. 817-829.
13. J. Y. Sheikh-Ahmad, *Mechanics of Chip Formation*, in *Machining of Polymer Composites*2009, Springer: New York.
14. H. Attia, A. Sadek, and M. Meshreki, *High speed machining processes for fibre-reinforced composites*, in *Machining Technology for Composite Materials: Principles and Practice*, H. Hocheng, Editor 2011, Woodhead Publishing.
15. S. Rawat and H. Attia, *Characterization of the dry high speed drilling process of woven composites using Machinability Maps approach.* CIRP Annals - Manufacturing Technology 2009. **58**(1): p. 105-108.

16. D. E. Brehl and T. A. Dow, *Review of vibration-assisted machining.* Precision Engineering, 2008. **32**(3): p. 153-172.

17. J.Y. Sheikh-Ahmad, *Conventional Machining of FRPs*, in *Machining of Polymer Composites*2009, Springer.

18. S. M. Bhatia, P. C. Pandey, and H. S. Shan, *The thermal condition of the tool cutting edge in intermittent cutting.* Wear, 1980. **61**(1): p. 21-30.

19. Y. K. Chou, *Hard turning of M50 steel with different microstructures in continuous and intermittent cutting.* Wear, 2003. **255**(7–12): p. 1388-1394.

20. E. O. Ezugwu and C. I. Okeke, *Tool life and wear mechanisms of TiN coated tools in an intermittent cutting operation.* Journal of Materials Processing Technology, 2001. **116**(1): p. 10-15.

21. T. Kitagawa, A. Kubo, and K. Maekawa, *Temperature and wear of cutting tools in high-speed machining of Inconel 718 and Ti・6Al・6V・2Sn.* Wear, 1997. **202**(2): p. 142-148.

22. Z. Pálmai, *Cutting temperature in intermittent cutting.* International Journal of Machine Tools and Manufacture, 1987. **27**(2): p. 261-274.

23. E. Shamoto and T. Moriwaki, *Study on elliptical vibration cutting.* CIRP Annals - Manufacturing Technology, 1994. **43**(1): p. 35-38.

24. F. Itoigawa, et al., *Experimental study on lubrication mechanism in MQL intermittent cutting process.* MACHINING SCIENCE and TECHNOLOGY, 2007. **11**(3): p. 355-365.

25. R. Lindqvist, I. Eriksson, and M. Wolf. *Orbital drilling of sandwich constructions for space applications*. in *2001 Aerospace Congress*. 2001. Seattle, Washington: SAE Aerospace Automated Fastening Conference.

26. E. Persson, I. Eriksson, and L. Zackrisson, *Effects of hole machining defects on strength and fatigue life of composite laminates.* Composites Part A: Applied Science and Manufacturing, 1997. **28**(2): p. 141-151.

27. E. Persson, I.E.a.P.H., *Propagation of Hole Machining Defects in Pin-Loaded Composite Laminates.* Journal of Composite Materials, 1997. **31**(4): p. 383.

28. R. Iyer, P. Koshy, and E. Ng, *Helical milling: An enabling technology for hard machining precision holes in AISI D2 tool steel.* International Journal of Machine Tools and Manufacture, 2007. **47**(2): p. 205-210.

29. E. Brinksmeier, S. Fangmann, and I. Meyer, *Orbital drilling kinematics.* Production Engineering, 2008. **2**(3): p. 277-283.

30. A. Sadek, M. Meshreki, and M.H. Attia, *Characterization and optimization of orbital drilling of woven carbon fiber reinforced epoxy laminates.* CIRP Annals - Manufacturing Technology, 2012. **61**(1): p. 4.

31. D. Liu, Y. Tang, and W.L. Cong, *A review of mechanical drilling for composite laminates.* Composite Structures, 2012. **94**: p. 1265–1279.

32. Arul, S., et al., *Influence of tool material on dynamics of drilling of GFRP composites.* The International Journal of Advanced Manufacturing Technology, 2006. **29**(7-8): p. 655-662.

33. J. Devine, *Ultrasonically assisted metal removal.* SAMPE Quarterly, 1979. **10**(3): p. 1-6.

34. L.P. Litvinov, *Vibration-assisted drilling of deep holes.* Soviet Engineering Research, 1990. **10**(5): p. 5-8.

35. V. I. Babitsky, A. V. Mitrofanov, and V. V. Silbershcmidt. *Ultrasonically assisted turning of aviation materials: simulations and experimental study*. 2004. Granada, Spain: Elsevier.

36. V.K. Astashev and V.I. Babitsky, *Ultrasonic processes and machines*, ed. V.I. Babitsky and J. Wittenburg2007, Berlin: Springer.

37. P.N. Chhabra, et al., *Low-frequency modulation-assisted drilling using linear drives.* Proceedings of the Institution of Mechanical Engineers, Part B: Journal of Engineering Manufacture, 2002. **216**(3): p. 321-330.

38. S.S.F. Chang and G.M. Bone, *Thrust force model for vibration-assisted drilling of aluminum 6061-T6.* International Journal of Machine Tools and Manufacture, 2009. **49**(14): p. 1070-1076.

39. L. B. Zhang, et al., *Mechanical model for predicting thrust and torque in vibration drilling fibre-reinforced composite materials.* International Journal of Machine Tools and Manufacture, 2001. **41**(5): p. 641-657.

40. V. Babitsky and V. Astashev. *Nonlinear dynamics and control of ultrasonically assisted machining*. 2005. Long Beach, CA, United States: American Society of Mechanical Engineers, New York, NY 10016-5990, United States.

41. V. Babitsky and V. Astashev, *Nonlinear dynamics and control of ultrasonically assisted machining.* JVC/Journal of Vibration and Control, 2007. **13**(5): p. 441-460.

42. V. I. Babitsky, A. N. Kalashnikov, and F. V. Molodtsov, *Autoresonant control of ultrasonically assisted cutting.* Mechatronics, 2004. **14**(1): p. 91-114.

43. H. Paris, et al., *Influence of the ploughing effect on the dynamic behaviour of the self-vibratory drilling head.* CIRP Annals - Manufacturing Technology, 2008. **57**(1): p. 385-388.

44. H. Paris, S. Tichkiewitch, and G. Peigné, *Modelling the vibratory drilling process to foresee cutting parameters.* CIRP Annals - Manufacturing Technology, 2005. **54**(1): p. 367-370.

45. G. Peigne, et al., *Self-excited vibratory drilling: a dimensionless parameter approach for guiding experiments.* Proceedings of the Institution of Mechanical Engineers, Part B (Journal of Engineering Manufacture), 2005. **219**(B1): p. 73-85.

46. H. G. Toews, W. D. Compton, and S. Chandrasekar, *A study of the influence of superimposed low-requency modulation on the drilling process.* Journal of Precision Engineering, 1998. **22**: p. 9.

47. J. Jallageas, et al., *Modeling and optimization of vibration-assisted drilling on positive feed drilling unit.* International Journal of Advanced Manufacturing Technology, 2012. **67**: p. 1205–1216.

48. Deyuan, Z. and W. Lijiang, *Investigation of chip in vibration drilling.* International Journal of Machine Tools and Manufacture, 1998. **38**(3): p. 165-176.

49. J. Ramkumar, S.A., S. K. Malhotra, R. Krishnamurthy, *An enhancement of the machining performance of GFRP by oscillatory assisted drilling.* International Journal of Advanced Manufacturing Technology, 2004. **23**: p. 240–244.

50. Ramkumar, J., S.K. Malhotra, and R. Krishnamurthy, *Effect of workpiece vibration on drilling of GFRP laminates.* Journal of Materials Processing Technology, 2004. **152**(3): p. 329-332.

51. S. Arul, et al., *The effect of vibratory drilling on hole quality in polymeric composites.* International Journal of Machine Tools and Manufacture, 2006. **46**(3-4): p. 252-259.

52. X. Wang, L.J.W., J.P. Tao, *Investigation on thrust in vibration drilling of fiber-reinforced plastics.* Journal of Materials Processing Technology, 2004. **148**: p. 239–244.

53. Neugebauer, R. and A. Stoll, *Ultrasonic application in drilling.* Journal of Materials Processing Technology, 2004. **149**(1-3): p. 633-639.

54. Koplev, A., A. Lystrup, and T. Vorm, *The cutting process, chips, and cutting forces in machining CFRP.* Composites, 1983. **14**(4): p. 371-376.

55. W.-C. Chen, *Some Experimental Investigations In the Drilling of Carbon Fiber-Reinforced Plastic (CFRP) Composite Laminates.* International Journal of Machine Tools and Manufacture, 1997. **37**(8): p. 1097-1108.

56. Kim, D. and M. Ramulu, *Drilling process optimization for graphite/bismaleimide-titanium alloy stacks.* Composite Structures, 2004. **63**(1): p. 101-114.

57. Stephen Batzer, A.G., Sergey Voronov, *Modeling Vibratory Drilling Dynamics.* Vibration and Acoustics, 2001. **123**: p. 9.

58. L.R. Castro, P.V., P.Lipinski, *Correction of dynamic effects on force measurements made with piezoelectric dynamometers.* International Journal of Machine Tools & Manufacture, 2006. **46**: p. 1707-1715.

59. Otho, N.T.a.A., *Dynamometer Performance Modeling and Experimental Assessment.* Journal of Dynamic Systems, Measurement, and Control, 2000. **122** p. 477-482.

60. F. Girardin, D.R.a.J.F.R., *High Frequency Correction of Dynamometer for Cutting Force Observation in Milling.* Journal of Manufacturing Science and Engineering, 2010. **132**: p. 1-8.

61. Okamura, k., *Low Frequency Vibration Drilling of Titanium Alloy.* JSME international journal. Series C, Mechanical systems, machine elements and manufacturing 2006. **49**(1).

62. Sadek, A., et al., *Characterization and optimization of vibration-assisted drilling of fibre reinforced epoxy laminates.* CIRP Annals - Manufacturing Technology, 2013. **62**(1): p. 91-94.

63. Takeyama, H. and N. Iijima, *Machinability of Glassfiber Reinforced Plastics and Application of Ultrasonic Machining.* CIRP Annals - Manufacturing Technology, 1988. **37**(1): p. 93-96.

64. Bhatnagar, N., et al., *On the machining of fiber reinforced plastic (FRP) composite laminates.* International Journal of Machine Tools and Manufacture, 1995. **35**(5): p. 701-716.

65. Zhang, L.C., Zhang, H. J. , Wang, X. M., *A force prediction model for cutting unidirectional fibre-reinforced plastics.* Machining Science and Technology, 2001. **5**(3): p. 12.

66. Arola, D., M. Ramulu, and D.H. Wang, *Chip formation in orthogonal trimming of graphite/epoxy composite.* composites Part A: Applied Science and Manufacturing, 1995. **27A**: p. 13.

67. H. Y. Pwu, H.H., *Chip Formation Model of Cutting fiber-reinforced plastics perpendicular to fiber axis.* Transactions of the ASME, 1998. **120**: p. 5.

68. Wern, C.W., M. Ramulu, and A. Shukla, *Investigation of Stresses in the Orthogonal Cutting of Fiber-reinforced Plastics*, in *SEM Spring Conference*1994: Baltimore, MD. p. 9.

69. Wang, D.H., M. Ramulu, and D. Arola, *Orthogonal cutting mechanisms of graphite/epoxy composite. Part I:Uni-directional laminate.* international Journal of Machine Tools & Manufacture, 1995. **35**(12): p. 16.

70. H. Hocheng, H.Y. Puw, and Y. Huang, *Preliminary study on milling of unidirectional carbon fibre-reinforced plastics.* Journal of Composites Manufacturing, 1993. **4**(2): p. 103-108.

71. Watson, A.R., *Drilling model for cutting lip and chisel edge and comparison of experimental and predicted results. I - Initial cutting lip model.* International journal of machine tool design and research, 1985. **25**(4): p. 19.

72. Watson, A.R., *Drilling model for cutting lip and chisel edge and comparison of experimental and predicted results. II - Revised cutting lip model.* International journal of machine tool design and research, 1985. **25**(4): p. 19.

73. Watson, A.R., *Drilling model for cutting lip and chisel edge and comparison of experimental and predicted results. III - Drilling model for chisel edge.* International journal of machine tool design and research, 1985. **25**(4): p. 16.

74. Williams, R.A., *Dynamic geometry of a twist drill.* International Journal of Production Research, 1968. **7**(4): p. 15.

75. E. J. A. Armarego, C.Y.C., *Drilling with flat rake face and conventional twist drills--I. Theoretical investigation.* International journal of machine tool design and research, 1971. **12**: p. 19.

76. A. Paul, S.G.K., R. E. DeVor, *A Chisel Edge Model for Arbitrary Drill Point Geometry.* Journal of Manufacturing Science and Engineering, 2005. **127**: p. 10.

77. Wang, D.H., M. Ramulu, and D. Arola, *Orthogonal cutting mechanisms of graphite/epoxy composite. Part II:Multi-directional laminate.* international Journal of Machine Tools & Manufacture, 1995. **35**(12): p. 10.

78. Yagishita, H., *Cutting mechanism of drilling CFRP laminates and effect of ultrasonic torsional mode vibration cutting.* Transactions of the north American manufacturing research institution of SME, 2006. **34**: p. 8.

79. Guillaumat, L. and Z. Hamdoun, *Reliability model of drilled composite materials.* Composite Structures, 2006. **74**(4): p. 467-474.

80. Jain, S. and D.C.H. Yang, *Delamination-Free Drilling of Composite Laminates.* Journal of Engineering for Industry, 1994. **116**: p. 7.

81. Mathew, J., N. Ramakrishnan, and N.K. Naik, *Trepanning on unidirectional composites: delamination studies.* Composites Part A: Applied Science and Manufacturing, 1999. **30**(8): p. 951-959.

82. Won, M.S. and C.K.H. Dharan, *Chisel Edge and Pilot Hole Effects in Drilling Composite Laminates.* Journal of Manufacturing Science and Engineering, 2002. **124**(2): p. 242-247.

83. Mohan, N.S., A. Ramachandra, and S.M. Kulkarni, *Machining of Fiber-reinforced Thermoplastics: Influence of Feed and Drill Size on Thrust Force and Torque during Drilling.* Journal of Reinforced Plastics and Composites, 2005. **24**(12): p. 1247-1257.

84. Tsao, C.C. and H. Hocheng, *Evaluation of thrust force and surface roughness in drilling composite material using Taguchi analysis and neural network.* Journal of Materials Processing Technology, 2008. **203**(1): p. 342-348.

85. Herbert, M.A., et al., *Evaluation of thrust force in drilling of BD-CFRP composite using taguchi analysis, response surface methodology and neural network.* European Scientific Journal, 2013. **9**(27).

86. Rajamurugan, T.V., K. Shanmugam, and K. Palanikumar, *Mathematical Model for Predicting Thrust Force in Drilling of GFRP Composites by Multifaceted Drill.* Indian Journal of Science & Technology, 2013. **6**(10).

87. Velumania, S., et al., *Mathematical modeling and prediction of the thrust force and torque in drilling of sisal/glass-vinyl ester hybrid composite using the RSM, MLPNN, RBFN and ENN methods.* INDIAN JOURNAL OF ENGINEERING AND MATERIALS SCIENCES, 2013. **20**(4): p. 289-298.

88. Lastres, M. and C. Dharan, *A thrust and torque prediction for drilling of fiber reinforced syntactic foam.* 2013.

89. D-M Guo, Q.W., H Gao, Y-J Bao, *Prediction of the cutting forces generated in the drilling of carbon-fibre-reinforced plastic composites using a twist drill.* Journal of engineering manufacture 2011. **226**.

90. M. Elhachimi, S.T., P. Joyot, *Mechanical modelling of high speed drilling. 2: predicted and experimental results.* International Journal of Machine Tools and Manufacture, 1999. **39**(4): p. 569-581.

91. M. Elhachimi, S.T., P. Joyot, *Mechanical modelling of high speed drilling. 1: predicting torque and thrust.* International Journal of Machine Tools & Manufacture, 1999. **39**: p. 16.

92. Oxley, P.L.B., *Modelling machining processes with a view to their optimization and to the adaptive control of metal cutting machine tools.* Robotics and Computer-Integrated Manufacturing, 1988. **4**(1–2): p. 103-119.

93. Palani, V., *Finite element simulation of 3D drilling in unidirectional CFRP composite* in *Department of Mechanical Engineering*2006, Wichita State University. p. 109.

94. Vijayaraghavan, A., *Drilling of Fiber-Reinforced Plastics - Tool Modeling and Defect Prediction*, 2006. p. 52.

95. Zitoune, R. and F. Collombet, *Numerical prediction of the thrust force responsible of delamination during the drilling of the long-fibre composite structures.* Composites Part A: Applied Science and Manufacturing, 2007. **38**(3): p. 9.

96. Singh, I., N. Bhatnagar, and P. Viswanath, *Drilling of uni-directional glass fiber reinforced plastics: Experimental and finite element study.* Materials & Design, 2008. **29**(2): p. 546-553.

97. O. Isbilir, E.G., *Three-dimensional numerical modelling of drilling of carbon fiber-reinforced plastic composites.* Journal of Composite Materials, 2013: p. 12.

98. Chandrasekharan, V., S.G. Kapoor, and R.E. DeVor, *A Mechanistic Approach to Predicting the Cutting Forces in Drilling: With Application to Fiber-Reinforced Composite Materials.* Journal of Engineering for Industry, 1995. **117**: p. 12.

99. A. Langella, L. Nele, and A. Maio, *A torque and thrust prediction model for drilling of composite materials.* Journal of composites, part A: Applied science and manufacturing, 2005. **36**: p. 11.

100. D. Kalla, J.S.-A., J. Twomey, *Prediction of cutting forces in helical end milling fiber reinforced polymers.* International Journal of Machine Tools & Manufacture, 2010. **50**: p. 10.

101. Kalla, D.K., *Committee neural network force prediction model of fiber reinforced polymers*, in *Department of industrial and manufacturing engineering*2008, Wichita State University. p. 216.

102. Ahmad, J., *Machining of Polymer Composites*2009, New York: Springer. 230.

103. Ramulu, M., D. Kim, and G. Choi, *Frequency analysis and characterization in orthogonal cutting of glass fiber reinforced composites.* Composites Part A: Applied Science and Manufacturing, 2003. **34**(10): p. 949-962.

104. Sievers, M., et al., *Sludge Dewatering and Aggregate Formation Effects through Taylor Vortex Assisted Flocculation.* Separation Science and Technology, 2008. **43**(7): p. 1595-1609.

105. Boutarfa, R. and S. Harmand, *Local convective heat transfer for laminar and turbulent flow in a rotor-stator system.* Experiments in Fluids, 2005. **38**(2): p. 209-221.

106. Beretta, G.P. and E. Malfa, *Flow and heat transfer in cavities between rotor and stator disks.* International Journal of Heat and Mass Transfer, 2003. **46**(15): p. 2715-2726.

107. Saniei, N., E.D. Erturan, and A.B. Olcay, *Heat Transfer Augmentation of a Co-Rotating Disk Assembly with Special Emphasis on the Lower Disk.* Heat Transfer Engineering, 2004. **25**(4): p. 80-89.

108. Özerdem, B., *Measurement of convective heat transfer coefficient for a horizontal cylinder rotating in quiescent air.* International Communications in Heat and Mass Transfer, 2000. **27**(3): p. 389-395.

109. H.-S. Carslaw, J.-C.J., *Conduction of Heat in Solids*. 2nd edition ed1978: Oxford University Press.

110. Yovanovich, M.M., ed. *Theory and Applications of Constriction and Spreading Resistance Concepts for Microelectronic Thermal Management,* . ed. W. Aung1991 Hemisphere Publishing Corporation.

111. Tsao, C.C., *The effect of pilot hole on delamination when core drill drilling composite materials.* International Journal of Machine Tools and Manufacture, 2006. **46**(12-13): p. 1653-1661.

112. Tsao, C.C. and H. Hocheng, *The effect of chisel length and associated pilot hole on delamination when drilling composite materials.* International Journal of Machine Tools and Manufacture, 2003. **43**(11): p. 1087-1092.

113. Tsao, C.C. and H. Hocheng, *Effects of exit back-up on delamination in drilling composite materials using a saw drill and a core drill.* International Journal of Machine Tools and Manufacture, 2005. **45**(11): p. 1261-1270.

114. Tsao, C.C. and H. Hocheng, *Effect of eccentricity of twist drill and candle stick drill on delamination in drilling composite materials.* International Journal of Machine Tools and Manufacture, 2005. **45**(2): p. 125-130.

115. Tsao, C.-C. and W.-C. Chen, *Prediction of the location of delamination in the drilling of composite laminates.* Journal of Materials Processing Technology, 1997. **70**(1-3): p. 185-189.

116. Drake, P.J., *Dimensioning and tolerancing handbook*, ed. M.-H. handbooks1999, New York: McGraw Hill.

117. Ewins, D.J., *Encyclopedia of Vibration*, S.G. Braun, Editor 2001, Elsevier, : Oxford. p. 805-813.

118. X.M. Wang, L.C.Z., *An experimental investigation into the orthogonal cutting of unidirectional fibre reinforced plastics.* international journal of machine tools and manufacture 2003. **43**: p. 8.

119. Altintas, Y., *Manufacturing Automation*2012: Cambridge University Press.

120. Abrate, S. and D.A. Walton, *Machining of composite materials. Part I: Traditional methods.* Composites Manufacturing, 1992. **3**(2): p. 75-83.